Fakultät für Physik

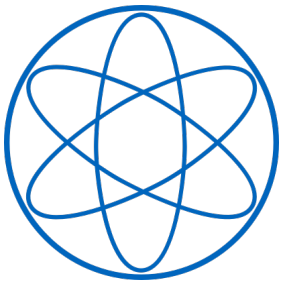

On-Surface Synthesis of Organic Nanostructures and Post-Synthetic Treatments: Decoupling, Structural and Chemical Modifications

Dissertation

von

Atena Rastgoo Lahrood

Technische Universität München

Technische Universität München
Fakultät für Physik
Oskar-von-Miller Lehrstuhl für Wissenschaftskommunikation

On-Surface Synthesis of Organic Nanostructures and Post-Synthetic Treatments: Decoupling, Structural and Chemical Modifications

Atena Rastgoo Lahrood

Vollständiger Abdruck der von der Fakultät für Physik der Technischen Universität München zur Erlangung des akademischen Grades eines

Doktors der Naturwissenschaften

(Dr. rer. nat.)

genehmigten Dissertation.

Vorsitzender: Prof. Dr. Martin Zacharias

Prüfer der Dissertation:

1. Priv.-Doz. Dr. Markus Lackinger
2. Prof. Dr. Florian Klappenberger
3. Prof. Dr. Michael Gottfried (nur schriftliche Beurteilung)

Die Dissertation wurde am 24.05.2017 bei der Technischen Universität München eingereicht und durch die Fakultät für Physik am 05.09.2017 angenommen.

Abstract

In this thesis, the synthesis of low dimensional organic nanostructures on metal surfaces under ultra-high vacuum conditions is studied. Furthermore, post-synthetic treatments of nano-architectures either to decouple them from the underlying substrate or to transform them into new structures have been investigated. Three specific cases are presented here.

In the first case, decoupling of nanostructures from metal substrates is explored. Many important coupling reactions proceed on reactive metal surfaces. However, for many applications, e.g. electronics, conducting supports are precluded. Therefore, methods are introduced to reduce the electronic coupling between synthesized organic networks and metal surfaces. Here we show the detachment and electronic decoupling of synthesized polyphenylene networks on Ag(111) and Au(111) substrates through intercalation of an iodine monolayer. This is achieved through exposure of the sample to iodine vapor. The idea of using iodine for this purpose originates from results of 1,3-diiodobenzene on Cu(111), where in contrast to usual Ullmann couplings, the reaction products were adsorbed atop a closed iodine monolayer.

In the second case, structural transformations of nanostructures through annealing are presented. Room temperature deposition of a thiol-functionalized aromatic molecule on Au(111) results in a less well ordered molecular assembly due to kinetic trapping, stabilized by intermolecular adatom mediated S—Au—S linkages. This assembly is converted into more ordered Au-thiolate chains by annealing. Moreover, an additional step of annealing leads to the formation of covalently linked Sierpinski triangles through a chemical transition, i.e. conversion of Au—thiolate to covalent thioether linkages.

In the third case, a topochemical photopolymerization is targeted to form a defect free long-range ordered covalent structure. The underlying concept was to use an ordered non-covalent assembly and convert it into a covalent network, while maintaining the order. Among various polymerization methods, topochemical photopolymerization provides maximal control of supplied energy at reactive sites of the self-assembled structure. Therefore, the fantrip molecule (FAN) with three photoactive anthracene blades was chosen for this experiment. Yet, the self-assembled structure of FAN on Au(111) deemed not suitable for the photopolymerization, due to improper molecular arrangements steered by strong molecule-substrate interactions. However, a self-assembled structure with appropriate molecular arrangements can be engineered by passivation of Au(111) with an iodine monolayer. While the current data are promising, prospective experiments are needed to prove the success of the photopolymerization.

All nanostructures are characterized by scanning tunneling microscopy (STM) and two powerful surface-sensitive spectroscopic techniques, namely X-ray pho-

toelectron spectroscopy (XPS) and near edge X-ray absorption fine structure (NEXAFS). STM and NEXAFS reveal structural properties of nanostructures, while XPS provides information about the chemical state of specific elements. Moreover, XPS and NEXAFS have the potential to clarify the electronic structure of organic adsorbates on surfaces. Hence, the combination of these three techniques facilitates a comprehensive characterization of synthesized nanostructures.

Contents

Abstract **i**

1 Introduction **1**

2 Tools to Study Surface-Supported Nanoarchitectures **5**
2.1 Scanning Tunneling Microscopy 5
2.1.1 Theoretical Principle 6
2.1.2 STM Image Analysis 7
2.1.3 Experimental Methods and Setup 9
2.2 X-Ray Photoelectron Spectroscopy 10
2.2.1 Theory 10
2.2.2 XP spectra and types of the lines 11
2.2.3 Interpretation of XPS-Data 13
2.2.4 Experimental Setup 14
2.3 Near Edge X-Ray Absorption Fine Structure 15
2.3.1 Theoretical Background 15
2.3.2 Experimental and Data Analysis 18

3 Bottom-Up Synthesis of Organic Nanostructures on Atomically Flat Surfaces **21**
3.1 Supramolecular Self-Assembly 21
3.1.1 Molecule-Substrate Interactions 23
3.1.2 Molecule-Molecule Interactions 25
3.2 On-Surface Polymerization 29
3.2.1 On-Surface Ullmann Coupling 30
3.2.2 Cycloaddition Reactions 31

4 An Exceptional Case of On-Surface Ullmann Coupling **33**
4.1 Introduction 34
4.2 Results and Discussion 34
4.3 Conclusions 41
4.4 Experimental Details 42

5 Post-Synthetic Decoupling of On-Surface-Synthesized Covalent Nanostructures **43**
5.1 Decoupling of Polyphenylene Networks from Ag(111) by Iodine Intercalation 45
5.1.1 Introduction 46
5.1.2 Results and Discussion 46

5.1.3 Conclusions . . . 54
5.1.4 Experimental Details . . . 56
5.2 Decoupling of Polyphenylene Networks from Au(111) by Iodine Intercalation . . . 58
5.2.1 Introduction . . . 59
5.2.2 Room Temperature Iodination . . . 59
5.2.3 Hot Iodination . . . 67
5.2.4 Reversible Iodine Intercalation . . . 69
5.2.5 Conclusions . . . 71
5.2.6 Experimental Details . . . 72

6 Chemical / Structural Modifications of a Thiol-Functionalized Molecule by Annealing 73
6.1 Abstract . . . 75
6.2 Introduction . . . 75
6.3 Results and Discussion . . . 76
6.4 Summary and Outlook . . . 88
6.5 Experimental Details . . . 89

7 Structural / Photochemical Modifications of an Assembly of Fantrip Molecules 91
7.1 2D Crystal Engineering of Fantrip Monolayers . . . 93
7.2 Topochemical Photopolymerization of a FAN Monolayer . . . 100
7.3 Conclusion and Outlook . . . 110
7.4 Experimental Details . . . 111

8 Conclusion 113

A Supplementary Information for DIB on Cu(111) 119

B Supplementary Information for BIB 129
B.1 Supplementary DFT Calculations for BIB on Ag(111) . . . 129
B.2 Supplementary STM Images for BIB on Au(111) . . . 132

C Supplementary Information for TMB on Au(111) 135
C.1 DFT Simulations . . . 135
C.2 Monte-Carlo Simulations . . . 135
C.3 Supplementary STM Images . . . 138

List of Abbreviations 145

List of Figures 147

List of Publications 151

Bibliography 153

Aknowledgments 171

Chapter 1

Introduction

The bottom-up synthesis of low-dimensional organic nanostructures is generally divided into two main categories: supramolecular self-assembly and on-surface polymerization. Synthesis of nanostructures by covalent coupling of monomers on solid surfaces is subject of ever increasing research efforts.[1, 2, 3, 4] Unmatched mechanical, thermal, chemical, and electronic properties of covalent nanostructures render them promising candidates for various nanotechnological applications, as in photovoltaics, photocatalysis, and molecular electronics.[5, 6] Therefore, with a view to potential applications, covalent networks offer crucial advantages over self-assembled supramolecular structures. Hence, on-surface polymerization of several monomers with different methods are investigated in this work.

To be able to characterize on-surface synthesized nanostructures appropriate surface-sensitive and chemically sensitive methods are necessary. Scanning Tunneling Microscopy (STM) as the main method is a powerful technique that resolves nanostructures with submolecular resolution. X-Ray Photoelectron Spectroscopy (XPS) determines chemical composition of the surface as well as chemical state of the elements of interest. Near Edge X-ray Absorption Fine Structure (NEXAFS) clarifies adsorbate orientations with respect to the surface plane and possibly provides information about the electronic structure of the nanoarchitectures. These techniques are described in detail in chapter 2.

The first step towards understanding surface-supported nanostructures is to identify underlying parameters responsible for the formation of nanoarchitectures. Therefore, a short overview of molecule-surface and intermolecular interactions is presented in chapter 3. This chapter gives an overview of supramolecular self-assembly and on-surface polymerization and covers the polymerization reactions used in this thesis.

Diverse coupling strategies have successfully been employed for the on-surface synthesis of covalent organic networks.[7, 8] Among different on-surface synthetic strategies, Ullmann coupling has matured into a well-established method.[9, 10] Except for a few special cases,[11, 12] the critical step of Ullmann coupling, i.e. carbon-halogen bond dissociation, requires reactive metal surfaces. The reaction on metal surfaces, however, inevitably results in adsorption of reaction products, i.e. covalent nanostructures, on these strongly interacting and conducting surfaces. This is unfavorable for electronic applications. Moreover, strong interactions result in structural changes and hybridization of electronic states of the

covalent networks and the underlying metal surface. Hence, the actual properties of the nanostructures are strongly modified on metal surfaces. Consequently, there is a high demand for straightforward methods for post-synthetic decoupling of on-surface synthesized covalent nanostructures from metal surfaces. We propose a solution based on our observations from Ullmann coupling under idodine excess conditions. Under these conditions, the Ullmann coupling does not proceed in a predictable manner. As a noteworthy example, the surface chemistry of 1,3-diiodobenzene (DIB) on Cu(111) is presented in chapter 4. In this case, reaction products adsorb atop a closed iodine monolayer formed on Cu(111), instead of directly on the metal surface. In other words, covalent nanostructures are detached from Cu(111) surface by an iodine buffer layer. The affinity of iodine to metals is apparently strong enough to overcome interactions between the surface and organic nanostructures.

Motivated by the above observations, the exposure of metal-adsorbed covalent nanostructures to iodine vapor is investigated in chapter 5 as a novel and straightforward approach for post-synthetic decoupling. Two-dimensional (2D) porous covalent polyphenylene networks derived from 1,3-bis(*p*-bromophenyl)-5-(*p*-iodophenyl)benzene (BIB) precursors on Ag(111) are chosen as the model system. Moreover, the practicality of the protocol on Ag(111) is investigated on more noble Au(111) surfaces.

With a view to electronic applications, fabrication of conductive nanostructures is desirable. Specific linkages like RS—Au—SR are promising candidates for electronic applications due to their electric conductivity. Therefore, synthesizing nanoarchitectures containing such linkages probably results in a material with favorable electronic properties. In chapter 6, 1,3,5-tris(4-mercaptophenyl)benzene (TMB), a 3-fold symmetric, thiol-functionalized aromatic molecule, is studied on Au(111) with the aim of realizing extended Au—thiolate-linked molecular architectures. The known affinity of thiols to gold[13, 14] results in spontaneous formation of Au—thiolate bonds on Au(111). Moreover, owing to both the extended triphenylbenzene backbone and the three-point anchoring via strong thiolate-surface bonds, planar adsorption is anticipated as an important prerequisite for extended networks. However, extended 2D nanostructures based on RS—Au—SR linkages were never observed. Yet, annealing the samples at 250 °C results in the unexpected conversion of intermolecular Au—thiolate bonds to covalent thioether linkages and formation of 2D Sierpiński triangles based on C—S—C bonds.

For nanotechnological applications, defect free long-range ordered covalent structures are advantageous. Yet, this is challenging due to the irreversibility of covalent bonds. A promising concept is to take an ordered non-covalent assembly of molecules and convert it into robust covalent networks. Among various polymerization reactions, topochemical photopolymerization seems to be a promising candidate. Since, it facilitates the maximal control of the supplied energy at reactive sites of the self-assembled structure. The fantrip molecule (FAN) with three photoactive anthracene blades is chosen for this experiment. In chapter 7, the self-assembly of FAN and its photopolymerization are studied. The photopolymerization of FAN was previously studied in a single-crystal-to-single-crystal approach.[15] However, bottom-up synthesis of 2D polymers (2DPs) by photopolymerization on solid surfaces provides unmatched analytical possibilities and allows us to study photopolymerization reactions on solid surfaces fundamen-

tally. Moreover, the tedious exfoliation process essential to get individual 2DP sheets in single-crystal approach is dispensable here. Yet, deposition of FAN on Au(111) results in a molecular self-assembly that is not suitable for the photopolymerization, due to improper molecular alignments steered by strong molecule-substrate interactions. To solve this, the self-assembled structure with appropriate molecular arrangements is engineered by passivation of Au(111) with an iodine monolayer. With the suitable self-assembled structure of FAN monomers on iodine terminated Au(111), photopolymerization of the structure is investigated in chapter 7.

Chapter 2

Tools to Study Surface-Supported Nanoarchitectures

In this chapter the basic principles of the microscopical and spectroscopical techniques and the corresponding theories are discussed. Scanning Tunneling Microscopy (STM) as main technique together with X-Ray Photoelectron Spectroscopy (XPS) and Near Edge X-Ray Absorption Fine Structure (NEXAFS) as complementary techniques are utilized to study structures and chemical states of organic adsorbates on surfaces. STM provides real space images of the surface-supported nanostructures with resolutions down to the atomic scale, as well as means for manipulation of atoms and molecules on surfaces.[16] STM is almost insensitive to the chemical properties of the structures, hence XPS can be used to gain information about the chemical state. XPS is sensitive to the topmost few nanometers of the surface and provides detailed information about the chemical environment of specific elements. In addition to STM, NEXAFS can add more detailed structural information. Principally, it can also provide information about the electronic structure of the nanoarchitectures. However, a well-established application of NEXAFS measurements is to determine the orientation of adsorbates or their subgroups with respect to (w.r.t.) the surface plane.
The combination of these three techniques facilitates a more complete characterization of the surface-supported nanostructures. It is noteworthy that STM provides local information of the surface due to the limitation of the scan area to a few hundred nanometers. On the contrary, measurements areas of XPS and NEXAFS depend on the size of the X-ray beam, which is usually on the millimeter scale. Consequently, the acquired spectra represents the average information of this area. In the following, the theoretical backgrounds and principles of operation of each technique are introduced.

2.1 Scanning Tunneling Microscopy

In the last two decades STM has been extensively employed to study nanostructures on surfaces.[2, 10, 17] The STM's popularity in this field is related to its variety of applications, from acquiring high resolution images with sub-molecular resolution, to manipulation of the nanostructures on surfaces (see section 5.1 for an example). Moreover, the possibility of recording topographic and spectroscopic data simultaneously (by using STM for Scanning Tunneling Spectroscopy

(STS)) makes this technique more attractive. The local electronic structure of metals, semiconductors, and thin insulators at the atomic scale with amazing spatial resolution can be probed by STS.

2.1.1 Theoretical Principle

STM's operation principle is based on the quantum mechanical tunneling effect. Selected areas on a surface can be scanned with a sharp tip positioned approximately one nanometer away from the surface. According to classical physics, electrons of either tip or sample can not penetrate the gap between the tip and surface. However, according to quantum mechanics view of wave-particle duality, electrons can also behave as waves. If the gap between the tip and sample is small enough that the wave functions of their electrons can overlap, it is possible for the electrons of tip and sample to tunnel from one to the other. This results in an electrical current which can be amplified and used as the signal for indirect measure of tip-sample distance. Gerd Binnig and Heinrich Rohrer constructed such a microscope in 1981, that was able to measure the tunneling current between a sharp tip and a conductive surface while scanning the substrate. Their invention was honored with the Nobel Prize in physics in 1986. The first significant application of STM was the image of a 7×7 reconstruction of Si(111).[18]
A detailed description of the basic principle of the STM can be found in text books.[19, 20] Considering the standard quantum mechanical problem of a particle encountering a rectangular one-dimensional potential barrier facilitates the understanding of the tunneling process.[20] In the tunneling junction the electrons tunnel between tip and sample until the Fermi levels of both materials become equal. To maintain the tunneling current a voltage has to be applied between sample and tip. The tunneling current is directly linked to the transmission probability of the electrons through the energy barrier from filled into empty states of the tip or the substrate. The transmission probability can be determined by the wave function of the electrons using Fermi's golden rule. In conclusion, the tunneling current can be expressed in terms of the equation 2.1.

$$I_T \propto \sum_{E_n=E_F-eV}^{E_F} |\Psi_n(0)|^2 e^{-2\kappa d} \tag{2.1}$$

with E_F as the Fermi energy, E_n the energy of the state n and V the tunneling voltage. Ψ_n is the wave function of the electrons of the state n. d is the distance between tip and sample. The decay constant κ is equal to $\kappa = \hbar^{-1}\sqrt{2m(\varphi - E)}$, with φ as the potential barrier height, E the energy of the electron, and m the electron mass. Equation 2.1 can be rewritten in terms of the local Density of States (LDOS: $\rho(0, E_F) \equiv \frac{1}{eV} \sum_{E_n=E_F-eV}^{E_F} |\Psi_n(0)|^2$) at the Fermi level for sufficiently small tunneling voltages:

$$I_T \propto V \rho(0, E_F) e^{-2kd} \tag{2.2}$$

From equation 2.2, it is evident that the tunneling current decays exponentially with the tunneling distance. This makes STM highly sensitive to the variations of the surface electron density of the outmost atomic layers. For instance, a decrease

of the sample-tip distance of 1 Å results in a ten times larger tunneling current. The high vertical resolution of STM is based on this fact. Moreover, the tunneling current is proportional to the applied voltage and the local Density of States (LDOS) near the Fermi level. Therefore, STM images result from the convolution of the surface and tip's geometric and electronic properties at each point. For this reason, STM images don't feature the pure topographic properties of the surface. Consequently, the measured heights in STM images can not readily be interpreted as geometrical heights of the nanostructures on the surface. A specific structure with larger LDOS, that is geometrically lower than other structures may appear in STM brighter and higher. A well-known example is the adsorption of oxygen atoms on metal surfaces. In STM images adsorbed oxygen atoms appear as depressions despite sitting on top of the metal surface.[21, 22, 23]

2.1.2 STM Image Analysis

The STM calibration can be done by imaging atomically resolved single crystal surfaces. The main challenge after acquiring the STM images is the assignment of the observed features to a structural model based on the chemical structure of the molecular building blocks. In this process, the contrast of the STM images plays a crucial role. An STM image can be affected by parameters such as electrostatic or chemical forces, the distance between tip and surface, or the applied voltage. [22] Out of these parameters, the applied tunneling voltage, especially its polarity influences the STM contrast the most. To understand the contrast mechanism on a surface with adsorbates, the new tunneling junction, i.e. tunneling through the molecules, must be considered. Figure 2.1 illustrates the energy level diagram of the substrate and the STM-tip and the position of the frontier molecular orbitals HOMO (Highest Occupied Molecular Orbital) and LUMO (Lowest Unoccupied Molecular Orbital) of the adsorbed molecules for different tunneling voltage polarities. The work functions of the substrate and the tip (Φ) are assumed to be equal. The positive tunneling voltage is defined as electrons tunneling from the sample into the tip. Hence, a positive tunneling voltage corresponds to a negative sample bias. Figure 2.1(a) demonstrates the case of the positive tunneling voltage, whereby the electrons tunnel out of HOMO into the empty states of the tip. By reversing the polarity of the tunneling voltage, the electrons tunnel from filled states of the tip into the LUMO as shown in Figure 2.1(b). The tunneling junction shown in Figure 2.1 is based on two assumptions: 1) molecule-surface interactions are strong enough that applying a voltage between the substrate and tip does not change relative positions of energy levels of substrate and adsorbed molecules, 2) these interactions are weak enough to allow considering single molecular energy levels instead of hybridized states. Depending on the predominantly involved molecular orbitals in the tunneling process, the same molecular structure might appear with different contrasts and features in STM images.
In reality the situation may be significantly more complex as shown in Figure 2.1. For example, the electronic coupling between adsorbate and metal substrate results in broadening and shifting of the molecular orbital energies, and consequently affects the STM contrast. Moreover, the thermal broadening of the electron energy distributions has to be taken into account.

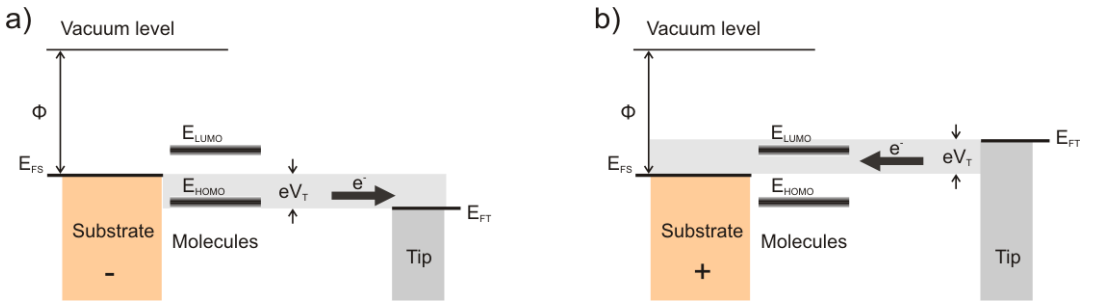

Figure 2.1: Schematic representation of the energy levels for a typical STM tunneling process through an organic molecule for a) positive tunneling voltage (negative sample bias) and b) negative tunneling voltage (positive sample bias). E_{FS} and E_{FT} are the Fermi energies of substrate and tip respectively. The approximate position of HOMO and LUMO can be estimated by pinning the vacuum level of the isolated molecule to that of the substrate. [25]

For the effect of tunneling voltage polarity on the STM contrast, an interesting observation is presented in chapter 4. The di-radicalic terphenyl adsorbed atop of an iodine monolayer on Cu(111) was imaged by positive sample voltages. However, the same structures were invisible to STM with negative sample voltages. The decisive point in this case is the existence of the iodine monolayer between the adsorbates and the metal surface. The iodine layer acts as decoupling layer and also reduces the broadening and shifting of HOMO and LUMO energy levels of the terphenyl. Further examples of contrast variations owing to changes in the electronic coupling of the adsorbate to the surface are presented in sections 5.1 and 5.2. Nevertheless, in many cases the STM contrast of organic adsorbates is independent of the tunneling voltage within a certain range. This phenomenon was explained by the resemblance of HOMO and LUMO of the investigated structures.[24]

Although understanding the underlying reasons of the observed STM contrast is a great help for deriving structural models, in some cases the assignment is not trivial. For instance, if the monomers undergo an unanticipated chemical reaction on the surface, the reaction products might be unidentifiable. The first step to determine the observed structures is to overlay the STM images with scaled optimized geometry of proposed chemical structures. The perfect match is not sufficient to interpret the acquired STM images completely. Supplementary tools such as STM image simulation can yield decisive information. It links theoretical and experimental results and provides a basis for a reasonable determination of the observed architectures.

Modeling of the STM images can be broken down into four steps: creating a model of the surface and of the tip, modeling the interactions between the tip and surface, and last but not least calculating the current. A detailed explanation of all the steps can be read in the work of Hofer and the references herein.[22]

There are four main approaches for estimating the tunneling current: (i) the Tersoff–Hamann approach,[26] (ii) the transfer Hamiltonian or the Bardeen approach,[27] (iii) the scattering or Landauer–Büttiker approach,[28] and (iv) the Keldysh or non-equilibrium Greens function approach.[29] The Tersoff–Hamann

model has established itself as the standard model for three dimensional tunneling in the research of molecular adsorption. Despite several simplifying assumptions, this model provides a reliable qualitative picture of the surface topography. The Tersoff-Hamann approach has also been applied to simulate STM images of studied system in chapter 4.

2.1.3 Experimental Methods and Setup

There are two different measurements modes for STM experiments: constant height and constant current mode. In constant height mode the average height of the tip is fixed and consequently surface's corrugation and topology result in variations of the tunneling currents. The advantage of this mode is the feasibility of fast scanning, since the tip height over the surface doesn't need to be adjusted by the feedback loop. However, for rough surfaces the possibility to damage the tip is very high. In the constant current mode the tunneling current is kept constant through a feedback loop. Depending on the changes in the LDOS of the surface or its topography at each point, the tip-surface distance is adjusted with a piezoactuator to keep the current constant. Hence, the changes in tip height are the signal in this mode.

All the STM images in this thesis are acquired with the constant current mode under ultra-high vacuum (UHV) conditions at a base pressure below 3×10^{-10} mbar. The bias voltages were applied from the sample to the tip. Two different home-built microscopes were used. The STM images in chapters (4 and 6) were acquired with a beetle type STM driven by a SPM100 controller from RHK. The rest of the STM images were acquired with another home-built STM driven by a Nanonis BP4 SPM control system. The main difference between the two microscopes used in this work is their coarse approach mechanisms. Although, both are based on the known stick-slip effect, the structural design of the approach unit is different. In beetle type STM, the position of the tip is fixed and piezoelectric tubes are used for sliding the sample holder on its ramps. In the second microscope the position of the sample holder is fixed and a stacked piezo is used in a nanopositioner to move the tip.[30]

To achieve atomic resolution the systems have to be isolated from internal and external vibrations. Therefore, both UHV chambers are installed on optical tables with four pneumatic damping legs to minimize the disturbing external vibrations. The scanning unit can be suspended by three springs, and additionally using eddy current for damping by a set of mounted magnets, reduces the vibrations further.

Low temperature imaging at sample temperatures ~80 K was done by connecting the STM's scanning unit to a continuous flow cryostat for liquid nitrogen. All STM experiments were done with electrochemically etched tungsten tips. Cu(111), Ag(111) and Au(111) single crystal surfaces and epitaxial Au(111) films on mica were prepared by repeated cycles of Ne^+ or Ar^+ ion-sputtering and electron-beam annealing. The surface cleanliness was verified by STM imaging prior to deposition of the monomers.

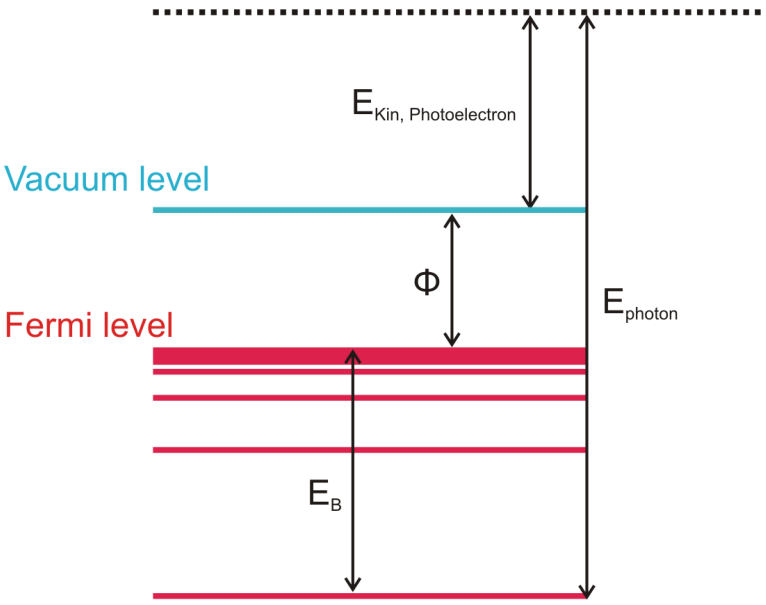

Figure 2.2: Energy level diagram for the emitted photoelectrons in XPS to illustrate equation 2.3.

2.2 X-Ray Photoelectron Spectroscopy

XPS is a powerful surface sensitive spectroscopic technique. It is commonly utilized to obtain information about chemical composition of the surface as well as chemical state of the elements of interest. Furthermore, XPS also provides detailed information about electronic properties of the adsorbates. An example is presented in section 5.1, where a change in the XP spectra of C 1s from an asymmetrical line shape to a symmetrical line shape indicates electronic decoupling of the nanostructures from the metal surface.

2.2.1 Theory

The working principle of XPS is based on the external photoelectric effect. Irradiating the sample with X-ray results in the interaction of core level electrons with the X-ray and consequently the ionization of atoms. These photoelectrons are collected and their kinetic energy is measured by an analyzer. By knowing the kinetic energy of the emitted electrons, their binding energy with respect to the Fermi level can be calculated from equation 2.3, with $h\nu$ as the known photon energy of the monochromatic X-ray radiation and Φ as the work function of the sample. Figure 2.2 shows the related energy diagram to visualize equation 2.3.

$$E_B = h\nu - E_{Kin} - \Phi \tag{2.3}$$

The only missing part to be able to calculate E_B is the work function of the sample. However, simultaneous determination of the work function and a reference level for the binding energy is experimentally challenging. The solution in the modern spectrometers is to connect the sample and the analyzer electrically to equalize their Fermi levels and use the work function of the spectrometer.

The binding energy of the core level electrons is element specific. Accordingly, recording the kinetic energy distribution of the emitted photoelectrons makes it possible to determine the chemical composition of the sample. Moreover, the concentrations of each constituent in the sample can be calculated as well. The stoichiometric ratio of the different chemical species can be determined from the ratio of the different peak intensities in a spectrum. However, the peak intensity also depends on the photoionization cross-section. The photoionization cross-section is in turn element specific and a function of the X-ray energy. Taking these aspects into account, the number of detected photoelectrons per unit time for element x is given by:

$$I_x = n_x f \sigma_x \theta y_x \lambda_{in} A T = n_x S_x \tag{2.4}$$

In equation 2.4 n_x is the number of atoms of an element x per cm^3, f is the X-ray flux, σ_x is the photoionization cross-section for the core level under investigation, θ is the angular efficiency factor of the instrument, y_x is the efficiency in the photoelectron formation process, λ_{in} is the inelastic mean free path of the photoelectrons, A is the analysis area on the sample, and T is the detection efficiency.[31] Introducing the parameter S_x, the atomic sensitivity factor, as $S_x = f \sigma_x \theta y_x \lambda_{in} A T$ simplifies the equation. Consequently, the concentration of each element x can be attained by:

$$C_x = \frac{n_x}{\sum\limits_i n_i} = \frac{I_x / S_x}{\sum\limits_i I_i / S_i} \tag{2.5}$$

In principle, this can also be used to determine the coverage of organic nanostructures on the surface, for instance by calculating the ratio of C_C to $C_{Substrate}$. However, the problem is that the substrate peak doesn't include only the photoelectrons from the first monolayer. Yet, the intensity of the substrate peak without the photoelectrons from deeper atomic layers can be roughly estimated using the inelastic mean free path of the photoelectrons (λ_{in}) in the substrate. The corrected intensity of the substrate peak can be used to calculate the coverage of nanoarchitectures approximately. Nevertheless, the more exact solution is having the ratio of C_C to $C_{Substrate}$ from a sample with defined monolayer coverage and use it as the reference for other experiments.
Apart from the hard X-ray photoelectron spectroscopy, the typical energy range of the X-ray in XPS measurements is around 100-1500 eV. Although the penetration depth of the X-ray with this energy in the sample amounts to several microns, the information depth of XPS is in the range of 1 to 10 nm.[32] The reason is the small inelastic mean free path (λ_{in}) of electrons in solids on the order of nm (0.5 nm to 5 nm).[32] Therefore, only photoelectrons generated in the top few atomic layers can leave the sample, rendering XPS a surface sensitive spectroscopic tool.

2.2.2 XP spectra and types of the lines

XPS spectra record the photoelectron intensity at different binding or kinetic energies. A typical spectrum consists of well-defined sharp peaks (photoelectron lines) originating from the electrons from inner shells of the atoms over a background. There is always a slight increase of the background towards higher

Orbital	Orbital quantum number l	$j_{\pm} = l \pm s$	Intensity ratio$=\frac{2j_{-}+1}{2j_{+}+1}$
s	0	1/2	-
p	1	1/2, 3/2	1/2
d	2	3/2, 5/2	2/3
f	3	5/2, 7/2	3/4

Table 2.1: Quantum numbers relevant for understanding the spin-orbit splitting and the intensity ratio of spin-orbit-doublets in XPS.

binding energies (lower kinetic energies) after each peak. Part of the photoelectrons lose part of their kinetic energy through inelastic scattering in the sample; consequently this results in the increase of the background at higher binding energies. Beside photoelectron lines, there are other types of peaks and features in XPS spectra. The most important ones are Auger lines, shake-up lines, X-ray satellites, spin-orbit splitting, and valence lines/bands. A detailed explanation of each feature can be found in the handbook of XPS.[31] Here, the spin-orbit splitting is described; because of its relevance for the measurements in this thesis. For electrons from the same core level, spin-orbit coupling results in the emergence of two peaks (spin-orbit doublet) in XP spectra. The reason for the existence of two energy sub-levels for the electrons in the same core level is the interaction between their spin magnetic momentum and orbital angular momentum. In other words, the magnetic field form the electron spin interacts with the magnetic field from its rotation around the nucleus. Two possible spin orientations, namely up and down, result in existence of two energy sub-levels. Moreover, the splitting of the core levels takes place only for the shells with a non-zero orbital quantum number ($l \neq 0$). Therefore, the spin-orbit effect doesn't exist for s orbitals.
From the quantum mechanical point of view, all electron's energy states in an atom can be described by assignment of four quantum numbers (the principal n, the azimuthal (orbital) l, the magnetic m_l, and the spin s quantum number) to each electron.[33] A detailed explanation of these quantum numbers can be found in quantum mechanics text books. [33, 34] As mentioned before the spin-orbit coupling is the result of the interaction between spin magnetic momentum and orbital angular momentum, related to the quantum numbers s and l respectively. The total angular momentum $j_{\pm} = l \pm s$ of the core level characterizes the allowed energy states due to this interaction. With spin quantum number $s = \frac{1}{2}$, the total angular momentum is equal to $j_{\pm} = l \pm \frac{1}{2}$.
The energy spacing and intensity ratio of spin-orbit doublets have defined values. The number of degenerated states amounts to $2j+1$ for each quantum number j. Therefore, the intensity ratio of the two peaks in the doublet can be calculated accordingly as shown in the table 2.1.
For instance, the spin-orbit coupling of the electrons in the p orbital results in two states for each quantum number j, namely $p_{1/2}$ and $p_{3/2}$ with intensity ratio of 1/2. The state with larger j (e.g. $2p_{3/2}$) has the lower binding energy. An example is shown in Figure 2.3 indicating the XP spectrum of a S 2p doublet of the molecules studied in chapter 6.

The energy difference between the peaks of the doublet is larger for stronger spin-orbit coupling. The stronger the interaction of the electrons with the nucleus, the

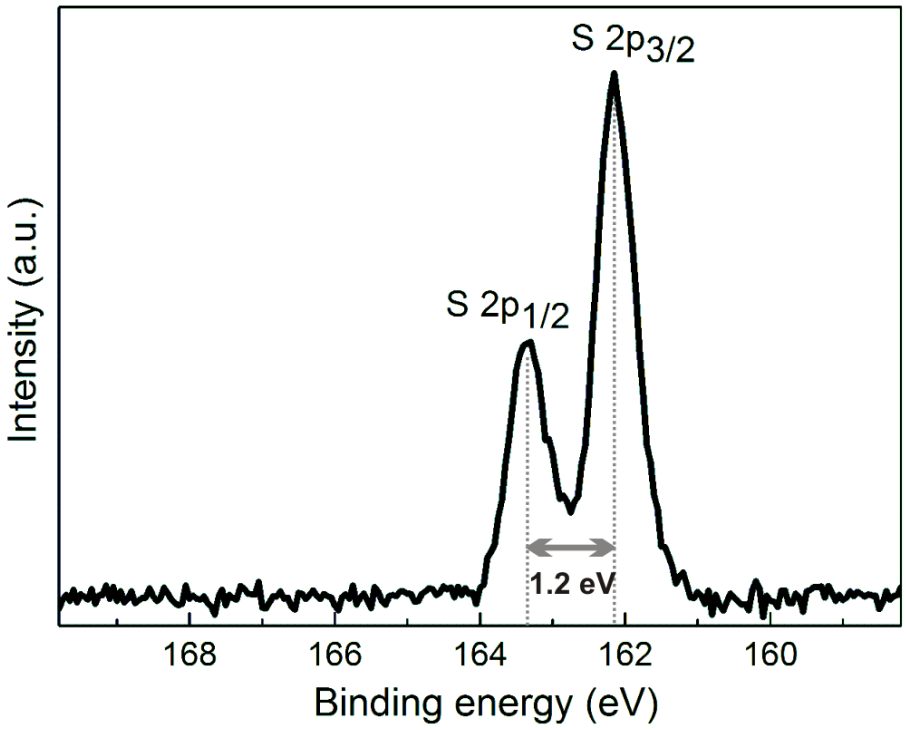

Figure 2.3: XP spectrum of S 2p consists of a 1/2 and 3/2 spin-orbit doublet. The two peaks of the doublet (S $2p_{1/2}$ and S $2p_{3/2}$) with a fixed energy separation of 1.2 eV and a fixed intensity ratio of 1/2 are indicated.

more distinct is the energy spacing of the doublet. Consequently, for states with the same n and l the energy spacing increases with increasing atomic number Z. For light elements (Z<18) the energy spacing in the doublet is very small and can only be resolved by high resolution spectrometers.[35] For same Z, the energy spacing decreases with increasing n for the same l values and with increasing l for the same n. The weaker interaction of the electrons with the nucleus can be explained through the larger distances of the electrons in energy levels with higher n and l to the nucleus.

2.2.3 Interpretation of XPS-Data

To fit an XPS peak appropriately two factors have to be considered: type of background and shape of the photoelectron line (singlet or doublet). The different background signals, such as Shirley and Tougaard are discussed in various XPS books.[35] In this work linear backgrounds were subtracted from all XP spectra, suggested by the linear routine of the background progression. Although it is a simple approach, it can provide reasonable results. The most challenging part is to determine the number of components of the peak. For peaks consisting of more than one component, the choice of the number of components has to be done based on chemical intuitions supported by secondary data and with the help of the known binding energies of different species from literature (see fitting the peak S 2p after annealing in chapter 6). Generally, the existence of more than one component is due to the various chemical bonds of the atom under study to surrounding atoms. Although, core levels are usually not involved in the chemical

bonds, changes in the chemical environment, i.e. in the valence electron density, can impose a partial charge on the atom. This fractional charge is sufficient to modify the electrical potential experienced by the core level electrons and result in a shift in their binding energies. Using these shifts, the chemical state of the elements under study can be assessed. To be able to compare the binding energies of the same elements from different measurement series, the designation of a common reference for the binding energy in necessary. Commonly, the binding energy of the substrate peak is used for this purpose. In this thesis, an Ag $3d_{5/2}$ binding energy of 367.9 eV or an Au $4f_{7/2}$ binding energy of 83.8 eV were used as internal references.
Beside determining the chemical nature of the bonds, XPS can also be applied to trace the desorption of specific species from the surface (e.g. iodine in 5.2). Moreover, another application of XPS is to monitor a chemical reaction progress. This application is described in detail in chapter 6 by observing the changes in the spectra of S 2p.

2.2.4 Experimental Setup

XPS experiments were conducted at the BESSY II synchrotron (Helmholtz-Zentrum Berlin) at the HE-SGM (High Energy-Spherical Grating Monochromator) beamline. The advantages of the synchrotron to the conventional laboratory X-ray sources (typical photon energies larger than 1 keV) are high intensities and the possibility to change the photon energy. The higher X-ray flux of synchrotron radiation facilitates to measure weak signals in a relatively short time. Moreover, the variable photon energy is beneficial, because it allows the measurement of various elements at photon energies that maximize their photoionization cross-sections.
Different beamlines of BESSY II provide synchrotron radiations with different properties (energy range, flux, polarization,...). The HE-SGM beamline is a dipole beamline with a photon energy range of 100 eV to 750 eV and a X-ray flux up to 5×10^{11} photons/(s $\cdot$ 100 mA). Moreover, the X-ray is horizontally polarized with a degree of 91 %.[36] The size of the elliptical X-ray spot on the sample is 1.2 mm $\times$ 0.5 mm.[36] Proper experimental data from organic molecular thin films with coverage down to 0.1 monolayer can be achieved at this beamline.[36]
HE-SGM is equipped with a Prevac end station consisting of four separate chambers: a load lock, an UFO shaped chamber for sample transfer and distribution as well as preparation and analysis chambers. The load lock chamber was used for iodination experiments to avoid the contamination of the other parts. The installed continuous flow cryostat for liquid nitrogen in the analysis chamber allowed to perform the measurements at sample temperatures around 80 K if desired.
Sample preparation was similar to the STM experiments. The surface cleanliness was verified by overview XPS measurements and additional C1s measurements prior to deposition of the monomers. The XP spectra were acquired using a VG Scienta R3000 hemispherical electron energy analyzer. The electrons with a kinetic energy in range of 0.5 eV to 1500 eV can be detected by this analyzer.[37] The pass energies of the electrons can be set from 2 to 200 eV.[37] All the XP spectra in this thesis were acquired with a pass energy of 50 eV. The X-ray

beam had an incidence angle of 45° relative to the surface normal, however, the photoelectrons were detected at normal emission.

2.3 Near Edge X-Ray Absorption Fine Structure

NEXAFS is an X-ray absorption spectroscopy which can be used for the characterization of nanostructures, as it provides valuable information about the electronic structure, chemical states and orientation of molecular adsorbates on surfaces. In this thesis, it was mainly used to determine the orientation of phenyl rings in nanostructures w.r.t. the surface. NEXAFS is based on resonant excitation of core level electrons into unoccupied electronic states by linearly polarized X-rays. The photoabsorption cross-section (directly correlated to the absorption intensity) depends on the relative orientation of X-ray electric field and transition dipole moment (TDM). Since the TDM has a defined orientation w.r.t. the molecule, this facilitates a tilt angle quantification of specific functional groups w.r.t. the surface based on the resonance intensities. To determine the tilt angle of a specific chemical group the changes in the resonance intensity due to the variation of the X-ray incidence angle is used. For instance, phenyl tilt angles in an organic compound can be quantified from the incidence angle dependence of intensities of C 1s$\rightarrow\pi^*$ transitions.

2.3.1 Theoretical Background

The basic principle of NEXAFS similar to the one for XPS is based on the photoelectric effect. However, in XPS the external photoelectric effect is used, while in NEXAFS the internal photoelectric effect is utilized. X-ray radiation is used to excite the core level electrons into unoccupied molecular states. In contrast to XPS, the photon energy is not kept constant in NEXAFS measurements. The X-ray absorption is measured as a function of photon energy. While scanning over a photon energy interval, an absorption peak will be observed when the core level electrons are excited into an unoccupied state. Therefore, NEXAFS spectra indicate the dependency of the photoabsorption cross-section on the photon energy for values from just below the absorption edge up to approximately 50 eV above. This energy range typically shows the marked variations in the X-ray absorption and usually features intense and distinct resonances.
For an oversimplified case of an electron located in a single bound state without any further unoccupied electronic states, the NEXAFS spectrum would resemble a step function. For photon energies below the "binding energy" of the electron no X-ray absorption can take place, whereas for photon energies above the "ionization threshold" an excitation of the electron into the continuum of final states would occur. However, even for a free single atom the situation is more complicated, due to the existence of considerably more final states. The electrostatic potential of the positively charged nucleus, gives rise to a number of empty electronic states below and above the ionization threshold. For atoms incorporated in larger molecules there are even more final states available, including the unoccupied molecular states. For instance, the schematic potential of a diatomic molecular group and the corresponding absorption possibilities (NEXAFS spectrum) can be seen in the review of Hähner.[38]

The transition of core level electrons into discrete unoccupied molecular orbitals accounts for the absorption fine structure and provides information about the local bonding environment. Therefore, NEXAFS is an appropriate tool to investigate the bond-specific properties of a molecule. Absorption peaks at distinct photon energies corresponds to specific elements. Even, the same element in chemically different surroundings in an organic compound give rise to chemically shifted resonances in NEXAFS spectra.[39, 40]
As mentioned before, NEXAFS can be used to determine the orientation of specific molecular groups, or more precisely the orientation of a molecular orbital into which the core level electron is excited w.r.t. the surface. The X-ray absorption intensity is proportional to the dot product of X-ray electric field vector and TDM ($I \sim \overrightarrow{E} \cdot \overrightarrow{TDM}$). Therefore, if the electric field vector of the X-ray is parallel to TDM, the maximal X-ray absorption is observed. It results in an intensity maximum in NEXAFS. For aromatic molecules the transition from the C 1s state to the unoccupied π^* and σ^* orbitals, can be efficiently studied by NEXAFS. The reason is the distinct TDM orientation of these transitions to π^* or σ^* orbitals, being perpendicular or parallel to the aromatic ring, respectively. Therefore, the alignment of molecules w.r.t. the surface can be determined by acquiring NEXAFS spectra with various X-ray incidence angles. A simple example, i.e. NEXAFS spectra of a flat lying benzene molecule on a surface, is illustrated in Figure 2.4. The NEXAFS spectra for two different X-ray incidence angles are depicted. For a flat benzene ring the TDM of π^* resonance is perpendicular to the surface (TDM of σ^* resonance parallel to the surface). Consequently, for normal X-ray incidence, the electric filed vector and TDM of π^* resonance are perpendicular to each other (lower part of the Figure 2.4). Therefore, the electrons can not be excited into the π^* unoccupied states, and no X-ray are absorbed in the energy range of C 1s$\rightarrow\pi^*$ transition, resulting in a π^* resonance intensity zero in the NEXAFS spectra. On the other hand, for grazing incidences the dot product of X-ray electric field vector and TDM is larger resulting in an increase of the π^* resonance intensity. Obviously, the process is vice versa for σ^* resonances, being largest at normal incidence and smallest at grazing incidence angles. However, the strong and sharp peaks of π^* resonances are commonly used for data evaluations, rather than σ^* resonances.
The intensity of the π^* resonances as a function of X-ray incidence angles can be calculated theoretically for various TDM orientations.[41] The orientation of an arbitrary TDM vector, analogous to every spatial vector, can generally be specified by a combination of polar angle α and azimuthal angle φ. However, the azimuthal dependence of resonance intensities is eliminated in many cases by the surface symmetry. For molecules adsorbed on a surface with an at least threefold symmetry, there is an averaging over the azimuthal angle φ. Consequently, NEXAFS resonance intensities as a function of X-ray incidence angles θ can be expressed as:

$$I \propto P\cos^2\theta(1-\frac{3}{2}\sin^2\alpha)+\frac{1}{2}\sin^2\alpha \tag{2.6}$$

where P stands for the degree of X-ray polarization. Therefore, for sufficiently well ordered molecules on surfaces the molecular orbital orientation α can be deduced from the angle-dependent X-ray absorption. Experimental examples of

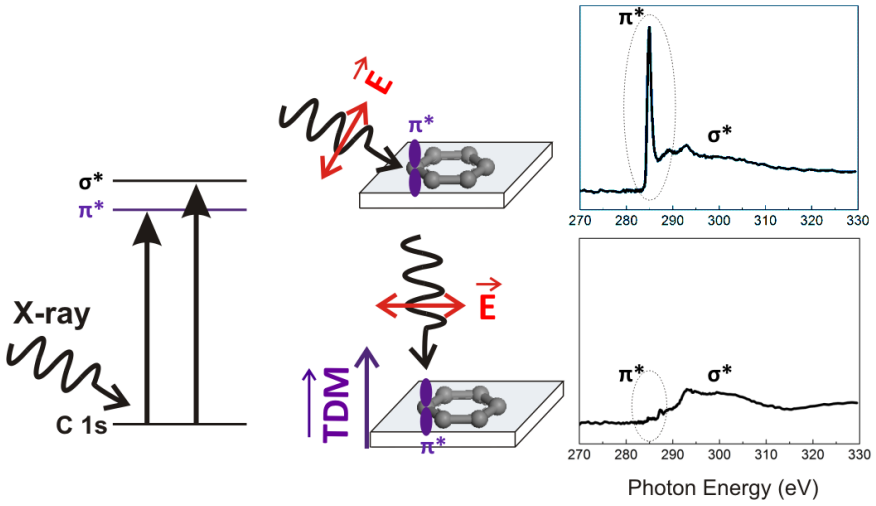

Figure 2.4: The X-ray incidence angle dependence of π^* and σ^* resonances intensities for a flat lying benzene molecule on the surface (σ^* orbitals are not shown for clarity).

molecular orientation determination can be found in sections 5.1 and 5.2 and chapter 7.

NEXAFS can also be used to obtain information about the electronic structure of the unoccupied molecular states. A well-known example is the difference in the NEXAFS spectra of physisorbed and chemisorbed benzene with respect to gas phase spectra. These changes arise from physical (e.g. final state effects, screening of the core hole by the metal substrate) as well as from chemical (e.g. changes of electronic structure as a result of the benzene-metal bonding) interactions. For the case that benzene adsorbs on transition metal surfaces, the strong interaction between benzene and substrate results in the formation of a stable chemical adsorbate-substrate bond. The strongest modifications in the NEXAFS spectra is observed for the benzene π^* resonance. The chemisorption leads to a significant broadening of the π^* resonance, since the corresponding orbitals are involved in the bonding to the substrate. Even the physisorption of benzene on the most inert metal Au results in broadening of the π^* resonance as compared to the gas phase.[42] Experimental evidence for tracking the changes in the electronic structure by NEXAFS is presented in section 5.1. Detachment of the nanostructures from the Ag(111) surface by iodine intercalation results in sharpening of the C 1s NEXAFS spectra. However, the coadsorption of iodine on the Au(111) surface (without detachment of nanostructures) also results in sharpening the π^* resonance (see section 5.2). The precise origin of the latter effect is not completely understood, but it might be related to the change in the screening of the core hole by the metal substrate in the presence of iodine. Generally, the measured width of a resonance is determined by the resolution of the instrument (resulting in a Gaussian lineshape), the lifetime of the excited state (resulting in a Lorentzian lineshape), and the vibrational motion of the molecule leading to an unsymmetrical broadening.[43] A more detailed overview on NEXAFS technique can be found in references.[38, 41]

From the basic principle of this technique it is obvious that a linearly polarized X-ray is required to do these experiments. It is important to keep in mind that the spatial resolution of NEXAFS is determined by the spot size of the X-rays on the surface and the acceptance area of the analyzer. Therefore, the obtained information are values averaged over a macroscopic (mm-sized) area.
There are different ways to measure the X-ray absorption. For reasonably thin samples, where the X-ray can pass through the whole sample, it can be done directly by recording the transmitted X-ray intensity. However, to perform surface sensitive experiments the absorption has to be measured indirectly. The core hole resulting from the excitation of the core electron into unoccupied molecular states, is subsequently filled by an electron from a higher energy state. This results in the emission of either an Auger electron or characteristic X-rays. The intensity of the emitted Auger electrons or photons is an indirect measure of the X-ray absorption. In this thesis, NEXAFS spectra were acquired by detecting the Auger electrons.

2.3.2 Experimental and Data Analysis

For NEXAFS measurements a tunable and linearly polarized X-ray light source is required to be able to scan over a photon energy range. Synchrotron radiation fulfills this criterion. The wide energy range of the synchrotron radiation allows the excitation of the core electrons of a large variety of elements. Moreover, the high intensity of the X-rays facilitates studies at submonolayer coverage. Therefore, like XPS experiments, NEXAFS measurements were conducted at the BESSY II synchrotron in the same end station.
As mentioned before, the spectra are acquired by detecting the emitted Auger electrons generated by the decay of the core hole. However, the inelastic scattering of the emitted Auger electrons leads to an electron cascade. Among these generated secondary electrons, the ones with sufficient kinetic energy can escape the surface and reach the detector as well. The most common modes for measuring NEXAFS spectra are total and partial electron yield modes (TEY and PEY respectively). In TEY mode, all electrons that emerge from the surface including both Auger and secondary electrons are detected. In PEY mode the main part of the secondary electrons are filtered out. For this purpose, the detector features a grid where a retarding voltage is applied. This voltage also allows to adjust the surface sensitivity of the measurement, since dependent on its value either all secondary electrons or just part of them with relatively low kinetic energies from deeper atomic layers can be filtered out. The PEY mode has a better signal-to-background ratio than the TEY mode. This makes PEY detection mode more suitable for investigation of adsorbates on surfaces.
C 1s NEXAFS spectra in this thesis were acquired in the analysis chamber using a home-built double channel plate detector in PEY mode, i.e. with a counter voltage of -150 V. Spectra were acquired for X-ray incidence angles (w.r.t. the surface plane) of 30°, 45°, 55°, 70°, and 90°. Photon energies were corrected with an internal carbon reference. For background correction, the spectra of clean substrates, i.e. Ag(111) or Au(111), were used. Moreover, the spectra of clean Au(111) were used for photon flux correction for all kind of substrates. For quantitative determination of the phenyl tilt angles, the intensities of the C

1s$\rightarrow\pi^*$ (the peak maximum values) were plotted versus incidence angles. The best possible match between the theoretically determined curves for different tilt angles and the measured data yields the tilt angle. The beamline-specific degree of linear polarization of P=0.92 was considered for the calculation of theoretical curves. However, the results of the tilt angle determination are only at best within a certainty interval of $\pm5°$, typically $\pm10°$.

Chapter 3

Bottom-Up Synthesis of Organic Nanostructures on Atomically Flat Surfaces

In general, the bottom-up synthesis of organic nanoarchitectures on surfaces can be divided into two distinct classes: assembly of functional molecular building blocks and surface-supported covalent linking of molecular building blocks (polymerization).
The first class, molecular self-assembly, is a well-established strategy for the bottom-up fabrication of long-range ordered nanostructures. Moreover, assembly of functional molecules on surfaces is also particularly promising for the fabrication of electronic circuits based on the functionalities of individual molecular species.[44, 45] The self-assembled structures are formed by various intermolecular interactions such as van der Waals interactions, hydrogen bonds, halogen bonds, and metal-coordination bonds. The reversibility of these bonds fulfill the requirements needed to fabricate long-range ordered structures without defects.[17, 46] However, such structures are less stable due to the weak intermolecular interactions, resulting in poor mechanical, chemical and thermal stability and low charge-transport efficiency. Consequently, these assemblies are less relevant for many potential technological applications.[47, 48]
In the second class of bottom-up synthesis, the molecular arrangements are stabilized through covalent linking. Although there are various covalent on-surface polymerization reactions, they all have common aspects. Owing to the irreversibility of the covalent bonds, fabrication of defect-free long-range ordered structures is challenging. However, the strong nature of the covalent bonds provides high stability and robustness to the resulting nanostructures. Moreover, it can facilitate the efficient charge transport through bonds.[49, 50, 51] These properties are indispensable for potential use in technological applications. In the next sections the characteristics of supramolecular self-assembly and surface-supported polymerization are discussed thoroughly.

3.1 Supramolecular Self-Assembly

The term self-assembly was coined in the 1960s.[17] Self-assembly can be defined as the process by which a supramolecular species forms spontaneously from its

components.[52] For many synthetic systems it appears to be a simple convergent process, giving rise to the assembled target in a straightforward manner.[53] To conceive the self assembly process, one can consider the individual molecules as building blocks, endowed with the ability to seek out, recognize and associate with their appropriate partners in the final assembly.[53] Self-assembly can be found in an extensive field of chemical systems, as for instance in crystal growth[54], liquid crystal formation[55, 56], synthesis of metal coordinated complexes[57, 58] and arrangements of molecules on surfaces.[59] The present work is limited to surface-supported self-assembly under UHV conditions.

The study of molecular self-assembly on surfaces is the process of turning the primarily random distribution of molecules into a defined arrangement, mostly a well-ordered pattern as well as seemingly irregular ones. This process is driven by non-covalent interactions, including metal-coordination bonds, $\pi - \pi$ interactions, and van der Waals forces. The natural reversibility of these bonds drives the self-assembled system towards its thermodynamic equilibrium. The reason is that the equilibrium can only be reached if a large number of rearrangements and reorientations of the molecules are probed. This in turn is only possible if the intermolecular bonds can be broken and form over and over.

Systems in thermodynamic equilibrium are simultaneously in thermal, mechanical and chemical equilibria. Under UHV the experimental systems can be assumed isobaric and isothermal. This implies that systems are anyhow in mechanical and thermal equilibrium. Therefore, only if chemical equilibrium is achieved the system will be in complete thermodynamic equilibrium.

At constant pressure and temperature, chemical equilibrium is reached through the minimization of Gibbs free energy. Accordingly, the change in the Gibbs free energy (ΔG in equation 3.1) of the system in the self-assembly process for a stable final structure has to be negative.

$$\triangle G = \triangle H - T \triangle S \tag{3.1}$$

ΔH is the enthalpy change and ΔS is the entropy change of the system. For a self-assembled structure of molecules on a surface formed under UHV conditions ΔS is negative, due to the restriction of the degree of freedom of molecular motions and orientations. As a result, the only way to obtain a negative ΔG is having a negative ΔH with a magnitude larger than TΔS. This is the case for stable self-assembled structures, where the enthalpy of the system is reduced (or even reached its minimum) through optimization of molecule-molecule and molecule-substrate interactions during the self-assembly process.

For assemblies with weak or moderate bonds, however, the reduction in the enthalpy of the system may not be sufficient to overcome the entropy term, rendering self assembly thermodynamically unstable. Hence, self assembly can not occur spontaneously.

In some cases, the self-assembled structures may still form under kinetic control rather than thermodynamic. Although ΔG is negative in these cases, the system is only in a relative minimum rather than the absolute one. This situation is more likely for large molecules with many intermolecular contacts, especially when more flexible building blocks are involved. It also tends to occur when metal ions, especially kinetically inert ones, are incorporated into the supramolecular structure.[52] The transition into the thermodynamically favorable structure is in

these cases kinetically hindered. An example of a self-assembled structure formed due to kinetic trapping is presented in chapter 6. The competition between kinetic and thermodynamic control in the formation of self-assembled structures is significantly influenced by the temperature of the system. Increasing the system temperature enables transitions from metastable to thermodynamically more stable phases that are kinetically hindered at room temperature[17] (see chapter 6).
The most crucial point in the definition of molecular self-assembly on surfaces is its occurrence without external stimuli. It is just governed by local molecule-molecule and molecule-substrate interactions.[60, 61] To understand the important parameters for self-assembly the following subsections describe these interactions.

3.1.1 Molecule-Substrate Interactions

Molecule-surface interactions are decisive for the self-assembly of organic adsorbate on surfaces and can affect it in several ways.[62] First, upon adsorption the molecules on a surface are confined into two dimensions. Consequently, they encounter limitations in their translational, rotational and vibrational movements.[46] Moreover, the surface can affect the mobility and conformation of the molecules depending on its symmetry, reactivity or electronic properties.[17] In this way surfaces can directly influence the self-assembly.
Surfaces have properties absent in the bulk, which make them highly attractive for molecular studies. These characteristics are due to the breaking of the crystal periodicity leaving the surface with unsaturated bonds. The interactions between adsorbed molecules and surfaces is classified into two different types: physisorption and chemisorption. Physisorption is a weak adsorption where polarization (dispersion) forces, such as van der Waals interactions, bind the adsorbates to the surface. This type of interaction usually occurs on less reactive surfaces and leaves the geometrical and electronic structure of adsorbent and adsorbates rather unchanged. Chemisorption, in contrast, is a strong adsorption interaction in which orbital overlap and electron sharing result in chemical bond formation. While covalent bond formation between atoms or molecules results in bonding and antibonding orbitals of two atomic orbitals (see 3.1.2), in chemisorption the bond formation mechanism is not straightforward. In this case the adsorbate orbitals do not interact with a single state, but rather with a continuum of states. In other words, the hybridization of substrate electronic states with the molecular orbitals of the adsorbate result in chemisorption.
As mentioned before, surface characteristics such as symmetry, reactivity or electronic properties can affect the self-assembly. Binding energies of the organic molecules and their mobility on metal surfaces depend on the surface properties. Therefore, the same monomer on different metal surfaces can form various self-assembled structures. For instance, deposition of 1,3,5-tris(4-mercaptophenyl)benzene (TMB) on Cu(111), Ag(111) and Au(111) resulted in different self-assemblies.[63, 64] The room temperature deposition of TMB on Cu(111) and Ag(111) resulted in an ordered self-assembled close packed trigonal structure[63], while on Au(111) less well ordered aggregates were observed (See chapter 6). Hence, investigating the difference in reactivities of various metal

surfaces is useful for understanding molecule-surface interactions.

All experiments in this thesis have been carried out on coinage metal surfaces with defined crystallographic orientations. In the following, the role of the transition metals electronic structure in the bond strength of the adsorbates on the surface and origin of different reactivities in various transition metal surfaces are explained.

First of all, it is necessary to know how the molecular orbitals interact with the s and d bands of the metal, and how this affects the binding energy. Generally, the chemisorption of an atom on transition metal surfaces can be considered as a two step process. First the frontier orbitals are broadened and shifted by the interaction with the s band. The s band of transition metals is very broad and results in a bonding state far below the Fermi level with a weak chemisorption nature. The strength of these interactions is almost the same for all transition metals. In the second step the interaction of the bonding level with the metal d band leads to the formation of bonding and antibonding states. The bonding state is at lower energy than the original bonding state and the antibonding state is slightly higher in energy than the unperturbed metal d band. The total energetic effect on the resulting states depends on the coupling strength between the adsorbate-s band hybrid and the d band, and the extent of filling of the antibonding state. The latter depends on the position of the antibonding state with respect to the Fermi energy. Since both coupling strength and Fermi energy are metal specific properties, differences in the second step explain the different chemisorption bond strength on various metals. The energy of the antibonding state follows the metal dependent position of the d bands. The center of the d band moves further below Fermi energy from left to right across a row of transition metals in the periodic table. For Cu, Ag and Au on the right side of the table the d band and accordingly the antibonding state are below the Fermi energy. Hence, the antibonding orbitals are filled, resulting in repulsive forces that might cancel out the attractive forces from step 1 and bonding state. For transition metals on the very left side of the table the antibonding state lies above the Fermi level and is not filled. This results in overall attractive forces and highly exothermic chemisorption.

However, Cu is also more reactive than Ag and Au, even though the antibonding orbital is filled for all these metals from the same group. The reason is the difference in the magnitude of the coupling in these metals. The coupling strength is linked to the orthogonalization energy between adsorbate and metal d orbitals. The orthogonalization energy is repulsive and increases for more extended d orbitals. Consequently, the 5d orbitals of Au, which are broader than the 3d orbitals of Cu have a higher energy cost of orthogonalization of the orbitals. This renders Au the most noble metal. A more detailed discussion can be found in the theoretical work of Hammer and Norskov.[65, 66, 67]

The role of the surface reactivity in the self-assembled structure can also be seen in the experiment presented in chapter 7 (FAN on pristine Au versus iodine-terminated Au). In these experiments the passivation of the metal surface by a closed layer of chemisorbed iodine and its effect on the self-assembled structure is investigated.

The crystallographic orientation of the surface can affect the self-assembly as well. For instance, Classen *et al.* demonstrate the formation of $[-Cu-TMA-$

$Cu-]_n$ 1D chains on Cu(110)[68], while TMA on Cu(100) resulted in cloverleaf-shaped arrangements.[69] The 1D character of metal–organic coordination chains on Cu(110) is due to the fact that the molecule–molecule interaction (favoring hexagonal geometries) is overcome by the molecule–substrate interaction.

3.1.2 Molecule-Molecule Interactions

Generally the intermolecular forces can be classified into two categories: short-range and long-range interactions.[70, 71, 72] Short-range interactions are mainly accompanied by sharing of electrons and orbital overlap, as known from covalent bond formation. They represent one of the strongest bonds present in a molecular system. Long-range interactions include hydrogen bonds, halogen-halogen bonds, metal-coordination bonds, $\pi - \pi$ interactions, van der Waals, and electrostatic interactions. These are fundamental forces in the formation of supramolecular assemblies. The common feature of these forces is their proportionality to r^{-m}, where r is the internuclear distance and m a positive integer. The individual molecular components involved in these interactions forming a supramolecular assembly usually remain chemically unchanged. It means, in contrast to covalent bonds, the wave functions of the respective molecular components are hardly changed. This is also the reason of the weakness of these bonds. In a very weakly bound supramolecular assembly, the net sum of all the intermolecular interaction energies will seldom be higher than $\sim$100 $kJ\ mol^{-1}$, whereas the weakest covalent bonds are on the order of 150 $kJ\ mol^{-1}$.[52] In the following, intermolecular interactions relevant to the systems studied in this work are discussed in more detail.

Van der Waals Interactions

Van der Waals interactions actually belong to the group of electrostatic forces. Electrostatic interactions can be divided into three main groups: permanent-permanent dipole interactions (also known as Keesom forces), permanent-induced dipole interactions (also named as Debye forces), and van der Waals interactions. As long-range interactions, they can act over an area generally larger than the total spatial extent of the electron clouds of the participating molecules. The first two groups are counted as classical inductive forces and are referred to as polar interactions.[73] The electrostatic forces in the absence of permanent dipoles are known as van der Waals interactions. They form due to the non-zero instantaneous dipole moments of all atoms and molecules. The momentary random fluctuations of the electron density within the electron cloud of the molecules result in the formation of a fluctuating dipole. This can induce another dipole in a neighboring molecule. These fluctuating dipole-induced dipole interactions are also known as London dispersion forces, and are quantum mechanical in nature. The dispersion force is present in all materials even between non-polar molecules or in atom-atom interactions. It is also worth to note that the strength of London dispersion forces is proportional to the polarisability of atoms and molecules. This in turn depends on the total number of electrons and their spatial distribution. Hence, an atom with a large number of electrons will have a greater associated London force rather than a smaller one.

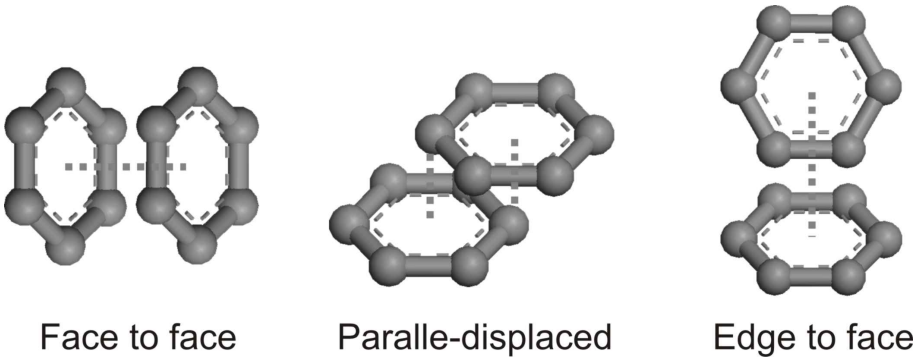

Figure 3.1: Three different geometrical configurations of benzene dimers with the lowest energies.

$\pi - \pi$ Interactions

$\pi - \pi$ interactions are a type of non-covalent interactions with at least one of the associates involving a π system. There are different kinds of $\pi - \pi$ interactions such as: aromatic-aromatic (π-stacking) interactions, π donor-acceptor interactions, anion/cation-π interactions, etc. Aromatic-aromatic interactions will be explained in this part in detail, since the self-assembly of the Fantrip molecules on iodinated Au(111) is stabilized by this type of interaction (see chapter 7).
The most prevalent example of π-stacking is the benzene dimer interaction with its fully conjugated π-cloud. Fig 3.1 illustrates the three lowest energy geometries of benzene dimers. Attractive interactions exist between the benzene molecules in all of these arrangements. However, among these possibilities parallel-displaced and edge-to-face are the most favorable configurations with an enthalpy of $\sim$2.3 kcal/mol and $\sim$2.0 kcal/mol, respectively.[74] The face-to-face configuration on the contrary is the least stable one due to high electrostatic repulsion of the electrons in the π orbitals.[74] Modeling of these geometries revealed that the two most stable conformations are essentially isoenergetic and represent energy minima, whereas the face-to-face configuration represents an energetic saddle point.[75] The experimental data are also in accordance with the theoretical expectations. Edge-to-face and parallel-displaced configurations can be observed in the crystal structures of many simple aromatic compounds.[76, 77] The face-to-face configuration is relatively rare in X-ray crystal data, although it is additionally stabilized by van der Waals interactions.

Several studies have been carried out to conceive the occurrence of $\pi - \pi$ interactions. Hunter and Sanders in 1990 proposed a conceptually simple model of the charge distribution in a π-system to explain the strong geometrical requirements for interactions between aromatic molecules.[78] The main feature of their model is the separate consideration of σ-framework and π-electrons. From the electrostatical point of view there is no attraction between electrons in π orbitals. Hunter's model concludes that net favorable $\pi - \pi$ interactions are due to the attractive interactions between the π-electrons and the σ-framework ($\pi - \sigma$ attractions), where it outweighs the unfavorable $\pi - \pi$ repulsion. Therefore, electrostatic $\pi - \sigma$ interactions steer the preferred geometry of the aromatic molecules. This model is based on the concept of an idealized π-system, namely a positively

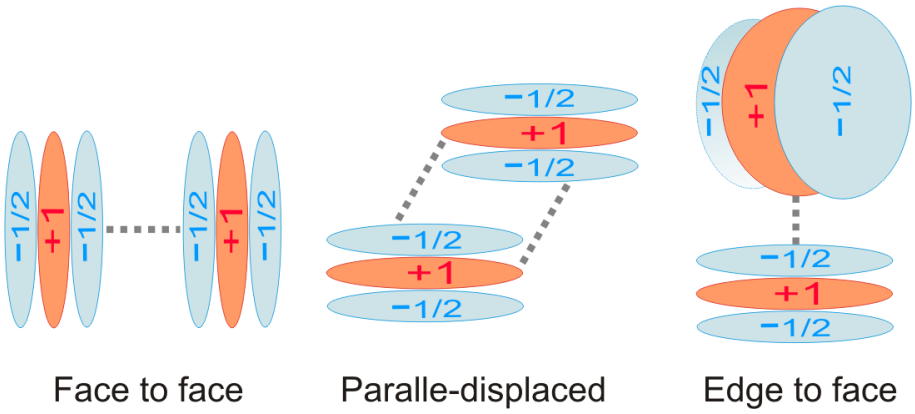

Figure 3.2: Bonding configurations of benzene dimers as idealized π-system, namely a positively charged σ-framework ($+1e$) sandwiched between two clouds of π-electrons (each with $-\frac{1}{2}e$) with the same electron density distribution (Hunter and Sunders' model). In the face to face interaction repulsion between $\pi-$electrons dominates, whereas in edge to face and parallel-displaced configurations $\pi - \sigma$ attractions dominate.

charged σ-framework ($+1e$) sandwiched between two clouds of π-electrons (each with $-\frac{1}{2}e$) with the same electron density distribution. Considering benzene as an ideal π-system with such an electrical charge distribution for its σ-framework and π-electrons elucidates why specific geometrical arrangements of benzene dimers are more favorable. The three different geometrical arrangements of benzene dimers shown in Figure 3.1 are displayed again in Figure 3.2, but with each benzene represented as a σ-framework with a net positive electrical charge surrounded by π-electrons. The energetic disadvantage of the face-to-face configuration due to repulsive forces between the π-electrons is obvious from the image. In contrast, the other two configurations are stable owing to the dominance of attractive interactions between σ-framework and π-electrons of the neighboring benzene.

The substituents in the aromatic ring play a crucial role in the electrostatic and dispersion interaction of the whole system and their electronic properties influence the strength of the attraction.[79] For instance, $\pi - \pi$ stacking in the case of arene-perfluoroarene are relatively strong since an electron-rich benzene interacts with an electron poor hexafluorobenzene. For more complex systems, for example π- systems polarized by heteroatoms, the modification of the charge values of σ-framework and π-electrons, compared to an ideal π-system, has to be taken into account. These values can be obtained from molecular orbital (MO) calculations.[52] A detailed set of rules based on such calculations governing the interaction of π- stacked aromatic systems (also the polarized ones) can be found in the work of Hunter and Sanders.[78]

Metal-Coordination Bonds

Previously, the influence of the molecule-substrate interactions on the self-assembled structure was discussed. Additionally, the substrate may contribute to the self-assembly process through its adatoms as well. The free adatoms available on metal surfaces can play an important role for molecule-molecule interactions

by coordinating the organic adsorbates.
Metal-coordination bonds are defined as bonds between organic ligands and metal atoms[80] with the exceptional case of carbon-metal bonds, referred to as organometallic bonds. For the formation of metal-coordination bonds electron rich ligands are required. Metal-coordinative bonds can be formed either by anionic ligands such as carboxylates and thiolates[63, 81, 82] or by neutral ligands such as nitriles and pyridines.[83, 84] In the latter case, the electron lone pairs of the nitrogen atoms form attractive coordination bonds with the positively charged metal adatoms. Formation of a metal-coordination bond based on molecular orbital theory can be described in four steps.[85] First, electrons are removed from the metal center providing a cation. In the second step, hybridization of the metal atomic orbitals occurs resulting in a set of equivalent hybrid orbitals directed towards the ligands. Subsequently, metal electrons rearrange to ensure that the hybrid orbitals are unoccupied. Finally, bonds are formed between metal center and ligand by the overlap of metal hybrid orbitals with ligand orbitals containing lone-pair electrons. The binding energies of metal-coordination bonds are relatively strong, ranging between 50 $kJ\ mol^{-1}$ and 200 $kJ\ mol^{-1}$.[17]
The metal atoms involved in the metal-coordination bonds do not need to originate from the surface. They can also be co-deposited to the surface. Various examples of organic adsorbates binding to Fe or Co metal atoms on coinage metal surfaces are represented in Lin's article.[86]
The incorporation of intrinsic substrate adatoms in the metal-organic bonds is also well known from different systems. Sirtl *et al.* studied a large trinitrile molecule on Cu(111) surface, where the organic adsorbates were coupled via the Cu adatoms to each other forming a hexagonal metal coordinated network.[84] Another structure with N-Cu bonds was reported for pyridine containing molecules on Cu(100).[87] Metal-organic bonds have also been observed for copper carboxylate complexes on Cu(100)[69] and on Cu(110) surfaces.[68] In some of these experiments the metal atoms can be identified as round protrusions in STM images. On Au(111) the metal adatoms have rarely been observed. However, Maksymovych *et al.* reported the observation of gold adatoms as bright dots in their experiments, where short-chain alkanethiolate species are interlinked through Au adatoms.[88]
The intrinsic adatoms originate from temperature-dependent evaporation / condensation equilibrium at step edges. In the case of Au(111) there is an additional adatoms reservoir available due to the surface reconstruction. In the well known herringbone reconstruction 23 surface atoms are uniaxially compressed in the $[1\bar{1}0]$ direction to fit into the space of 22 bulk lattice sites.[89] This gold atom "excess" can be harvested for metal-coordination bonds. Particularly, some chemical moieties such as thiol facilitate the release of gold adatoms from the herringbone reconstruction.[88] This results in local modifications of the herringbone reconstruction. Another example of metal-coordination bonds on Au(111) is presented in chapter 6 showing a coordinated assembly of thiolates through Au adatoms.

Covalent Bonds

Covalent bonds are among the strongest type of bonds in the nature and as mentioned in the previous parts formed through overlap of atomic orbitals that

leads to electron sharing between atoms. Covalent bonds are directed and rigid with binding energies between 150 $kJ\ mol^{-1}$[52] and 870 $kJ\ mol^{-1}$.[90]
The overlap of atomic orbitals results in the formation of molecular orbitals. The atomic orbitals are solutions of the Schrödinger equation for electrons in an atom. Therefore, their overlaps could be constructive (in phase interference of the wave functions) or destructive (out of phase interference of the wave functions) that lead to bonding or antibonding molecular orbitals, respectively.[91, 92] Compared to the original atomic orbitals, bonding orbital represents states with enhanced electron density among the nuclei. This implies that the energy of bonding orbitals is lower than the original energy of the atomic orbitals. On the contrary, a molecular orbital becomes antibonding when the electron density between the two nuclei is lower than in no-bond interaction (separate atoms). Antibonding orbitals have higher energies and their occupation results in destabilization of the bond.
The strength of covalent bonds depends on many variables. However, the extent of orbital overlap is a determining factor. Larger overlap means more electron sharing between two nuclei, and therefore a stronger covalent bond. The extent of orbital overlap clearly depends on the geometrical characteristics of the orbitals. In bonds of spherical s-orbitals, the atomic orbitals overlap head to head, so that the maximum of the electron density is located along the nuclei axis. This type of bonds is called σ-bonds. The bonds between two s-orbitals or a s-orbital and a hybrid orbital belongs to this category as well. In the second type of covalent bonds, known as π-bonds, the non-spherical atomic p-orbitals overlap side by side and accordingly the maximum of the electron density is localized above and below the nuclei axis. The σ-bonds are stronger than π-bonds, and π-bonds can be formed only if the nuclei are primarily linked through a σ-bond.

3.2 On-Surface Polymerization

As mentioned before on-surface polymerization is one of the bottom-up strategies for the synthesis of covalent nanostructures. The idea of covalent interlinking of molecules to build larger architectures was originally proposed by Coté *et al.* about one decade ago.[93] They succeeded in synthesizing 3D porous periodic extended organic networks from covalently linked building blocks. The formation of 2D covalent nanoarchitectures, utilizing on-surface chemistry, was achieved only two years later. Almost simultaneously several groups reported on the synthesis of different covalent nanostructures through various chemical reactions on surfaces. Grill *et al.* showed the possibility to build covalent nanoarchitectures on Au(111) and tune their topology based on the chemical structure of the initial monomer.[10] In another work synthesis of imine from an aldehyde and an amine was presented by Weigelt *et al.*.[94] Generally, there are various polymerization reactions to synthesize covalently linked structures, such as surface-assisted Ullmann coupling, Glaser coupling, condensation reactions, *etc.*. In this thesis, on-surface Ullmann coupling is used in chapter 4 and 5 and is described in section 3.2.1.
Despite studying different polymerization reactions on various surfaces, fabrication of defect-free long-range ordered covalent structures is still an unsolved challenge. One can benefit from the reversibility of non-covalent assemblies to

overcome this challenge. Less stable non-covalent assemblies can form a long-range ordered structure without defects due to the bond reversibility. A smart idea is to take advantage of these long-range ordered molecular arrangements and convert them into robust covalent networks. However, this idea is not readily possible and a well designed system has to be chosen for this purpose. In the following three types of non-covalent interactions among building blocks of a self-assembly are presented, and possible obstacles regarding the conversion of these self-assemblies into covalent networks are discussed.
If the self-assembly is stabilized through hydrogen or halogen bonds, creation of covalent bonds among molecules is not possible due to lack of active sites (i.e. surface stabilized radicals). Additionally, breaking these bonds may destabilize and destroy the complete self-assembly.
For self-assembled systems stabilized through metal-coordination bonds, the required radicals for covalent bond formation are already available on the surface. However, to break these bonds external energy has to be supplied to the system, e.g. through annealing. Besides breaking the bonds, the energy uptake can also activate surface diffusion and rearrangement of radicals. This may destroy the ordered structure, resulting in irregular networks. Therefore, the amount of supplied energy to the self-assembled system must be precisely controlled.
Self-assembled structures can also be stabilized through van de Waals and $\pi - \pi$ interactions. In this case, creation of surface-stabilized radicals is not necessary for polymerization. The topochemical photopolymerization is a promising method, since it provides maximal control over the supplied energy at targeted (reactive) sites. For this purpose, an appropriate photoactive system has to be chosen. In this thesis, the photopolymerization of a hexagonal assembly of Fantrip molecules with three photoactive anthraceno blades was studied (see chapter 7). In this case, the photodimerization occurs by a cycloaddition reaction (see section 3.2.2 for details).

3.2.1 On-Surface Ullmann Coupling

The most famous on-surface polymerization reactions like on-surface Ullmann coupling drew inspiration from conventional solution chemistry. The Ullmann reaction in solution chemistry has a long history since its discovery in the early 20th century.[95] Ullmann *et al.* found out that heating of iodobenzene with copper results in almost pure biphenyl as reaction product.[96] Generally, the Ullmann reaction is a coupling reaction between aryl halides and copper as catalyst. Thereby, existence of copper facilitates the dissociation of halide and formation of biaryls. However, the role of the copper in this reaction was controversial. Xi and Bent could transfer Ullmann coupling reaction from solution to a Cu(111) single crystal surface for iodobenzene to form biphenyl under ultrahigh-vacuum conditions.[97] The mechanism of this coupling on the surface is thoroughly explained in their later work.[98] They presented two different pathways for this reaction depending on the surface coverages. For low coverages (submonolayer), iodobenzene molecules dissociate on Cu(111) at 175 K resulting in adsorbed phenyl radicals and iodine adatoms. At higher temperatures of 370 K, the phenyl intermediates are mobile on the surface and can couple and form biphenyl. For high coverages the biphenyl formation could be detected at considerably lower temperatures of

210 K over another reaction pathway. In this low temperature pathway coupling proceeds between adsorbed phenyl radicals and molecularly intact iodobenzene. However, a specific orientation of molecular iodobenzene with respect to the surface is necessary for this reaction. The aromatic plane should be tilted significantly away from the surface plane and the iodine atom should have access to the copper surface. Such a tilted configuration allows phenyl radicals that result from C-I bond dissociation to react with adjacent phenyl groups rather than binding directly to the copper surface. It is obvious that the high surface coverage plays the key role for molecular iodobenzene to adopt this specific orientation. Therefore, this reaction pathway could not be observed for lower surface coverages.
The first reaction pathway occurring at low coverages with radicals coupling at higher temperatures is the basis of Ullmann coupling used in most on-surface polymerizations. This reaction pathway was also studied in detail by Blake *et al.* investigating the Ullmann coupling of bromobenzene by means of scanning tunneling microscopy and spectroscopy on Cu(111).[99] Upon deposition on the surface, the dehalogenation of the aryl halides takes place and the dehalogenated monomers form an intermediate state by coupling to the free electron gas of the surface with their active sites. These surface-stabilized radicals can bind to metal adatoms available on the surface, forming a metastable organometallic structure. An example of such protopolymer formation can be found for 1,3,5-tris(4-bromophenyl)benzene on Cu(111).[9] Increasing the temperature converts these organometallic bonds to covalent bonds by ejecting the metal adatoms. It is also noteworthy that the split off halogen atoms chemisorb on the surface.
Although most of the on-surface Ullmann coupling reactions follow the previously introduced reaction pathway, it is not the exclusively existing pathway as illustrated before by Xi and Bent. Another exceptional case of on-surface Ullmann coupling not following the conventional pathway is presented in chapter 4 for 1,3-diiodobenzene on Cu(111). The reaction products in this study adsorb atop of a closed iodine monolayer instead of on the metal surface, and the organometallic intermediates were not observed at all. Moreover, the polymerization mainly terminated at the trimer stage. This study highlights that even a widely used and studied reaction, can proceed in an unpredictable manner.
Despite the exceptional cases, surface-supported Ullmann coupling is still a powerful method to produce tailored nanostructures on catalytically active surfaces. The final structure of nanoarchitectures can be designed by selecting the appropriate chemical structure of the initial monomers. Size and geometry of molecular building blocks, as well as, substitution pattern of pendant groups (halogens) can be used to tailor structures.
There are many examples of on-surface Ullmann coupling on silver[100, 101] and gold surfaces[102, 103]. The covalent networks presented in chapter 5 are also synthesized on Ag(111) and Au(111) utilizing the conventional reaction pathway.

3.2.2 Cycloaddition Reactions

Cycloaddition is a type of pericyclic reactions in organic chemistry. The most famous example of cycloaddition reactions is the Diels-Alder reaction, in which a ring of six carbon atoms is formed by the coupling of a conjugated diene and an alkene. In this reaction two π-bonds are replaced by two σ-bonds through the

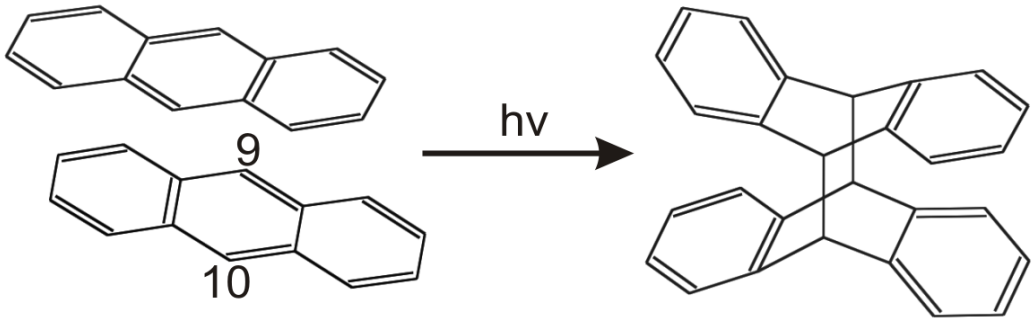

Figure 3.3: Dimerization of two parallel anthracene molecules through photopolymerization by a [4 + 4] cycloaddition reaction.

migration of electrons out of the π-orbitals into the σ-orbitals. Such a reaction is called a cycloaddition. The transition state of this reaction has six delocalized π-electrons and can be seen as a benzene ring having all its π-bonds, but missing two σ-bonds. The cycloadditions are usually designated with a shorthand symbol before the name that indicates how many π-electrons are involved in the reaction. For instance, [4 + 2] cycloaddition means that 4 π-electrons of one molecule and 2 π-electrons of another molecule are participating in the reaction. This special case is the most common cycloaddition reaction. The Diels-Alder reaction also belongs to this category.
Some of the cycloaddition reactions do not result in ring formation as in the Diels-Alder reaction. The dimerization of anthracene is such an example, whereby two parallel anthracene molecules can be interlinked at their 9 and 10 positions through a [4 + 4] cycloaddition reaction.[104] In this reaction two π-bonds of the middle phenyl rings of the anthracene molecules are replaced by two σ-bonds connecting the carbon atoms at positions 9 and 10 of one anthracene molecule to their corresponding partners in the second anthracene molecule. Figure 3.3 shows this reaction.

Cycloaddition reactions can be activated either thermally or photochemically. Based on Woodward–Hoffmann's orbital symmetry rules,[105] the cycloaddition reactions of (4n + 2) π-electrons are thermally allowed, while reactions of 4n π-electrons are photochemically allowed (n is integer).[106] In the case of [4 + 4] cycloaddition of two anthracene blades, the reaction can occur through photopolymerization. Photochemically activated cycloaddition occurs when one reactant has an electron excited from the HOMO (π-bonding) to the LUMO (π^*-antibonding). The probability of photopolymerization directly depends on the lifetime of the photoexcited state.
As described before in section 3.2 photoinduced polymerization of a presynthesized self-assembled structure can be very rewarding. In chapter 7 the [4 + 4] cycloaddition of Fantrip molecules that consist of three anthraceno blades, were studied. Anthraceno units were chosen based on their well-known photodimerization by [4 + 4] cycloaddition that can be realized both in solution[104, 107, 108, 109] and solid state.[110].

Chapter 4

An Exceptional Case of On-Surface Ullmann Coupling

In this chapter, Ullmann coupling of 1,3-diiodobenzene on Cu(111) surfaces under ultra-high vacuum conditions is presented. In contrast to the conventional Ullmann coupling on Cu(111), the metastable organometallic intermediates were never observed. *In situ* Scanning Tunneling Microscopy at room temperature revealed an unexpected ordered arrangement of highly uniform reaction products adsorbed atop a closed iodine monolayer.*

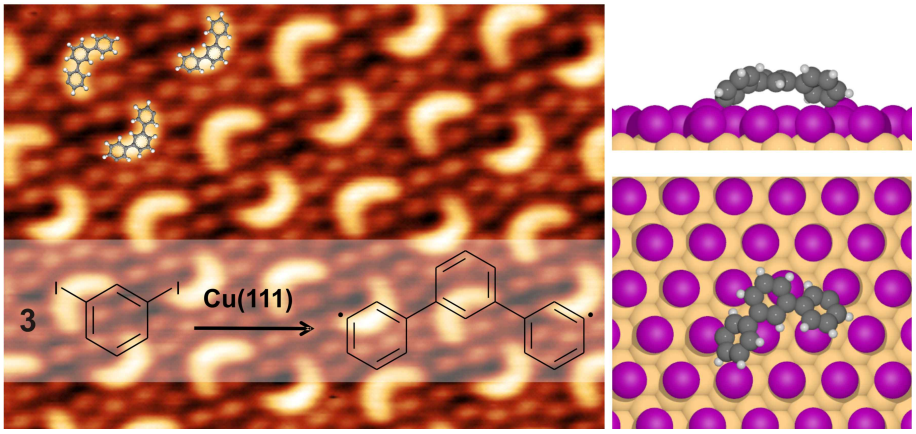

* This chapter was published as: A. Rastgoo-Lahrood, J. Björk, W. M. Heckl and M. Lackinger. **1,3-Diiodobenzene on Cu(111) – An Exceptional Case of On-Surface Ullmann Coupling.** *Chem. Commun.* 51 (2015), 13301-13304. Reproduced with permission from The Royal Society of Chemistry. Copyright 2015 by The Royal Society of Chemistry.
I performed all the STM measurements, the corresponding data analysis and interpretation, and prepared the manuscript under supervision of Prof. Lackinger. STM simulations and DFT calculations were done by Prof. Jonas Björk from the Linköping University.

4.1 Introduction

The basic principle of on-surface Ullmann coupling, extensively explained in section 3.2.1: halogenated precursor molecules are deposited onto metal surfaces. The weakly bonded halogen substituents are dissociated by virtue of the surface's reactivity[111] and remain chemisorbed on the surface. The thereby generated surface-stabilized radicals diffuse and couple through C–C bond formation into covalent nanostructures. Depending on the type of metal surface, coupling proceeds either directly[10, 102, 103, 112] or via a metastable organometallic intermediate.[9, 100, 113, 114] As a noteworthy exception to this commonly observed scheme, the surface chemistry of 1,3-diiodobenzene (DIB, Figure 4.1(b)) on Cu(111) is presented here. This study was initially motivated by the question: how the reduced symmetry of DIB monomers in combination with a highly symmetric surface affects the final structures, i.e. whether well-defined reaction products, such as zig-zag chains or closed rings, can be observed as for dibromo-meta-terphenyl.[115] DIB was deposited under UHV conditions through a leak valve onto clean Cu(111) held at room temperature and characterized by *in situ* STM (see section 4.4 for details).

4.2 Results and Discussion

A typical STM image obtained after deposition is shown in Figure 4.1. Surprisingly, instead of irregular oligomers as for DIB on Cu(110)[113], a regular arrangement of identical crescent shaped objects surrounded by a hexagonal lattice of fainter dots is observed. The measured dot–dot spacing of 0.45 ± 0.01 nm corresponds to the lattice parameter of the known $\sqrt{3} \times \sqrt{3}R30°$ iodine superstructure on Cu(111).[116] Since for room temperature on copper iodine cleavage and its subsequent chemisorption are well documented,[48, 113, 117] the dots are assigned to split-off iodine. The crescents are entirely unexpected and attempts to relate their structure to DIB monomers inevitably lead to covalent trimers, i.e. 1,3-diphenylbenzene (meta-terphenyl, Figure 4.1(c)). The respective overlay yields a perfect match. Yet, this assignment triggers two immediate questions: (1) are the trimers just surrounded by iodine, or adsorbed atop a closed monolayer? Even though the trimers appear significantly brighter this is not obvious from STM. (2) Are the trimers iodine-terminated or deiodinated, i.e. surface-stabilized diradicals?

The first question was unambiguously addressed by bias dependent STM imaging (Figure 4.2). At positive sample bias, a contrast similar to Figure 4.1 was observed, whereas the crescents became invisible to STM at reversed sample bias, revealing a closed and densely packed hexagonal monolayer. The original contrast was restored upon switching back to positive sample bias. Thus, the trimers are adsorbed on a closed monolayer of iodine.

Clarifying the trimer termination is more intricate and addressed by comprehensive density functional theory (DFT) and STM image simulations (see appendix A for details). Adsorption geometries of both iodinated and deiodinated (diradicalic) trimers were optimized on iodine-terminated Cu(111) using an extensive set

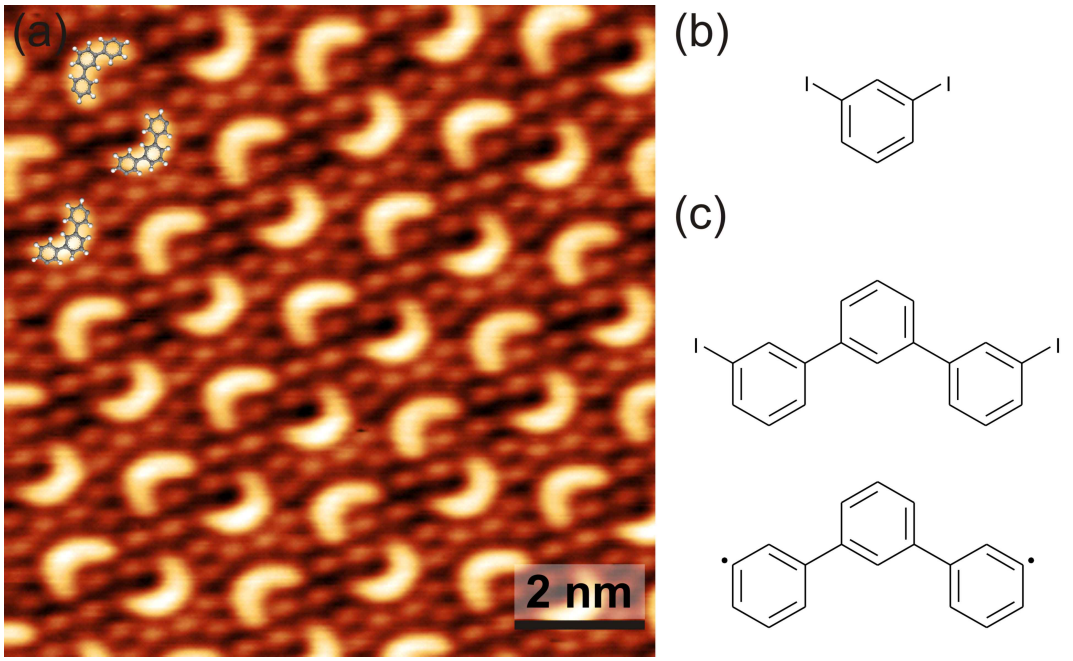

Figure 4.1: STM image (V = +0.84 V, I = 39 pA) obtained after deposition of DIB onto Cu(111). The crescent shaped features are overlaid with 1,3-diphenylbenzene, i.e. covalent DIB trimers. (b) Chemical structure of DIB. (c) Iodinated vs. deiodinated trimer; conformational isomers are also possible by σ-bond rotation.

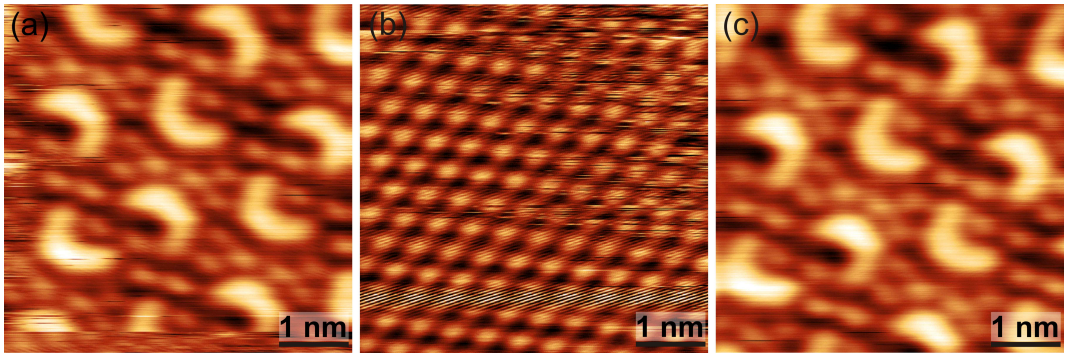

Figure 4.2: Bias dependent STM imaging (V = ±0.70 V, I = 37 pA). The same sample area was consecutively imaged with (a) positive, (b) negative, (c) positive sample bias. Similarity of (a) and (c) assures that no major tip or sample changes have occurred.

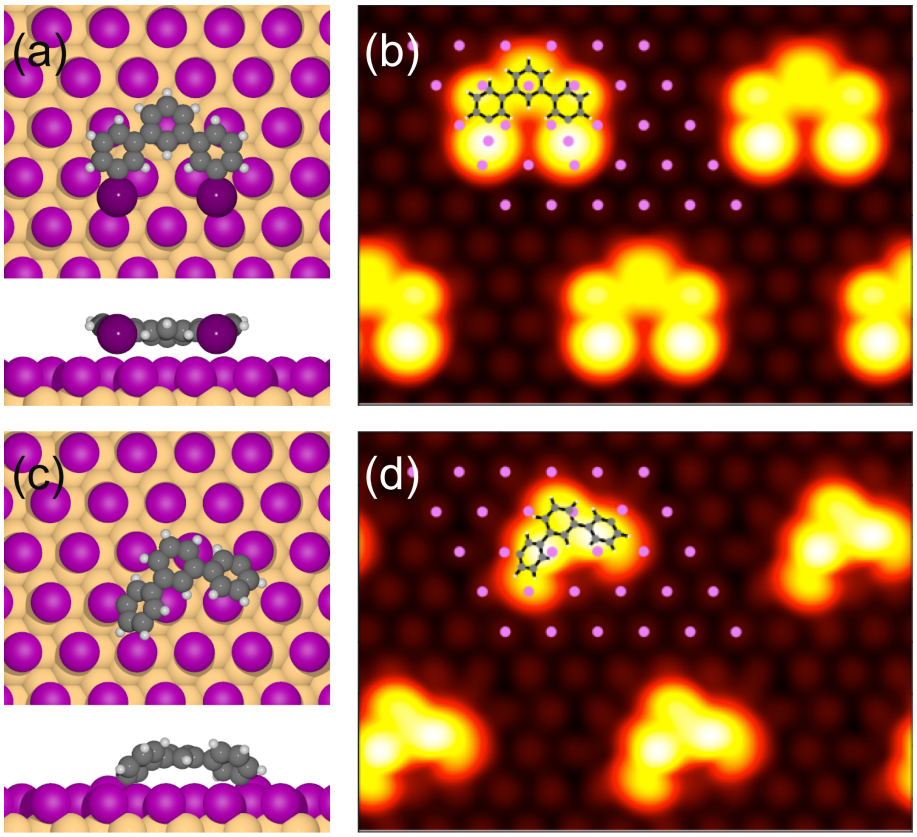

Figure 4.3: Top and side view of DFT derived lowest energy adsorption geometries and corresponding STM image simulations of (a)/(b) iodinated and (c)/(d) deiodinated trimers. In these image simulations, contributions from unoccupied electronic sample states between E_F and $E_F + 1.0$ eV were considered.

of start geometries (see Figure A.2 and A.3 in appendix A). The lowest energy configurations for both cases are depicted in Figure 4.3, along with the corresponding STM image simulations. In this case, the STM contrast was evaluated for empty states up to $E_F + 1.0$ eV, i.e. at a sample bias of +1.0 V, but was virtually independent of sample bias (see Figure A.4 and A.5 in appendix A). These simulations indicate that iodine substituents give rise to prominent spherical protrusions in STM images, whereas no such features occur for the deiodinated species. This is in accordance with previous studies where pronounced spherical protrusions were similarly observed for iodine substituents.[118]

Visual inspection already suggests a much better agreement for the deiodinated species with the experiment. Overlaying the simulated images with the structures elucidates how much larger the iodinated species appears than the terphenyl backbone, whereas for the deiodinated species the size match is much closer to the experiment. The slightly bent geometry of the terphenyl backbone gives rise to two peripheral protrusions in the STM image simulation. However, corresponding intramolecular contrast features were not resolved by STM, possibly due to thermal motion at room temperature. This is not taken into account in the simulations. Furthermore, the orientation of the deiodinated trimer with respect to the iodine lattice shows a good agreement between theory and experiment.

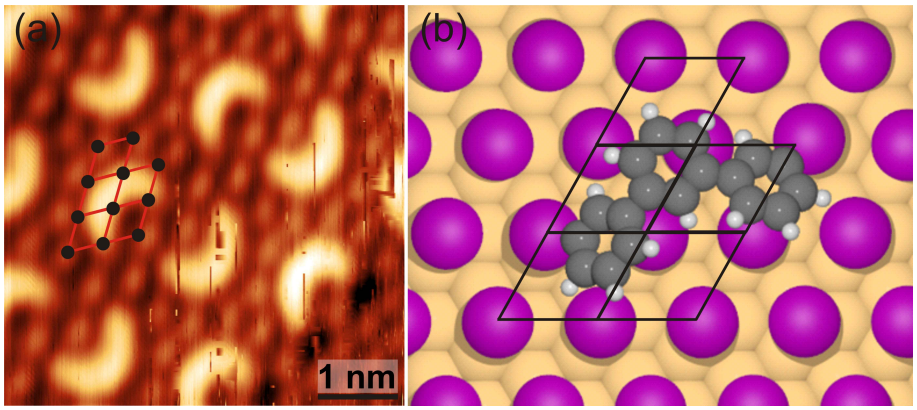

Figure 4.4: (a) STM image (V = +0.84 V, I = 39 pA) and (b) DFT derived lowest energy structure (see Figure A.3(f)) of the deiodinated trimer. Experiment and simulation consistently result in the same orientation of the trimer with respect to the hexagonal iodine superstructure.

In Figure 4.4 part of the iodine lattice in STM image and in DFT optimized structure is marked with a grid for a better visualization of deiodinated trimer orientation.

Apart from the STM contrast, DFT provides further evidence for deiodination; the energy variation between all considered adsorption geometries is relatively small for the iodinated trimer, suggesting a comparatively low diffusion barrier. This contradicts the experimentally observed room temperature stability. A common feature of all converged structures of the deiodinated trimer is that the radical sites form single bonds to individual surface-bound iodine atoms. Seen as a requirement, this strongly constrains the number of reasonable adsorption geometries, because the iodine positions are defined by the lattice and molecular deformations result in a high energy cost. The DFT calculations indicate electron accumulation between radical sites and surface-bound iodine atoms (see Figure A.6 in appendix A). Furthermore, the partial density of states (PDOS) of carbon atoms shows spin-pairing on the surface, as well as hybridization of frontier molecular orbitals (see Figure A.7 in appendix A). All aspects indicate covalent bond formation, i.e. the deiodinated trimers can be considered as still iodinated, whereby the iodines are predominantly part of the monolayer. The relatively large energy differences between different adsorption geometries for the deiodinated species suggest a high diffusion barrier.
It is also instructive to compare stoichiometries of the adsorbed structure with the unreacted DIB monomer. Each unit cell contains 4 trimers. Formation of one deiodinated trimer releases six iodine atoms, i.e. 24 per unit cell. However each unit cell of the self-assembled structure contains more than twice as many iodine atoms in the underlying monolayer. The actual disbalance is even larger, because parts of the surface covered solely with iodine (e.g. the left sides of STM images in Figure 4.5). This indicates that DIB radicals can desorb again after deiodination and leave dissociated iodine on the surface.
Ullmann coupling of DIB on Cu(111) deviates from previous comparable results in several respects. The organic structures are not directly adsorbed on the metal, but atop an iodine buffer layer. Covalent bonds are formed directly, whereas

metastable organometallic intermediates with C–Cu–C interlinks are commonly observed on copper.[9, 47, 113, 115, 119] DIB coupling terminates at the trimer stage, and moreover, results in a well-defined self-assembled pattern. In contrast, for DIB on Cu(110) organometallic intermediates were observed directly after room temperature deposition, and mild annealing converted them into irregular covalent oligomers.[113]
The origin of these fundamental differences is not entirely clear. Commonly observed organometallic intermediates form with abundantly available surface adatoms. Hence, it appears plausible that in the present case adsorbed monomers are screened after their dehalogenation by the readily abstracted iodines. An observation pointing in this direction was made for hexaiodo-substituted macrocycle cyclohexa-m-phenylene (CHP) on Cu(111).[48] These results show that the split off iodines are rather immobile at room temperature and remain adsorbed in the vicinity of the dehalogenated precursor. Adsorption of Ullmann reaction products on top of an iodine buffer layer rather than directly on the metal surface was also previously reported on Au(111),[120] similarly under conditions with iodine excess. Since dehalogenation requires direct contact to the reactive metal surface, adsorption on top of an inert iodine monolayer indicates subsequent detachment. The driving force is the notoriously high affinity of iodine to metals. Taking the overstoichiometric amount of iodine into consideration, the following scenario appears plausible: Initially, DIB adsorbs directly on Cu(111) and becomes deiodinated. The iodine coverage increases – also due to additional contributions from desorbing radicals – and eventually displaces the diradicals from the bare copper surface. Once the surface is fully covered, no further adsorption and dehalogenation occurs. Intact DIB monomers have never been observed, indicating that their room temperature adsorption is not stable on iodine-terminated Cu(111). Based on the STM experiments, it cannot be clarified whether C–C bond formation between DIB radicals takes place when they are still adsorbed on the metal or after their displacement on the iodine monolayer.
Termination of the coupling at the trimer stage remains even more enigmatic. The most plausible explanation is provided by increasing diffusion barriers as the aggregates grow in size. Evidently, the trimer is the smallest oligomer that is just stable at room temperature. Yet, at domain edges residual mobility of trimers is frequently observed (see Figure 4.5), indicating that this size is close to the stability threshold.

Explaining self-assembled patterns with a relatively large inter–trimer spacing inevitably requires trimer–trimer interactions. In addition, the interplay between repulsive interactions and a relatively high diffusion barrier of covalently anchored diradicalic trimers effectively prevents formation of larger oligomers. Yet, hexamers, i.e. cyclo-sexiphenylene, that might result from the fusion of trimers were occasionally observed at domain edges. STM images in Figure 4.6 depict the appearance of such an annular hexamer.

More direct experimental evidence for trimer–trimer interactions is provided by the concerted movement of whole rows of trimers as shown in Figure 4.7. The origin of repulsive interactions could either be direct or substrate-mediated. Considering the relatively large trimer–trimer spacing, repulsion is most likely related

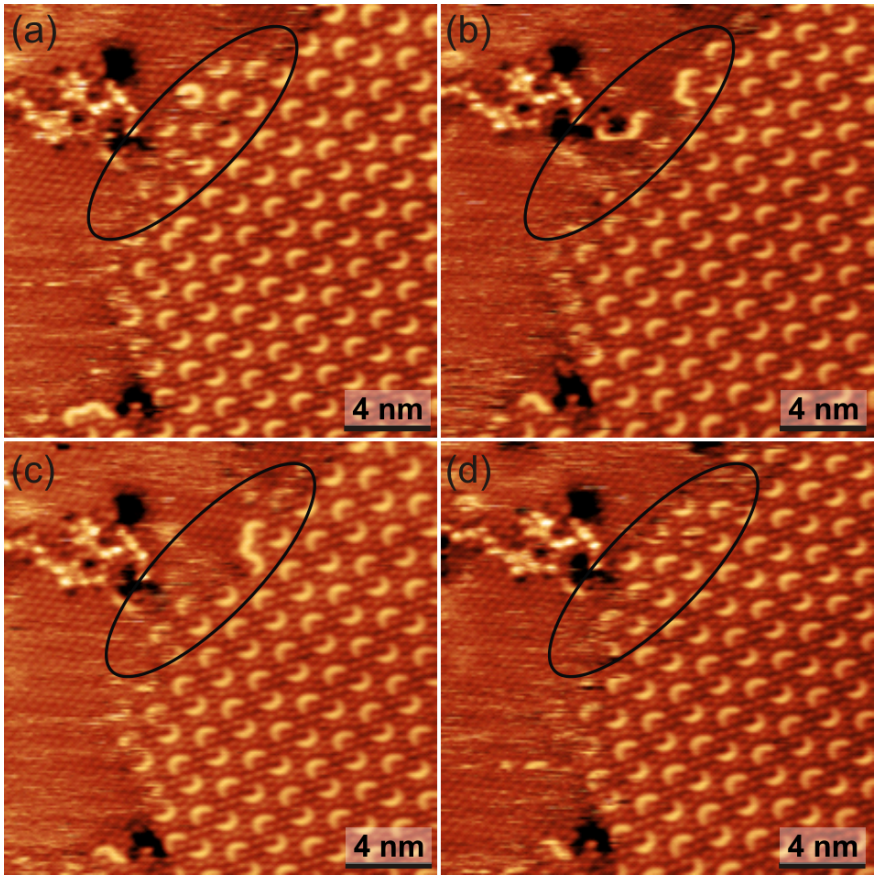

Figure 4.5: Series of STM images consecutively acquired from the same sample area (V = +0.84 V, I = 39 pA). The black oval highlights dynamic processes observed at domain edges, including lateral mobility of trimers and coupling of trimers into larger, less well defined aggregates.

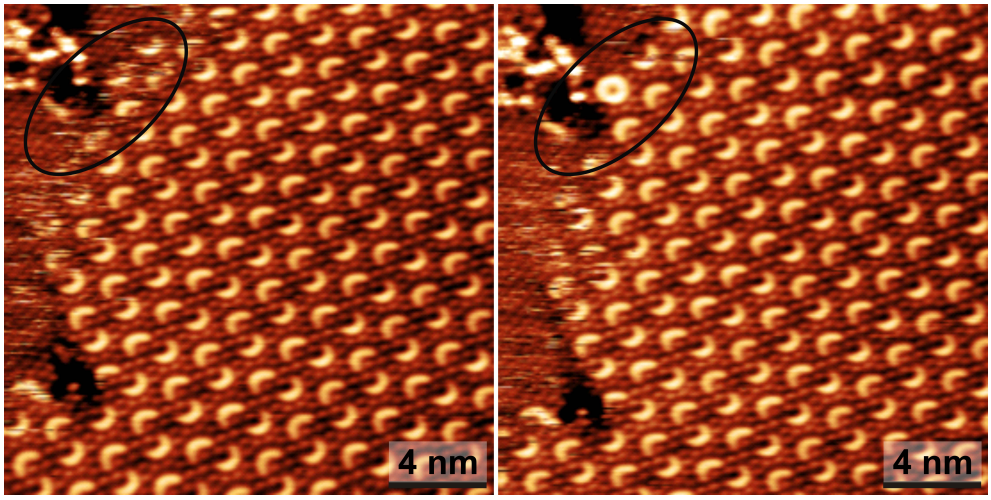

Figure 4.6: Two STM images consecutively acquired from the same sample area (V = +0.84 V, I = 39 pA). The black oval highlights the appearance of a closed ring, i.e. cyclo-sexiphenylene, in the second image. A conclusion whether this ring has formed on-site by coupling of two trimers or whether it diffused to this site is not possible based on these STM experiments.

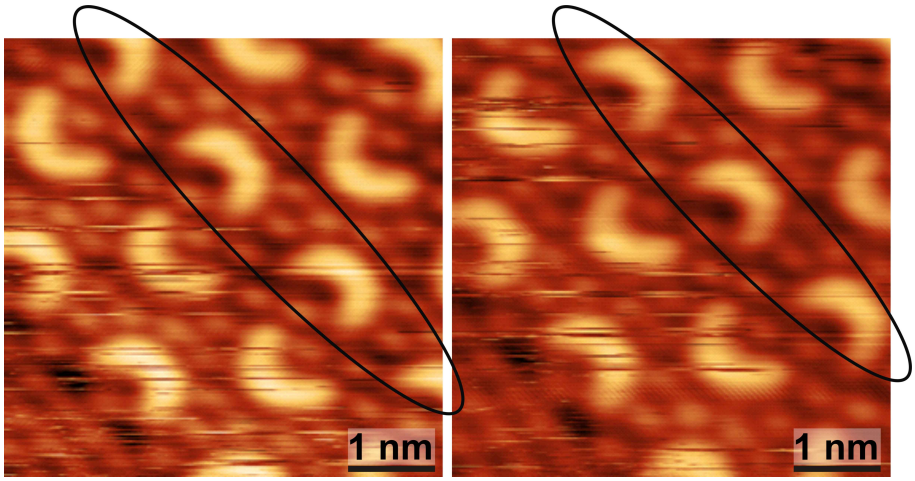

Figure 4.7: Two STM images consecutively acquired from the same sample area (V = +0.84 V, I = 39 pA). The black oval highlights lateral displacement of a row of trimers as a whole. This concerted movement of trimer rows indicates an effective long-range interaction as also required for self-assembly of the observed patterns.

to electrostatic interactions. Interestingly, Bader charge analysis of our DFT calculations indicate electron donation from iodine to the former carbon radicals (see Figure A.8 in appendix A). This renders the iodine atoms bonded to the trimer, positively charged, among the otherwise negatively charged iodine atoms. Hence, two positively charged iodine atoms next to each other are energetically unfavorable. Furthermore, DFT calculations show a vertical displacement of 0.65 Å for the iodine atoms binding to the trimer. This adsorbate-induced corrugation in the iodine monolayer also modifies the potential energy landscape. The single iodine atom spacing between trimers in the self-assembled pattern can be interpreted as experimental evidence for substrate-mediated repulsion.

Even more complex regular patterns with two larger motifs – closed rings and S-shaped entities – were occasionally observed (see Figure 4.8(a) and Figure A.1 in appendix A). Based on a geometrical assignment, these motifs are identified as hexamers that formed from two trimers either by a single 3–3 interlink (S-shaped) or by a two-fold 3–3″ and 3″–3 interlink (closed ring). In the closed ring all bonds are saturated. In analogy to the single trimer, absence of a prominent iodine signature at the termini in the STM images of the S-shaped entity is indicative of deiodination. The complexity of this pattern is remarkable, considering its emergence from DIB monomers through a polymerization process without external control. Albeit deciphering the underlying processes in detail is hardly possible, an important clue is the obvious structural relation between the two patterns. As illustrated in Figure 4.8(b) the normally observed trimer pattern can be converted into the more complex pattern by pairwise addition of crescents to either rings or S-shaped motifs. This scheme also yields the correct spatial arrangement, where each closed ring is surrounded by a hexagonal arrangement of S-shape motifs. Accordingly, we postulate that the more complex pattern emerged from the normally observed pattern through a concerted set of secondary coupling reactions. Attempts to initiate this conversion by mild heating were not successful.

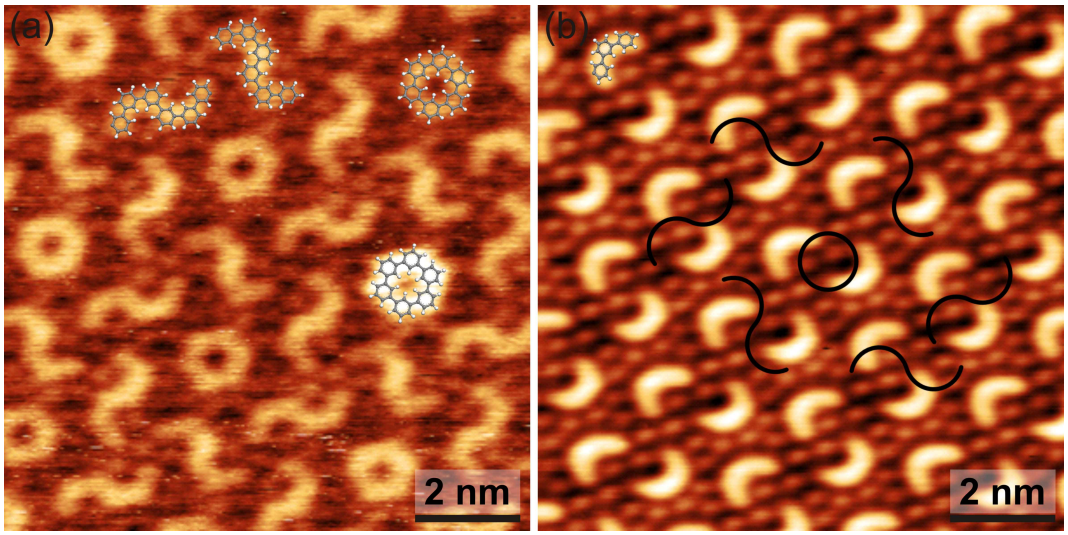

Figure 4.8: (a) STM image of an occasionally observed more complex self-assembled pattern (V = +0.81 V, I = 38 pA). The two distinct types of hexamers are overlaid to scale. (b) Sketch of the structural relation between the complex and the normally observed pattern.

4.3 Conclusions

In summary, Ullmann coupling of DIB on Cu(111) unexpectedly yielded self-assembled patterns of trimers, and occasionally more complex patterns of hexamers. Instead of being directly adsorbed on the metal surface that initiated the Ullmann coupling by dehalogenation, the covalent aggregates were adsorbed atop a closed iodine monolayer. STM image simulations suggest that the trimers are deiodinated. Covalent bonds between the radical sites and surface bound iodine atoms are largely responsible for the stabilization of the structure at room temperature.

DIB on Cu(111) exemplifies that even a well characterized and commonly employed on-surface reaction as Ullmann coupling does not always proceed in a predictable manner. In this respect, the absence of organometallic intermediates represents a further exception to the rule. Kinetics – in particular surface diffusion – is playing an important role for termination of the polymerization at the trimer stage. Concerted movements of trimer rows provide experimental evidence for long-range trimer–trimer interactions – a prerequisite for self-assembly of the ordered patterns. The origin of the differences between DIB Ullmann coupling on Cu(111) vs. Cu(110) surfaces is not yet clear. A possible explanation is offered by reactivity differences, as the dehalogenated DIB adsorbs ∼0.7 eV more strongly on Cu(110) than on Cu(111) (see Figure A.9 and A.10 in appendix A). However, an additional influence from kinetic reaction parameters, e.g. monomer deposition rate that also determines the adsorption rate of iodine, cannot be ruled out at this point.

4.4 Experimental Details

All STM images were recorded at room temperature in ultra-high vacuum at a base pressure below 3×10^{-10} mbar with a home-built STM (see section 2.1.3 for details). The STM was calibrated by means of atomically resolved Cu(111) images. This facilitates extraction of lattice parameters and distances with an accuracy of ∼5%. STM images were processed by a mean value filter. Cu(111) single crystal surfaces were prepared by cycles of Ne^+ ion-sputtering at 1 keV and electron-beam annealing at ∼773 K. 1,3-diiodobenzene (DIB, CAS 626-00-6, obtained from Sigma Aldrich, purity 98%) was dosed through a precision leak valve, equipped with a stainless steel capillary aiming at the sample.

Chapter 5

Post-Synthetic Decoupling of On-Surface-Synthesized Covalent Nanostructures

The on-surface synthesis of covalent organic nano-sheets driven by reactive metal surfaces leads to strongly adsorbed organic nanostructures, which conceals their intrinsic properties. Hence, reducing the electronic coupling between the organic networks and commonly used metal surfaces is an important step towards characterization of the true material. In this chapter, a method for post-synthetic decoupling of the nanostructures form Ag(111) und Au(111) surfaces by iodine intercalation is described.*

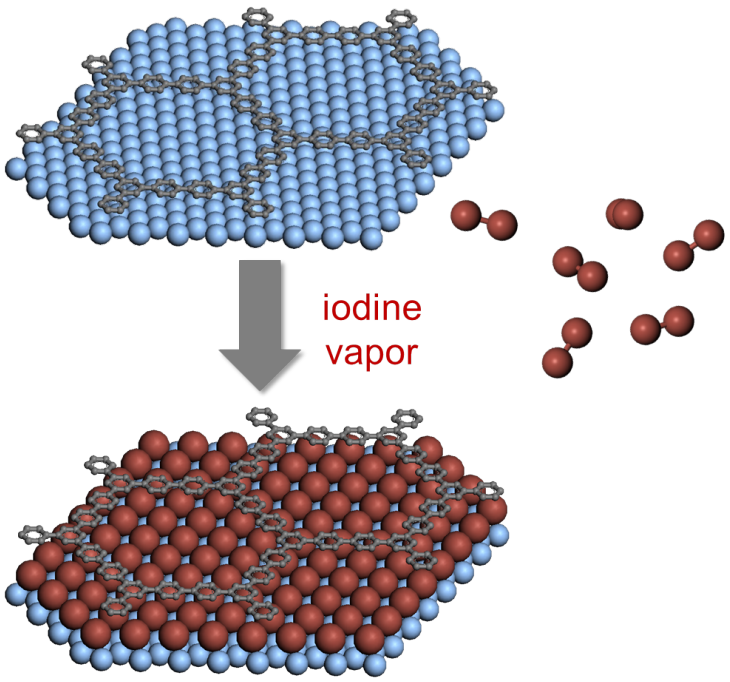

* Two sections of this chapter were published as two articles:
1) A. Rastgoo-Lahrood, J. Björk, M. Lischka, J. Eichhorn, S. Kloft, M. Fritton, T. Strunskus, D. Samanta, M. Schmittel, W. M. Heckl and M. Lackinger. **Post-Synthetic Decoupling of On-Surface-Synthesized Covalent Nanostructures from Ag(111).** *Angew. Chem. Int. Ed.* 55 (2016), 7650-7654. Reproduced with permission from John Wiley & Sons, Inc, Copyright 2016.
2) A. Rastgoo-Lahrood, M. Lischka, J. Eichhorn, D. Samanta, M. Schmittel, W. M. Heckl and M. Lackinger. **Reversible Intercalation of Iodine Monolayers between On-Surface Synthesised Covalent Polyphenylene Networks and Au(111).** *Nanoscale,* 9 (2017), 4995-5001. Reproduced with permission from the Royal Society of Chemistry, Copyright 2017.
I performed all the experiments and the corresponding data analysis and interpretation, and prepared the manuscript under supervision of Prof. Lackinger. DFT calculations were provided by Prof. Jonas Björk from the Linköping University. The molecules were synthesized in the group of Prof. Schmittel at Siegen University. The measurements at synchrotron were done in collaboration with other co-authors.

5.1 Decoupling of Polyphenylene Networks from Ag(111) by Iodine Intercalation

In this section, the detachment of covalent polyphenylene networks from Ag(111) through iodine intercalation by a combination of microscopic and spectroscopic techniques is demonstrated. Post-synthetic exposure of the samples at room temperature to iodine vapor was sufficient for a successful iodine intercalation between polyphenylene networks and Ag(111) surfaces. Moreover, the experimentally observed changes from surface-bound to detached nanosheets are reproduced by DFT simulations. These findings suggest that the intercalation of iodine provides a material that shows geometric and electronic properties substantially closer to those of the free-standing network.

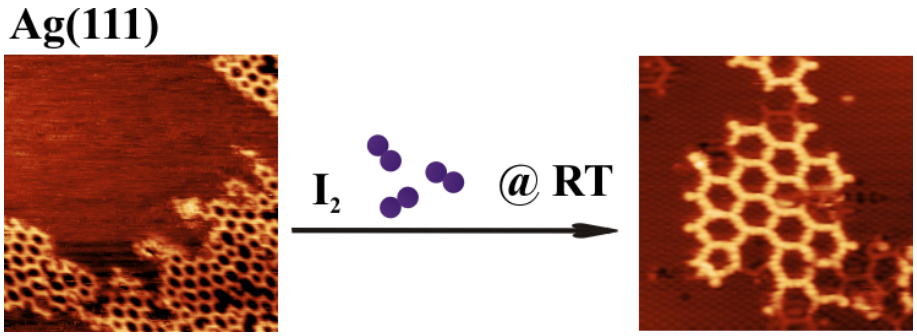

5.1.1 Introduction

The synthesis of extended 1D and 2D organic nanostructures by direct covalent coupling of monomers on solid surfaces is a rapidly advancing field.[1, 2, 3, 4, 121] Diverse coupling strategies have successfully been employed for the on-surface synthesis of unique covalent organic nanosheets that are inaccessible by other synthetic means.[7, 8] With a view to potential applications,[6] the extraordinary mechanical, thermal, and chemical stabilities of covalent networks offer crucial advantages over self-assembled supramolecular structures. Moreover, the prospect of electrical conductivity renders these materials particularly promising for molecular electronics.[5] However, many important coupling reactions proceed on reactive metal surfaces. Among different on-surface synthetic strategies, Ullmann coupling has matured into a well-established method.[10] On-surface Ullmann coupling is in most cases initiated on metals by a surface-supported dissociation of the carbon–halogen bonds.[9, 111] The approach has also been demonstrated on graphene and hexagonal boron nitride on Ni(111), but the restricted diffusion of the dehalogenated species only facilitated growth of smaller oligomers.[12] In principle, thermally activated Ullmann coupling is also feasible on insulator surfaces, but requires appropriate anchoring to prevent desorption.[11] Nevertheless, metal surfaces bear many advantages, but for many, and in particular for electronic applications, conducting supports are precluded. Pursuing the reaction on metal surfaces, inevitably results in adsorption of the reaction products, i.e. the covalent nanostructures, on these strongly interacting surfaces. Hence, the actual properties of the nanostructures are strongly modified on metal surfaces. In cases where coupling does not proceed on inert surfaces, post-synthetic transfer, as routinely applied for graphene grown by chemical vapor deposition (CVD),[122] is a conceivable alternative. Even though the proof of principle has been demonstrated for bottom-up-fabricated covalent nanostructures, for example, by template stripping,[123] transfer of these structures remains challenging. Therefore, methods to decouple the nanostructures from surfaces are exceedingly required.

Ullmann coupling under conditions with iodine excess—both under ambient conditions and ultrahigh vacuum (UHV)—provided evidence for the detachment of smaller covalent nanostructures from the metal surface after their formation and subsequent adsorption on top of a closed iodine monolayer.[120, 124] The affinity of iodine to metals is apparently strong enough to overcome interactions between the surface and organic nanostructures. Motivated by these observations, this chapter aims to explore the deliberate exposure of metal-adsorbed covalent nanostructures to iodine vapor as a novel and straightforward approach for post-synthetic decoupling. Samples were characterized *in situ* before and after iodine exposure by STM, XPS, NEXAFS. Alterations in the geometric and electronic structures were studied by density functional theory (DFT) calculations (see appendix B.1 for computational details).

5.1.2 Results and Discussion

Two-dimensional porous covalent polyphenylene networks derived from 1,3-bis(*p*-bromophenyl)-5-(*p*-iodophenyl)benzene precursors (BIB, see inset in Figure 5.3(c) for structure) on Ag(111) were chosen as the model system.[100] In a first step,

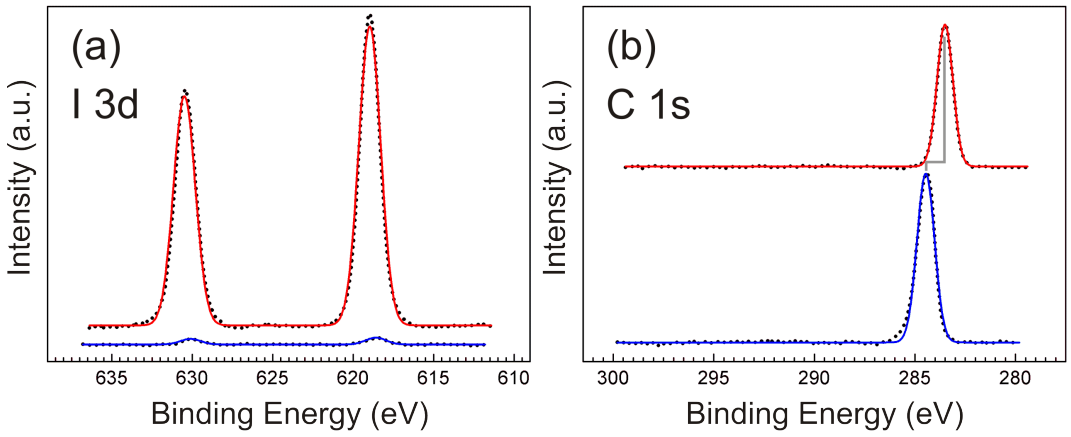

Figure 5.1: a) I 3d and b) C 1s XP spectra acquired before (lower spectra, blue lines) and after (upper spectra, red lines) exposure to iodine (offset for clarity). I 3d consists of a 3/2 and 5/2 spin-orbit doublet. The small amount of pre-adsorbed iodine originates from the deiodination of BIB preceding formation of the covalent network.

covalent networks were prepared by deposition of BIB onto Ag(111) at room temperature followed by annealing at about 270 °C. In the next step, samples were exposed to I_2 vapor (5×10^{-7} mbar, ca. 5 min). XPS measurements conducted before and after iodination are depicted in Figure 5.1. The I 3d spectrum shows a marked increase in surface-bound iodine after exposure, whereas the C 1s spectrum indicates a constant amount of carbon. The measured $I3d_{5/2}$ binding energy of 619.0 eV agrees with references for chemisorbed atomic iodine,[125] thus confirming dissociative adsorption of I_2. C 1s exhibits a shift of about 0.92 eV to lower binding energies after iodination, while the line shape changes from slightly asymmetric to symmetric.

The asymmetric feature of C 1s on bare Ag(111) with a small shoulder at higher binding energies originates from direct interactions with the free electron gas of the metal and Kondo-like screening of the core-holes by these electrons.[126] Hence, its disappearance after exposure to iodine indicates both detachment and decoupling of the structure. The mismatch of the Gaussian fit with the measured data is obvious from Figure 5.1(b). Accordingly, fitting the C 1s peak before iodination with an asymmetric lineshape (Asym2Sig) results in an obvious improvement. For a direct comparison, Figure 5.2 indicates C 1s pre-exposure spectrum with Gaussian and Asym2Sig fits and the post-exposure spectrum with the Gaussian fit.

The initial structural characterization was carried out by STM. The overview image in Figure 5.3(a) depicts covalent networks that grow over step edges, but otherwise appear higher (brighter) than the respective terraces, while the close-up image in Figure 5.3(b) reveals a new hexagonal structure with a lattice parameter of (0.50±0.03) nm, which corresponds to the known $\sqrt{3}\times\sqrt{3}$ R30° iodine superstructure on Ag(111).[125] In accordance with XPS, this new structure is identified as a densely packed iodine monolayer. Another iodine superstructure was also occasionally observed. Figure 5.4 shows both iodine superstructures. The STM data clearly confirm the adsorption of iodine, but cannot settle the

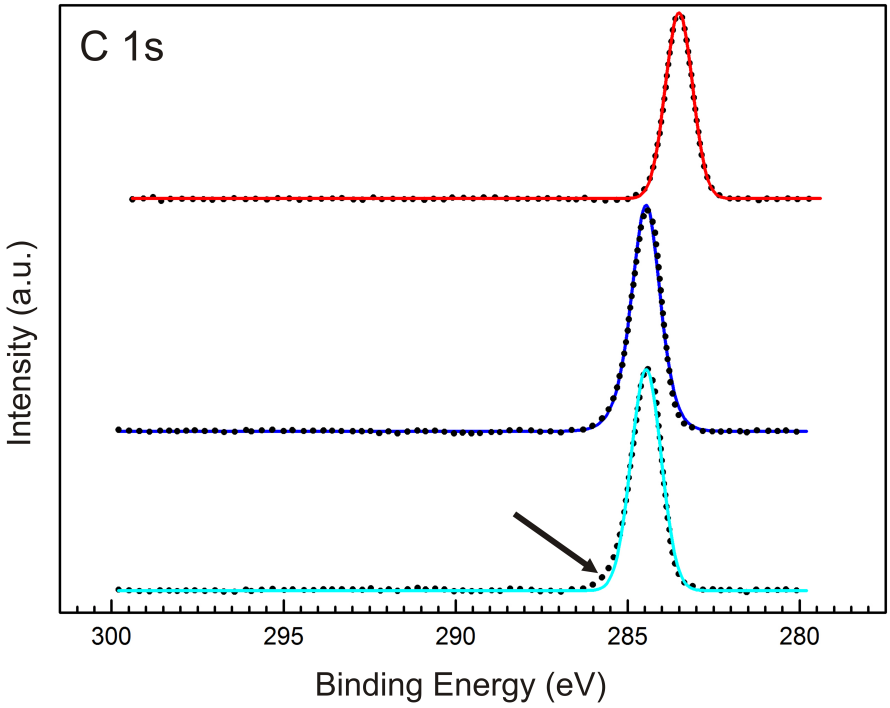

Figure 5.2: XP spectra of C 1s acquired before (lower, turquois line – middle, blue line; same data, different fits) and after (upper, red line) iodine exposure. The black dots represent experimental data, the solid lines are fits. The lower and upper spectra are fitted with Gaussians: the fit matches very well for the post-exposure spectrum (red line), whereas there is an obvious mismatch for the pre-exposure spectrum (turquoise line) due to an asymmetry caused by a small shoulder at the higher binding energy side (marked by black arrow). Fitting the pre-exposure spectrum with an asymmetric lineshape (Asym2Sig) results in an obvious improvement (blue line). The presence of this spectroscopic signature at the high binding energy side indicates an intimate contact of carbon, i.e. the networks, to the metal surface. Consequently, its disappearance after iodine exposure indicates both detachment of the networks from the metal surface and significant decoupling.

central question: Does iodine only coadsorb on the free surface areas or does it detach the covalent networks and form a closed monolayer underneath? This crucial point was addressed by lateral manipulation of a covalent domain, which revealed a close-packed iodine monolayer underneath. The corresponding STM images are shown in Figure 5.3(c,d).

Rapid refilling of the large void space, which would be created directly after displacement of the covalent network, by surface diffusion of iodine from the metal can be excluded: even monoatomic iodine vacancies remain immobile for more than five minutes at the imaging temperature of about 80 K. Figure 5.5 indicates series of subsequent STM images from the same sample area, demonstrating the immobility of the iodine vacancies.

Moreover, a pronounced variation in the height and contrast was observed occasionally within the covalent networks; an example is marked in Figure 5.3(b). Integral parts of the network appear lower, thus indicating direct adsorption on the metal surface. Conversely, this implies that the majority of the polyphenylene network is indeed detached from the Ag(111) surface. Figure 5.6 facilitates a direct comparison of the apparent heights w.r.t. the iodine monolayer of these two parts, i.e.$\sim$236 pm for detached vs. $\sim$66 pm for networks directly adsorbed on Ag(111).

In addition, the part of the network on the iodine layer not only appears higher, but also exhibits internal contrast, which is unprecedented for networks directly absorbed on metals. This STM contrast resembles the HOMO/LUMO of the free-standing network (see Figure 5.7), thereby providing further experimental evidence for substantial weakening of the coupling.[127]

Additional structural characterization was carried out by NEXAFS.[38] The samples were again measured before and after exposure to iodine. The normalized C 1s NEXAFS spectra are summarized in Figure 5.8. The most evident changes are increased intensities at larger X-ray incidence angles (e.g. 90°) and decreased intensities at smaller incidence angles (e.g. 30°) after idodine exposure, thus already indicating a change in the adsorption geometry towards increased tilt angles of the phenyl groups w.r.t. the surface plane.

From a more detailed analysis of the dependence of the intensities on the X-ray incidence angle, tilt angles of (15 $\pm$ 5)° and (35 $\pm$ 5)° for the phenyl groups were extracted before and after iodination, respectively (see Figure 5.9). This pronounced change can be explained consistently by intercalation of an iodine monolayer: According to DFT simulations, the phenyl groups in a free-standing polyphenylene network would feature relatively large tilt angles of about 23° as a result of steric hindrance of the ortho-hydrogen atoms (see Figure 5.7(a) for DFT-optimized structure). Upon adsorption on a metal, this steric hindrance is partly overcome by attractive molecule–surface interactions, thereby resulting in smaller tilt angles. Interestingly, these interactions are not strong enough on Ag(111) to enforce a fully planar adsorption. After intercalation of an iodine

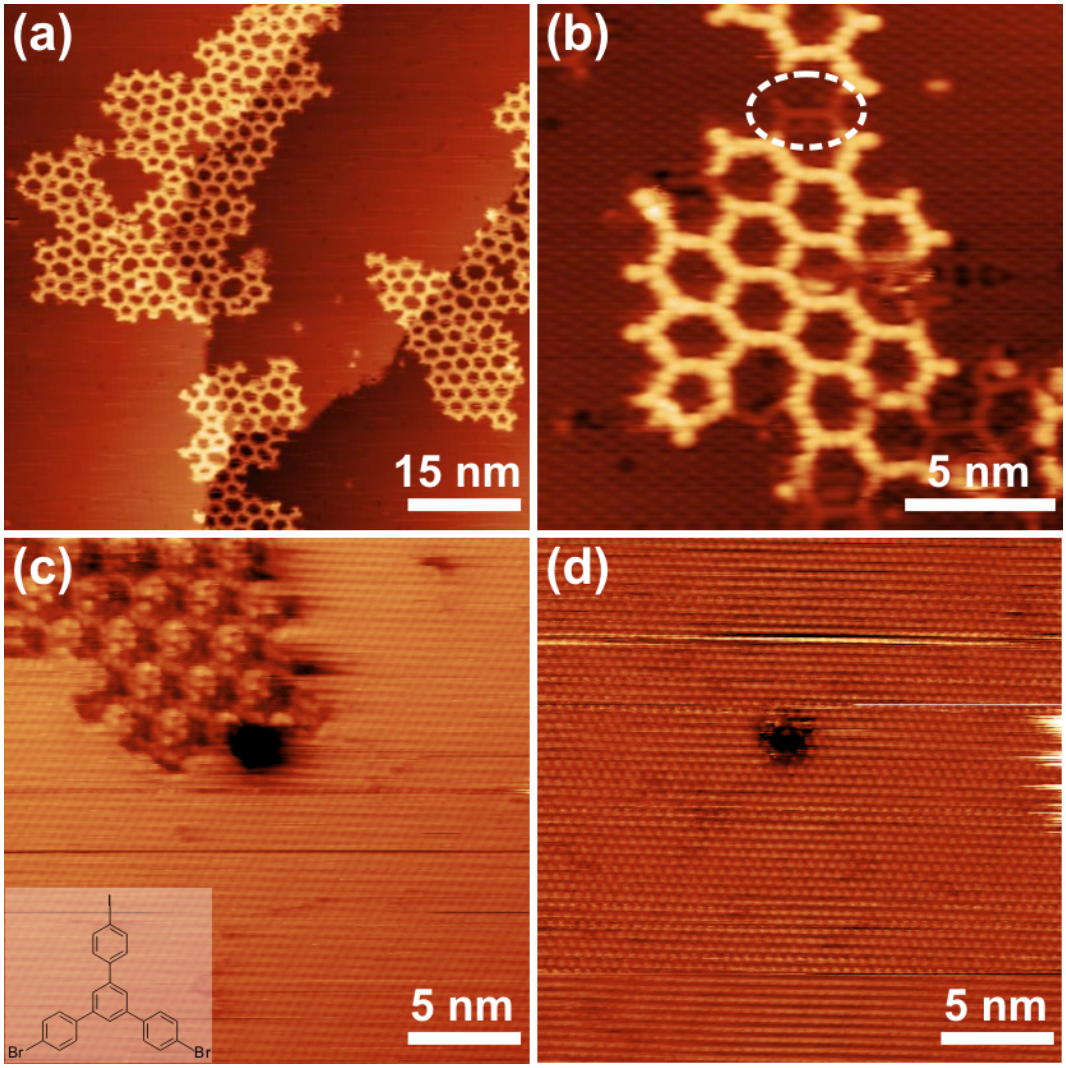

Figure 5.3: STM images acquired after exposure to iodine. a) Overview (U_T = -516 mV, I_T = 20 pA) and b) close-up (U_T = +800 mV, I_T = 20 pA). The dashed oval marks an occasionally observed contrast variation within the network. Lateral manipulation of a covalent network revealed a close-packed iodine monolayer underneath. STM images of the same sample area c) before (U_T = +500 mV, I_T = 30 pA) and d) after (U_T = -500 mV, I_T = 30 pA) the network was removed. The dark area is an iodine vacancy island and serves as a site marker. Inset in (c): chemical structure of BIB.

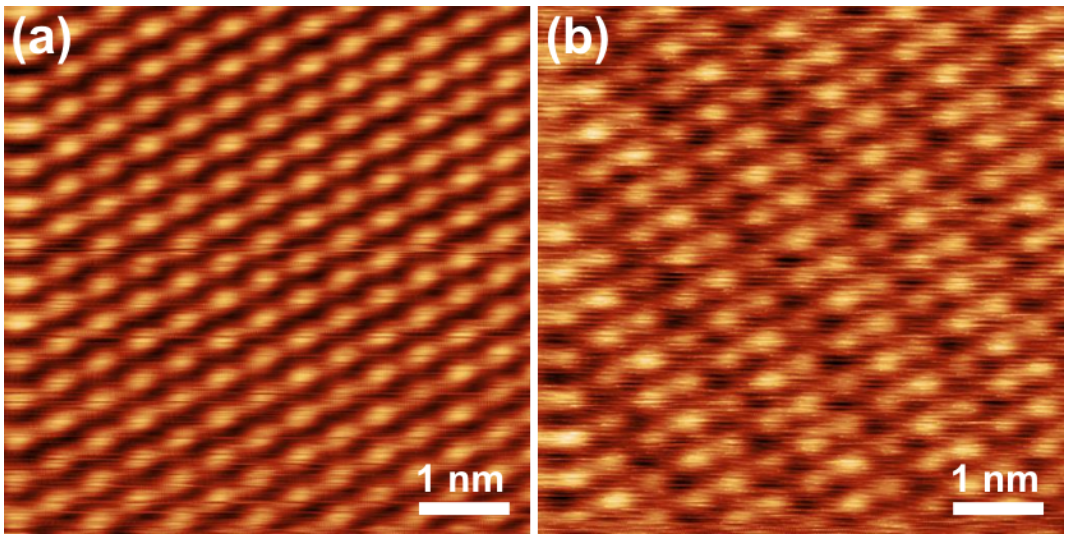

Figure 5.4: (a) Commonly observed $\sqrt{3} \times \sqrt{3}$ R30° iodine superstructure on Ag(111) with a lattice parameter of (0.50 ± 0.03) nm (U_T = +300 mV, I_T = 30 pA). (b) Occasionally observed alternative iodine superstructure (U_T = -63 mV, I_T = 40 pA) with superimposed contrast modulation, but similar iodine-iodine nearest neighbor distance within experimental accuracy.

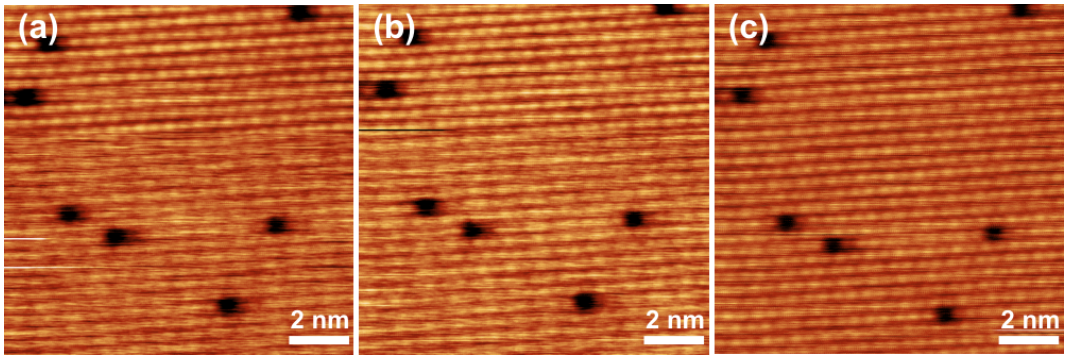

Figure 5.5: Time series of STM images of a close packed iodine monolayer with single vacancies ((a): U_T = +0.66 V, I_T = 25 pA; (b) & (c): U_T = +0.51 V, I_T = 25 pA). These images were acquired at a sample temperature of ∼80 K with a frame time of ∼105 s. The iodine vacancies remained immobile on a time scale of more than 5 minutes, indicating a very low surface diffusion coefficient of iodine on Ag(111) at liquid nitrogen temperatures.

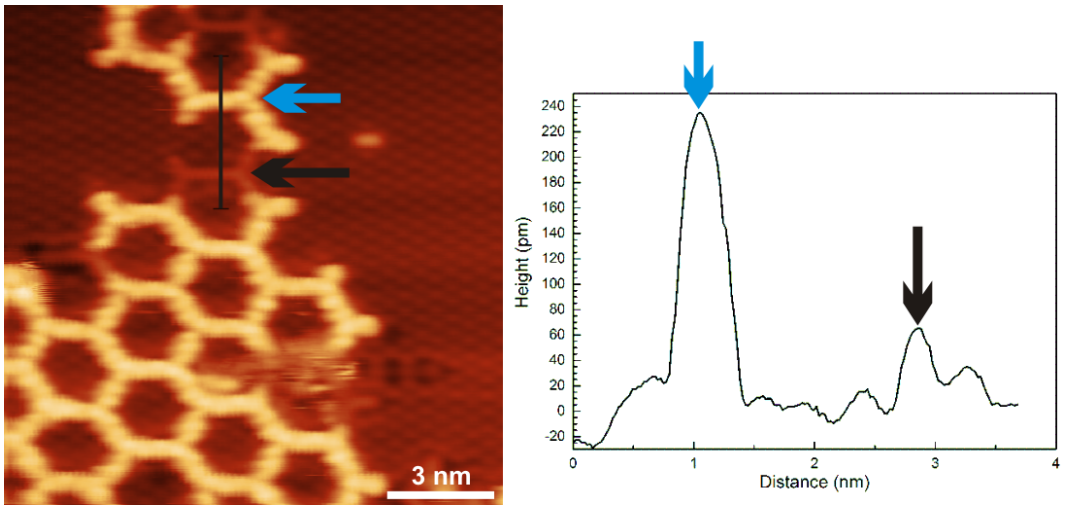

Figure 5.6: Left side: STM image acquired after iodination (U_T = +800 mV, I_T = 20 pA). Right side: Corresponding line-profile along the black line. The darker appearing parts of the network (black arrow) are directly adsorbed on the metal surface, whereas the bright appearing, i.e. majority of the networks, are detached and adsorbed on top of a closed iodine monolayer.

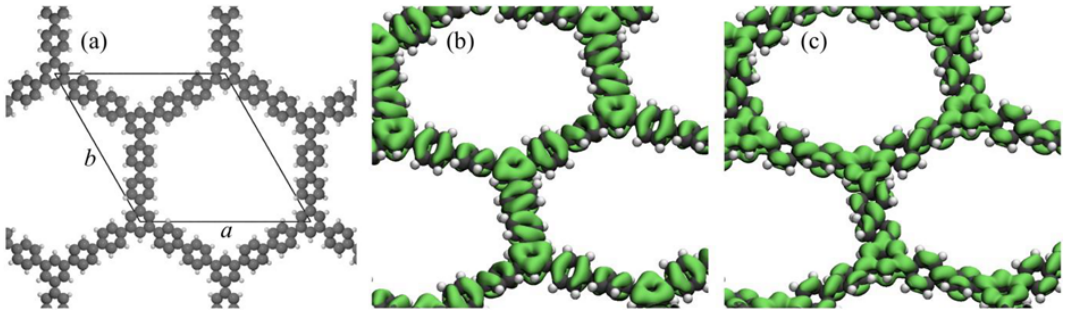

Figure 5.7: (a) DFT-optimized structure of a free-standing polyphenylene network, yielding phenyl tilt angles of 23° with respect to the three-fold connected phenyl rings which necessarily remain untilted. The lattice was constrained to hexagonal, and optimization of the lattice parameter resulted in a = b = 2.25 nm. Corresponding electron density contour plots of (b) HOMO and (c) LUMO (plotted at an electron density of 0.005 e/Å^3). The spatial electron density distribution of these orbitals resembles the STM contrast of the covalent networks on top of the iodine monolayer. An orbital dominated STM contrast indicates weak coupling to the underlying metal surface.

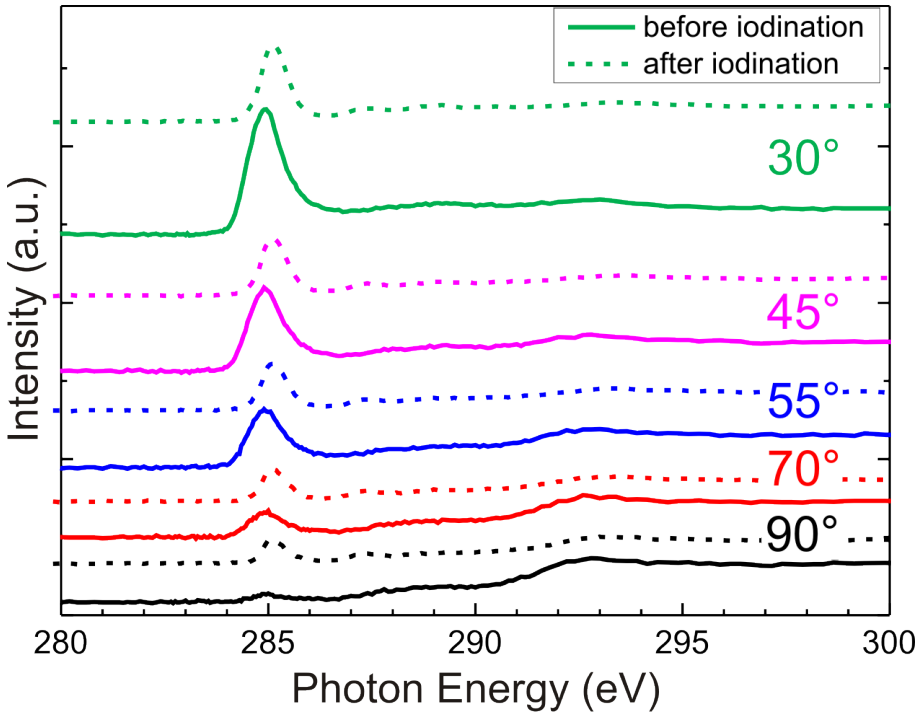

Figure 5.8: NEXAFS spectra acquired for various incidence angles before (solid lines) and after (dashed lines) exposure to iodine (offset for clarity). Note that the incidence angle is defined with respect to the surface plane, that is, 90° corresponds to normal incidence. The prominent resonance at a photon energy of about 285 eV arises from a C 1s→π^* transition.

monolayer, molecule–surface interactions become significantly weaker than on the bare metal surface. This facilitates relaxation toward the structure of a free-standing network, that is, larger tilt angles of the phenyl groups.

Complementary DFT calculations were conducted on bare and iodine-terminated Ag(111) to substantiate the hypothesis that larger tilt angles indicate polyphenylene networks on top of a closed iodine monolayer. *p*-Terphenyl was chosen as a reasonably sized model system as its phenyl–phenyl σ bonds represent the main structural feature of the actual polyphenylene network. Optimized structures for the lowest energy adsorption sites are depicted in Figure 5.10 (see appendix B.1 for additional results). The DFT-optimized structure of *p*-terphenyl on bare Ag(111) shows planar adsorption, whereas on iodine-terminated Ag(111) it exhibits a tilt angle, that is, half of the phenyl–phenyl dihedral angle, of 19°. However, an adsorption geometry with a tilt angle of 9.5° was found to be energetically equal to fully planar adsorption on bare Ag(111). In any case, DFT and NEXAFS agree insofar as the tilt angles of phenyl groups on iodine-terminated Ag(111) are larger than on pristine Ag(111), hence providing further evidence for the intercalation of iodine. In addition, DFT results in a substantial reduction of the adsorption energy from -1.49 eV on pristine Ag(111) down to -0.84 eV on iodine-terminated Ag(111). Moreover, DFT provides complementary evidence for electronic decoupling of the organic networks from the metal surface by the iodine monolayer. Figure 5.10(b,d) shows the partial density of electronic states (PDOS) projected onto the carbon atoms of *p*-terphenyl on both surfaces compared to in the gas phase. The PDOS changes significantly upon adsorption on

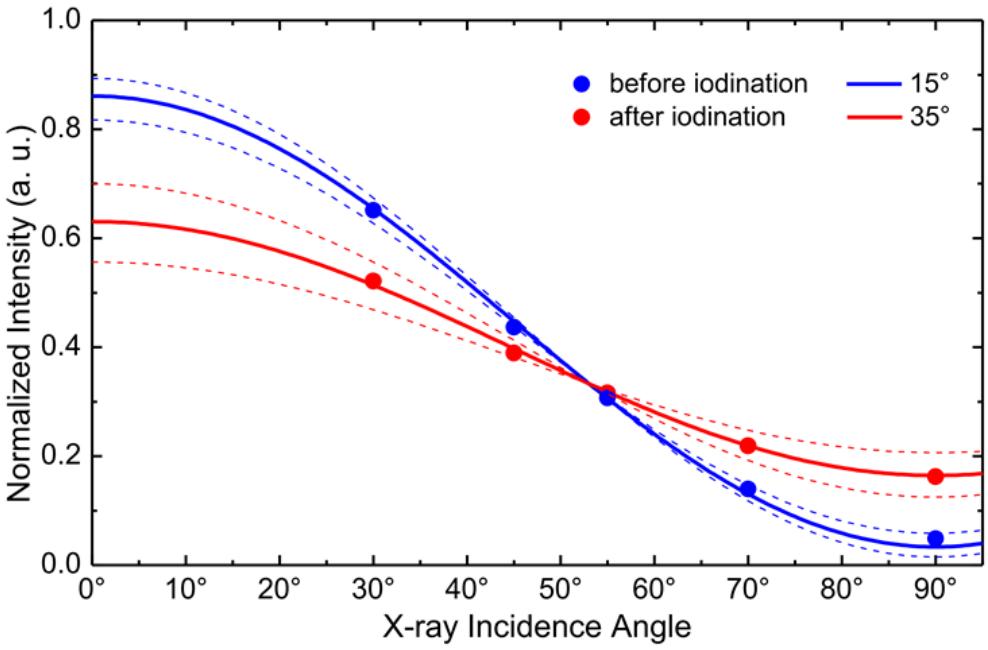

Figure 5.9: Normalized intensities (i.e. peak maxima) of the C 1s→π^* resonance vs. X-ray incidence angle (with respect to the surface) before (blue dots) and after (red dots) iodination. The solid lines represent theoretical curves for phenyl tilt angles with respect to the surface of 15° (blue curve) and 35° (red curve), plotted for the beamline-specific degree of linear polarization of P=0.92. The dashed curves delineate uncertainty intervals of ±5° to the stated angles.

bare Ag(111), whereas changes on iodine-terminated Ag(111) are minor, hardly affecting the frontier molecular orbitals.

Further experimental evidence for a significantly weakened electronic coupling between the polyphenylene networks and Ag(111) after exposure to iodine comes from NEXAFS. For an incidence angle of 45° the full-width at half-maximum (FWHM) of the C 1s→π^* resonance is reduced from 0.99 eV on Ag(111) down to 0.73 eV after iodine intercalation (see Figure 5.11). Similar effects are well known for monolayers versus multilayers,[128, 129] and indicate significantly weaker coupling to the surface.

5.1.3 Conclusions

In summary, we propose iodine intercalation as a novel, straightforward, and widely applicable approach for the post-synthetic decoupling of on-surface-synthesized covalent organic nanostructures from Ag(111). Through a combination of STM, XPS, and NEXAFS, it was demonstrated that exposure of covalent polyphenylene networks adsorbed on Ag(111) to iodine vapor results in their detachment from the metal surface through intercalation of an iodine monolayer. NEXAFS and DFT consistently find a structural relaxation as the tilt angles of the phenyl groups increased after iodine intercalation, thereby indicating a weakened molecule–surface interaction for the iodine monolayer compared to the

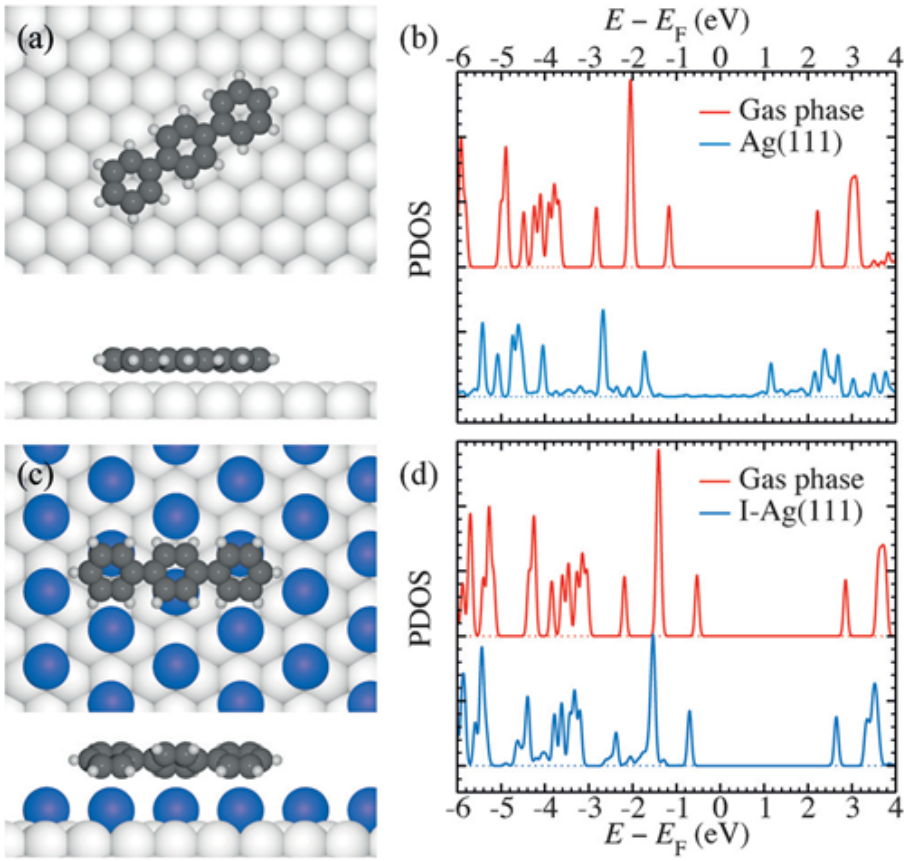

Figure 5.10: DFT-optimized adsorption geometries and corresponding PDOS of carbon atoms for *p*-terphenyl on: a,b) pristine and c,d) iodine-terminated Ag(111). The upper and lower parts of (a) and (c) show the top and side views, respectively. The PDOS were evaluated for the optimized equilibrium positions (lower spectra in (b) and (d), blue and violet lines) as well as in the gas phase (upper plots, red lines), with the vacuum level aligned to those of the surface systems.

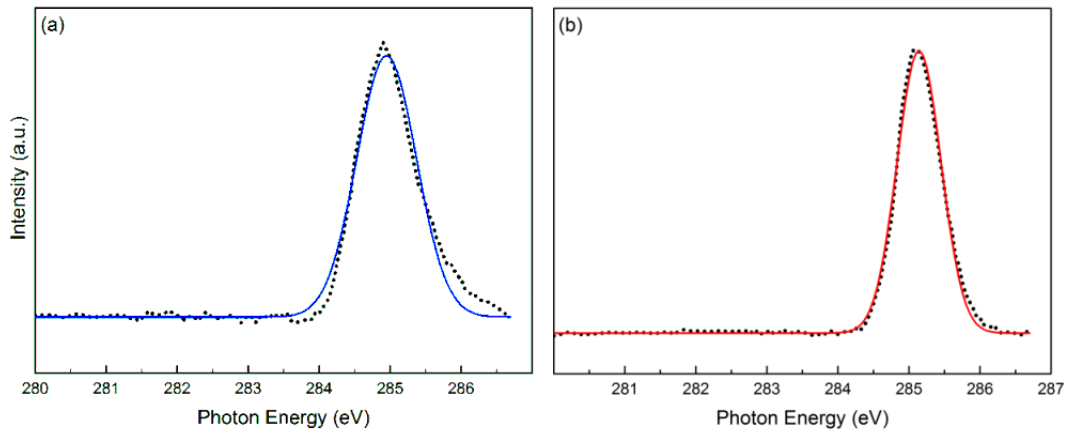

Figure 5.11: Normalized C 1s NEXAFS spectra acquired at an X-ray incidence angle of 45° (a) before and (b) after iodine exposure. In both cases the C 1s→π^* resonances were fitted with Gaussians, resulting in FWHM of 0.99 eV (σ=0.42 eV) before vs. 0.73 eV (σ=0.31 eV) after iodine exposure. Narrowing of the C 1s→π^* resonance indicates a longer lifetime of the excited state due to reduced coupling of the covalent networks to the metal surface.

bare metal. This is consistent with the markedly reduced adsorption strength on iodine-terminated surfaces found from DFT calculations. In addition, DFT simulations suggest a significant weakening of the electronic coupling to the metal surface through the presence of a single monolayer of iodine. Experimental evidence is provided both by the change in the line shape by XPS as well as sharpening of the C 1s→π^* resonance by NEXAFS after exposure to iodine. Charge transfer, hybridization, and surface polarization affect the electronic structure of molecular networks directly adsorbed on metals.[130] Since these effects are not easily taken into account by simulations, decoupling by the intercalation of iodine facilitates more meaningful comparisons, for example, of electronic band gaps, between theory and experiment. In particular, our approach allows the characterization of intrinsic electronic properties of covalent nanostructures. We also anticipate advantages for transfer by stamping, as the reduced adsorption strength promotes detachment.

5.1.4 Experimental Details

All preparation and analysis steps were carried out under UHV. Ag(111) single crystal surfaces were prepared by repeated cycles of Ar^+ ion-sputtering at 1.0 keV and electron-beam annealing at ∼460 °C for ∼8 minutes. The surface cleanliness was verified either by STM imaging (for STM experiments) or by XPS (for XPS and NEXAFS experiments) prior to deposition of the monomers. The synthesis of 1,3-bis(*p*-bromophenyl)-5-(*p*-iodophenyl)benzene (BIB) precursors was previously described.[103] BIB molecules were deposited by means of a home-built evaporator[131] at a crucible temperature of ∼170 °C for ∼3 minutes onto the surface held at room temperature. Covalent networks were obtained by subsequent annealing at ∼270 °C.[100] Iodination of the covalent networks on Ag(111)

was carried out at $\sim 5\times10^{-7}$ (2×10^{-6}) mbar for $\sim$5 (10) minutes for STM (XPS /NEXAFS) experiments in a small auxiliary chamber to avoid contamination of the main UHV chamber. All STM data were acquired in-situ at $\sim$80 K and a base pressure below 3×10^{-10} mbar with a home-built microscope driven by a Nanonis BP4 SPM control system. STM images were leveled and processed by a mean value filter.
XPS and NEXAFS experiments were conducted at the BESSY II synchrotron (Helmholtz-Zentrum Berlin). Sample preparation was similar to the STM experiments. Iodine 3d and carbon 1s XP spectra were acquired with a pass energy of 50 eV using a Scienta R3000 electron analyzer at normal electron emission and photon energies of 750 eV and 450 eV, respectively.
I 3d spin-orbit doublets were fitted with two Gaussians of equal width, applying a fixed energy separation of 11.52 eV. C 1s peaks were fitted with Gaussians. The asymmetric C 1s peak was additionally fitted with an asymmetric double sigmoid function (Asym2Sig) (see Figure 5.2). C 1s NEXAFS spectra were acquired for X-ray incidence angles (w.r.t. to the surface plane) of 30°, 45°, 55°, 70°, and 90°. Phenyl tilt angles with respect to the surface plane were quantified from the incidence angle dependence of the C 1s$\rightarrow\pi^*$ intensities.

5.2 Decoupling of Polyphenylene Networks from Au(111) by Iodine Intercalation

In this section, post-synthetic decoupling of polyphenylene networks by intercalation of a chemisorbed iodine monolayer from Au(111) surface is investigated. On the more reactive Ag(111) surfaces, presented in the previous section, intercalation was readily accomplished by exposing the samples to iodine vapor at room temperature. On more noble Au(111), however, STM, XPS and NEXAFS consistently indicate that the same protocol merely results in co-adsorption of iodine on uncovered surface areas, whereas the covalent networks remain adsorbed on the metal. Yet, performing the iodine exposure at elevated surface temperatures similarly results in detachment of the organic networks via intercalation of an iodine monolayer also on Au(111) as evidenced by characteristic changes in STM. In addition, owing to the high thermal stability of the covalent networks and the comparatively low iodine desorption temperature, the reversibility of the process is demonstrated: sample annealing at 400 °C results in complete desorption of the iodine monolayer, whereby the covalent networks re-adsorb directly on Au(111).

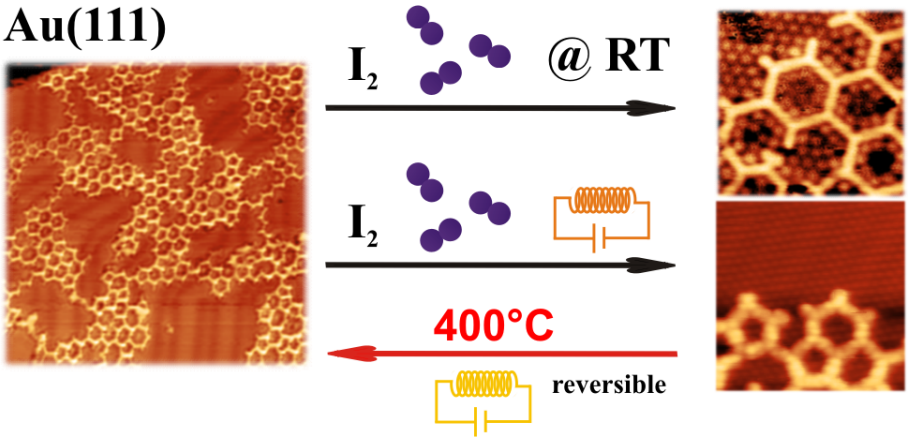

5.2.1 Introduction

As mentioned in the previous section, for many applications particularly for electronic applications adsorption of the covalent nanostructures on metal surfaces are adverse. Strong interactions with the substrate result in structural changes and hybridization of electronic states of the covalent networks and the underlying metal surface. Therefore, characterizing the real properties of the nanoarchitectures is not really possible. For instance, even though the successful synthesis of graphene nano-ribbons with zig-zag edge topology on Au(111) was recently reported, spectroscopy of the proposed edge-state was intricate due to strong interactions with the metal surface.[132]
Consequently, there is a high demand for generally applicable methods for post-synthetic decoupling of on-surface synthesized covalent nanostructures from metal surfaces especially from technologically more relevant Au(111) surfaces. The detachment of covalent two-dimensional polyphenylene networks from Ag(111) by intercalation of an iodine monolayer in between the nanostructures and the metal surface was demonstrated in the last section.[133] Exposing the samples to iodine vapor at room temperature was already sufficient, as intercalation is driven by the high adsorption strength of iodine on Ag(111). In addition to STM, both XPS and NEXAFS provided experimental evidence for efficient decoupling by just a single layer of iodine. Even though iodine intercalation on Ag(111) was introduced as a straightforward approach for post-synthetic decoupling of nanostructures from metals, it is not clear whether the same protocol would generally apply also to less reactive metal surfaces with Au(111) as the most important and widespread example. This open question is tackled here by applying a similar protocol with iodine exposure at room temperature to pre-synthesized covalent nanostructures on Au(111). The entire preparation, including iodine exposure, was carried out in ultra-high vacuum, and samples were *in situ* characterized by STM, augmented by XPS and NEXAFS experiments.

5.2.2 Room Temperature Iodination

For direct comparability with the previous study on Ag(111),[133] similar covalent polyphenylene networks are now studied on Au(111). The two-dimensional porous covalent polyphenylene networks were synthesized by depositing 1,3-bis(*p*-bromophenyl)-5-(*p*-iodophenyl)benzene (BIB, cf. Figure 5.12 for structure) precursors onto Au(111) at room temperature, followed by sample annealing.[103] On Au(111), BIB-derived covalent networks are typically less regular and exhibit lower structural quality as compared to those on Ag(111), where bond reversibility in an intermediate organometallic state facilitates error correction and equilibration.[100] These differences in network morphology between Ag(111) and Au(111), however, are not important for the present study of decoupling. After on-surface synthesis of the covalent networks, samples were exposed to iodine vapor (5×10^{-7} mbar, ∼15 min) with the surface held at room temperature. Before STM imaging, samples were mildly annealed at 140 °C to desorb volatile contamination. This temperature is sufficiently low to safely exclude any changes of the covalent networks or iodine desorption. Samples were characterized *in situ* before and after iodine exposure at room temperature by STM, XPS, and NEXAFS.

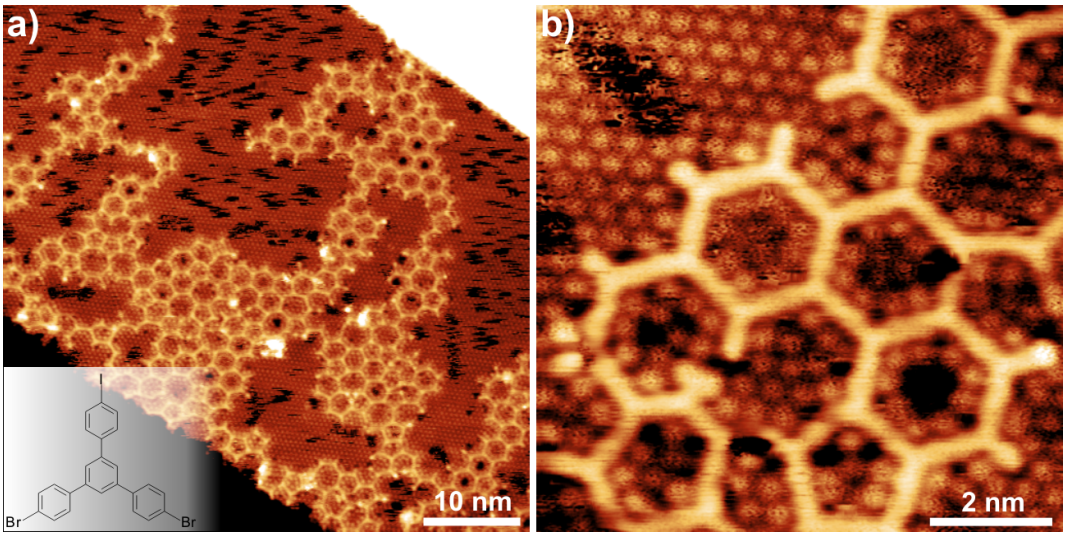

Figure 5.12: STM images of BIB-derived covalent polyphenylene networks on Au(111) acquired after iodine exposure (5×10^{-7} mbar, ~15 min) with the sample held at room temperature. a) Overview (U_T = +858 mV, I_T = 25 pA), the color scale is adjusted to optimize the contrast of the center terrace (cf. Figure B.4 in B.2 for alternative color scale); the inset depicts the chemical structure of BIB. b) Close-up (U_T = +1200 mV, I_T =20 pA).

The STM images acquired after iodination in Figure 5.12 revealed beside the covalent networks a new closely packed hexagonal structure with a lattice parameter of (0.48 ± 0.02) nm, corresponding to the known $\sqrt{3} \times \sqrt{3}$ R30° iodine superstructure on Au(111).[134, 135, 136] In particular for a wet chemical preparation of iodine monolayers on Au(111) from iodide solutions various superstructures with different packing densities are reported,[135] whereas for iodine adsorption from vapor this hexagonal superstructure is most common.

Iodine adsorption is further confirmed by XPS through a marked increase of I 3d intensity after iodine exposure (cf. Figure 5.13). The small amount of iodine adsorbed on the surface before deliberate exposure originates as by-product of the BIB-polymerization. The I $3d_{5/2}$ binding energy of 618.5 eV (before iodination 618.6 eV, after iodination 618.4 eV) is in a good agreement with the literature value for chemisorbed atomic iodine on Au(111),[120] proving dissociative chemisorption.

On Au(111), however, iodine exposure just leads to iodine co-adsorption on the uncovered surface areas, but not in intercalation. Convincing evidence for this hypothesis is already provided by STM: The overview image in Figure 5.12(a) shows many dark areas between the covalent networks that can only be interpreted as iodine vacancy islands. The close-up image in Figure 5.12(b) reveals incomplete filling of the network's pores with iodine. These observations stand in vast contrast to our previous results on Ag(111), presented in the last section, where the iodine layer was fully closed and all pores were completely filled. In addition, the fringed boundaries of the darker patches indicate residual mobility of surface-bound iodine even at the imaging temperature of 80 K. The movement of iodine atoms within and between not fully closed pores can be traced in the

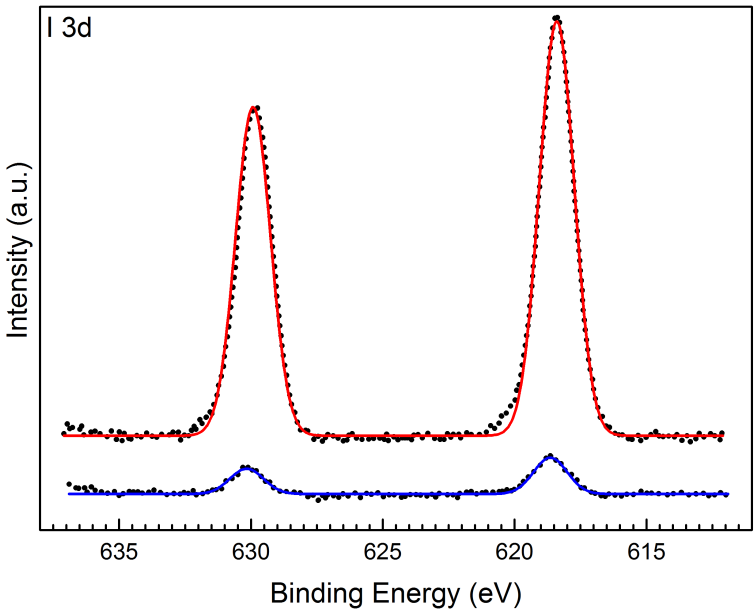

Figure 5.13: XP spectra of iodine 3d core levels of BIB-derived covalent polyphenylene networks on Au(111) acquired before (lower spectra, blue line) and after (upper spectra, red line) exposure to iodine vapor (offset for clarity). The two peaks of I 3d are due to spin-orbit splitting.

series of consecutive STM images shown in Figure 5.14. Increasing the iodine exposure time and pressure (2×10^{-6} mbar for ∼20 min) was not successful to improve the iodine coverage and obtain a closed monolayer.

The internal STM contrast of the covalent networks is a further notable difference to Ag(111). After iodine exposure on Ag(111) the covalent networks appeared with an STM contrast resembling frontier molecular orbitals of free-standing networks. This was taken as indication for detachment. On Au(111), however, the STM contrast does not change at all after iodination, and comparable internal contrast features were never observed. Lastly, the apparent STM heights of the networks were evaluated. The best way to achieve this is a direct comparison between the covalent networks after iodination and similar molecules that are definitely adsorbed on top of the iodine monolayer. To exclude any tip and bias voltage influences such a comparison should preferentially be carried out within the same image. To this end additional BIB molecules were deposited after iodination. The corresponding STM image in Figure 5.15 additionally shows isolated BIB molecules on top of the iodine monolayer. The asymmetric appearance with a bright feature on one of the lobes is in accord with the molecular structure of BIB and the known prominent STM contrast of iodine substituents,[118, 124] indicating intact molecules. Apparent height measurements with respect to the underlying iodine layer result in a significantly larger value of ∼59 pm for the single BIB molecules vs. ∼32 pm for the covalent network (cf. Figure 5.15 for line-profile). Even though the electronic structures of single molecules and net-

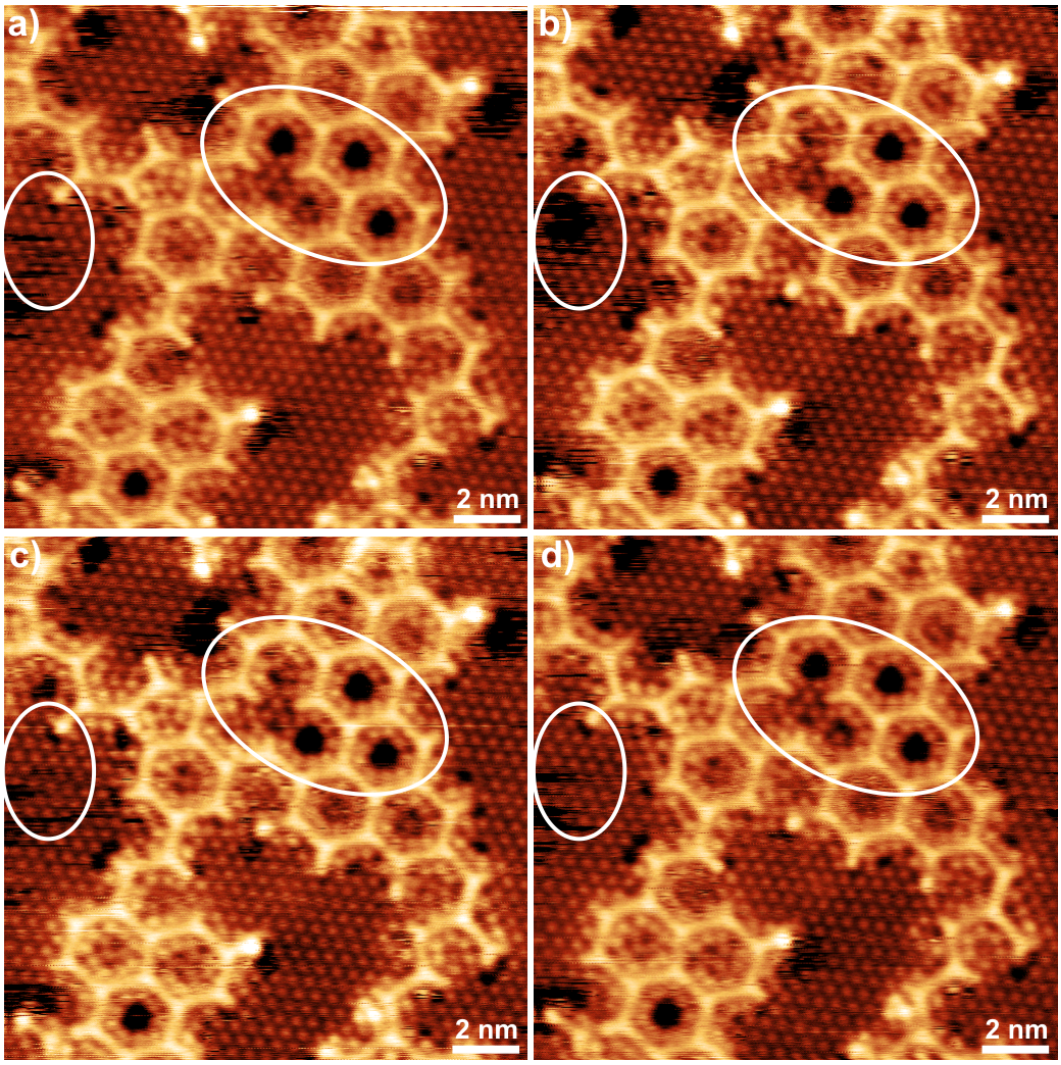

Figure 5.14: Series of consecutive STM images of BIB-derived covalent polyphenylene networks on Au(111) acquired at ∼80 K after iodine exposure at room temperature (U_T = +858 mV, I_T = 25 pA, 102 seconds per frame). The white ovals highlight reconfigurations of iodine both within pores and adjacent to the covalent networks.

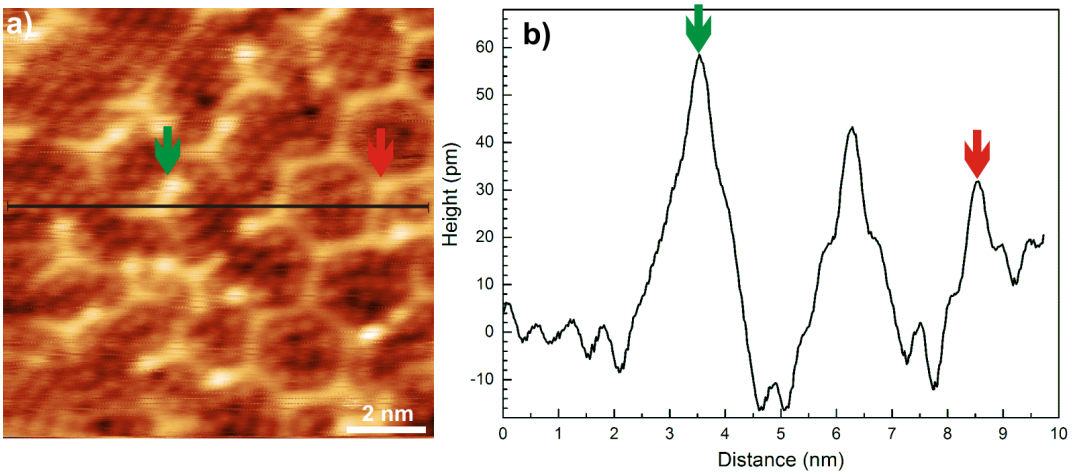

Figure 5.15: a) STM image acquired after deposition of additional BIB molecules on previously iodinated samples (U_T = +1260 mV, I_T = 30 pA). b) Line-profile along the black line indicated in a). The apparent height of unreacted BIB molecules (marked by the green arrow) with respect to the iodine layer of ∼59 pm is larger than the apparent height of the polyphenylene networks of ∼32 pm (marked by the red arrow).

works are not identical, this large apparent height difference further supports the hypothesis of unsuccessful detachment.

To complete the spectroscopic comparison to Ag(111), C 1s XP spectra were also acquired before and after iodination (cf. Figure 5.16). As anticipated, the total amount of adsorbed carbon remains similar. Yet, before iodination the C 1s peak is asymmetric owing to a small shoulder at higher binding energies. This is due to screening of the core hole by the free electron gas of the metal. After iodination this asymmetry does not disappear completely, but becomes slightly less pronounced, whereas on Ag(111) the C 1s peak becomes entirely symmetric after iodination. This indicates the persistence of a direct interaction between covalent networks and Au(111) after room temperature iodination. Interestingly, C 1s exhibits a slight shift of ∼0.35 eV to lower binding energies after iodination. However, this shift disappears with thermal desorption of iodine after annealing the samples at 350 °C. (cf. Figure 5.20). A similar, but more pronounced shift of 0.92 eV was also observed on Ag(111) after iodination. Clarifying the origin of the C 1s binding energy shift requires theoretical efforts. However, chemisorbed iodine on metals is negatively charged, hence a larger amount of surface-bound iodine might modify the surface electronic properties with conceivable consequences for the charge transfer to adsorbed molecules. An additional influence from the resulting dipole layer cannot be excluded.

NEXAFS was performed to study possible changes of the adsorption geometry, i.e. the average phenyl tilt angle upon iodination. Similar NEXAFS measurements on Ag(111) indicated a drastic change from (15° ± 5°) to (35° ± 5°) that was consistently explained by iodine intercalation. Normalized C 1s NEXAFS spectra obtained on Au(111) before and after iodine exposure for a series of X-ray incidence angles are shown in Figure 5.17. All spectra exhibit a pronounced

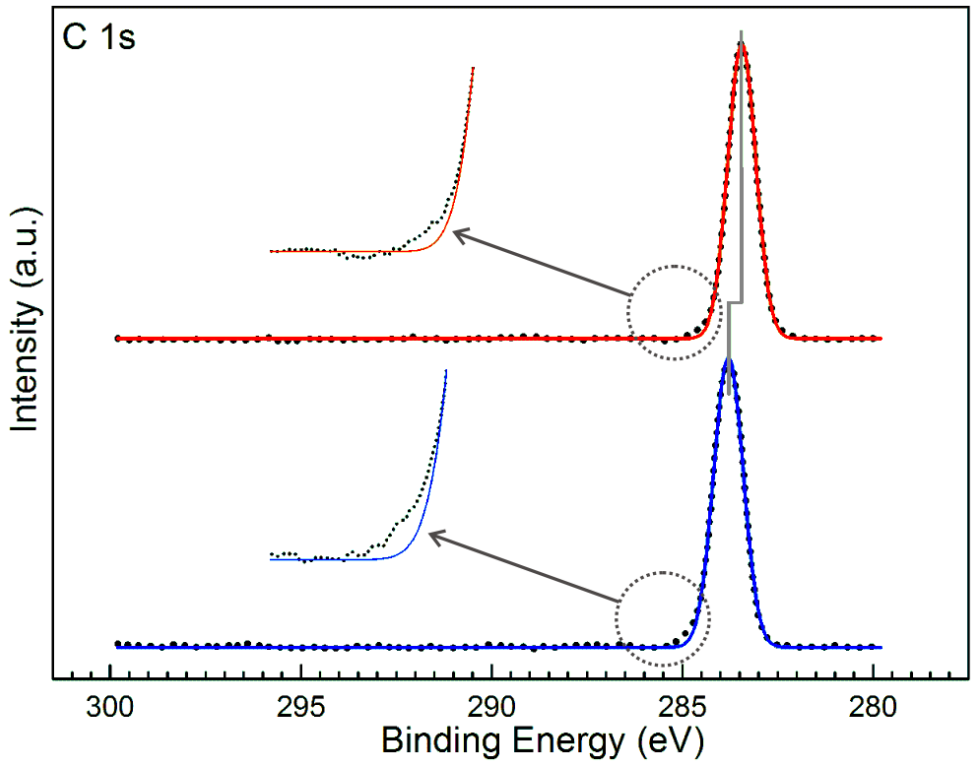

Figure 5.16: XP spectra of C 1s of BIB-derived covalent polyphenylene networks on Au(111) acquired before (lower spectra, blue lines) and after (upper spectra, red lines) exposure to iodine vapor (offset for clarity). The C 1s line shape still remains asymmetric after exposure to iodine as evident by deviations from the symmetric Gauss fit. In addition, a shift towards lower binding energies by ∼0.35 eV is observed.

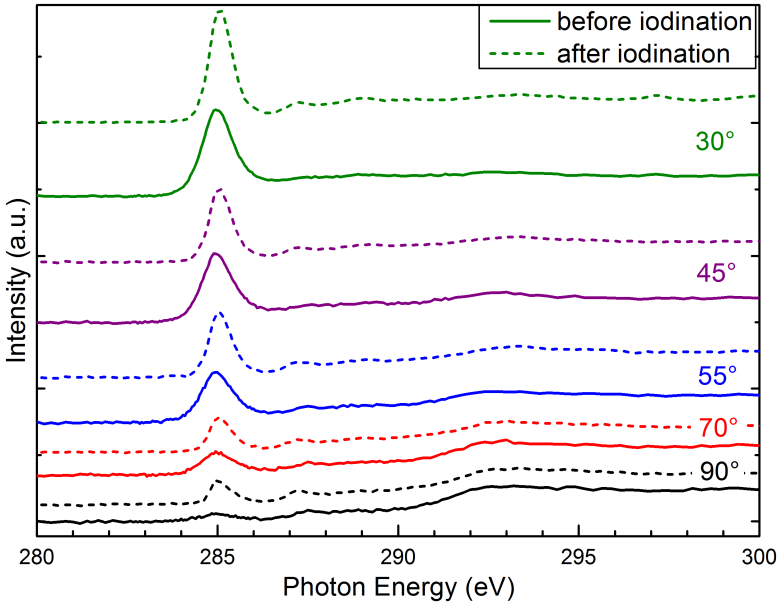

Figure 5.17: C 1s NEXAFS of covalent polyphenylene networks on Au(111) acquired before (solid lines) and after (dashed lines) iodine exposure (offset for clarity). Respective X-ray incidence angles are indicated next to the curves, with 90° corresponding to normal incidence. The spectra are dominated by a C 1s→π^* resonance at 285.0 eV. The intensity shows a clear incidence angle dependency.

resonance at a photon energy of 285.0 eV arising from a C 1s→π^* transition. At a first glance, the intensity at normal incidence (90°) appears significantly enhanced after iodination, which would indicate enlarged phenyl tilt angles. Yet, this enhancement similarly applies to all incidence angles. So it is not surprising that a quantitative analysis results in similar average phenyl tilt angles of (15° ± 5°) before and after iodination (see Figure 5.17 and 5.18).

Again, these NEXAFS results stand in vast contrast to the previous study on Ag(111) and further support the STM-based conclusion of mere iodine coadsorption on Au(111). Interestingly, sharpening of the NEXAFS resonances as observed on Ag(111) is also present here as shown in Figure 5.19.

On Au(111) for an incidence angle of 45° the FWHM of the resonance is reduced from 0.99 eV before down to 0.75 eV (0.99 eV vs. 0.73 eV on Ag(111)) after iodination. To prove that this sharpening is indeed related to the presence of coadsorbed iodine, samples were annealed at 350 °C for ∼20 min. Thereby, as shown by XPS (cf. Figure 5.20), most of the iodine was thermally desorbed and the original FWHM of 0.99 eV was restored. Furthermore, XPS indicates a ∼27 % loss of carbon after annealing to 350 °C (cf. Figure 5.20), but the continued existence of the NEXAFS resonance indicates integrity of the aromatic system, and hence resilience of the covalent networks. In any case, these experiments also suggest

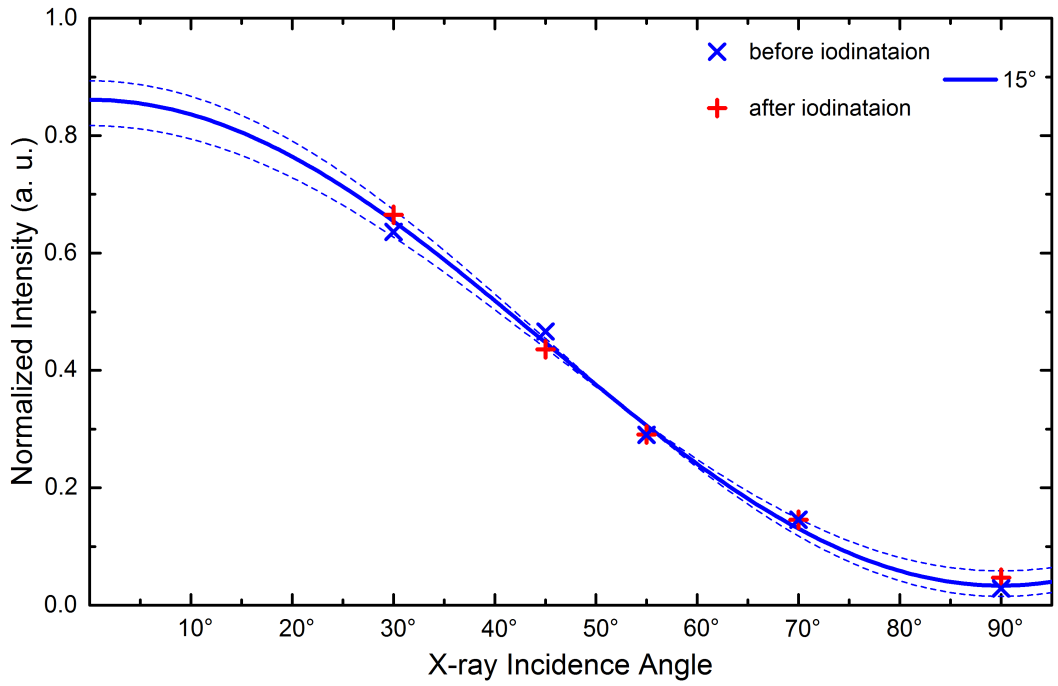

Figure 5.18: Normalized intensities (peak maxima) of the C 1s→π^* resonance vs. X-ray incidence angles before (blue crosses) and after (red crosses) iodination (2×10^{-6} mbar, ∼20 min) at room temperature. Incidence angles are referred to the surface plane, i.e. 90° corresponds to normal incidence. The solid line represents the theoretical curve for an average phenyl tilt angle with respect to the surface of 15° (evaluated for the known degree of linear polarization of P=0.92). The dashed curves delineate uncertainty intervals of ±5° to 15°.

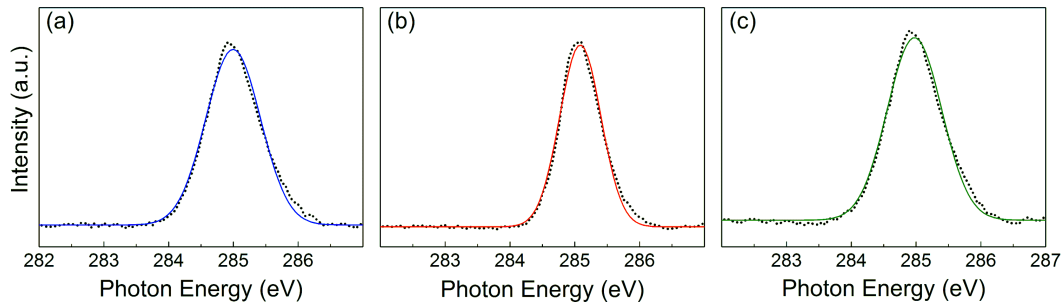

Figure 5.19: Normalized C 1s NEXAFS spectra acquired at an X-ray incidence angle of 45° (a) before and (b) after iodine exposure at room temperature and (c) after thermal desorption of iodine by sample annealing at 350 °C. In all cases the C 1s→π^* resonances were fitted with Gaussian, resulting in FWHM of a) 1.00 eV (σ=0.42 eV), b) 0.75 eV (σ=0.32 eV) and c) 0.99 eV (σ=0.42 eV). Sharpening of the C 1s→π^* resonance is commonly associated with a longer lifetime of the excited state. Since this sharpening is reversible, i.e. disappears again after iodine desorption, it most likely already results from co-adsorption of iodine, and does not require decoupling of the covalent networks from the surface.

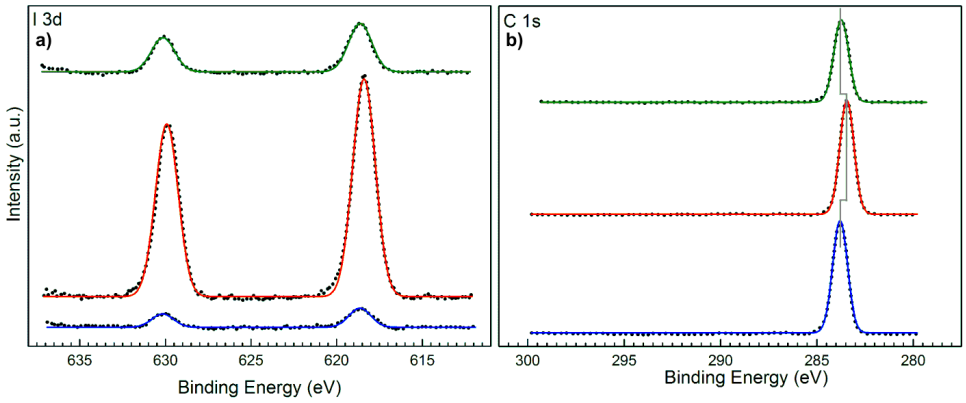

Figure 5.20: XP spectra of a) I 3d and b) C 1s core levels acquired from BIB-derived covalent polyphenylene networks on Au(111) before (lower spectra, blue line) and after (middle spectra, red line) iodine exposure (2×10^{-6} mbar, ∼20 min) at room temperature. Additional spectra were acquired after annealing the sample at 350 °C for ∼20 min (upper spectra, green line). All spectra are offset for clarity. After annealing the sample at 350 °C the majority of iodine is desorbed from the surface. I 3d shows a significant decrease of surface-bound iodine almost back to the level before deliberate iodination. The ∼0.35 eV shift of C 1s to lower binding energies is entirely restored after iodine desorption.

that sharpening of the NEXAFS resonance is related to iodine co-adsorption rather than detachment of the covalent networks similar to the observed shift in C 1s XPS spectrum.

An important conclusion of both NEXAFS and XPS experiments on Au(111) is that already iodine co-adsorption can affect spectroscopic results of the networks. While XPS shifts could be related to the above discussed effects of adsorbed iodine, the detailed mechanism how the width of NEXAFS resonances is affected remains unclear at the moment.
In summary, STM, NEXAFS, and XPS consistently indicate that on Au(111) detachment of the covalent networks by iodine intercalation was not successful for room temperature exposure. Iodine only co-adsorbs on free surface areas that are not covered by the covalent networks.

5.2.3 Hot Iodination

To promote detachment of the covalent networks also from technologically more relevant Au(111) surfaces, further experiments were carried out with iodine exposure at elevated sample temperatures. The underlying idea of this "hot iodination" was to supply additional thermal energy to loosen bonds of the covalent networks to the metal surface, but also to enhance the surface mobility of iodine. To this end, covalent networks were similarly synthesized on Au(111). Then these samples were heated up to ∼300 °C, immediately transferred to the load lock, and exposed to iodine vapor (1×10^{-6} mbar, ∼6 min). The sample temperature during iodination was not precisely known and controlled, but since transfer and begin

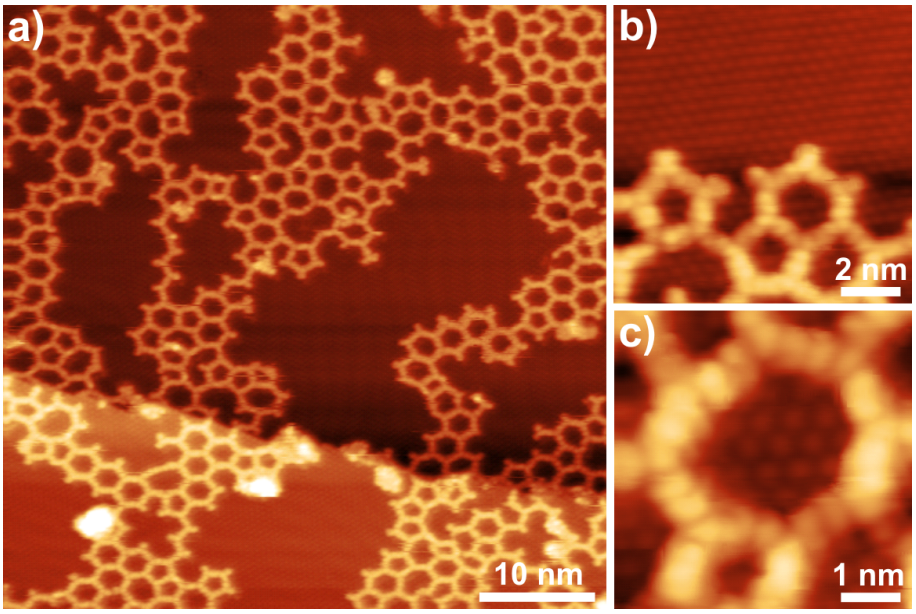

Figure 5.21: STM images of BIB-derived covalent polyphenylene networks on Au(111) acquired after "hot iodination", i.e. iodine exposure at elevated sample temperature. a) Overview (U_T = +825 mV, I_T = 20 pA). b) and c) close-ups (U_T = -561 mV, I_T = 20 pA).

of iodination required less than ∼1 minute, an initial surface temperature well above 200 °C is plausible.
The STM images in Figure 5.21 acquired after "hot iodination" appear entirely different from those in Figure 5.12. Again, the same hexagonal structure in the background indicates iodine adsorption. However, important differences are immediately evident: now the entire surface, including the pore interior, is completely covered with a closed iodine layer. The iodine vacancy islands disappeared completely.

Moreover, after "hot iodination" all adsorbed iodine atoms, i.e. on either side of the covalent networks as well as within the pores, occupy sites of a coherent lattice (cf. Figure 5.22), whereas this was not the case after room temperature iodination (cf. Figure B.5 in B.2). This provides further evidence for a closed and continuous iodine monolayer.

Further evidence for iodine intercalation is provided by the increase of the apparent height of the covalent networks in STM to ∼232 pm after "hot iodination" (cf. Figure 5.23). Although the apparent height is in principle dependent on the sample bias, the marked increase as compared to ∼32 pm after room temperature iodination, provides further evidence for detachment. Interestingly, these apparent height differences compare well to ∼236 pm for detached networks vs. ∼66 pm for networks adsorbed on Ag(111) presented in Figure 5.6 in the last section.

Yet, the most important difference observed after "hot iodination" is the STM contrast of the networks, now showing the characteristic internal features, as clearly recognizable in Figure 5.21(b) and 5.21(c). In analogy to the results on

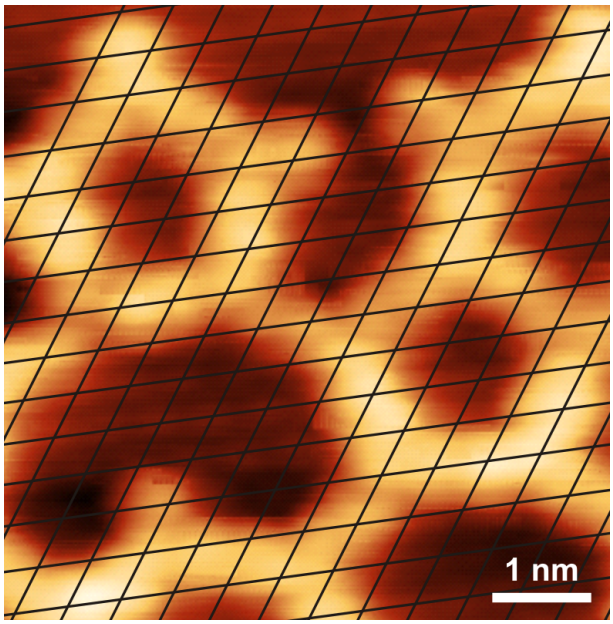

Figure 5.22: STM image acquired after "hot iodination" (U_T = -561 mV, I_T = 20 pA). The coincidence of the overlaid iodine lattice on both sides of the covalent networks points towards formation of a closed iodine monolayer.

Ag(111), this STM contrast is interpreted as orbital dominated: it resembles the spatial distribution of the HOMO/LUMO of a free-standing network, and hence indicates the absence of hybridization between electronic states of the covalent network and the metal surface. More orbital dominated STM images are presented in Figure B.6 in B.2.

5.2.4 Reversible Iodine Intercalation

All STM observations consistently substantiate the conclusion that iodine exposure at elevated sample temperatures results in detachment of covalent organic nanostructures via intercalation of an iodine monolayer also on less-reactive Au(111) surfaces. The most plausible explanation for the differences between Au(111) and Ag(111) is the lower adsorption strength of iodine on the former.[111, 137] Interestingly, the same argument applies to the covalent networks themselves, which also interact less strongly with Au(111). Accordingly, these results suggest a more decisive influence of the iodine adsorption strength. The weak iodine adsorption on Au(111) has further interesting implications, such as iodine desorption temperatures should be lower on Au(111) than on Ag(111). Systematic surface-dependent studies of iodine desorption temperatures by temperature programmed desorption are not available, but our own XPS based experiments suggest an onset of iodine desorption already at ∼250 °C. However, the actual value might strongly depend on the adsorption state, i.e. whether iodine adsorbs in a closed monolayer or just as a few scattered atoms as a by-product of Ullmann coupling. In any case, iodine desorption takes place at a temperature well within the thermal stability range of covalent polyphenylene networks. This motivated us to further study the possibility of thermally desorbing the intercalated iodine, while the covalent networks remain intact and

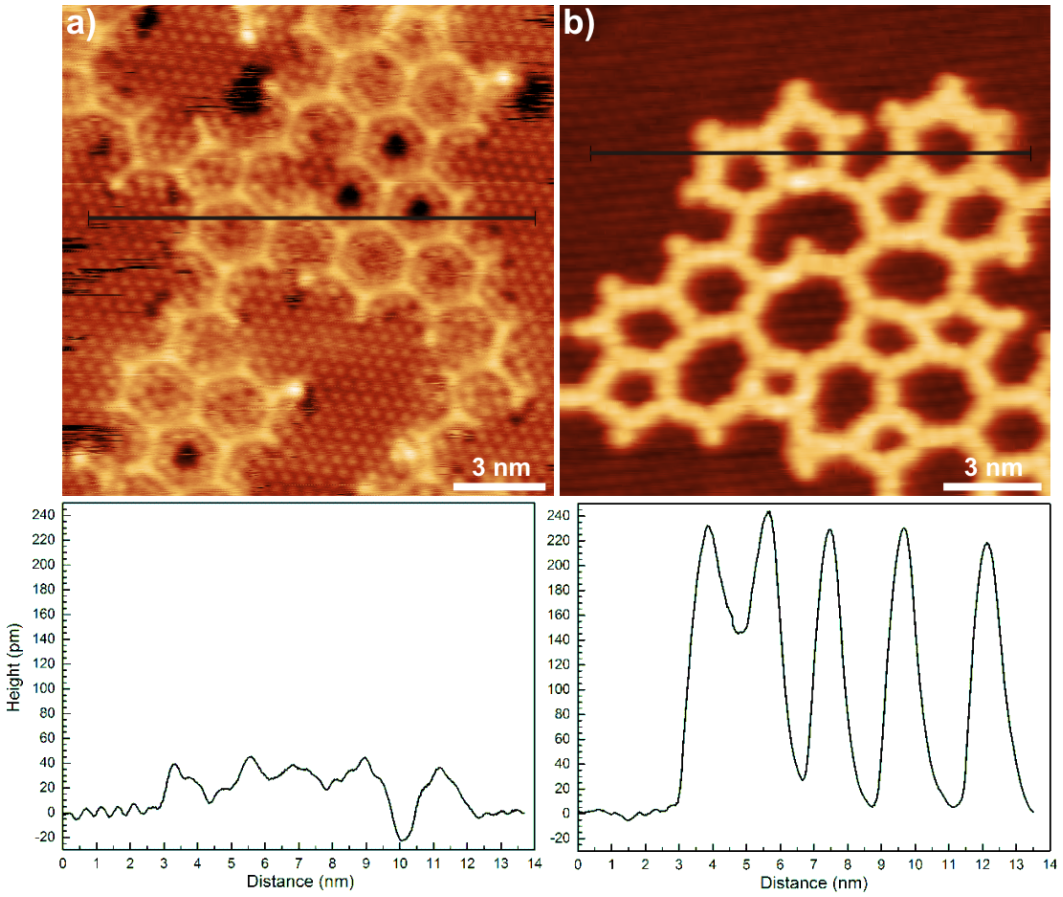

Figure 5.23: Upper row: STM images of BIB-derived covalent polyphenylene networks on Au(111) acquired after a) room temperature iodination (5×10^{-7} mbar, ∼15 min, U_T = +858 mV, I_T = 25 pA) vs. b) "hot iodination" (1×10^{-6} mbar, ∼6 min, U_T = -561 mV, I_T = 20 pA) Lower row: corresponding line-profiles along the black lines. The apparent height of the networks after "hot iodination" is almost 200 pm larger than after room temperature iodination.

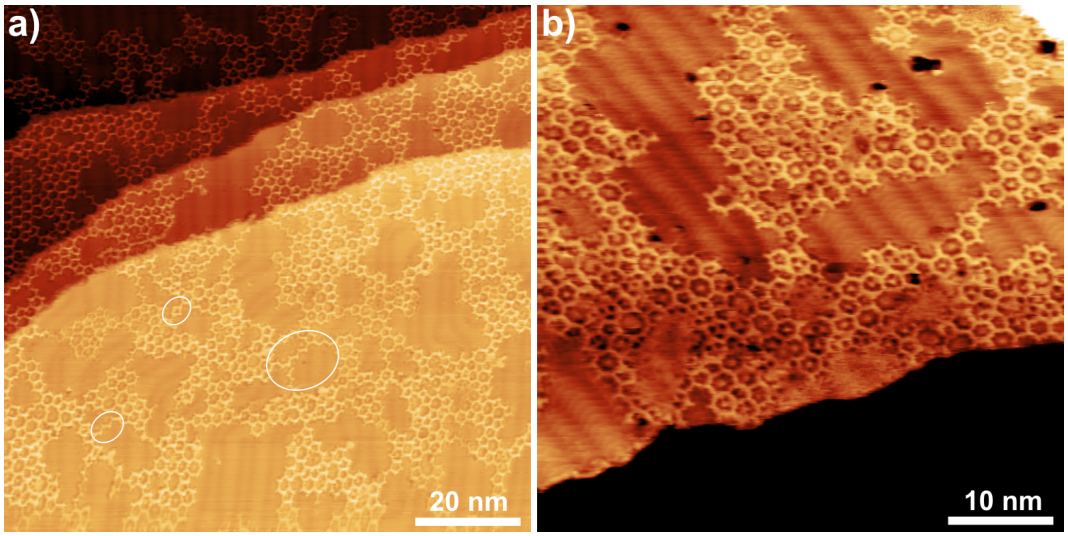

Figure 5.24: STM images acquired at room temperature after annealing a hot iodinated sample with a covalent network again at 400 °C for 30 min. in order to induce thermal desorption of iodine a) Overview (U_T = +844 mV, I_T = 20 pA). b) close-up (U_T = +704 mV, I_T = 20 pA). The ovals highlight filamentous connections between domains.

re-adsorb on the metal surface. Since XPS still indicated iodine remnants after heating to ∼350 °C (cf. Figure 5.20), a higher temperature of 400 °C was chosen for these experiments. Representative STM images acquired after annealing a hot iodinated sample again are shown in Figure 5.24. First of all the topology of the covalent networks did not change. Even the filamentous connections between more compact domains (examples marked in Figure 5.24(a) that are frequently observed directly after synthesis on Au(111)[103] are still present and apparently unaffected. The closed iodine layer disappeared, instead the Au(111) herringbone reconstruction reappeared. Moreover, the orbital mediated STM contrast disappeared and the typical STM contrast of networks directly on the metal was restored. These observations indicate re-adsorption of the covalent networks back on Au(111).

5.2.5 Conclusions

In summary, detachment of on-surface synthesized covalent organic nanostructures by intercalation of an iodine monolayer is also feasible on more important, but less reactive Au(111) surfaces. However, just iodine exposure at room temperature – a protocol that reliably worked on Ag(111) – is ineffective on Au(111) due to the weaker adsorption strength of iodine. Overwhelming experimental evidence was found for a mere co-adsorption of iodine on the free surface areas, whereby the covalent networks remain adsorbed on the metal surface: STM reveals incomplete iodine coverages, NEXAFS shows that the phenyl rings remain essentially parallel to the surface, and the asymmetry of the C 1s peak in XPS – indicating direct interaction with the metal – prevails. Interestingly, iodine co-adsorption also resulted in sharpening of the C 1s→π^* resonances in NEXAFS and a shift of C 1s to lower binding energies in XPS. Albeit the effects on

Au(111) are less pronounced than for successful decoupling on Ag(111), these results suggest that also iodine co-adsorption can affect spectroscopic signatures in a similar manner as successful detachment. Here a detailed understanding of the underlying mechanisms with a strong support from theory would be very beneficial.
Yet, successful detachment was achieved also on Au(111) by carrying out the iodination at elevated sample temperatures. STM imaging revealed marked differences to room temperature iodination: the iodine layer was fully closed without any vacancies. The apparent height of the covalent networks with respect to the underlying iodine increased almost seven-fold as compared to room temperature iodination. Moreover, the STM contrast of the covalent networks exhibited internal features that resemble the spatial distribution of frontier molecular orbitals of free-standing networks. This is a strong indication for the absence of hybridization of molecular electronic states with states of the metal surface, hence detachment. Interestingly, the desorption temperature of iodine from Au(111) is sufficiently low to render the whole process reversible. By means of annealing the samples to 400 °C the iodine layer underneath the covalent networks can be fully desorbed again, while the networks remain intact and re-adsorb on the metal. Thereby the reversibility of the spectroscopic changes could be unambiguously related to iodine co-adsorption. Since iodine-terminated Au(111) surfaces are rather inert, reversible iodine intercalation might also be useful for protecting samples under ambient conditions, e.g. for transport through atmosphere.

5.2.6 Experimental Details

Epitaxial Au(111) films on mica (Georg Albert Physical Vapor Deposition, Silz, Germany) were used as substrates and prepared by cycles of Ar^+ ion-sputtering at 0.5 keV and annealing at ∼460 °C. BIB molecules were deposited by means of a home-built evaporator[131] onto the surface held at room temperature. Covalent networks were obtained by subsequent annealing above 150 °C for at least 20 min. Iodination of the covalent networks on Au(111) was carried out at $\sim 5\times10^{-7}$ (2×10^{-6}) mbar for ∼15 (20) minutes for STM (XPS /NEXAFS) experiments in a small auxiliary chamber with a base pressure of 2×10^{-8} mbar. All STM data were acquired *in situ* at 80 K (unless indicated otherwise) and a base pressure below 3×10^{-10} mbar. The other experimental parameters and conditions were the same as in the section 5.1.4.

Chapter 6

Chemical / Structural Modifications of a Thiol-Functionalized Molecule by Annealing

In this chapter, self-assembly of 1,3,5-tris(4-mercaptophenyl)benzene, a 3-fold symmetric, thiol-functionalized aromatic molecule, was studied on Au(111) with the aim of realizing extended Au—thiolate-linked molecular architectures. The focus lay on resolving thermally activated structural and chemical changes by a combination of microscopy and spectroscopy. STM provided submolecularly resolved structural information, while the chemical state of sulfur was assessed by XPS.*

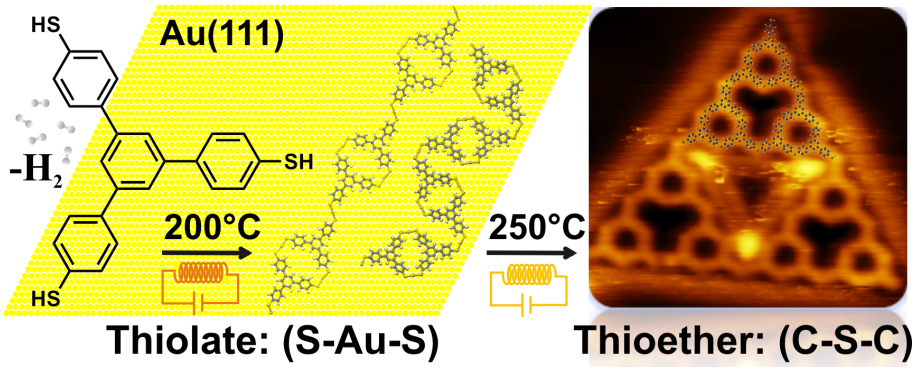

*This chapter is adapted with permission from A. Rastgoo-Lahrood, N. Martsinovich, M. Lischka, J. Eichhorn, P. Szabelski, D. Nieckarz, T. Strunskus, K. Das, M. Schmittel, W. M. Heckl and M. Lackinger, **From Au—Thiolate Chains to Thioether Sierpiński Triangles: The Versatile Surface Chemistry of 1,3,5-Tris(4-mercaptophenyl)benzene on Au(111).** *ACS Nano.* 10 (2016),

10901-10911. Copyright 2016 American Chemical Society.
I performed all the experiments and data analysis and prepared the manuscript under supervision of Prof. Lackinger. DFT calculations were done by Dr. Natalia Martsinovich from the University of Sheffield. Monte Carlo simulations were carried out by Dr. Pawel Szabelski and Damian Nieckarz. The molecules were synthesized in the group of Prof. Schmittel at Siegen University. The XPS measurements were done at synchrotron in collaboration with other co-authors.

6.1 Abstract

Room-temperature deposition of 1,3,5-tris(4-mercaptophenyl)benzene (TMB) on Au(111) resulted in a self-assembly of less well ordered structures. Mild annealing promoted the first structural transition into ordered molecular chains, partly organized in homochiral molecular braids. Further annealing led to self-similar Sierpiński triangles, while annealing at even higher temperatures again resulted in mostly disordered structures. Both the irregular aggregates observed at room temperature and the chains were identified as metal–organic assemblies, whereby two out of the three intermolecular binding motifs are energetically equivalent according to density functional theory (DFT) simulations. The emergence of Sierpiński triangles is driven by a chemical transformation, i.e. the conversion of coordinative Au–thiolate to covalent thioether linkages, and can be further understood by Monte Carlo simulations. The great structural variance of TMB on Au(111) can on one hand be explained by the energetic equivalence of two binding motifs. On the other hand, the unexpected chemical transition even enhances the structural variance and results in thiol-derived covalent molecular architectures.

6.2 Introduction

The notorious affinity of thiols to gold is beneficial for molecular nanoscience.[138] Important examples include ligation of gold nanoparticles,[139, 140] two probe conductance measurements of single molecules,[141, 142, 143, 144] and surface functionalization of Au(111) by self-assembled monolayers (SAMs).[13, 14] All of these applications rely on anchoring via strong Au–thiolate bonds. Even though thiolate SAMs are widespread, structural details of the anchor bond were discussed controversially for a long time. However, a consensus seems to be reached insofar as Au–thiolate complexes formed with gold adatoms play an important role.[88] The promising properties of RS–Au–SR linkages, in particular their electric conductance and their ability to form spontaneously on Au(111), inspired the present study with the aim of utilizing these linkages for extended molecular nanostructures. Toward this end TMB as a 3-fold functionalized and suitable model compound for network formation is studied on Au(111). Owing to both the extended triphenylbenzene backbone and the three-point anchoring via thiolate-surface bonds, planar adsorption is anticipated as an important prerequisite for extended networks. In contrast to SAMs, where the prevalent monothiols adopt upright adsorption geometries, the linkages here are directly accessible by high-resolution scanning tunneling microscopy. In addition, previous study of TMB on Cu(111) showed an interesting temperature evolution: After room-temperature deposition deprotonated TMB anchored via covalent copper–thiolate bonds to the surface, thereby forming a densely packed regular structure dominated by molecule–surface interactions.[63] Mild annealing converted this initial structure into two coexisting polymorphs stabilized by lateral coordination bonds. In light of these results, the present study also aims at comparing self-assembly and thermally activated surface chemistry of TMB on more inert Au(111) surfaces that, however, feature a high Au–thiolate bond strength.

6.3 Results and Discussion

Room-temperature deposition of TMB onto Au(111) resulted in scattered aggregates as shown by the STM images in Figure 6.1. High resolution reveals a seemingly irregular arrangement of interconnected molecules. However, these structures feature only three basic intermolecular binding motifs (cf. Figure 6.1(b) that can be further classified into singly and doubly joined TMB units. The term "motif" is used in a broader sense here, also including different configurations of chemically equivalent intermolecular bonds. 2-fold connected molecules are linked via two of their mercaptophenyl groups, thereby enclosing a small pore. This motif 1 is mirror symmetric and features a center-to-center distance of 1.19 ± 0.05 nm (DFT: 1.19 nm). Singly connected molecules are linked via only one of their mercaptophenyl groups, whereby two different types can be distinguished: motif 2 interconnects appear nearly straight (closer inspection reveals a kink), whereas motif 3 exhibits a hairpin bend. The experimental direct center-to-center distance of molecules in motif 2 amounts to 1.79 ± 0.09 nm (DFT: 1.74 nm) with a lateral offset of 0.41 nm ± 0.08 nm (DFT: 0.46 nm). Binding motif 2 lacks mirror symmetry but exhibits 2-fold rotational symmetry and is accordingly prochiral on the surface. Motif 3 is again in most cases mirror symmetric with a center-to-center distance of 1.21 ± 0.03 nm (DFT: 1.16 nm) and a bending angle of 65 ± 6 °. Distances in parentheses refer to DFT simulations based on S—Au—S linkages (see below). Statistical analysis of more than 800 linkages resulted in 41.0% motif 1, 43.2% motif 2, and 15.8% motif 3. However, the scattering among different data sets is relatively large. For instance, the probability for finding motif 1 varied from ∼36% to ∼46% in different data sets; however, the lower probability of motif 3 is a common finding. Although all intermolecular connections correspond to one of these three motifs, not all thiolate groups form intermolecular bonds. Examples for such "loose ends" are marked in Figure 6.1(b). The exact chemical nature of these termini is not clear. Most likely, these thiol groups are similarly deprotonated and bind to Au surface or adatoms.

Emergence of noncrystalline structures is an interesting and occasionally observed phenomenon in self-assembly, indicating either metastability or energetic equivalency of different binding motifs.[145] To overcome a conceivable kinetic trapping, samples were stepwise annealed at 200, 250, and 300 °C for ∼30 min, and STM data were acquired after each annealing step. Heating at 200 °C resulted in mostly ordered 1D structures (cf. Figure 6.2 and Figure C.4 in appendix C.3), i.e., molecular chains or grouped chains (molecular braids). Shorter chains are already recognizable after room-temperature deposition in Figure 6.1(a), yet heating leads to more extended and more regular structures. Longer chains align along the Au(111) herringbone reconstruction, whereas shorter chain segments or chains in the vicinity of step-edges locally modify the herringbone reconstruction (cf. Figure C.5 in C.3) as similarly observed for alkanethiols on Au(111).[88] Two different types of chains can be distinguished: type A chains (Figure 6.2(b) appear mostly as molecular braids, whereas type B chains (Figure 6.2(c) were only observed as individuals.

Both types of chains feature alternating orientations of molecules. In type A

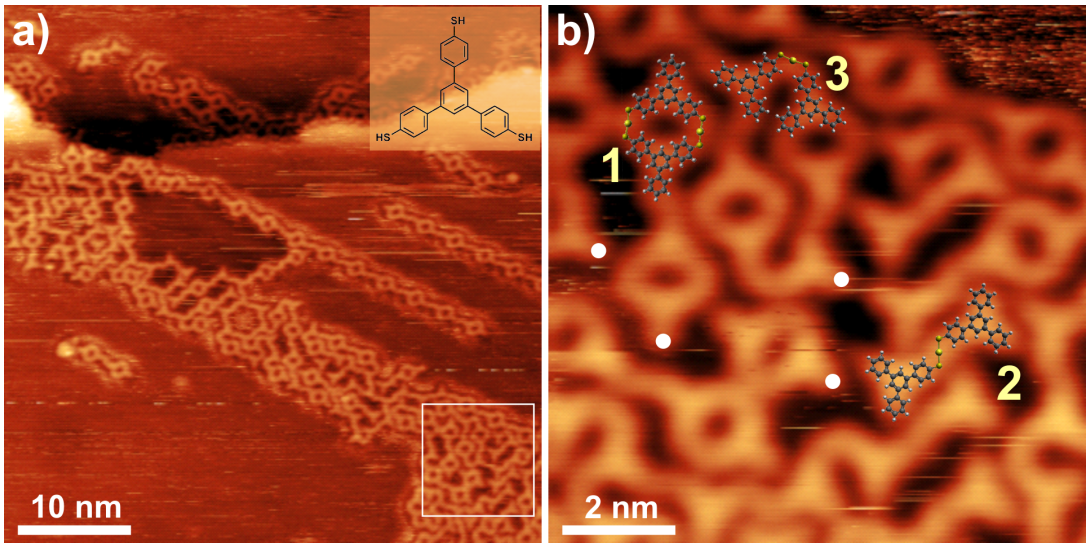

Figure 6.1: STM images acquired after room-temperature deposition of TMB onto Au(111): (a) overview (U_T = +1.83 V, I_T = 48.7 pA); upper right inset, chemical structure of TMB; (b) close-up of the area marked in (a) (U_T = +1.66 V, I_T = 48.3 pA). This less regular arrangement features binding motifs 1–3; respective examples are overlaid by DFT-optimized dimers based on S–Au–S linkages. The white dots highlight examples of "loose ends", where thiolate groups do not form further intermolecular bonds.

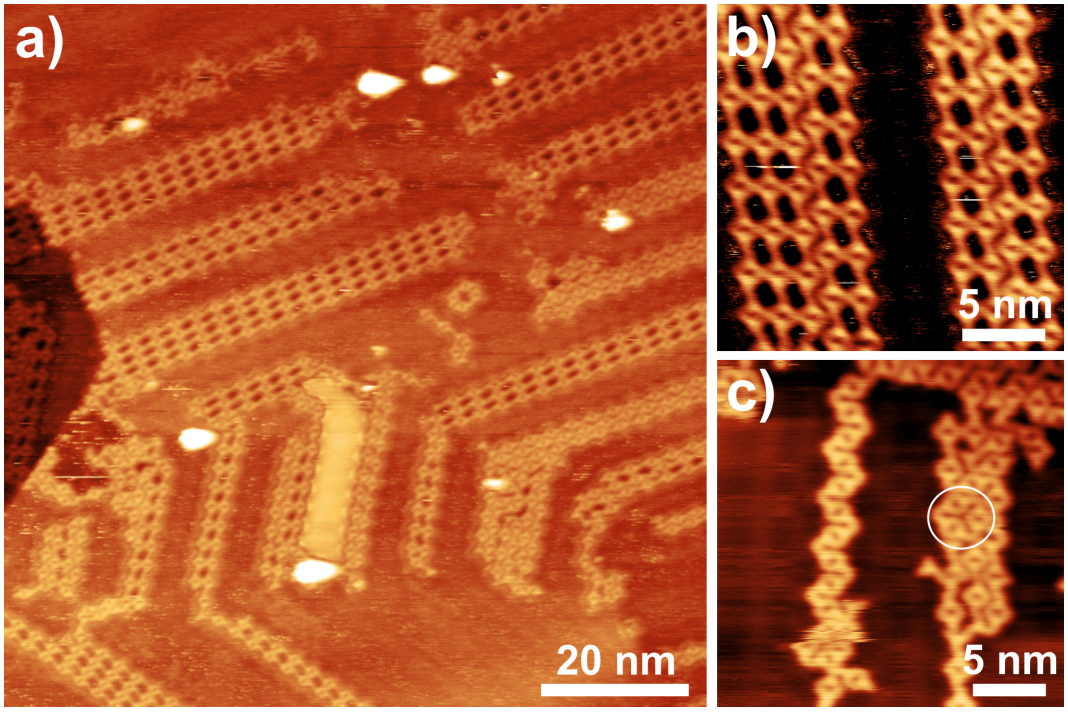

Figure 6.2: STM images of TMB on Au(111), acquired after annealing at 200 °C: (a) overview (U_T = +1.64 V, I_T = 38.1 pA); (b) close-up of braided type A chains (U_T = +1.64 V, I_T = 38.5 pA); (c) close-up of a single type B chain (left-hand side), along with frequently observed less regular aggregates (right-hand side) (U_T = +1.79 V, I_T = 37.1 pA). The white circle marks a hexameric closed-ring structure.

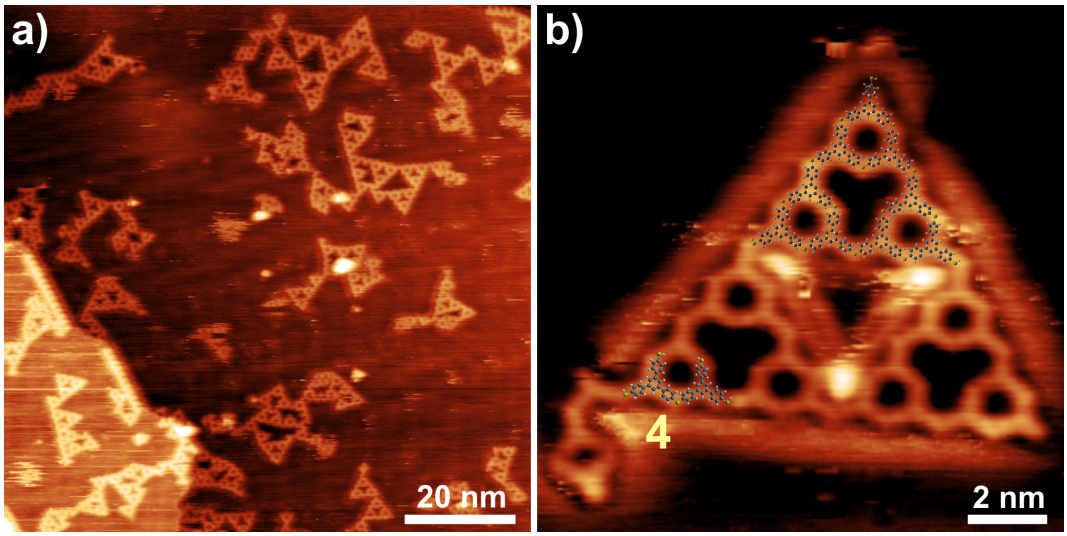

Figure 6.3: STM images of TMB on Au(111), acquired after annealing at 250 °C: (a) overview (U_T = +1.80 V, I_T = 39.4 pA); (b) close-up of a second-generation ST (U_T = − 1.63 V, I_T = 38.1 pA). The upper part was overlaid to scale with a DFT-optimized structure of a covalent first-generation ST. The lower left corner of the triangle is overlaid with a DFT-optimized motif 4 dimer featuring a C—S—C interlink.

chains, binding motifs 1 and 2 alternate, whereby homochirality is observed along all motifs 2. Interestingly, the homochirality of a single type A chain is preserved even at the next higher level of organization, i.e., the molecular braids. A noteworthy further observation is the defined phase relation between adjacent chains in the braids, either aligned or shifted by half a repeat distance; examples for both cases are depicted in Figure 6.2(b). Type B chains are composed of an alternating sequence of binding motifs 1 and 3, but are less regular with only short periodic segments. The right-hand side of Figure 6.2(c) also shows less well-ordered structures that predominantly consist of alternating binding motifs 1 and 3, yet with interspersed motif 2 defects. Since motif 3 can bend in either direction, curled up or even closed-ring structures were also observed; an example is marked in Figure 6.2(c). Remarkably, the structural versatility obtained after annealing at 200 °C results from just alternating motif 1 with either motif 2 or 3.

An unexpected structural transition occurred after sample annealing at 250 °C, converting the chains into mostly triangular aggregates of various sizes. An overview STM image is shown in Figure 6.3 (further images are presented in Figures C.6 and C.7 in appendix C.3). The depicted triangles feature just one intermolecular binding motif 4 (cf. Figure 6.3(b), where connected molecules have similar orientation and a center-to-center distance of 1.31 ± 0.06 nm. Hence, the transition from chains to triangles is also a transition from the coexistence of three binding motifs to exclusively one binding motif. The smallest triangular unit consists of three molecules. However, these trimeric triangles organize into larger self-similar triangles, a molecular realization of so-called Sierpiński triangles (ST).

Molecular materializations of regular fractals have recently attracted increasing

interest, not at least because they are particularly suitable for high-resolution microscopy. Sierpiński hexagons could be synthesized in solution from bisterpyridine building blocks coordinatively bound to 36 Ru and 6 Fe centers and imaged by STM after subsequent deposition onto Au(111).[146] More recently, self-assembly of STs directly on surfaces has emerged as alternative approach. Feasibility was first demonstrated with dibromoterphenyl and dibromoquaterphenyl on Ag(111), resulting in STs based on hydrogen and halogen bonds.[147] However, other types of noncovalent intermolecular bonds also proved suitable. For instance, by using 4,4″-dihydroxy-1,1′:3′,1″-terphenyl on Au(111), Zhang *et al.* demonstrated hydrogen-bonded STs.[148] Interestingly, co-deposition of Fe atoms similarly resulted in STs on Ag(111) and Ag(100) yet with enhanced stability through the formation of Fe—O coordination bonds.[149] Moreover, metal—organic STs could also be prepared by co-adsorption of 4,4″-dicyano-1,1′:3′,1″-terphenyl and Fe or Ni onto Au(111).[150, 151] All of these examples utilize V-shaped ditopic linkers with an *m*-terphenyl backbone, whereby the key to ST formation is the expression of 3-fold nodes either by cyclic halogen, hydrogen, or metal—coordination bonds. On the contrary, Gu *et al.* proposed the synthesis of covalent STs by using Schiff-base coupling of 1,3,5-tris(4-aminophenyl)benzene (TAPB) and [1,1′:3′,1″-terphenyl]-4,4″-dicarboxaldehyde (TPDAL) on Au(111).[152] Here, the required 3-fold symmetry originates from TAPB, whereas the imine linkages to three V-shaped ditopic TPDAL linkers result in a similar topology as for the examples above. This innovative approach yielded covalent STs; however, the formation of larger STs requires a specific conformation of the secondary TAPB(TPDAL)$_3$ building unit, and the frequent occurrence of deviating aggregates such as homotactic nodes can disrupt the ST growth. In this respect, the use of TMB as a single 3-fold symmetric tecton appears advantageous for ST formation. For TMB on Au(111) we observe STs up to the second generation consisting of 27 molecules. In retrospect, the possibility of forming STs from TMB was already alluded to in our earlier work on Ag(111), where cyclic trimers, but no larger STs, were observed after annealing.[63] The concomitant formation of various other less well-defined molecular aggregates presumably prevented the formation of larger STs.

Besides triangles, structurally deviant type C chains were also observed (Figure 6.4). In contrast to type A and B chains, these chains were only found along step-edges, suggesting an important role as template or stabilizer. Type C chains are solely composed of binding motif 4 arranged in a periodic linear fashion. Aggregation into pairs similarly occurred for type C chains, but only on the upper and lower side of step-edges. The opposite orientation and phase shift with half a period distance resembles a molecular zipper.

Sample annealing at even higher temperatures of 300 °C diminished the triangles and resulted in less ordered structures as illustrated in the STM images in Figure 6.5. Close- up images in Figure 6.5(b,c) show details: Dimers of oppositely oriented molecules as in motif 2, yet with a reduced center-to-center distance of 1.32 ± 0.06 nm and a straight geometry were regularly observed in independent experimental runs (cf. Figure C.10 in appendix C.3). Moreover, remnants of triangles, chains, and other motif 4 sequences were found across terraces.

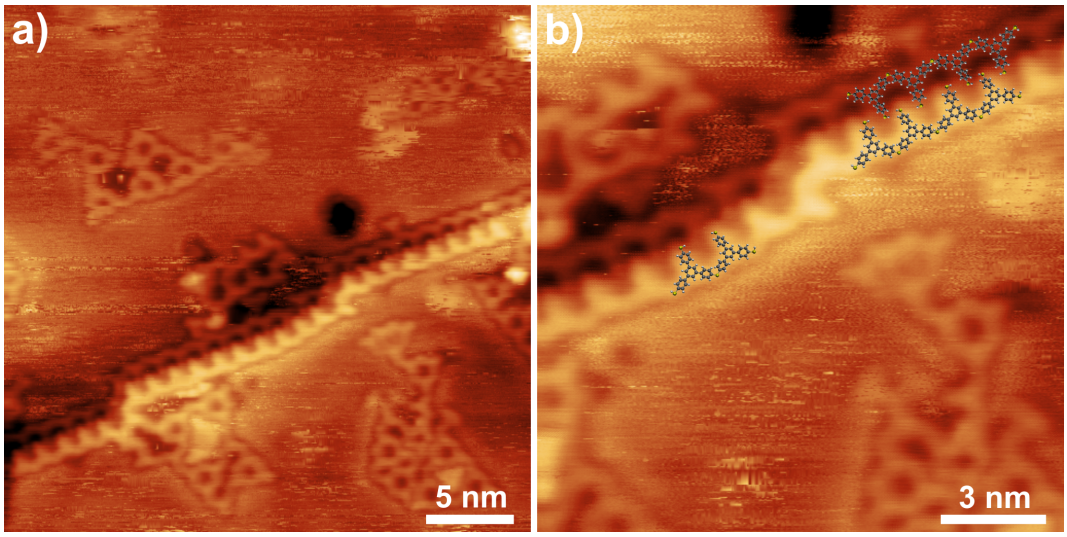

Figure 6.4: STM images of pairs of type C chains, "molecular zipper", formed on Au(111) step-edges after annealing at 250 °C: (a) overview (U_T = +1.00 V, I_T = 40.0 pA); (b) close-up of the molecular zipper overlaid with motif 4 dimers (U_T = +1.00 V, I_T = 40.0 pA).

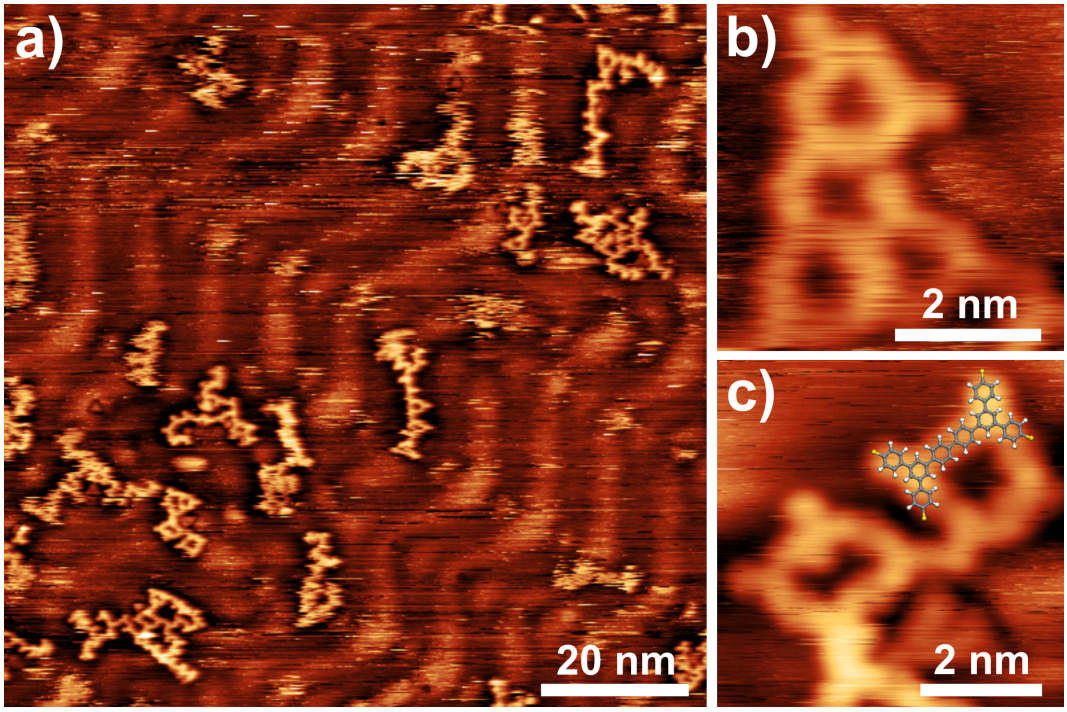

Figure 6.5: STM images acquired after annealing at 300 °C: (a) overview (U_T = +1.63 V, I_T = 50.8 pA); (b) close-up of a triangle remnant (U_T = +1.62 V, I_T = 39.1 pA); (c) close-up of a straight molecular dimer (U_T = +1.69 V, I_T = 40.2 pA) overlaid with a C–C linked dimer.

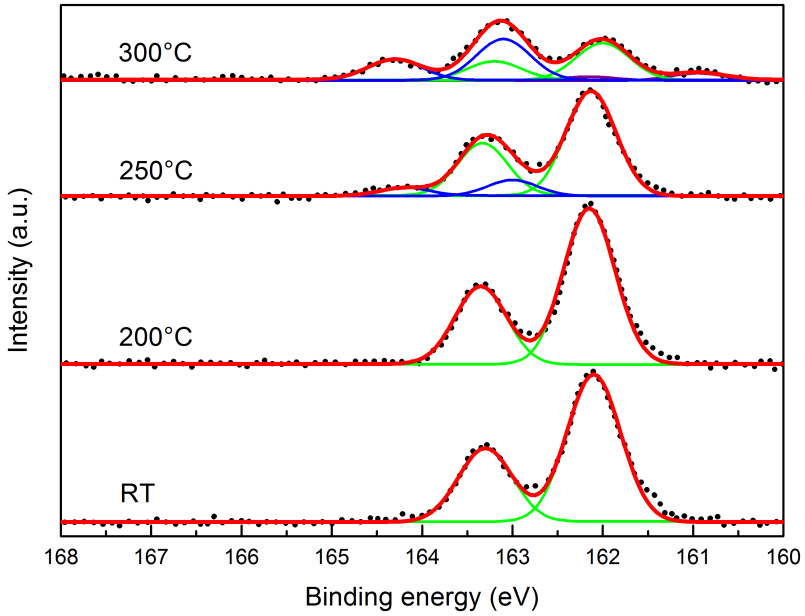

Figure 6.6: XP spectra of S 2p acquired after room-temperature deposition and after annealing at 200, 250, and 300 °C. All annealing steps were carried out successively with the same sample, and spectra were acquired after cooling to at least room temperature or below. S 2p consists of a 1/2 and 3/2 spin—orbit doublet. Spectra were fitted with a fixed energy separation of 1.2 eV and a fixed peak area ratio for $p_{1/2}$/ $p_{3/2}$ of 1:2. After annealing at 250 °C, a second doublet appears at higher binding energies. After annealing to 300 °C, this doublet increases in intensity and a third doublet appears at lower binding energy.

The first important step in understanding self-assembly of TMB on Au(111) is to resolve these structures, i.e., to clarify the nature of the intermolecular bonds. The most likely candidates are S—Au—S linkages or disulfide bridges. A clear contrast feature of Au atoms involved in coordination was not observed for motifs 1 – 4; hence, a distinction based solely on STM contrast is not easily possible. Although S—Au—S linkages and disulfide bridges can be distinguished by their markedly different bond lengths,[63] complementary data on the chemical state of sulfur is potentially useful. To this end, XPS measurements were carried out after room-temperature deposition and after each successive annealing step (Figure 6.6).

The XP spectrum of S 2p after room temperature deposition features a spin—orbit doublet that can be fitted with a single chemical sulfur species. This results in a S $2p_{3/2}$ binding energy of 162.1 eV, in good agreement with reported values of 162.0 eV for Au—sulfur bonds in thiophene and alkanethiol SAMs[153, 154] as well as 162.3 eV for benzenethiol on Au(111).[155] However, XPS does not allow us to distinguish whether the thiolates coordinate to gold surface atoms or adatoms. On Cu(111), TMB room-temperature deposition resulted in bonds with surface atoms.[63] According to a full structural refinement by quantitative LEED and in agreement with comprehensive DFT simulations, the Cu—thiolate

bonds were localized slightly off center of a fcc 3-fold hollow site.[156] Here, the missing structural information on the gold−thiolate bond can be deduced from STM: on Au(111) molecules appear interconnected without any apparent gaps or dips between them, whereas on Cu(111) single molecules were clearly resolved as separate entities. The combination of XPS (indicating Au−thiolate linkages) and STM (indicating direct intermolecular bonds) allows us to conclude that the room-temperature structures are stabilized by coordinative S−Au−S linkages as similarly proposed for low coverages of benzenethiol on Au(111).[157] Since motifs 1−3 coexist with notable proportions, this conclusion equally applies to all motifs.

XP spectra acquired after room-temperature deposition and after sample annealing to 200 °C are virtually identical, suggesting an unaltered chemical environment of sulfur. Consequently, type A and B chains are also stabilized by S−Au−S linkages. This assignment is consistent with STM, as both types of molecular chains are based on the same binding motifs already present at room temperature. To infer further structural details, DFT simulations of the three basic motifs and their periodic sequences based on S−Au−S linkages were performed in the gas phase; the optimized structures are depicted in Figure 6.7. All three dimer motifs are nonplanar in the gas phase, but the energy costs of planarization are comparatively small (0.29 eV for motif 1 and 0.40 eV and 0.43 eV for motifs 2 and 3). Moreover, inclusion of the less planar motif 3 dimer into periodic chains leads to a structure that is more planar than the isolated motif 3 dimer even in the gas phase. Scaled overlays of these S−Au−S-linked basic motifs result in perfect matches, as already demonstrated in Figure 6.1. The S−Au bond lengths correspond to 0.241 nm in all planarized motifs. In order to estimate the surface influence, additional simulations of adsorbed motif 2 dimers on Au(111) were carried out and resulted in a slightly reduced S−Au bond length of 0.233 nm (cf. Figure C.1 in appendix C). Therefore, it was assumed that all peripheral thiolate groups also bind to Au adatoms. This additional constraint resulted in a nonplanar adsorption geometry with tilted phenyl rings and consequently in a relatively large average carbon adsorption height of 0.351 nm with a large standard deviation of 0.051 nm. In contrast, similar simulations of a hydrogen-passivated motif 2 dimer that is not covalently anchored at its periphery resulted in a mostly planar structure with virtually similar S−Au bond length (0.234 nm) but a reduced average carbon adsorption height of 0.319 nm and lower standard deviation of 0.015 nm.

Periodic type A and B chains were also simulated by DFT in the gas phase. The optimized theoretical repeat distances of 2.87 ± 0.03 nm and 3.60 ± 0.02 nm agree well with experimental values of 2.84 ± 0.08 nm and 3.53 ± 0.07 nm, respectively. This concurrence provides strong evidence for the proposed chain structures as alternating sequences of motif 1 with either motif 2 or 3. However, total energies of the chains in DFT vary only weakly with repeat distances ($\Delta E \leq 0.1$ eV for $\pm$ 0.2 Å), resulting in large uncertainties. In any case, covalent disulfide bridges can be excluded due to their significantly shorter bond length and because they would appear in XPS as new sulfur species at higher binding energies.[158] Notably, with reference to protonated TMB and H_2 as deprotonation product, motifs 2 and 3 both feature a similar binding energy of 1.71 ± 0.10 eV, whereas motif 1 is more stable with a binding energy of 2.77 eV. The intermediate bond strength of the

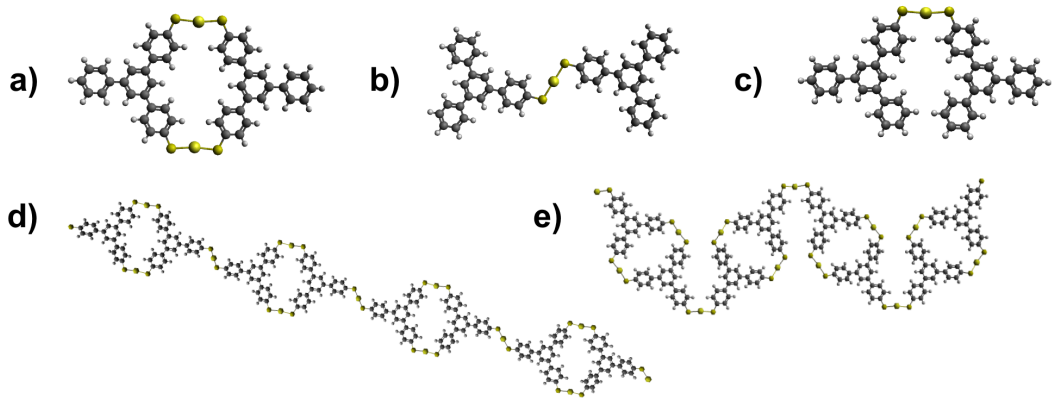

Figure 6.7: DFT-optimized structures in the gas phase of (a—c) planarized motifs 1—3 based on S—Au—S linkages and (d/e) periodic type A and B chains comprised of an alternating sequence of motif 1 and either motif 2 or 3.

S—Au—S linkages facilitates dynamic rearrangements at room temperature (cf. Figure C.3 in appendix C.3). Moreover, both motifs 2 and 3 feature an almost linear S—Au—S arrangement and can be viewed as *syn* and *anti* conformers, as previously proposed for phenyl—S—Au—S—phenyl complexes on Au(111).[157] These DFT results can already explain the observed chain formation: Owing to its higher stability, motif 1 is preferentially formed, but as it requires two mercaptophenyl groups per molecule it is not suitable for the formation of extended structures. However, motif 1 dimers can further interlink via their free mercaptophenyl groups. Thus, the energetic equivalency of motifs 2 and 3 gives rise to the coexistence of both motifs and, hence, the coexistence of type A and B chains. An interesting difference to the previous results on Cu(111) is that on Au(111) only one Au adatom is involved per coordinative bond, whereas on Cu(111) straight intermolecular bonds with two Cu adatoms were proposed.
First changes in XPS were observed after annealing to 250 °C. A second chemically shifted species appears at a higher S 2 $p_{3/2}$ binding energy of 163.0 eV and a peak area fraction of 13.3%. According to the previous assignment, the majority of sulfur is still in the Au—thiolate bonds, suggesting that the STs may also be stabilized by S—Au—S linkages. Additional annealing at 300 °C results in further changes. The sulfur species at higher binding energy increases in intensity, and an additional species with lower S 2 $p_{3/2}$ binding energy of 161.0 eV appears. In the literature, this species is assigned to chemisorbed sulfur on Au(111) with a reported binding energy of 160.95 eV.[155, 159, 160] According to a quantitative analysis, 43% of sulfur is still in S—Au—S linkages, 48% corresponds to the unassigned species, and the remaining 9% corresponds to chemisorbed sulfur.
Since there is no drastic change in XPS upon annealing at 250 °C—the temperature where the ST emerged—the initial assumption was that motif 4 is chemically equivalent to motif 2 and 3; i.e., molecules are connected via S—Au—S linkages. However, this hypothesis is untenable for two reasons: Motif 4 requires a S—Au—S angle of 120 °, yet, according to DFT, S—Au—S strongly prefers a nearly linear configuration as in motifs 1—3, resulting in instability of the 120 ° angle. Nev-

ertheless, a cyclic triangular structure of three molecules, i.e. a zero generation ST, with nearly linear S—Au—S linkages could be stabilized in simulations but at the expense of a highly nonplanar geometry. Hence, formation of such structural units appears highly unlikely. The second argument against Au—thiolate bonds in the ST is a significant size discrepancy to the experiment. A scaled overlay of a simulated metal—organic first generation ST with STM data results in a notable size mismatch and thereby excludes this type of interlink (cf. Figure C.8 in appendix C.3). However, a perfect size match is obtained with a new type of covalent thioether C—S—C interlink, as demonstrated by the scaled overlay in Figure 6.3(b) with a DFT-optimized structure of a corresponding first generation ST. Not only the bond lengths match very well, but also the bulge from the nonlinear C—S—C configuration is consistently present in both simulation and experiment. In addition, the formation energy of this first generation ST in the gas phase from nine molecules was estimated by DFT. Therefore, fully protonated TMB molecules were taken as reference state and H_2S molecules as formal reaction byproduct because the formation of each C—S—C thioether linkage releases two hydrogen and one sulfur atom. This results in a total stabilization energy of −0.45 eV for the entire ST, corresponding to −0.038 eV for each of the 12 thioether bonds, respectively. The proposed thioether C—S—C interlink can formally be derived from the original thiolate C—S—Au—S—C linkages by ejecting Au—S. Even though the geometric comparison unequivocally confirms the thioether bonds, important questions arise: (1) How does this chemical change affect XPS? (2) By what chemical process are the coordinative S—Au—S linkages converted into covalent C—S—C bonds? (3) How does this bond conversion lead to the observed fractals?

Chemical core level shifts in XPS originate from changes of the valence electron configuration. Consequently, even a change of bond type might not necessarily result in a detectable shift, provided that the valence electron configuration does not change significantly. For thioethers adsorbed on Au(111), the reported S $2p_{3/2}$ binding energies of 162.0 eV are virtually identical to those of Au—thiolates.[161] Therefore, the proposed chemical conversion from Au—thiolate to thioether linkages cannot directly be monitored by XPS on a gold surface. The absence of a pronounced sulfur core level shift is partly related to the comparable electronegativities of carbon and gold, 2.55 versus 2.40 on the Pauling scale. The chemical environment of sulfur changes from C—S—Au in the Au—thiolate to C—S—C in the thioether, i.e. sulfur exchanges Au for C as bond partner. This implies minor changes of the valence electron configuration, hence small core level shifts in XPS. The second reason is that the thiolates as well as the thioethers are both chemisorbed; i.e. sulfur features a hardly affected bond to the gold surface in both cases. The proposed conversion, however, also results in ejected sulfur. Accordingly, a conceivable core level shift of this species allows the monitoring of the reaction progress in XPS by tracing the byproduct.

The following hypothesis also closely relates to the driving force of this chemical transition. The conversion of coordinative to covalent bonds occurs at higher surface temperatures with enhanced Au adatom density. Hence, interactions of the coordinatively unsaturated Au adatoms with the sulfur atoms of the C—S—Au—S—C linkage become more likely and such binding should weaken the C—S bond. Finally, Au—S—Au is ejected along with C—S bond cleavage, and the

two remaining fragments combine to afford the thioether linkage. The overall conversion can be summarized as

$$\text{C}{-}\text{S}{-}\text{Au}{-}\text{S}{-}\text{C} + \text{Au} \rightarrow \text{C}{-}\text{S}{-}\text{C} + \text{Au}{-}\text{S}{-}\text{Au}$$

DFT simulations suggest that this chemical conversion is enthalpically almost neutral with an overall energy change of −0.02 eV in the gas phase. However, entropy is gained from releasing Au−S−Au complexes, rendering the proposed reaction thermodynamically feasible. In contrast, ejection of the formal Au−S complex with a DFT-derived energy cost of +1.94 eV is highly unfavorable. Unfortunately, it is not possible to clarify the elementary steps of the reaction mechanism, but a dissociative process where the C−S−Au−S−C linkages are entirely broken with the aid of Au adatoms appears feasible and would be favored at higher temperatures. Accordingly, the additional sulfur species in XPS that occurred at higher binding energies after annealing at 250 °C arises from the ejected sulfur and possibly traces back to adsorbed Au−S−Au complexes. The formation of sulfur molecules in subsequent surface reactions also appears possible and would be consistent with a S 2p core level shift to higher binding energies. The coexistence of coordinative and covalent bonds as observed by STM (cf. Figure 6.8 and also Figure C.9 in appendix C.3) as well as the increasing amount of the additional sulfur species in XPS with progressive heating both consistently indicate a gradual conversion.

The close to 50:50 ratio of tentatively assigned ejected sulfur and thioether sulfur obtained after annealing at 300 °C suggests a nearly complete conversion. However, appearance of chemisorbed sulfur in XPS also marks the onset of decomposition. Even though the proposed reaction mechanism cannot be experimentally verified, additional surface sensitive vibrational spectroscopy such as electron energy loss spectroscopy (EELS) or infrared reflection absorption spectroscopy (IRRAS) could contribute to independently confirm the thioether linkages and even identify reaction byproducts.
The third main question concerning emergence of STs is more intricate. As discussed above, the conversion of the thiolate S−Au−S linkages into covalent C−S−C thioether bonds proceeds gradually, i.e. in a sequential manner. Such a process initially leads to smaller covalent aggregates like dimers or trimers as basic units for the formation of the subsequent structures. In order to understand whether these basic units are suitable precursors for the observed fractals, Monte Carlo (MC) simulations were performed. MC simulations are highly useful in this context as they could predict the formation of similar fractals from ditopic linkers.[150, 162] Cyclic trimers would be ideal precursors for the STs because they already represent a complete structural subunit by themselves. However, DFT simulations of thioether linked dimers versus cyclic trimers result in almost similar energies per bond and hence exclude a pronounced energetic preference for trimerization by cooperative effects. However, as shown in Figure 6.9, MC simulations based on thioether linked motif 4 dimers with an idealized C−S−C bond angle of 120° similarly result in ST. Common structural features between MC simulations and STM experiments further support this hypothesis (cf. Figure C.11 in appendix C.3).

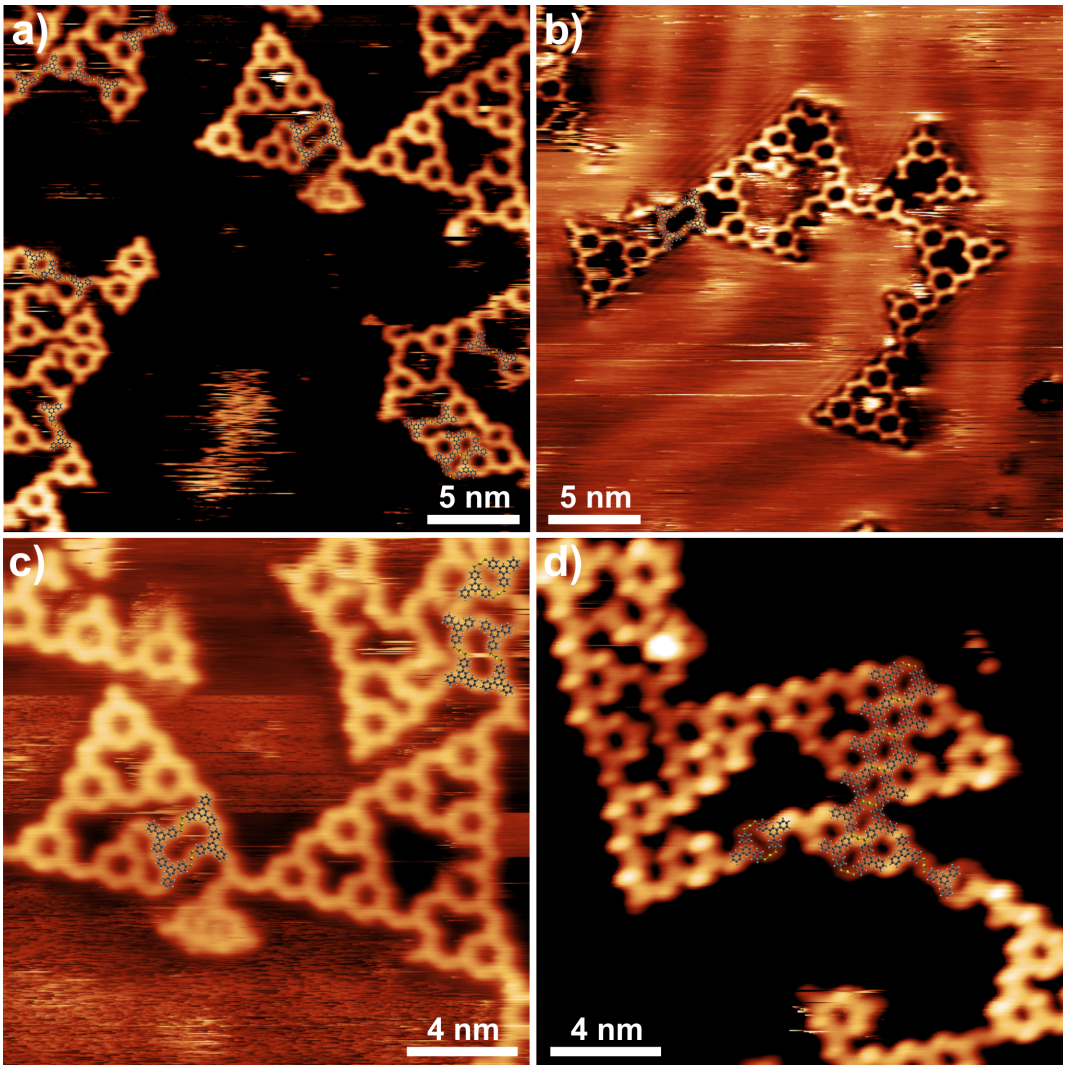

Figure 6.8: STM images of TMB on Au(111) acquired after annealing at 250 °C. These images demonstrate the coexistence of coordinative S-Au-S and covalent C-S-C linkages. For all overlays the metal-organic dimer motifs 1 and 2 were used. Tunneling parameters: (a) U_T = +1.67 V, I_T = 37.7 pA; (b) U_T = +1.60 V, I_T = 37.6 pA; (c) U_T = +1.67 V, I_T = 37.8 pA; (d) U_T = -1.97 V, I_T = 38.1 pA.

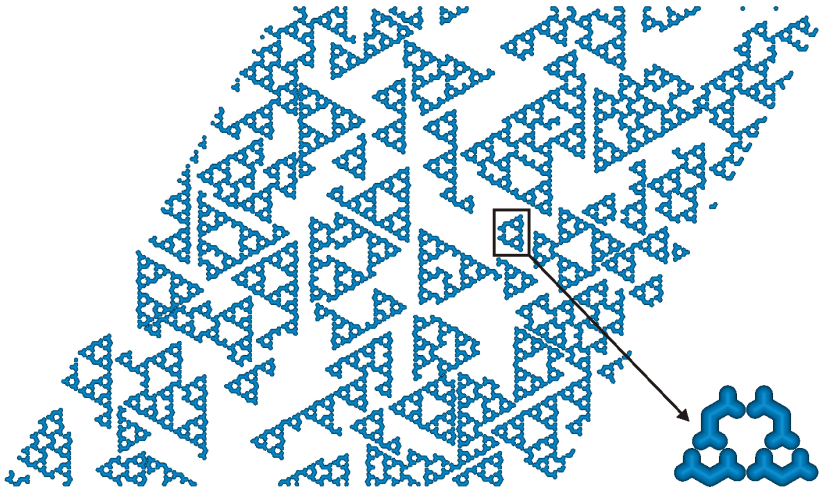

Figure 6.9: Representative result of a MC simulation based on rigid motif 4 dimers as basic building blocks. The sulfur atoms in the thioether linkages are not depicted for clarity. The close-up at the lower right highlights one possibility how four dimer building blocks can assemble into STs.

It is noteworthy that in these MC simulations the bonds are, in principle, reversible. However, the relatively low temperatures of the presented MC runs render detachment highly improbable. Interestingly, another series of MC simulations based on monomers yielded similar fractals when the growing aggregates become immobile already at the dimer stage (cf. Figure C.12 in appendix C.3), suggesting that combination of the 3-fold molecular symmetry with the 120° bond angle already plays a decisive role for ST formation. Interestingly, the size of STs appears to be limited to second generation in both experiments and MC simulations. The most likely reason for this is the absence of classical ripening and coalescence mechanisms known from the self-assembly of ordered monolayers as discussed in detail in previous work.[163] Accordingly, the size limitation arises from kinetic effects.

In contrast to the STs, the dimers of oppositely oriented molecules observed after the final annealing step at 300 °C are relatively trivial to explain. Their straight geometry already suggests the absence of sulfur, and indeed, the geometry perfectly matches with a covalent dimer based on a C—C interlink (cf. Figure 6.5(c) also Figure C.10 in appendix C.3). These STM observations are in accord with the appearance of chemisorbed sulfur in XPS. These high-temperature annealing experiments demonstrate that sulfur can be completely expelled from thioethers with subsequent formation of C—C bonds. Besides these covalent C—C linked dimers, thioether-linked motif 4 dimers as well as zero-generation STs can still be identified in agreement with XPS. However, not all structures can unambiguously be identified solely based on STM images and might also exhibit chemically deviant linkages.

6.4 Summary and Outlook

In summary, TMB on Au(111) is a particularly rich example for the formation of versatile molecular nanostructures on surfaces. It combines a range of important phenomena such as kinetic trapping, coordinative bonding to adatoms, hierarchical chirality, polymorphism, dynamic reconfiguration, templated self-assembly, chemical changes of intermolecular bond type, formation of regular fractals, and partial decomposition.

After room-temperature deposition of TMB onto Au(111), deprotonation initiates the formation of intermolecular S—Au—S linkages with Au adatoms. The resulting aggregates are mostly disordered due to kinetic trapping but can be reduced to only three basic intermolecular binding motifs. Mild annealing promotes formation of two types of regular 1D chains, both based on the room temperature binding motifs. Initially, it may appear surprising that a tritopic molecule such as TMB does not form 2D but only 1D structures. However, the dominant motif 1 that is present in both types of chains is a 2-fold link. Accordingly, there is only one free mercaptophenyl group per molecule left, resulting in a motif 1 dimer with two sticky ends at para position—a prototypical secondary building block for linear polymers. The chain polymorphism again is related to the energetic equivalence of motifs 2 and 3 which are the single linkages interconnecting the dimers into chains. Interestingly, the chirality of binding motif 2 does not only extend along the chains, but is even preserved to the level of molecular braids—an example of hierarchical chirality.

The most interesting and surprising experimental observation is the conversion of Au—thiolate chains into regular fractals, the STs. These triangles are constituted of only one intermolecular binding motif 4 with similarly oriented molecules. A linear periodic continuation of motif 4 leads to type C chains that were only observed along step-edges an example of templated self-assembly. Attempts at rationalizing the STs with S—Au—S thiolate linkages by geometric matching were not successful. The experimental bond lengths are markedly shorter and can only be explained by covalent thioether bonds. As a result, the structural transition from chains to triangles is driven by a chemical transition where coordinative S—Au—S linkages are converted into covalent C—S—C bonds. The mechanism of this conversion is not entirely clear, but ejection of just the formal Au—S unit is energetically highly unfavorable. However, ejection of Au—S—Au complexes formed with Au adatoms at higher surface temperatures is a chemically and thermodynamically plausible mechanism. Self-assembly of the fractals, on the other hand, is clearly reproduced by Monte Carlo simulations with covalent dimers or even just monomers as basic building blocks. In comparison, recent studies on ST self-assembly employed V-shaped tectons with *m*-terphenyl backbone. Here 3-fold halogen, hydrogen, or metal-coordination bonds gave rise to the triangular topology, whereas the 2-fold 120 ° connections between the triangle centers were realized by the *m*-terphenyl backbone. For TMB-derived ST, the situation is reverse: the 3-fold topology is encoded in the molecular structure, whereas the ∼120 ° geometry of the thioether linkages provides the required connectivity.

In addition to the microscopic characterization, XPS provided information on the chemical environment of sulfur. Interestingly, the structurally most important chemical change from Au—thiolate to thioether is not monitored by XPS because

S 2p binding energies do not shift to a measurable extent. However, according to the proposed mechanism, sulfur is also ejected. Hence, an additional sulfur species that appeared in XPS at higher binding energies after annealing was assigned to this reaction byproduct. The chemical state of the ejected sulfur is not entirely clear, but a physisorbed species appears likely and would be in accord with XPS. Both STM and XPS consistently indicate a gradual transition. However, after a thermal treatment where XPS indicated complete conversion of thiolate into thioether, the onset of decomposition was observed both in STM and in XPS.
On Au(111) the emergence of STs was quite robust in the intermediate coverage range studied here. While lower coverages presumably just lead to step-edge decoration, studies at higher coverages approaching one monolayer might indeed be interesting. For hydrogen-bonded STs, Zhang *et al.* observed the coexistence of STs and periodic structures with increasing coverages.[148] Accordingly, carrying out similar studies for the present system with its covalent intermolecular linkages could provide further insights into bond reversibility of the thioether linkages. An important point that deserves future attention is the generality of the proposed surface chemistry, i.e. whether a similar conversion into thioether linkages also occurs for other flat adsorbing thiol functionalized molecules on Au(111) surfaces. In any case, an important lesson learned from the present study is that even profound chemical changes are not necessarily detectable in high-resolution XPS experiments. This underlines once more the importance of combined microscopic and spectroscopic studies for the field of on-surface synthesis.

6.5 Experimental Details

All sample preparations and experiments were performed under ultrahigh vacuum conditions at a base pressure below 3×10^{-10} mbar. Epitaxial Au(111) films on mica (Georg Albert Physical Vapor Deposition, Silz, Germany) were used as substrates and prepared by cycles of Ne^+ (or Ar^+) ion sputtering at 0.5 keV and annealing at ∼480 °C. The surface cleanliness was proven either by STM imaging or XPS prior to deposition. The synthesis of TMB was described previously,[63] and deposition was carried out by means of a home-built evaporator[131] at a crucible temperature of ∼140 °C onto the surface held at room temperature, resulting in surface coverages of 0.35 ± 0.17 monolayers according to a statistical analysis of STM data. Full monolayer coverage refers to the densely packed $\sqrt{3} \times \sqrt{3}$ R ± 30° TMB superstructure observed on Cu(111),[63] corresponding to an area density of 0.656 molecules per nm^2. The coverages are slightly overestimated as STM imaging was preferentially carried out at surface areas with higher local coverage.
STM topographs were acquired with a home-built beetle-type microscope driven by a SPM100 controller from RHK. Images were recorded at room temperature and were leveled and mean value filtered.
XPS experiments were carried out at the BESSY II synchrotron (Helmholtz-Zentrum Berlin). Sulfur 2p XP spectra were acquired with a photon energy of 330 eV at normal electron emission using a Scienta R3000 electron analyzer with a pass energy of 50 eV. S 2p spin—orbit doublets were fitted with two Gaussians of equal width, applying a fixed energy separation of 1.2 eV and a fixed intensity ratio of 2:1 for the $p_{3/2}$: $p_{1/2}$ peak areas. Molecular coverages in XPS experiments

were comparable to those in STM experiments within ± 20%. Owing to the absence of pronounced coverage dependencies, STM and XPS results agree.

Chapter 7

Structural / Photochemical Modifications of an Assembly of Fantrip Molecules

In this chapter a topochemical photopolymerization of self-assembled fantrip (a fluorinated anthracene triptycene-based molecule) monolayers into two dimensional polymers was investigated. For this purpose, an appropriate self-assembled structure with a specific molecular arrangement was required. In the first part of the chapter, the self-assembly of fantrip on Au(111) is studied. Yet, the suitable self-assembled structure was not formed on Au(111). On the other hand, the passivation of metal surfaces with an iodine monolayer resulted in the formation of the appropriate molecular self-assembly for the photopolymerization. In the second part, the photopolymerization of the system is studied.*

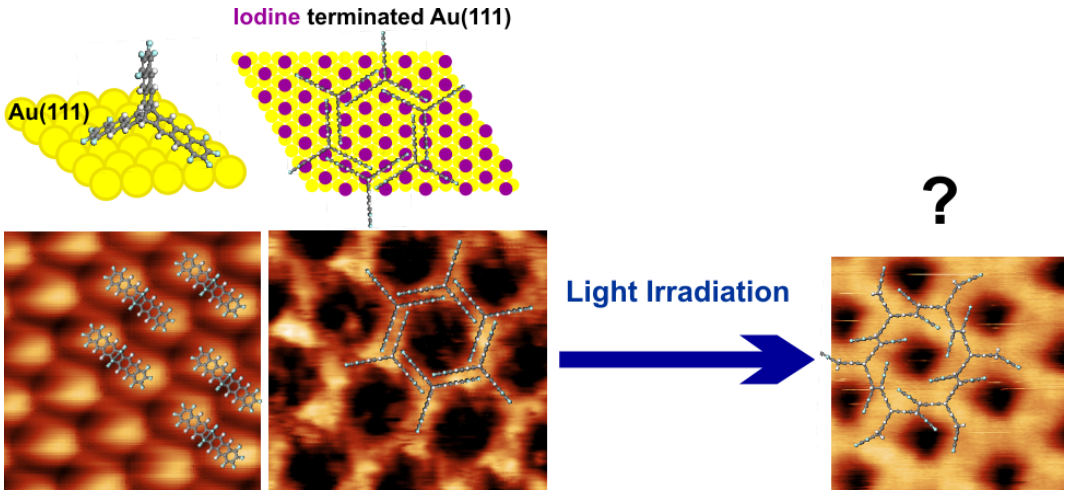

*I performed the main part of the STM experiments and all data analysis. Part of the STM images were acquired by Lukas Grossmann. DFT calculations were done by Prof. Jonas Björk from Linköping University. The molecules were synthesized in the group of Prof. Benjamin King at the University of Nevada. The NEXAFS measurements were done at the BESSY II synchrotron in collaboration with Matthias Lischka, Massimo Fritton, and Lukas Grossmann. The ToF-SIMS

measurements were performed in cooperation with Physical Electronics GmbH under the supervision of Stefan Reichlmaier.

7.1 2D Crystal Engineering of Fantrip Monolayers

Iptycenes derivatives are promising candidates as building blocks for the synthesis of various supramolecular structures via self-assembly due to their unique three-dimensional structure.[164] For instance, as early as 1986 a channel-shaped three-dimensional structure through packing of tritriptycene could be formed, in which the $\pi - \pi$ interactions between the phenyl rings of the molecules played an important role for the structure formation.[165] Fantrip (FAN) also belongs to the iptycenes family. FAN molecules are triptycene based molecules with three anthracene blades and four fluorine atoms at the end of each blade. The chemical structure of FAN can be seen in the inset in Figure 7.1(a). Fluorine atoms at the outer rims of the anthraceno blades were introduced to take advantage of the co-facial, antiparallel packing motif that is often observed for end-fluorinated acenes.[15] A bulk single-crystal of FAN molecules with lamellar structure was previously grown in the work of Kissel *et al.*.[15] In each single layer of this crystal, the monomer's anthraceno blades were stacked in a face-to-face configuration, facilitating stabilization by $\pi - \pi$ interactions between the anthracenes (see the left part of Figure 7.8 for structure). Moreover, this configuration provides the optimal molecular arrangement for the photopolymerization of the layer into a 2D polymer by a [4 + 4] cycloaddition reaction (see subsection 3.2.2) of two anthracene blades. However, bulk polymer crystals have to go through the tedious process of the exfoliation to obtain single 2D polymer layers, that is not necessary anymore in the case of monolayer photopolymerization.
In this section, self-assembly of FAN molecules on gold surfaces is studied. The goal is to examine, whether similar hexagonal assembly as in the layers of the FAN crystal can also be formed on surfaces. This molecular arrangement can then be used for the on-surface synthesis of single 2D polymer layers by photopolymerization.

Results and Discussion

The high thermal stability of FAN monomers facilitates their deposition on substrates under ultra-high vacuum conditions via thermal sublimation. Initially, FAN was deposited onto Au(111). The representative STM images in Figure 7.1 were acquired after deposition, and show a regular hexagonal structure. However, the observed structure could not intuitively be assigned to the molecular structure.

First step towards assessment of the structure in STM image was to clarify the molecular orientation w.r.t. the surface. Therefore, NEXAFS measurements were carried out. C 1s NEXAFS spectra (Figure 7.2) show four pronounced resonances. These are due to C 1s$\rightarrow\pi^*$-transitions from two types of carbon atoms in chemically different environments, i.e. carbon bound to fluorine or hydrogen atoms, into π_1^* and π_2^* orbitals of anthracene. Actually, the carbon atoms of FAN are at least in three chemically distinct environments, namely C-F, C-H, and C-C. However, the C 1s$\rightarrow\pi^*$-transitions from C-H and C-C can not be separately resolved in NEXAFS spectra. All resonances become weaker as

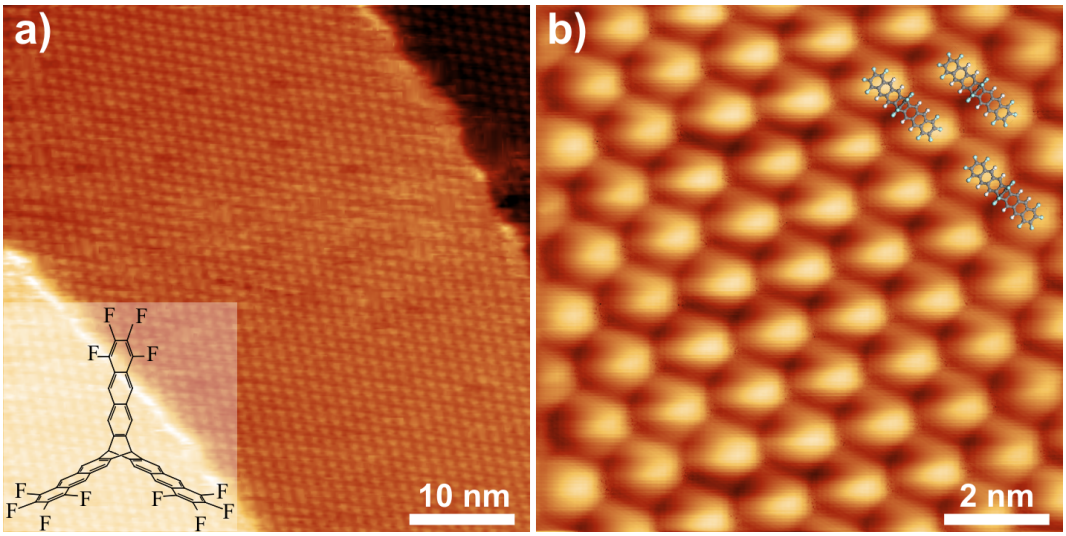

Figure 7.1: STM images acquired after deposition of FAN onto Au(111). a) Overview (U_T = +2.00 V, I_T = 30 pA) and b) close-up (U_T = +1.38 V, I_T = 40 pA) with scaled overlayes of FAN monomers in the adsorption geometry with two anthracene blades almost parallel to the surface and the third one perpendicular to it. The perpendicular blade is not visible in STM. Inset in (a): chemical structure of FAN.

the X-ray incidence angle approaches 90°. This indicates a predominantly flat adsorption geometry with the π-electron system parallel to the surface. However, the non-zero intensity at normal incidence clearly shows that not all parts of the monomer adsorb entirely flat on the surface. The angle dependence of intensities of the first resonance is shown in Figure 7.3. This data could be fitted with a model, where two of the anthracenes are almost flat, whereas the third one is perpendicular to the surface. This results in an angle of (10° ± 10°) for the two almost flat adsorbing anthracene blades on the surface.

To demonstrate the feasibility of this adsorption geometry, additional DFT calculations were carried out for single isolated FAN on pristine Au(111). The corresponding DFT optimized structures are shown in Figure 7.4. The highest adsorption energy of -2.24 eV indeed corresponds to the proposed adsorption geometry (Figure 7.4(a)). In contrast, an adsorption geometry with a molecular symmetry axis perpendicular to the surface results in a significantly lower adsorption energy of -1.26 eV (see Figure 7.4(b)). The proposed adsorption geometry on Au(111) is favoured due to strong interactions between anthracene blades and gold surface, resulting in almost flat adsorption of two anthracene blades on Au(111).

The suitable structure for photopolymerization is evidently dominated by molecule-molecule interactions. Hence, passivation of the metal surface with a monolayer of iodine seems to be an appropriate strategy to steer the molecular arrangement. Corresponding DFT calculations on iodine-terminated Au(111) suggest a slight energetic preference for the desired adsorption geometry with a molecular symmetry axis perpendicular to the surface with the adsorption energy of -1.05 eV,

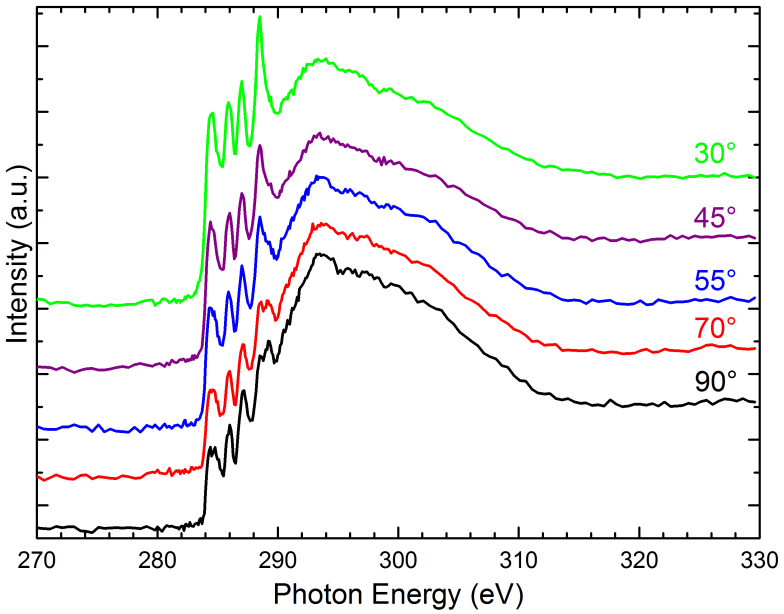

Figure 7.2: NEXAFS spectra of FAN on Au(111) acquired for various incidence angles (offset for clarity). Note that the incidence angle is defined with respect to the surface plane, that is, 90° corresponds to normal incidence. Pronounced resonances at photon energies about 285 eV arise from C 1s→π^* transitions. Four π^* resonances appear in the spectra, since the existence of π_1^* and π_2^* orbitals in anthracene in combination with two chemically inequivalent carbon atoms in FAN give rise to shifted C 1s→π^* transitions.

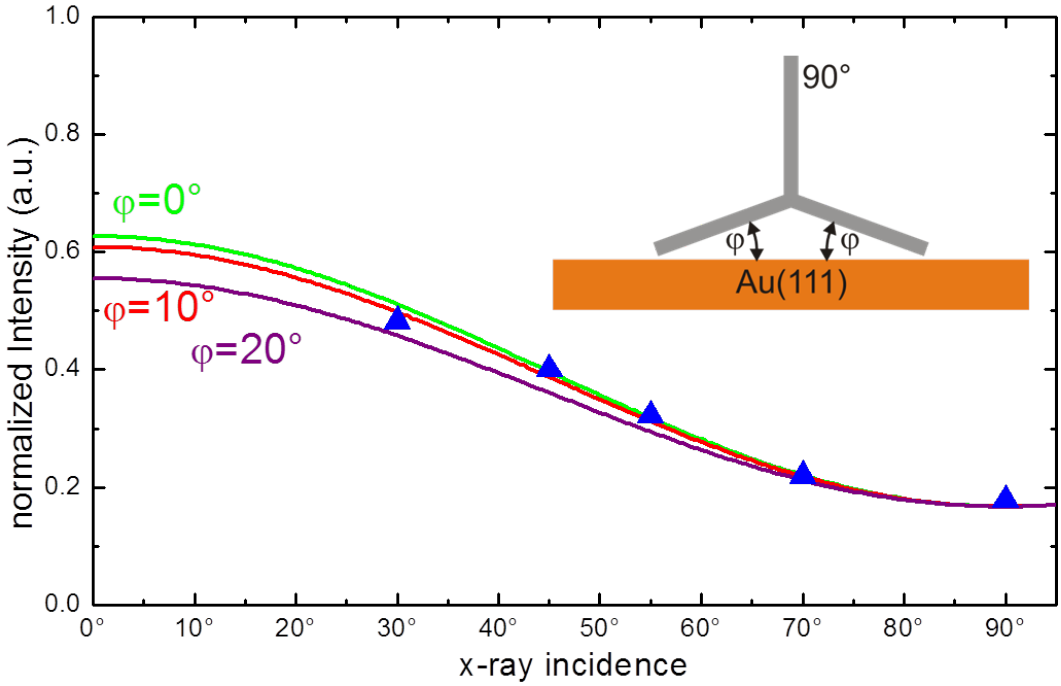

Figure 7.3: Normalized intensities (i.e. peak maxima) of the first C 1s→π* resonance vs. X-ray incidence angle (w.r.t. the surface) form a set of NEXAFS spectra acquired after deposition of FAN on Au(111). The solid lines represent theoretical curves for the case that two of the anthracene adsorb at a small angle φ (as defined in the inset), whereas the third one is perpendicular to the surface: $\varphi = 0°$ (green curve), $\varphi = 10°$ (red curve) and $\varphi = 20°$ (purple curve). These curves are plotted for the beamline-specific degree of linear polarization of P=0.92. Experimental data match the curve of $\varphi = 10°$ very well, indicating almost flat adsorption of the two anthracene blades.

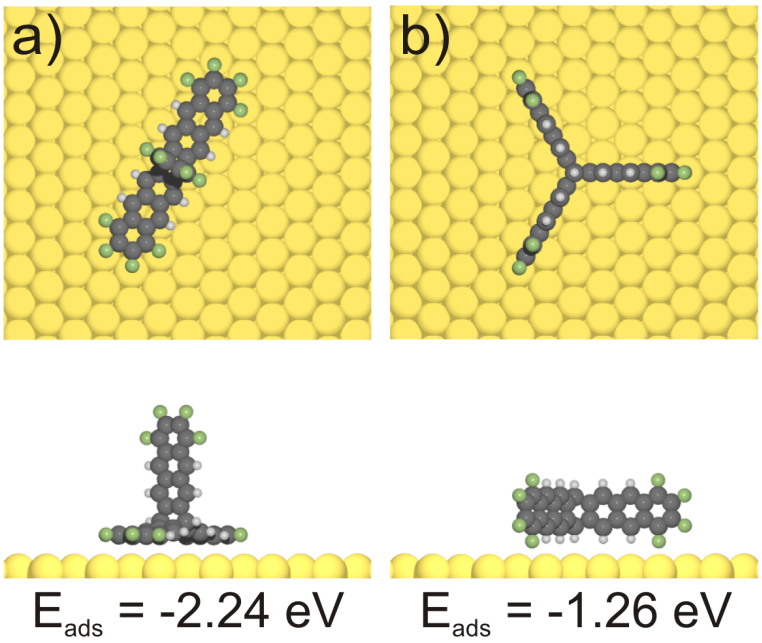

Figure 7.4: Top and side view of DFT-derived structures with highest adsorption energies for single FAN molecules on Au(111) with (a) two anthracene blades parallel to the surface and (b) the molecular symmetry axis perpendicular to the surface. The strong molecule-surface interaction on Au(111) results in the preference for flat adsorption of extended aromatic systems.

whereas the adsorption geometry with two anthracenes parallel to the surface features a lower adsorption energy of -0.92 eV. However, the highest adsorption energy of -1.05 eV is only obtained for a specific adsorption site w.r.t. the iodine lattice.

To passivate the metal surface, Au(111) samples were exposed to iodine vapor at a pressure of 5.5×10^{-7} mbar for 5 min (or 2×10^{-6} mbar for 10 min). The formation of an iodine monolayer was proven by STM imaging prior to FAN deposition. As initial experimental proof for the change in adsorption geometry of FAN monomers after iodination of Au(111) surfaces, NEXAFS measurements were performed. C 1s NEXAFS spectra for various incidence angles are shown in Figure 7.5. It is evident that the intensity of the π^* resonances increases with increasing incidence angle, indicating a more upright adsorption geometry. Fits of the angle dependence of the first and second π^* resonances result in anthracene angles of ($70° \pm 10°$) and ($80° \pm 10°$), respectively (see Figure 7.6). This means all three anthracene blades are almost perpendicular to the surface. Therefore, NEXAFS suggests an adsorption geometry of FAN monomers with the molecular symmetry axis perpendicular to the surface on iodine-terminated Au(111).

In the next step, the structures were characterized by STM, overview and close-up images are shown in Figure 7.7. The observed hexagonal structure has lattice parameters of a = b = (2.03 ± 0.09) nm. Comparing this value to FAN single-crystal lattice parameters of $\sim$ 2.06 nm, shows a good agreement.

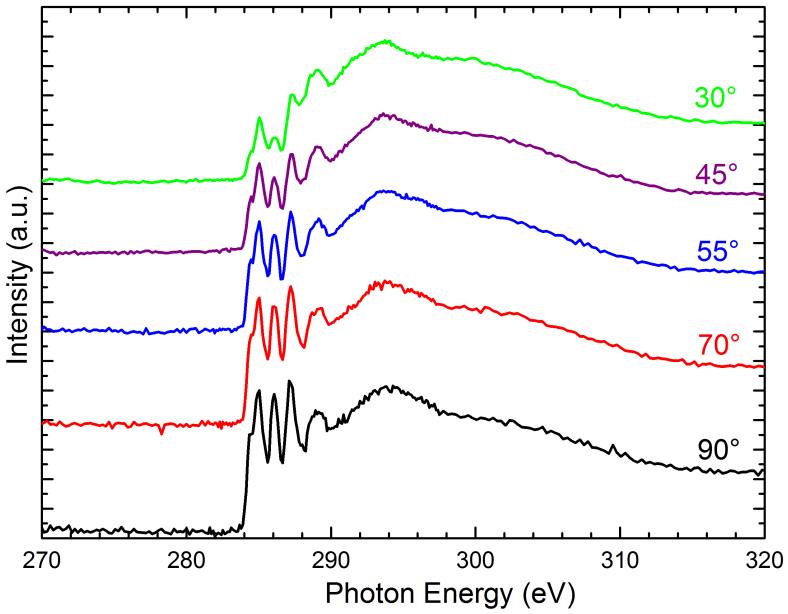

Figure 7.5: NEXAFS spectra of FAN on iodine-terminated Au(111) acquired for various incidence angles (offset for clarity). Pronounced resonances at photon energies about 285 eV arise from C 1s→π^* transitions. Four π^* resonances appear, owing to the existence of π_1^* and π_2^* orbitals in anthracene in combination with carbon atoms in two chemically distinct environments resulting in shifted C 1s→π^* transitions.

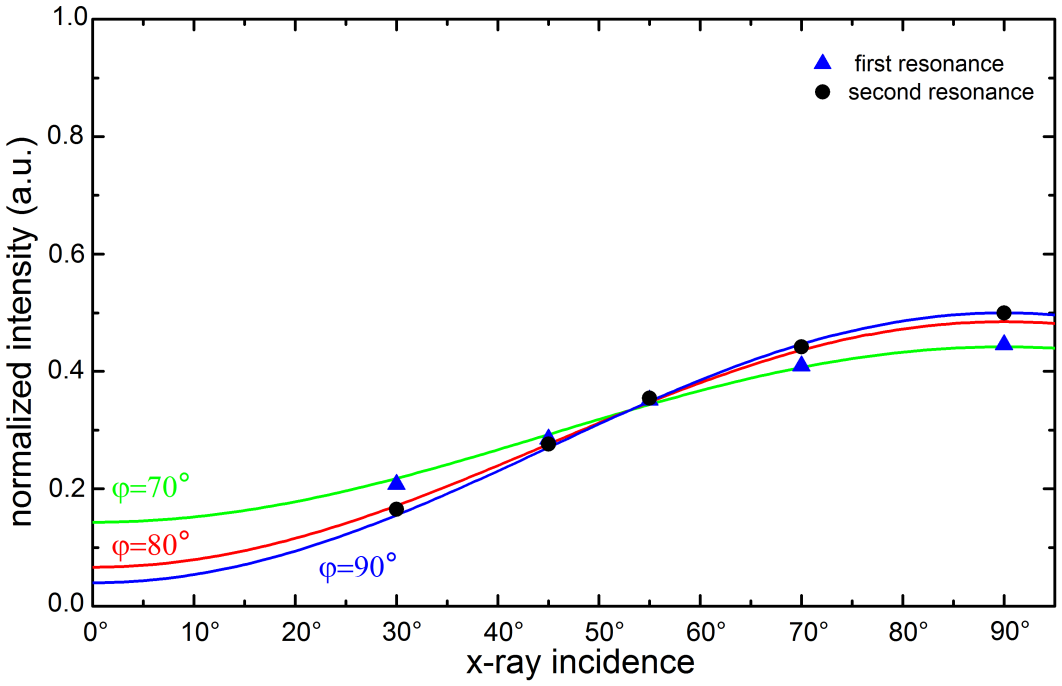

Figure 7.6: Normalized intensities (i.e. peak maxima) of the first and second C 1s→π^* resonances vs. X-ray incidence angle (w.r.t. the surface) form NEXAFS spectra shown in Figure 7.5. The solid lines represent theoretical curves for the case that FAN molecules adsorb completely upright on the surface, i.e. with the molecular symmetry axis perpendicular to the surface, for average anthracene tilt angles φ: 70° (green curve), 80° (red curve) and 90° (blue curve). These curves are plotted for the beamline-specific degree of linear polarization of P=0.92. The experimental data match the theoretical curves well, confirming the change in the adsorption geometry on iodinated Au(111).

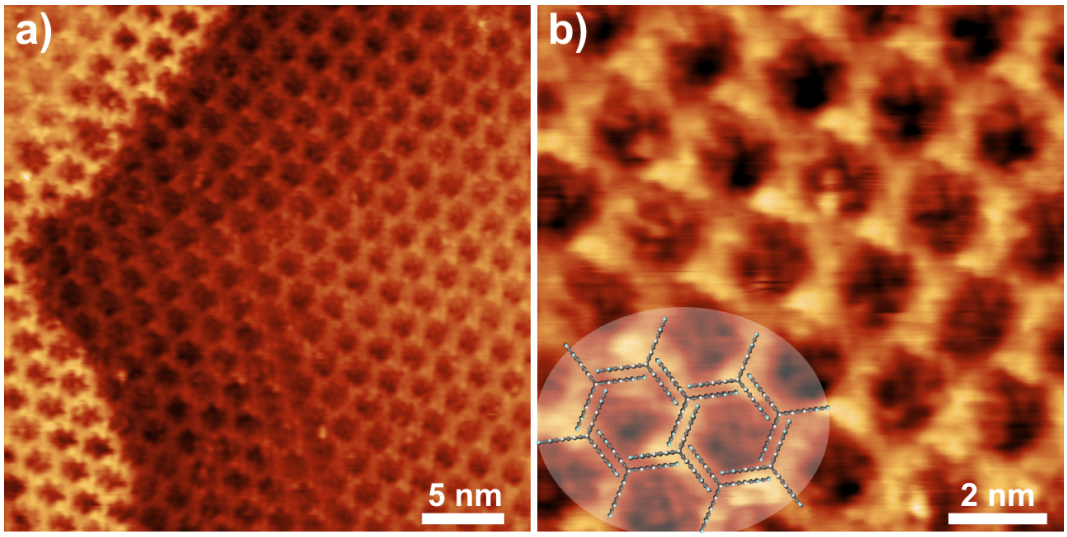

Figure 7.7: STM images acquired after deposition of FAN on iodinated Au(111) surfaces. a) Overview (U_T = +978 mV, I_T = 20 pA) and b) close-up (U_T = +1.08 V, I_T = 20 pA). Inset in (b): overlay of the proposed self-assembled FAN structure with upright molecules.

Lattice symmetry and parameters of the self-assembly of FAN on iodine-terminated Au(111) from STM as well as molecular orientation w.r.t. the surface from NEXAFS all consistently show that the only reasonable structure is the desired one with antiparallel stacking of all anthracenes. As mentioned before, this hexagonal assembly is mainly stabilized by molecule-molecule interactions, i.e. $\pi - \pi$ interactions between the anthracene blades. This self-assembled FAN structure provides the suitable molecular arrangement for a topochemical photopolymerization. Therefore, passivation of the Au(111) surface by iodine is a suitable method to reduce the strong molecule-surface interactions, and it allows to engineer the self-assembly of FAN. In the next section the photopolymerization of this structure is studied.

7.2 Topochemical Photopolymerization of a FAN Monolayer

Synthesis of 2D polymers (2DPs) by photopolymerization based on anthracene-anthracene dimerization has been successfully implemented in several systems.[15, 166, 167] One approach, presented in the work of Kissel *et al.,* using the same molecule as here, is the single-crystal-to-single-crystal photopolymerization.[15] In this method, the monomers are crystallized in a layered bulk single-crystal with suitable molecular arrangement within the layers. Accordingly, the single-crystal of monomers can be converted into a layered single-crystal of 2D polymers by an additional photopolymerization step. 2DPs are generated by the photodimerization of the FAN anthracene blades held in close proximity of one another, due to packing in the crystal lattice. The advantage of this single-crystal approach is the preparation of the 2DPs with bulk quantities (milligram to gram). Therefore, the structures can be assessed by X-ray diffraction (XRD). Moreover, the

polymerized structure possesses great lateral extension due to the extended size of the initial single-crystal. However, a severe disadvantage of this method is the subsequent procedure to obtain a single 2DP layer. For this purpose, the polymer crystals have to go through the tedious and intricate process of exfoliation into the individual 2DP sheets. Moreover, the size of the 2DP single layers is severely affected by the sonication.
Another approach for the synthesis of 2DPs by photopolymerization is using the Langmuir-Blodgett technique. A nanoporous 2DP at the air/water interface could be synthesized by this approach.[167] This method is facile and provide access to large area syntheses. Furthermore, the transfer techniques are established. However, monomers might require chemical modifications to become amphiphilic. Moreover, there is no possibility for high resolution characterizations of structures.
The aim here was to synthesize 2DPs on solid surfaces as an alternative method with unmatched analytical possibilities, and also to study photopolymerization reactions on solid surfaces fundamentally. Earlier studies of photopolymerization on surfaces utilized diacetylenes, but so far yielded only 1D polymer strands.[168, 169, 170] In this section, polymerization on the basis of anthracene-anthracene photodimerization of FAN molecules as an ideal model system was studied.

Results and Discussion

In the last section, engineering of FAN self-assembled structures by passivation of Au(111) surfaces through an iodine monolayer was shown. Deposition of FAN on iodine-terminated Au(111) results in a self-assembled structure with suitable molecular arrangement for a topochemical photopolymerization. Moreover, the iodine layer offers a further advantage for the photopolymerization process. Generally, metal surfaces are not ideal for photopolymerization reactions. The probability of photopolymerization directly depends on the lifetime of excited electrons in the LUMO. Molecules absorbed on metal face quenching through the underlying substrate. In this situation, the metal surface provides additional empty states for the de-excitation of the excited electrons, hence decreasing their lifetime in LUMO and consequently lowering the chance of photopolymerization. The iodine buffer layer decouples the molecules from the metal surface and reduces quenching of the photoexcited state by Au(111).
The polymerization is expected to occur by dimerization of antiparallel pairs of anthracene blades from two adjacent monomers at the 9 and 10 positions. Beside this common case, dimerization at other positions is also possible. The reaction scheme is shown in Figure 7.8.
An important experimental parameter for the photopolymerization is the orientation of the electric field vector of the incident light relative to the transition dipole moment (TDM) for the HOMO to LUMO transition. The photopolymerization is enhanced for the parallel alignment of the electric field vector of the light and the TDM. Although, the orientation of the TDM of anthracene is in the direction of its short axis,[171] in the case of FAN the situation is different. Fluorine substitution at the end of the anthracene blade affects the orientation of the TDM. Moreover, the surface below the molecules can also modify the TDM. Therefore, the exact orientation of the TDM is not easy to determine. Consequently, to have a symmetrical distribution of components of the electric field

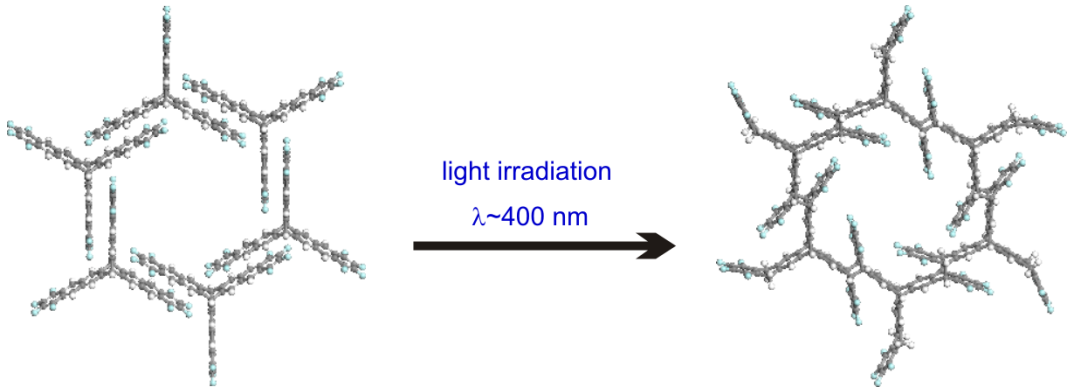

Figure 7.8: Reaction scheme of the transformation of the self-assembled structure of FAN on iodine-terminated Au(111) to poly(fantrip) through photopolymerization by a [4 + 4] cycloaddition. Carbon atoms are grey, fluorine atoms light blue, and hydrogen atoms white.

of the light, an incidence angle of 45° was chosen in all irradiation experiments presented here.

First illumination experiments were carried out by a LED with 5 W electric power (LZ1-00UA00, 400 nm VIOLET LED emitter, manufactured by LED Engin) and a wavelength of ∼ 400 nm. It has been shown that light with this wavelength leads to a successful single-crystal-to-single-crystal photopolymerization of FAN monomers to poly(fantrip).[15] The temperature of the sample in those single crystal experiments during the irradiation was 223 K. To similarly start the photopolymerization at lower temperatures as in the single crystal approach, the samples were cooled down to 80 K in STM and then transferred to the load lock for illumination. However, the sample was not cooled in the load lock anymore and its temperature during the irradiation was not precisely known or controlled. Subsequently, the sample was transferred back to the STM and cooled down again to 80 K. Thereafter, the structure was characterized by STM. However, no changes in STM images were observed after irradiation.
In the second set of experiments, an LED with ∼8 times higher power at 40 W (LZC-70UA00-00U5, 400 nm UV LED emitter, manufactured by LED Engin) was used to increase the radiant flux on the surface. The radiant flux decreases with increasing operating temperatures of high power LEDs. Therefore, the LED-holder was water-cooled to reduce the temperature during the operation. The other experimental conditions were the same as before. STM images acquired after ∼10 min irradiation are shown in Figure 7.9 indicating clear changes.

Bright “dots” appear on the surface and patches of the hexagonal network appear lower, i.e. with darker contrast. The nature of the bright dots is not clear at the moment. However, there are three possible explanations for their emergence. Both iodination and irradiation of the sample were carried out in the load lock. The temperature of the entire load lock chamber increases by the irradiation. Therefore, contaminations or adsorbed iodine on the chamber walls can desorb and readsorb on the sample surface. The second possibility, is the desorption of surface bound iodine atoms due to the temperature increase of the Au(111) sur-

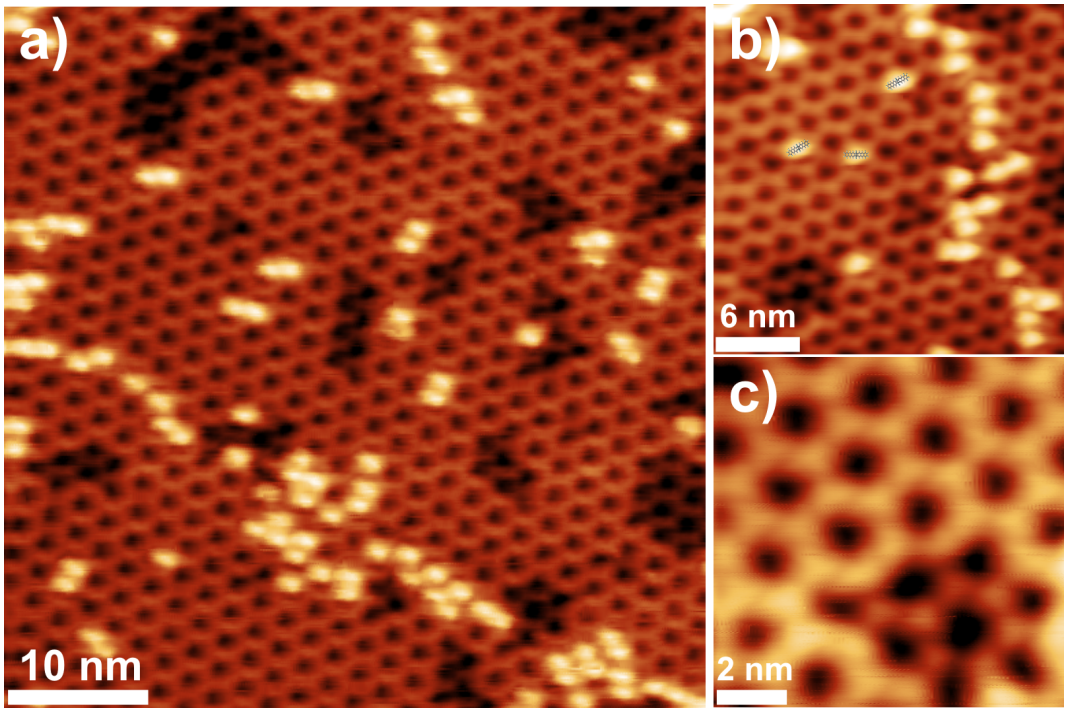

Figure 7.9: STM images acquired after 10 min irradiation of the FAN self-assembled structure on iodinated Au(111) by a 40 W LED. a) Overview (U_T = +1.20 V, I_T = 30 pA) and b) and c) close-ups (U_T = +1.04 V, I_T = 30 pA) and (U_T = -615 mV, I_T = 30 pA). Parts of the network appear darker after irradiation and new bright "dots" emerge. The scaled overlays of FAN monomers in the same adsorption geometry as on pristine Au(111) shown in (b) match the bright dots.

face under the illumination. These iodine atoms may form aggregates resulting in bright dots. The third possibility is that after the desorption of iodine atoms from Au(111) surface, the strong interaction between Au surface and affected FAN molecules may result in a new 90° rotated adsorption structure of these FAN molecules (conversion into the same adsorption geometry as on pristine Au(111), see previous section). These rotated FAN molecules may be the origin of the bright dots. The size of each bright dot almost corresponds to the size of one FAN monomer with the suggested adsorption geometry (see Figure 7.9(b)). However, FAN monomers on bare Au(111) appeared with two protrusions in STM images that is absent here. In any case, the second or third explanations seems to be more plausible based on two observations. First, the load lock chamber was "degassed" preceding to sample transfer for illumination by using the LED over a long period of time (more than one hour). Therefore, the first possibility i.e. the release of contaminants appears unlikely. Second, STM images acquired after irradiation of the sample for 60 min clearly indicate iodine desorption from the surface (see Figure 7.10). Hence, the emergence of bright dots is probably related to desorption of surface bound iodine either due to the irradiation or its associated thermal effects. Considering these arguments, there are two hypotheses to explain the patches of the hexagonal network with darker contrast. The contrast variations are either related to the structural and electronical changes of the FAN network due to the photopolymerization, or they just represent areas, where iodine desorbed from the surface underneath the network.

To prevent thermal damages an additional heat filter (IR cut-off filter, Heat protection glass KG-3, transparent for UV) was installed in front of the LED. Moreover, the samples were actively cooled by a cold-finger during the irradiation (see section 7.4 for experimental details). Increasing the illumination duration still leads to more pronounced changes. STM images for 15 min and 30 min light irradiation are shown in Figure 7.11.

After 15 min illumination (Figure 7.11(a)), most of the network is still intact. However, the number of bright dots increases dramatically as compared to the 10 min illumination. Furthermore, chain-like entities appear between network domains. It is not clear, whether the chains consist of the bright dots or are due to other entities.

To study whether the emergence of bright dots is related to thermal effects, a control experiment was performed. In this experiment, the sample was irradiated for a total time of 20 min under the same experimental conditions as in the case of 15 min illumination, though, with breaks in-between. The sample was irradiated in two separate 10 min illumination steps. After each step the sample was transferred to the STM and cooled down to 80 K and imaged. The 10 min illumination was performed in two steps, 5 min each with a break of 15 min in-between to cool the sample by the cold-finger in the load lock. STM images acquired after the first 10 min illumination indicated only a few bright dots on the surface. After STM measurements, the sample was transferred again to the load lock and irradiated for another 10 min as described above. Finally, i.e. after a total illumination time of 20 min the sample was imaged by STM. Interestingly, the number of bright dots was very low and the FAN network was

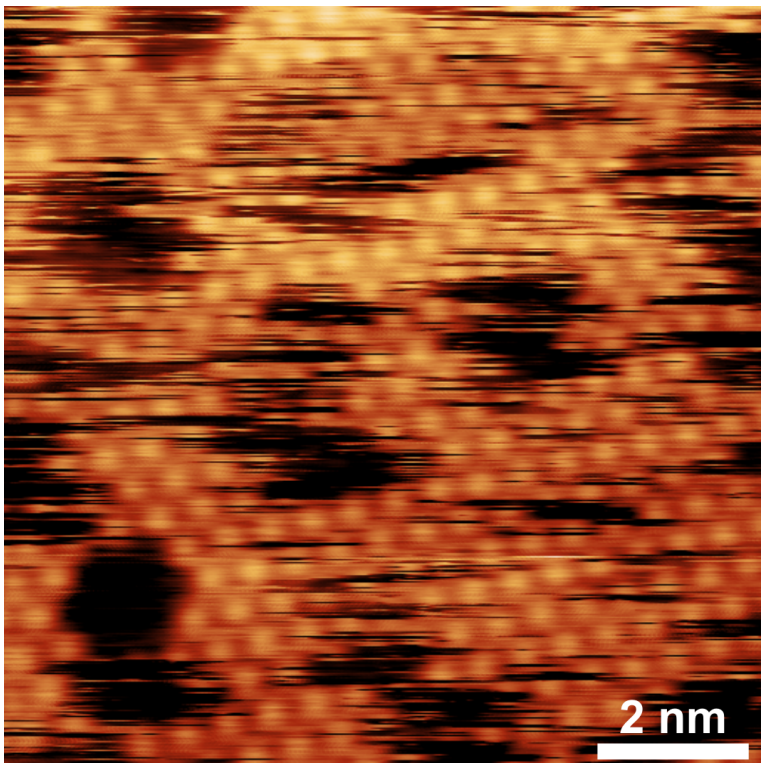

Figure 7.10: STM image acquired after 60 min irradiation of the FAN self-assembled structure on iodinated Au(111) by a 40 W LED (U_T = +374 mV, I_T = 30 pA). No FAN could be imaged anymore. Several iodine vacancy islands are recognizable on the surface.

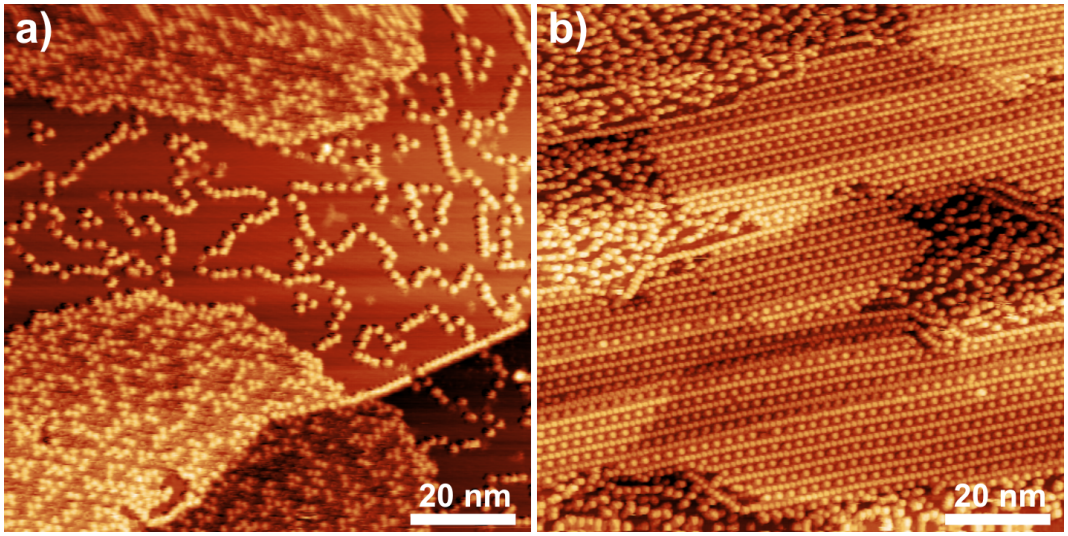

Figure 7.11: STM images acquired after a) 15 min (U_T = +1.00 V, I_T = 20 pA) and b) 30 min (U_T = -1.63 V, I_T = 20 pA) irradiation of the FAN self-assembled structure on iodinated Au(111) by a 40 W LED. After 15 min irradiation, number of bright dots increases severely. However, the intact FAN network can be still recognized in the background. After 30 min irradiation, the original hexagonal network disappears. The majority of the surface is covered with a new ordered structure, yet accompanied by areas covered with non-ordered entities.

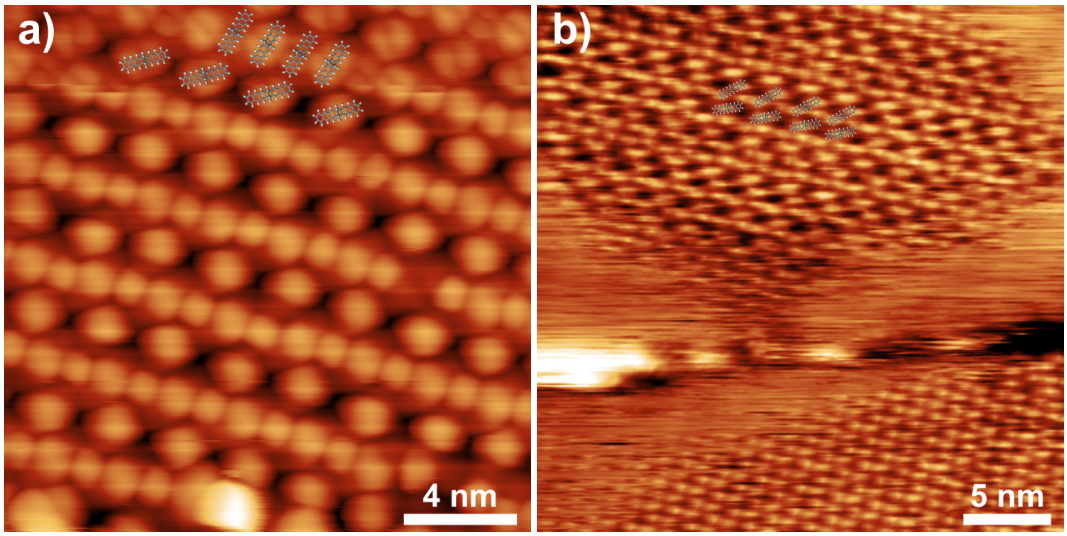

Figure 7.12: a) Close up of the ordered structure shown in the STM image of Figure 7.11(b) (U_T = +300 mV, I_T = 10 pA). b) Occasionally observed self-assembly of FAN after deposition on bare Au(111) (U_T = +800 mV, I_T = 30 pA). Scaled overlays of FAN monomers in a) indicate a possible assignment of the observed structure. In this assignment, the orientation of the symmetry axis of FAN monomers w.r.t. the surface is the same as in the case of on bare Au(111). The similarity between STM images a) and b) supports the hypothesis of iodine desorption after 30 min irradiation and rearrangement of FAN monomers.

intact. Continuous irradiation of the sample for 15 min results in the emergence of many bright dots as shown in Figure 7.11(a). However, after a longer irradiation time of 20 min with additional cooling in-between intervals, only a few bright dots appear on the surface. Consequently, this experiment confirms a relation between the number of bright dots and thermal effects.

With 30 min illumination, the original hexagonal network completely disappeared and a new partly ordered structure appeared on the surface (see Figure 7.11(b)). However, parts of the surface were also covered with non-ordered bright protrusions. The close-up image of the new ordered structure is shown in Figure 7.12(a).

The regularity of this structure suggests the formation of defined entities. This structure resembles an occasionally observed FAN self-assembly on bare Au(111) (Figure 7.12(b)). As a reminder, FAN molecules adsorb on Au(111) with two anthracene blades parallel to the surface and the third one perpendicular to it. Based on this molecular adsorption geometry, a structural model for the observed ordered pattern is proposed. The scaled overlays of FAN monomers in Figure 7.12(a) shows the tentative structural assignment. A closer look at the molecules on the upper part of the image reveals double lobed protrusions. This more detailed contrast is in agreement with the proposed structural assignment, where each lobe corresponds to one adsorbed anthracene blade of FAN. Emergence of this ordered structure suggests that iodine desorbs from the surface due to the temperature increase of the surface by irradiation. Consequently FAN monomers adsorb directly on Au(111) in the observed ordered structure. This is plausible,

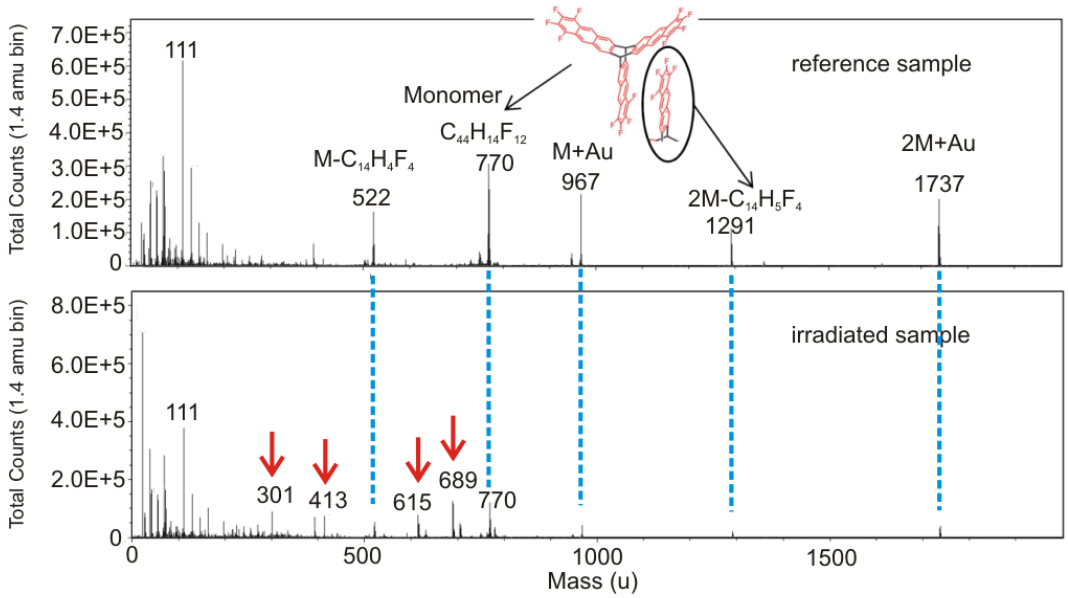

Figure 7.13: ToF-SIMS of the FAN reference sample (upper spectrum) and the irradiated sample (lower spectrum). Clear differences are observed as further discussed in the text.

since STM images acquired after irradiation of the sample for 60 min indicate iodine desorption from the surface (see Figure 7.10). The chains observed after 15 min irradiation might represent an intermediate state and have the same origin as this ordered structure.
In the irradiation experiments with the 40 W LED, only the dark patches observed after 10 min illumination might be an indication of successful photopolymerization. Hence, this sample was further studied by complementary methods. The lattice parameters of the FAN supramolecular assembly and photopolymerized covalent network are not distinguishable within the accuracy of STM. Therefore, other complementary analytics are necessary to figure out whether the network is polymerized. The irradiated sample with two contrasts and a not irradiated reference sample of FAN on iodine terminated Au(111) were studied by Time-of-Flight Secondary Ion Mass Spectrometry (ToF-SIMS). ToF-SIMS is a surface-sensitive analytical method that uses a focused pulsed ion beam (here Ga^+) to desorb species (molecular compounds and fragments of larger organic nanostructures) from the outermost layers of the surface. The knocked out particles are accelerated into a "flight channel" and their mass can be determined by measuring the exact time at which they reach the detector (time-of-flight). Results of ToF-SIMS measurements are presented in Figure 7.13.

ToF-SIMS data of the irradiated and the reference sample show pronounced differences. Peaks appear at different masses, pointing towards structural differences between these two samples. The peak related to FAN monomers at the mass of 770 u is present in both spectra, but is more intense for non-irradiated sample. The second most intense peaks in the spectrum of non-irradiated sample are the peaks related to (FAN + Au) and (FAN_2+ Au) at the masses of 967 and 1737 u. The signal of these masses is very weak for the irradiated sample. Moreover, peaks of monomer fragments, i.e. monomer or dimer where one anthracene arm

is missing, are highly pronounced in non-irradiated sample and only very weak for the irradiated sample. There are also several peaks e.g. at the masses of 301, 413, 615 and 689 u (red arrows in Figure 7.13) that are only present in the spectrum of the irradiated sample. However, an assignment of these masses to defined fragments is not possible. Given the large mass of FAN, the peaks at lower masses (0-120 u) might be due to contaminations adsorbed on the surface during the sample transport through atmosphere.

The differences between these spectra can be interpreted in two ways; they can either stem from photopolymerized parts of the network, or from other structural changes due to the above discussed radiative or thermal effects. For instance, if the observed dark patches indicate iodine desorption underneath the network, then corresponding parts of FAN networks adsorb on bare Au(111). These parts can be fragmented differently upon ion bombardment by ToF-SIMS, giving rise to additional peaks in the irradiated spectrum. Therefore, ToF-SIMS could not give a decisive evidence for photopolymerization.

Additional ToF-SIMS measurements on FAN deposited on bare Au(111) have the potential to add valuable information. If the spectra of FAN on iodine-terminated Au (the reference sample) and FAN deposited on bare Au(111) were similar, one could conclude that FAN on Au and on iodine-terminated Au fragment in the same way. Consequently, the changes in the irradiated sample would be due to the successful photopolymerization. Future experiments can settle this question.

To minimize the thermal effects and also increase the irradiation flux even more than with the 40 W LED, another set of experiments were performed with a violet diode laser (50 mW, λ= 405 nm from Opto Engine LLC). Contrary to LED experiments, irradiation with the laser was performed in the main chamber. The laser was installed at a UV transparent view port aligned to the STM. Prior to the illumination, the samples were cooled down to 80 K in the STM and during the irradiation the cooling was maintained. However, the exact temperature of the surface during the irradiation was not precisely known or controlled. The STM images acquired after 60 min irradiation are shown in Figure 7.14(a). The FAN hexagonal network is intact, only a few bright dots appear on the surface. The advantage of this experiment in comparison to the LED irradiation is the outlasting (survival) of FAN networks despite the relatively long irradiation time. This is probably due to the lower heat uptake of the sample during the laser irradiation. Although very slightly, but the laser warms up the sample as well. The reason is that the laser energy is in the order of the energy separation between sp- and d-bands of gold. Therefore, electrons can be excited from sp- to d-bands by ~400 nm laser, resulting in the heating of the sample. The emergence of the bright dots can be explained with the same arguments as before, either due to thermal effects or contaminations. Consequently, the drastic decrease in the number of bright dots compared to LED experiments despite longer irradiation time can also be explained in two ways. It is either the result of the smaller temperature increase of the surface upon laser irradiation or lower contamination in the main chamber. According to the previous discussions the former one is more probable.

All above experiments were performed on epitaxial Au(111) films on mica. The poor thermal conductivity of mica in combination with the low heat capacity of

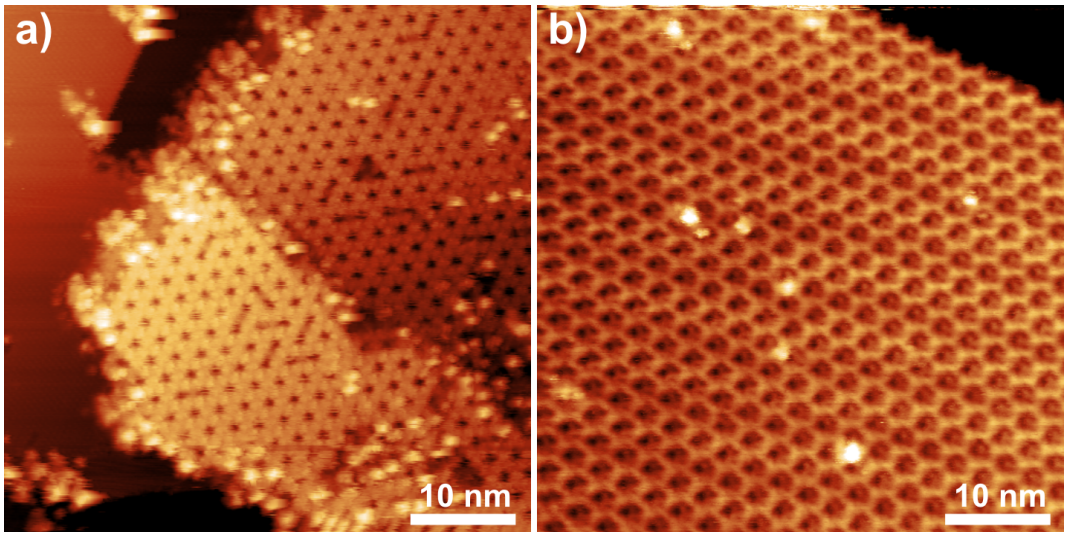

Figure 7.14: STM images acquired after irradiation of the self-assembled FAN structure on iodine-terminated Au(111) by laser a) gold film on mica after 1 h irradiation (U_T = -2.00 V, I_T = 20 pA) b) gold bulk single crystal after 15 h irradiation (U_T = +3.00 V, I_T = 20 pA). Despite the very long illumination time, the FAN network is still intact and there are only very few bright dots on the surface.

the initially ~300 nm thin Au films promotes temperature increase and thermal effects upon irradiation. Therefore, to check the potential influence of the type of Au sample on experimental results further laser irradiation experiments were performed on iodinated Au(111) bulk single crystals. A representative STM image acquired after 15 hours continuous irradiation is shown in Figure 7.14(b). Not only the hexagonal network of FAN is intact after this very long irradiation experiment, but there are just very few bright dots on the surface. This experiment provides further evidence that observed bright dots are due to thermal effects.

Interestingly, the change in the contrast of FAN networks, i.e. darker patches, was never observed for laser experiments. If dark patches of the network are related to photopolymerization, it seems that warming up the sample to a certain temperature could even be required for the polymerization. This can be understood, since at elevated sample temperatures molecular motions in the network increase, which facilitates adopting intermolecular distances appropriate for the photopolymerization. However, these required temperatures for a successful photopolymerization are apparently high enough to cause iodine desorption from the Au(111) surface. With iodine desorption the integrity of desired FAN self-assembled structure is jeopardized. Therefore, other surfaces with increased iodine adsorption strength might be more promising.

On Ag(111), the adsorption strength of iodine is higher.[137] Therefore, irradiation experiments, yet at elevated sample temperatures on iodinated Ag(111) might be more successful. For this purpose, the sample is heated during the irradiation (up to temperatures lower than the onset of thermal depolymerization or iodine desorption). However, Ag(111) might also not be the perfect candidate for the photopolymerization due to its strong light screening at wavelengths of ~400 nm due to the high dielectric constant of silver at these wavelengths.[172]

The dielectric constant of gold at wavelengths of ∼400 nm is much lower than silver.[173] Hence, a gold substrate covered with a few monolayers of silver is potentially a good candidate for these experiments. On one hand, it alleviates the strong light screening of pure silver, and on the other hand takes advantage of high adsorption strength of iodine on silver.

7.3 Conclusion and Outlook

In summary, the self-assembly of FAN monomers on Au(111) could be engineered by passivation of the metal surface. Exposure of the gold surface to iodine vapor resulted in the formation of an iodine monolayer and accordingly surface passivation. The self-assembled structure of FAN on iodinated Au(111) is the same as in the layers of FAN single-crystals.[15] This specific arrangement of FAN monomers is the required molecular assembly for the topochemical photopolymerization based on anthracene-anthracene dimerization.
To polymerize the self-assembled structure various irradiation experiments were carried out by LED or laser on iodinated Au(111) films or single crystals. Irradiating the sample with a 40 W LED for 10 min caused obvious changes in the network. Patches of the hexagonal network appeared with darker contrast and additional bright dots appeared on the surface. These samples were also analyzed by ToF-SIMS. However, based on the current data it is not clear, whether the dark areas of the network are polymerized domains or are just areas, where iodine desorbed from underneath the network. Increasing the irradiation time resulted in drastic changes. After 30 min illumination, the original hexagonal network completely disappeared. The surface was mostly covered with a new ordered structure, consisting of bright protrusions. This structure tentatively could be assigned to FAN monomers with a similar adsorption geometry as on bare Au(111). Emergence of this structure suggested that iodine desorbs from the surface due to the temperature increase of the surface by irradiation. Accordingly, FAN monomers adsorb directly on bare Au(111) and form the observed ordered structure.
To minimize the warming up of the surface upon irradiation, alternative illumination experiments were carried out with a laser. Thereby, best conditions for long time illuminations to maximize the radiation flux without damaging the FAN hexagonal network were achieved. After 1 h irradiation, the FAN hexagonal network was intact and only a few bright dots appeared on the surface. The poor thermal conductivity of gold films on mica was also alleviated by using a gold single crystal in the subsequent experiments. Even after 15 hours irradiation, the networks survived on Au(111) single crystals with only a few bright dots visible on the surface. However, the dark patches or other indications of photopolymerization were never observed in laser experiments.
If dark areas are indeed polymerized domains, this implies that the photopolymerization occurs at higher surface temperatures. Apparently, the required temperatures are sufficiently high to cause iodine desorption from the Au(111) surface as an unwanted side-effect. Therefore, alternative surfaces such as Ag(111) with higher adsorption strength of iodine might be better candidates for these experiments. On the other side, Ag screens light at wavelengths of ∼400 nm stronger than Au. One solution is to epitaxially grow a few layers of silver on a gold

substrate to eliminate the strong light screening of pure silver substrate, and simultaneously take advantage of high adsorption strength of iodine on silver. Other surfaces with lower electron densities and hence lower plasmon frequencies as compared to Ag(111) or Au(111) may also be appropriate candidates due to their weak or absent light screening at the required wavelength. For instance, highly oriented pyrolytic graphite (HOPG) or molybdenum disulfide (MoS_2) are two potential candidates. However, the primary requirement is the formation of the specific FAN assembly appropriate for photopolymerization on these surfaces. Therefore, prospective experiments are needed on HOPG and MoS_2surfaces.
The occurrence of photopolymerization could not be confirmed by STM and ToF-SIMS. Therefore, other experimental methods are required to study the irradiated samples. Spectroscopic techniques such as Tip-Enhanced Raman Spectroscopy (TERS), Infrared Reflection-Absorption Spectroscopy (IRRAS) and High Resolution Electron Energy Loss Spectroscopy (HREELS) are appropriate methods to study molecular vibrational/rotational modes of FAN networks to obtain evidence for polymerization. Moreover, STS as a powerful technique that provides information about the local electronic structure of the adsorbates at the atomic scale with amazing spatial resolution is also potentially useful for future experiments.

7.4 Experimental Details

All preparation steps and measurements were carried out in ultra-high vacuum. The samples were characterized *in-situ* by STM before and after irradiation. For further characterization by NEXAFS and ToF-SIMS samples were transported through atmosphere (except for NEXAFS experiments of FAN on bare Au(111)). Epitaxial Au(111) films on mica (Georg Albert Physical Vapor Deposition, Silz, Germany) were used as substrates (except for single crystal experiments). The samples were prepared by cycles of Ar^+ ion sputtering at 0.5 keV and annealing at ∼480 °C. The synthesis of FAN was described in the work of Kissel *et al.* [15]. FAN deposition was carried out by means of a home-built evaporator[131] at a crucible temperature of ∼290 °C onto the surface held at room temperature. Iodination of Au(111) films or single crystals was carried out at $\sim 5.5\times10^{-7}$ mbar for ∼5 minutes (or 2×10^{-6} mbar for 10 min) in a small auxiliary chamber to avoid contamination of the main UHV chamber.
All STM data were acquired *in-situ* at ∼80 K (except for FAN on bare Au(111) acquired at RT) and a base pressure below 3×10^{-10} mbar with a home-built microscope driven by a Nanonis BP4 SPM control system. STM images were leveled.
NEXAFS experiments were conducted at the BESSY II synchrotron (Helmholtz-Zentrum Berlin). C 1s NEXAFS spectra were acquired for X-ray incidence angles (referred to the surface plane) of 30°, 45°, 55°, 70°, and 90°. Anthracene angles with respect to the surface plane were quantified from the incidence angle dependence of the C 1s→π^* intensities.
ToF-SIMS measurements were performed at Physical Electronics GmbH using focused pulsed Ga^+ ion beam. The spectra were acquired by detecting positive ions.
The LED was installed at a distance of ∼6 cm from the surface at a UV transparent view port of the load lock. Contrary to LED experiments, irradiation with

the laser was performed in the main chamber. The laser was installed at a UV transparent view port aligned to the STM.
The copper cold-finger provided high thermal conduction to transfer heat out of sample. It was connected to a liquid nitrogen dewar at one end and the manipulator (and hence with the sample holder) in the UHV chamber at the other end.

Chapter 8

Conclusion

In this thesis, on-surface synthesis of organic nanostructures under ultra-high vacuum conditions is explored. The bottom-up synthesis of surface-supported nanostructures is generally divided into two main categories: Supramolecular self-assembly and on-surface polymerization. With a view to potential applications, the extraordinary mechanical, thermal, and chemical stability of covalent networks offer crucial advantages over self-assembled structures. Therefore, the focus of this work is on the study of various on-surface polymerization reactions for different functionalized monomers. Moreover, strategies for detachment and electronic decoupling of synthesized nanostructures from underlying metal substrates are explored. This step is essential to be able to characterize nanostructures without the influence of strongly interacting metal substrates and to use them for prospective nanotechnological applications.

As shown in chapter 4, even a well characterized and commonly used on-surface polymerization reaction as Ullmann coupling does not always proceed in a predictable manner. Ullmann coupling of DIB on Cu(111) unexpectedly yields self-assembled patterns of biradicalic trimers, or occasionally even more complex patterns of hexamers. Instead of being directly adsorbed on the metal surface that initiates the Ullmann coupling by dehalogenation, the covalent aggregates are adsorbed atop a closed iodine monolayer. The affinity of iodine to Cu(111) is apparently strong enough to overcome interactions between the surface and organic nanostructures.

Motivated by these observations, the deliberate exposure of metal-adsorbed covalent nanostructures to iodine vapor as a novel, straightforward, and widely applicable approach for post-synthetic decoupling is studied in chapter 5. Two-dimensional porous covalent polyphenylene networks derived from BIB precursors on Ag(111) and Au(111) are chosen as model systems. On Ag(111), RT iodination of samples readily results in iodine intercalation between polyphenylene networks and Ag(111) surfaces. A combination of STM, XPS, and NEXAFS consistently confirms that covalent networks are detached and electronically decoupled form Ag(111) upon intercalation of an iodine monolayer.

Lateral manipulation of a polyphenylene domain with the STM tip reveals a close-packed iodine monolayer underneath. Moreover, STM images of the networks appear with a orbital-dominated contrast, indicating the absence of hybridization of molecular electronic states with states of the metal surface, and hence detachment.

In XPS C 1s shifts to lower binding energies and an additional change to a symmetric line-shape suggests the absence of direct interaction with the free electron gas of Ag(111) after iodination.
NEXAFS results show an increase in the average tilt angle of the phenyl groups, i.e. structural relaxation, thereby indicating a weakened molecule–surface interaction for the iodinated sample as compared to the bare Ag(111). Furthermore, sharpening of C 1s $\rightarrow\pi^*$ resonances is also observed in NEXAFS, suggesting a significant weakening of the electronic coupling of polyphenylene to Ag(111) after iodination.
However, on technologically more important, but less reactive Au(111) surfaces, just iodine exposure at RT is ineffective to detach the polyphenylene network due to the weaker adsorption strength of iodine as compared to Ag(111). Overwhelming experimental evidence from STM, XPS and NEXAFS measurements is found for a mere co-adsorption of iodine on the free surface areas, whereby the covalent networks remain adsorbed on the metal surface:
STM reveals incomplete iodine coverages, NEXAFS shows that the phenyl rings remain essentially parallel to the surface, and the asymmetry of the C 1s peak in XPS – indicating direct interaction with the metal – prevails.
Interestingly, iodine co-adsorption also results in sharpening of the C 1s $\rightarrow\pi^*$ resonances in NEXAFS and a shift of C 1s to lower binding energies in XPS. These results suggest that also iodine co-adsorption can affect some spectroscopic signatures in a similar manner as successful detachment would do. Hence, one has to be careful in interpreting these changes as detachment.
However, successful detachment is achieved also on Au(111) by carrying out the iodination at elevated sample temperatures. STM reveals fully closed iodine layers without any vacancies. Moreover, the STM contrast of the covalent networks resembles the spatial distribution of frontier molecular orbitals of free-standing networks, therefore, indicating detachment and electronic decoupling.
Interestingly, the desorption temperature of iodine from Au(111) is sufficiently low to render the whole process reversible. Annealing the samples to 400 °C results in the full desorption of the iodine layer underneath the covalent networks, while the networks remain intact and re-adsorb on Au(111). Since iodine-terminated Au(111) surfaces are rather inert, reversible iodine intercalation might be useful for protecting samples under ambient conditions, e.g. for transport through atmosphere.
In chapter 6, synthesis of 2D networks from thiol-functionalized aromatic TMB monomers is pursued on Au(111). Although, 2D networks based on RS—Au—SR linkages could not be formed, important phenomena such as kinetic trapping, coordinative bonding to adatoms, polymorphism, dynamic reconfiguration, chemical changes of intermolecular bond type, formation of regular fractals, and partial decomposition are illustrated and discussed in this study.
RT deposition of TMB onto Au(111) results in the deprotonation of all thiol groups and formation of three basic binding motifs, stabilized by intermolecular RS—Au—SR linkages formed with Au adatoms. These motifs form mostly disordered aggregates at RT due to kinetic trapping. Mild annealing at 200 °C converts these less well ordered structures to regular 1D chains. The formation of 1D structures instead of 2D networks from a tritopic molecule such as TMB can be explained by the basic intermolecular binding motifs. The dominant motif is a

2-fold link via two mercaptophenyl groups, enclosing a small pore, that results in a dimer with two sticky ends at *para* position. Accordingly, there is only one free mercaptophenyl group per molecule left, i.e. a prototypical secondary building block for the formation of linear polymers is available.

The most interesting experimental observation is the conversion of Au—thiolate chains into regular fractals, i.e. the Sierpiński triangles, by annealing the samples at 250 °C. These triangles are constituted of one intermolecular binding motif featuring C—S—C bonds, i.e. covalent thioether bonds. Therefore, the structural transition from chains to triangles is driven by a chemical transition where coordinative S—Au—S linkages are converted into covalent C—S—C bonds. The mechanism of this conversion is not entirely clear, but ejection of just the formal Au—S unit is energetically highly unfavorable. However, ejection of Au—S—Au complexes formed with additional Au adatoms at higher surface temperatures is a chemically and thermodynamically plausible mechanism.

In addition to the microscopic characterization, XPS provides information on the chemical environment of sulfur. Interestingly, the structurally most important chemical change from Au—thiolate to thioether is not directly monitored by XPS because S 2p binding energies do not shift to a measurable extent. However, according to the proposed mechanism, sulfur is also ejected. Hence, an additional sulfur species that appeared in XPS at higher binding energies after annealing at 250 °C is assigned to this reaction byproduct. The chemical state of the ejected sulfur is not entirely clear, but a physisorbed species appears likely and would be in accord with XPS. Both STM and XPS consistently indicate a gradual transition. However, after a thermal treatment at temperatures around 300 °C, where XPS indicates complete conversion of thiolate into thioether, the onset of decomposition is observed both in STM and in XPS. An important lesson from this study is that even profound chemical changes are not necessarily detectable in high-resolution XPS experiments. Therefore, the importance of combined microscopic and spectroscopic studies for the field of on-surface synthesis is emphasized once more.

Defect free long-range ordered 2D polymers are required for many nanotechnological applications, such as nanoporous membranes or sensors, as molecular sieves or as growth templates for size selected nanoparticles. Therefore, an alternative method to fabricate such structures is investigated in chapter 7. The underlying idea is to use an ordered non-covalent assembly and convert it isostructurally into a covalent network through on-surface polymerization. Topochemical photopolymerization is chosen for this approach, since it provides maximal control of the supplied energy at reactive sites of the self-assembled structure, and thereby the highest chances to preserve the initial ordered structure.

Deposition of photoactive FAN molecules on Au(111) results in an ordered self-assembly, that is, however, inappropriate for photopolymerization. This self-assembly is steered by strong molecule-surface interactions, while the desired structure is governed by molecule-molecule interactions. Passivation of Au(111) surfaces by exposure to iodine vapor and subsequent formation of an iodine monolayer reduces molecule-surface interactions. Therefore, the suitable self-assembled structure for photopolymerization is engineered by deposition of FAN on iodine-terminated Au(111). This specific arrangement of FAN monomers is the required molecular assembly for the photopolymerization based on anthracene-anthracene

dimerization.
To polymerize the self-assembled structure various experiments were carried out by LED or laser irradiation on iodinated Au(111) films or single crystals. Irradiating the sample with a 40 W LED for 10 min causes obvious changes in the network. Patches of the hexagonal network appear with darker contrast and bright dots appear on the surface. These samples were also analyzed by ToF-SIMS. However, based on the current data it is not clear, whether the dark areas of the networks are polymerized domains or are just areas, where iodine desorbed from underneath the network. Increasing the irradiation time to enhance the amount of dark patches is unsuccessful. Illumination for 30 min results in the destruction of the original hexagonal FAN network and emergence of many bright protrusions.
Best condition for long time illuminations to maximize the radiation flux without damaging the FAN hexagonal network is achieved by laser experiments. On Au(111) single crystal, even after 15 hours irradiation the networks survive with only a few bright dots visible on the surface. However, the dark patches or other indications of photopolymerization are never observed in laser experiments. While the current data are promising, prospective experiments are needed to prove successful photopolymerization.

Outlook

In this thesis we have showed a novel approach to detach nanostructures from the underlying metallic substrate. As shown in chapter 5, iodine intercalation detaches covalent polyphenylene networks from underlying Ag(111) and Au(111) surfaces. This opens doors toward technological application of nanoarchitectures by separating them from the metal surfaces, necessary for their synthesis, without destruction. Decreased adsorption strength of nanoarchitectures on iodine surface facilitates their transfer to other technologically relevant surfaces using techniques like stamping. However, the practicability of this has to be proven in future studies. Moreover, further investigations are required to identify other influential parameters on the detachment process by iodine intercalation, for example the effect of domain size or structural characteristics of nanoarchitectures.
Beside detachment, iodine intercalation also electronically decouples the polyphenylene networks from the substrate. This in principal provides a possibility to characterize the intrinsic properties of 2D polymers without the influence of the substrate, that is an essential step for using the nanostructures in technological applications. For instance, 2D conjugated polymers are a target of interest because of their electronic properties. However, complete and precise characterization of their electronic structure is necessary to be able to use them for electronic applications. Under decoupled conditions, dispersion of electronic bands, and hence the electronic structure can be assessed by Angle-Resolved Photoemission Spectroscopy (ARPES). In this context, the iodine intercalation might be very useful. However, as shown before in chapter 5, iodine co-adsorption can affect spectroscopic signatures in a similar manner as successful iodine intercalation. Therefore, a detailed understanding of the influence of co-adsorbed iodine on spectroscopic signatures is needed. Further theoretical studies and simulations would help to push this field forward.

Synthesis of long-range ordered 2DPs without structural defects is still challenging, yet desired for many nanotechnological applications. Chapter 7 presented the conceptual ground works for isostructural conversion of a long-range ordered non-covalent assembly into 2DPs by on-surface polymerization. Using this concept for the topochemical photopolymerization of FAN, several future paths can be pursued. We suggest the following as next experimental steps:
1) Investigation of the photopolymerization of FAN on iodine-terminated Ag(111) by laser irradiation to maximize the radiation flux and simultaneous sample heating to provide the probably required higher surface temperatures for occurrence of photopolymerization (see chapter 7 for preliminary work on iodine-terminated Au(111)).
2) Using complementary spectroscopic techniques such as TERS, IRRAS, HREELS or STS to investigate the irradiated structures.
3) Substitute the underlying substrate with surfaces with lower electron densities to increase the probability of photopolymerization.

Appendix A

Supplementary Information for DIB on Cu(111)

STM image of the more complex and rare structure is shown in Figure A.1. Interestingly, the closed ring marked by the blue arrow appears significantly brighter, i.e. higher than all others. Since both geometry and adsorption site are similar to all other rings, we speculate that two rings are stacked on top of each other. The line profile on the right side indicates that the brighter ring has about twice the height of all other rings.

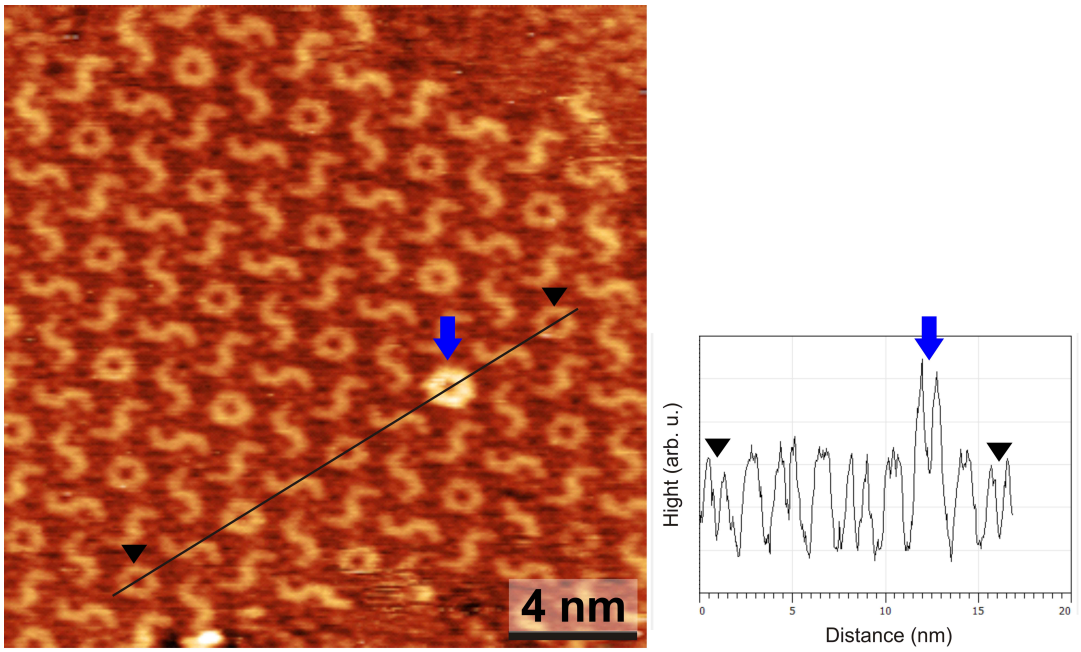

Figure A.1: Overview STM image of the more complex structure (V=+0.81 V, I=38 pA), comprised of two different hexamers: closed rings surrounded by a hexagonal arrangement of S-shaped entities. Right side: Corresponding line-profile along the black line.

Periodic DFT calculations were performed with the VASP code,[174] using the projector-augmented wave method[175] to describe ion-core interactions. Exchange-correlation were described by the van der Waals density functional (vdW-DF),[176, 177] in the recent form by Hamada,[178] denoted by rev-vdW-

DF2, which has shown to accurately describe molecular adsorption in a variety of systems.[178, 179] The Cu(111) surface was presented by a slab geometry of four layers. The iodine overlayer was placed in the known superstructure[116]. A p(5×6) surface unit cell was used (with respect to the primitive unit cell of the iodine overlayer). Furthermore, a 2×2 k-point sampling, and a 400 eV kinetic energy cutoff was used.
Figure A.2 and Figure A.3 show top and side views of DFT optimized adsorption geometries of iodinated and deiodinated (diradicalic) trimers on top of a close packed iodine $\sqrt{3} \times \sqrt{3}R30°$ superstructure on Cu(111) respectively.
STM simulations were performed with the Tersoff-Hamann approximation,[26] using the implementation by Lorente and Persson.[180] To simulate the STM images of iodinated and deiodinated trimers, the lowest energy structure i.e. the ones in Figure A.2(a) and Figure A.3(f) were respectively used. The results are presented in Figure A.4 and Figure A.5.
The diradicalic trimers bind covalently with their active sites to the surface-bound iodine atoms. Following calculations provide sufficient evidence for the covalent nature of these bonds. The DFT calculations indicate electron accumulation between radical sites and surface-bound iodine atoms. Figure A.6 represents the electron redistribution due to adsorption of the diradicalic trimer on the close packed $\sqrt{3} \times \sqrt{3}R30°$ iodine superstructure on Cu(111).
Comparing the partial density of states (PDOS) of carbon atoms of the diradicalic trimer in vacuum and in the case adsorbed on the close packed $\sqrt{3} \times \sqrt{3}R30°$ iodine superstructure delivers further evidence for the covalent nature of the bonds between trimers and iodine. The PDOS in both cases is depicted in Figure A.7.
For the formation of regular self-assembled pattern of trimers on Cu(111), trimer-trimer repulsive interactions are indispensable. The relatively large inter-trimer spacing suggests electrostatic interactions to be responsible for this repulsion. Therefore, Bader charge analysis based on DFT calculations was carried out. For this purpose the lowest energy structure of diradicalic trimer (Figure A.3(f)) was used.
To clarify the reason of different structures observed from DIB on Cu(110) and Cu(111), DFT calculations on benzene-1,3-diradical were done on both surfaces. For these calculations, a p(6×6) unit cell was used for Cu(111) and a p(4×6) unit cell for Cu(110) (6 atoms in the close-packed direction). In both cases a 4×4 k-point sampling was used, which ensured convergence of adsorption energies within 50 meV. Both surfaces were represented by four layers slabs, where the outermost two layers were allowed to fully relax. Figure A.9 and Figure A.10 show top and side views of DFT optimized adsorption geometries of the benzene-1,3-diradical on Cu(111) and Cu(110) respectively.

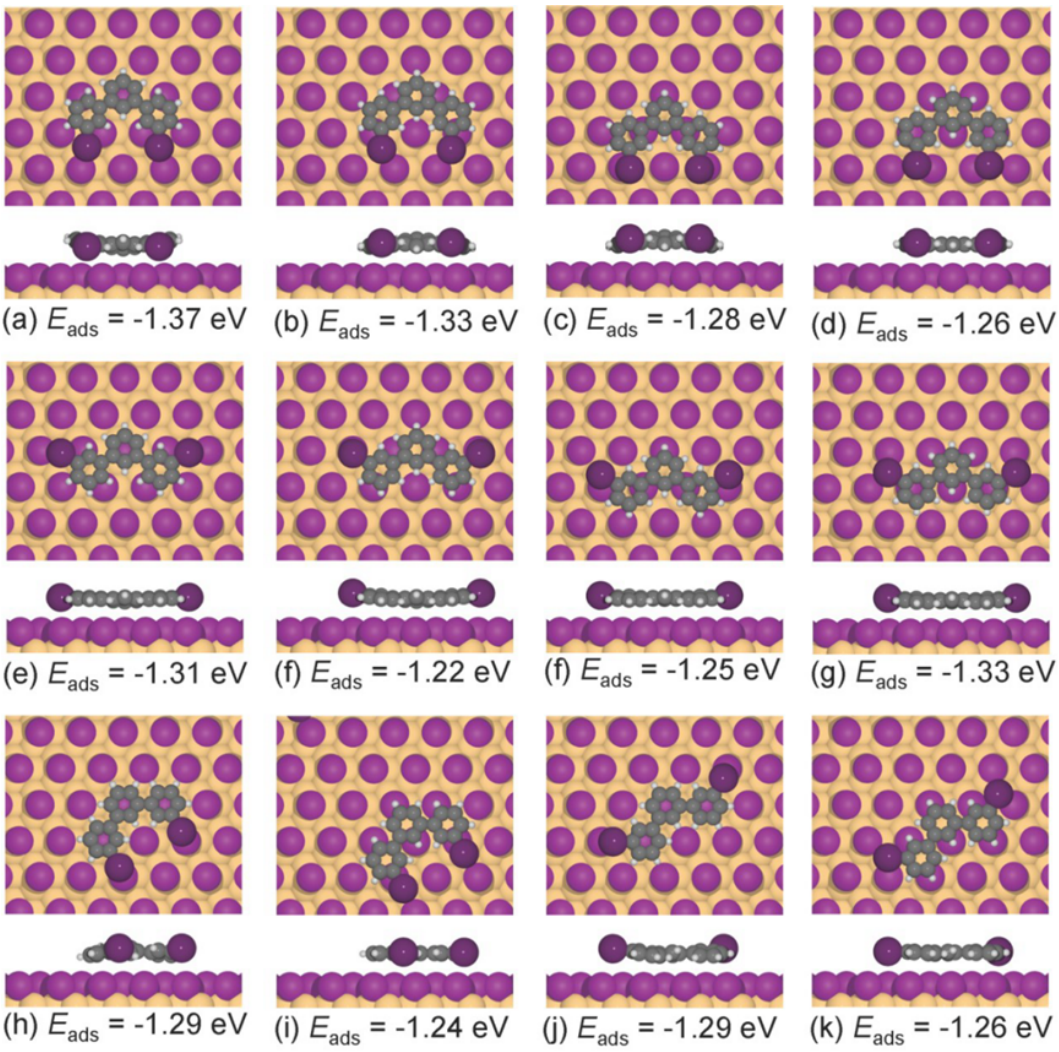

Figure A.2: (a) – (k): DFT optimized adsorption geometries of iodinated trimers. The adsorption energies, calculated with respect to isolated and surface-adsorbed molecule, are indicated below the respective structures. Structure (a) results in the lowest adsorption energy. However, energy differences between the different adsorption geometries studied here are relatively small, indicating a low surface diffusion barrier.

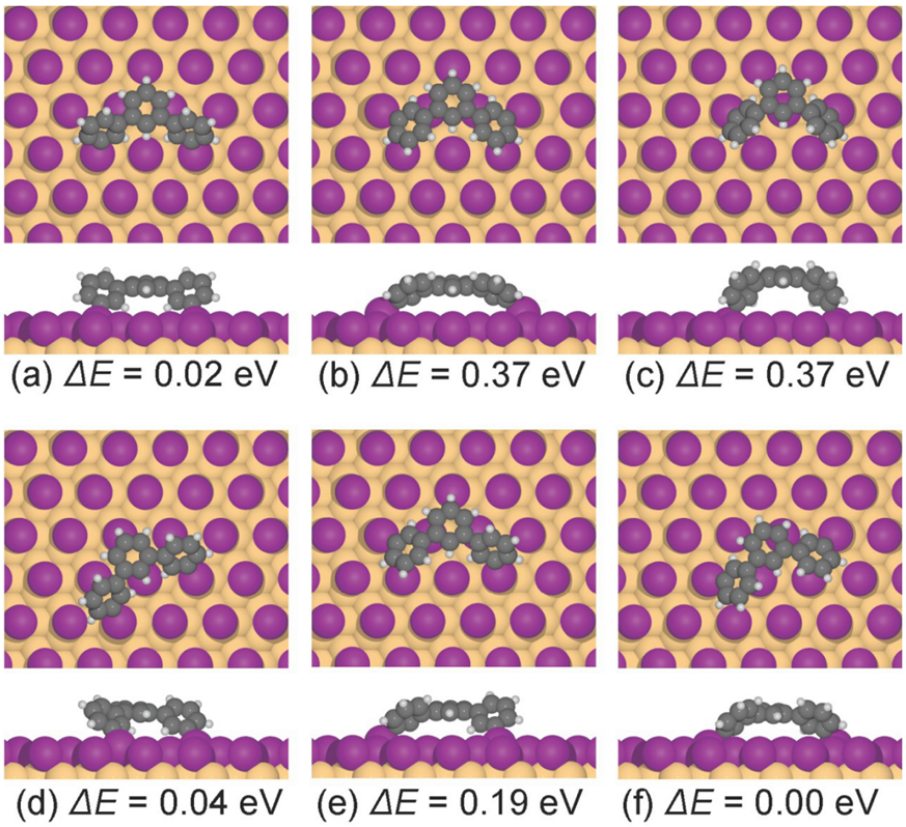

Figure A.3: (a) – (f): DFT optimized adsorption geometries of diradicalic trimers. Structure (f) results in the lowest energy. The energy differences $\triangle E$ with respect to the most stable geometry (f) are indicated below each structure.

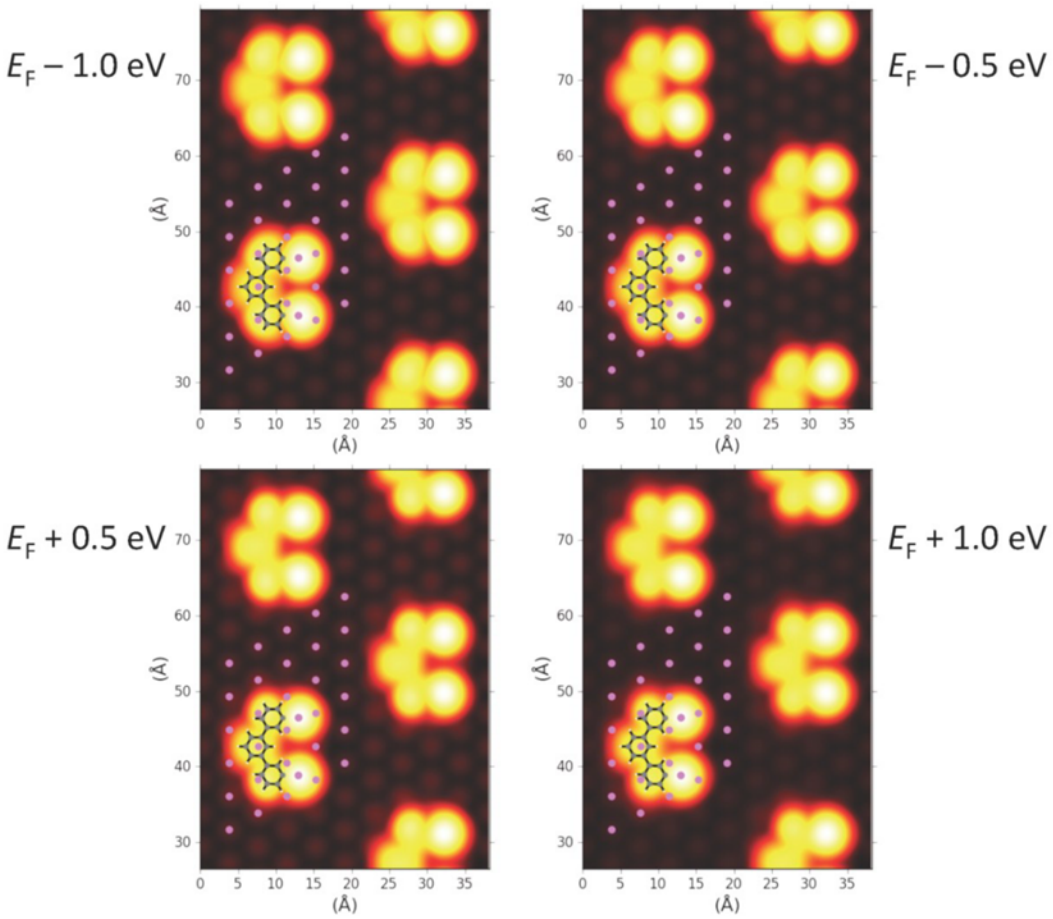

Figure A.4: STM image simulations of iodinated trimers. Electronic sample states were considered between the Fermi energy (E_F) and the respective energies stated on the margin; Accordingly, the upper row depicts STM image simulations of occupied electronic states (negative sample bias), whereas the lower row depicts STM image simulations of unoccupied electronic states (positive sample bias). The STM contrast was found to be virtually independent of sample bias and polarity.

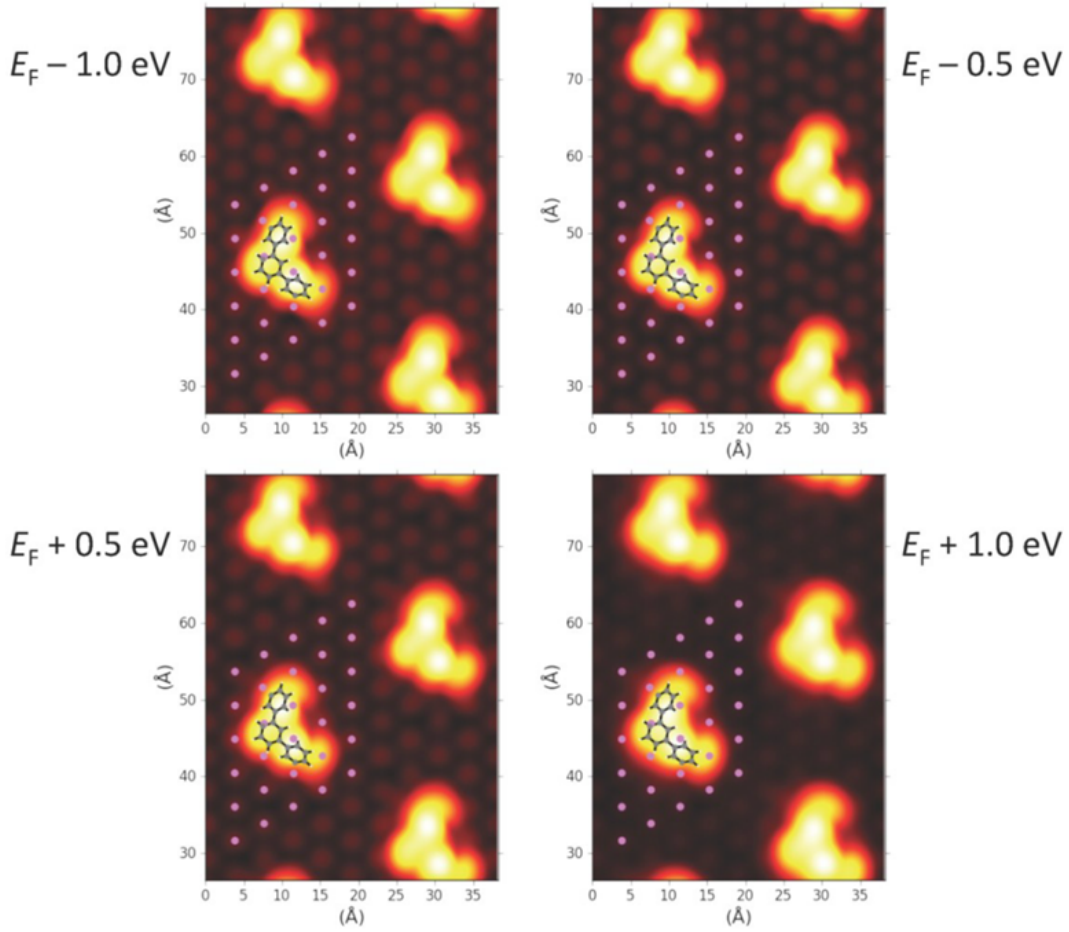

Figure A.5: STM image simulations of diradicalic trimers. Electronic sample states were considered between the Fermi energy (E_F) and the respective energies stated on the margin; Accordingly, the upper row depicts STM image simulations of occupied electronic states (negative sample bias), whereas the lower row depicts STM image simulations of unoccupied electronic states (positive sample bias). The STM contrast was found to be virtually independent of sample bias and polarity.

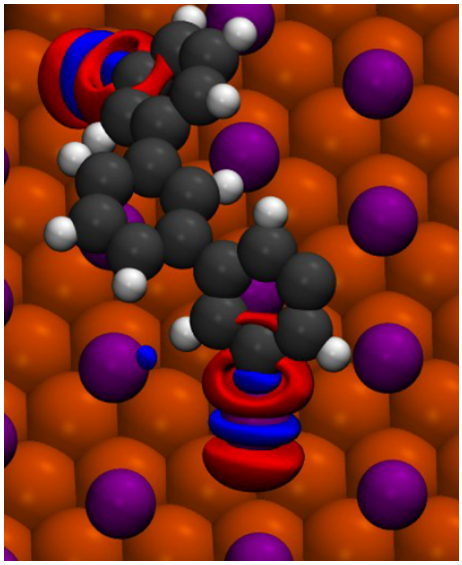

Figure A.6: Electron density difference plot. The blue and red contours show electron accumulation and depletion, respectively. The absolute value of the contours is 0.01 e/$\mathring{A}^3$.

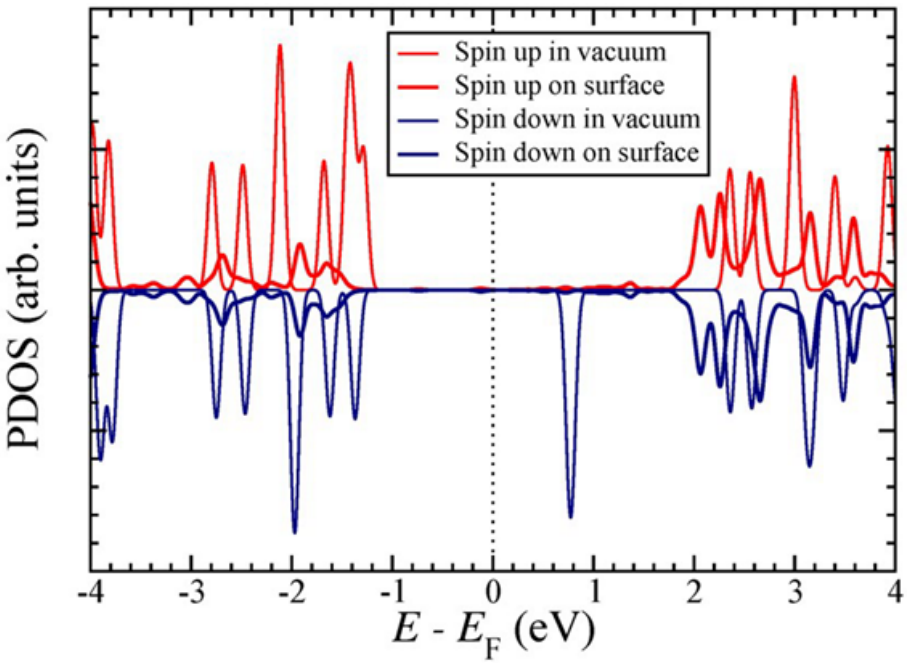

Figure A.7: PDOS on the carbon atoms of the diradicalic trimer in vacuum and on the surface. The vacuum levels of both systems were aligned, and the Fermi energy (E_F) refers to the surface. By coincidence, occupied and unoccupied states of the isolated molecule are below and above this Fermi energy, respectively. In vacuum, the spins of the diradicalic trimer are unpaired, but become paired upon adsorption on the surface, due to interactions with the surface. The frontier molecular orbitals are strongly hybridized, indicating the covalent character of the bond between the radical sites and the surface-bound iodine atoms.

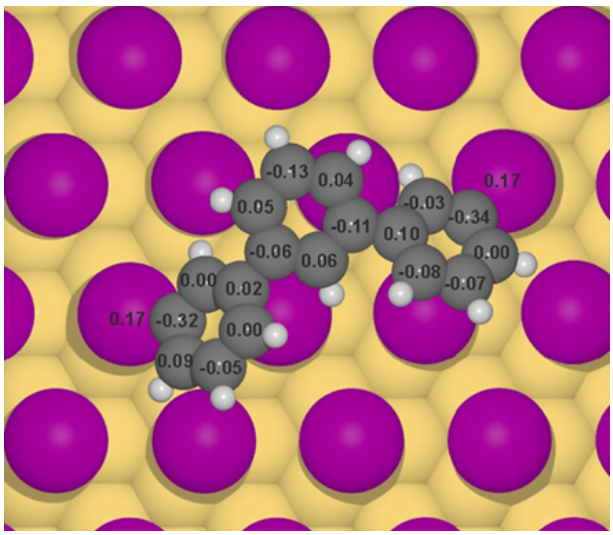

Figure A.8: Atom-wise Bader charge analysis of the carbon atoms of the deiodinated (diradicalic) trimer and the two adsorbed iodine atoms bonded to the trimer. Charges are given in units of e. The total charge of the molecule (including H atoms, but excluding the adsorbed iodine atoms) is -0.24 e. Notable, the two iodine atoms bonded to the trimer have positive Bader charges of +0.17 e each. In contrast, all other adsorbed iodine atoms have negative Bader charges in the range -0.23 e to -0.26 e. The local positively charged character of the iodine atoms bonded to the trimer might partly explain the repulsion between trimers.

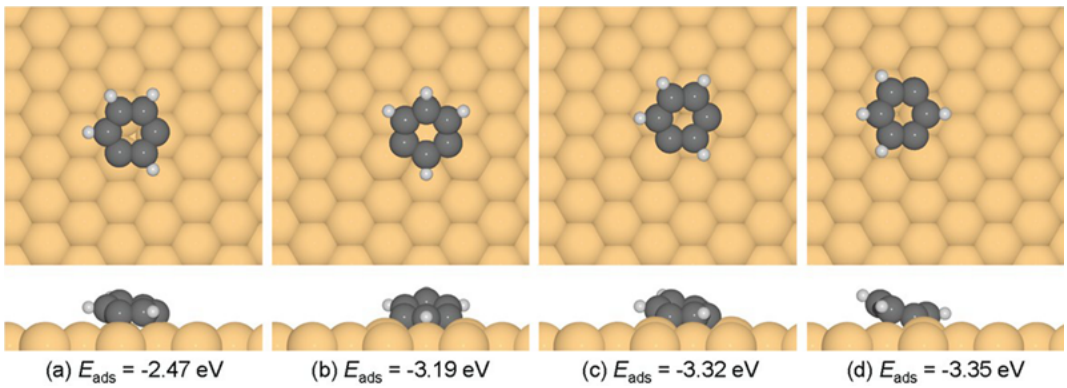

Figure A.9: DFT optimized adsorption geometries of the benzene-1,3-diradical on Cu(111). The adsorption energies, calculated with respect to isolated and surface-adsorbed molecule, are indicated below the respective structures. The most stable adsorption geometry is shown in (d).

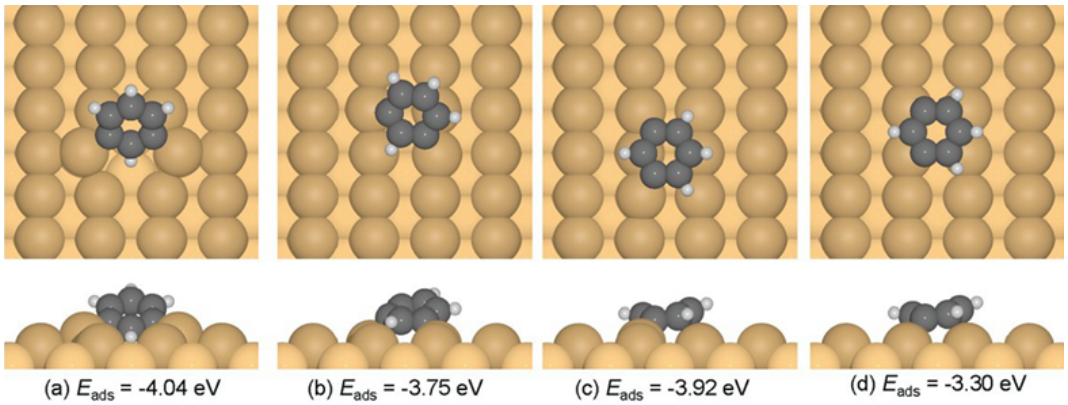

Figure A.10: DFT optimized adsorption geometries of the benzene-1,3-diradical on Cu(110). The adsorption energies, calculated with respect to isolated and surface-adsorbed molecule, are indicated below the respective structures. The most stable adsorption geometry is shown in (a).

Appendix B

Supplementary Information for BIB

B.1 Supplementary DFT Calculations for BIB on Ag(111)

Periodic density functional theory calculations were performed with the VASP code,[174] using the projector-augmented wave method to describe ion-core interactions.[175] Exchange-correlation were described by the van der Waals density functional (vdW-DF),[176, 177] in the recent form by Hamada,[178] denoted by rev-vdW-DF2, which has been shown to accurately describe molecular adsorption in a variety of systems.[178, 179] The Ag(111) surface was represented by a slab geometry of four layers. A p(9×6) surface unit cell was used (with respect to the primitive unit cell of Ag(111)), for the calculations both with and without the iodine overlayer. The iodine overlayer was placed in the known structure.[125] Furthermore, a 2×3 k-point sampling, and a 400 eV kinetic energy cutoff were used. Structural optimization were performed on all atoms – except the bottom two layers of the Ag slab, which were kept frozen – until the residual forces were smaller than 0.01 eV/Å.

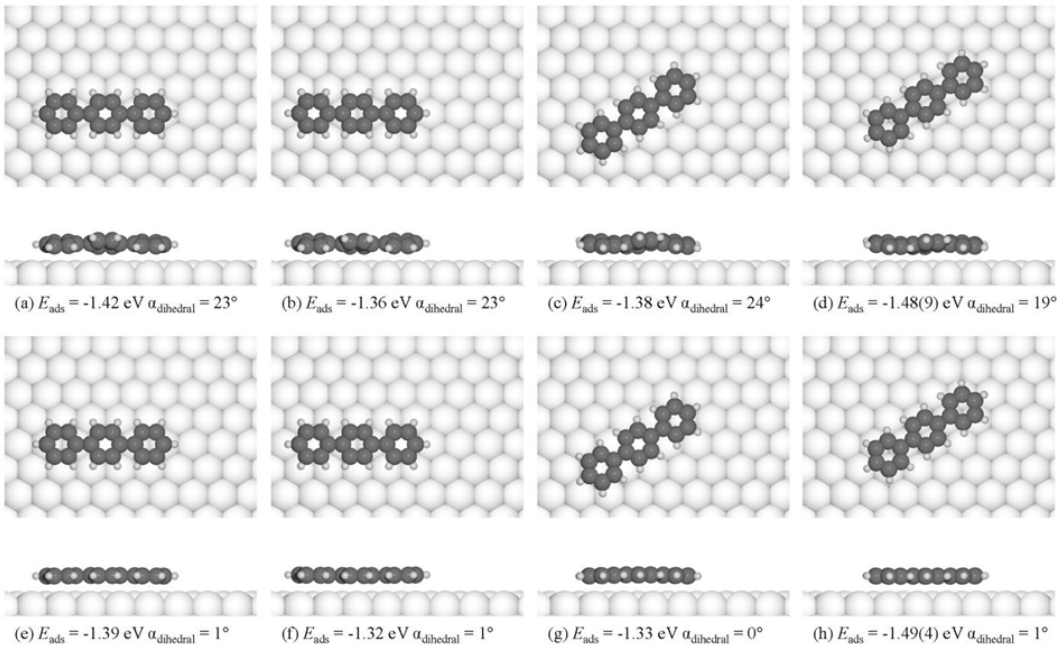

Figure B.1: (a) – (h) Top- and side-views of DFT-optimized adsorption geometries of terphenyl on pristine Ag(111). Corresponding adsorption energies E_{ads} and dihedral angles $\alpha_{dihedral}$ between adjacent phenyl rings are stated for each subfigure. Configurations (a-d) were optimized from an initial configuration with a $\alpha_{dihedral}$ of 40°, while configurations (e-h) were optimized from a planar initial configuration. The lowest adsorption energies were obtained for configuration (d), i.e. the structure with the smallest $\alpha_{dihedral}$ among the non-planar configurations, and the fully planar configuration (h). Interestingly, both optimized structures feature identical adsorption sites and azimuthal orientations. The corresponding adsorption energies are virtually identical, hence a DFT based energetic ordering is not possible.

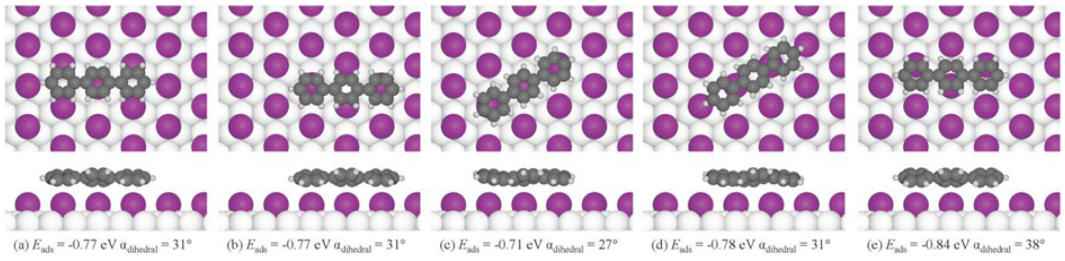

Figure B.2: (a) – (e) Top- and side-views of DFT-optimized adsorption geometries of terphenyl on top of a close packed iodine $\sqrt{3} \times \sqrt{3}$ R30° superstructure on Ag(111). Corresponding adsorption energies E_{ads} and dihedral angles $\alpha_{dihedral}$ between adjacent phenyl rings are stated for each subfigure. On iodine-terminated Ag(111) configuration (e) with the largest $\alpha_{dihedral}$ results in the lowest adsorption energy.

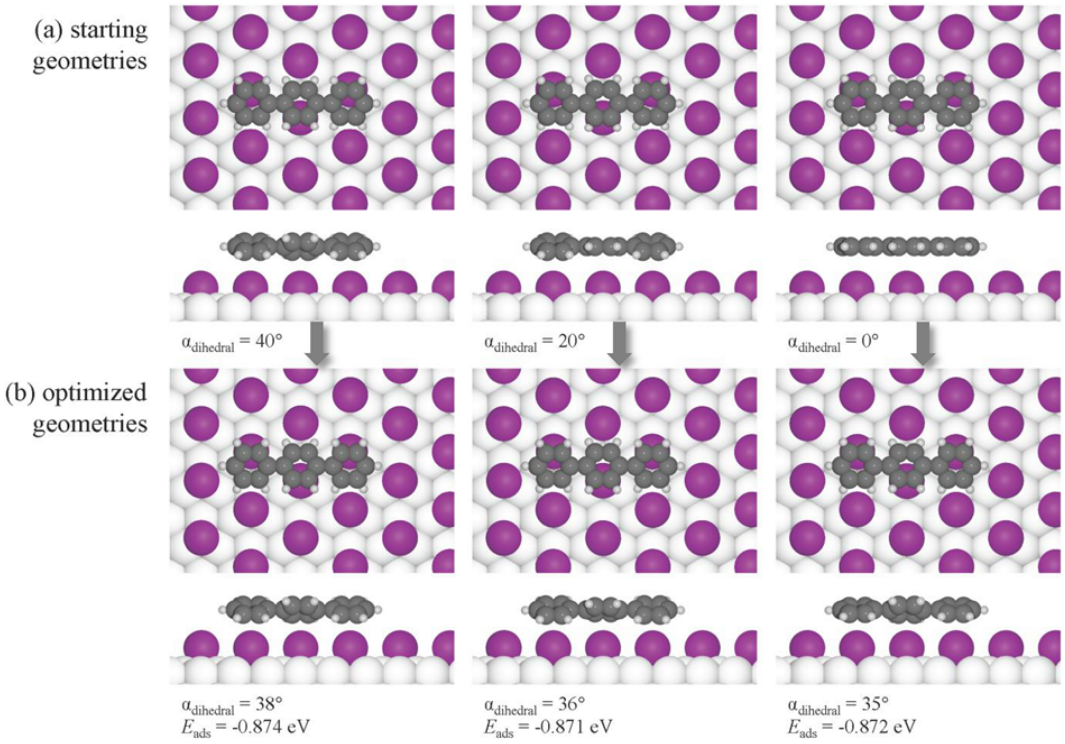

Figure B.3: Top- and side-views of (a) starting geometries and (b) corresponding DFT-optimized adsorption geometries of terphenyl on top of a close packed iodine $\sqrt{3} \times \sqrt{3}$ R30° superstructure on Ag(111). For (a) the preset dihedral angles $\alpha_{dihedral}$ are stated, whereas for (b) the optimized $\alpha_{dihedral}$ and the respective adsorption energies E_{ads} are stated. All starting geometries are based on the lowest-energy adsorption site depicted in Figure B.2(e). Optimization results in similar $\alpha_{dihedral}$ and E_{ads} irrespective of the initial starting geometry, indicating that the optimized structure represents the global energy minimum.

B.2 Supplementary STM Images for BIB on Au(111)

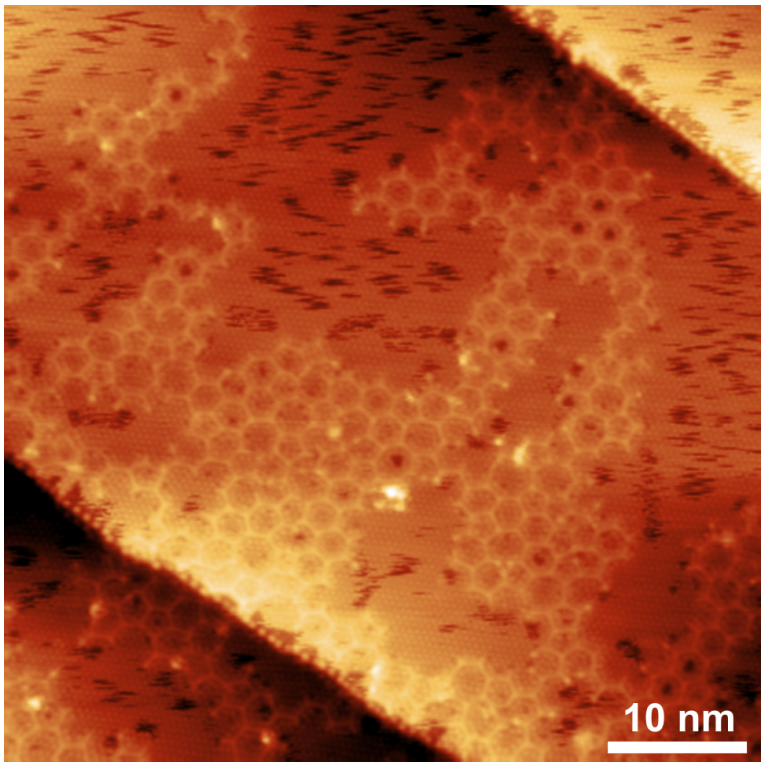

Figure B.4: STM image of BIB-derived covalent polyphenylene networks on Au(111) acquired after room temperature iodine exposure (5×10^{-7} mbar, ∼15 min, U_T = +858 mV, I_T = 25 pA). Same image as Figure 5.12 a) depicted with alternative color scale.

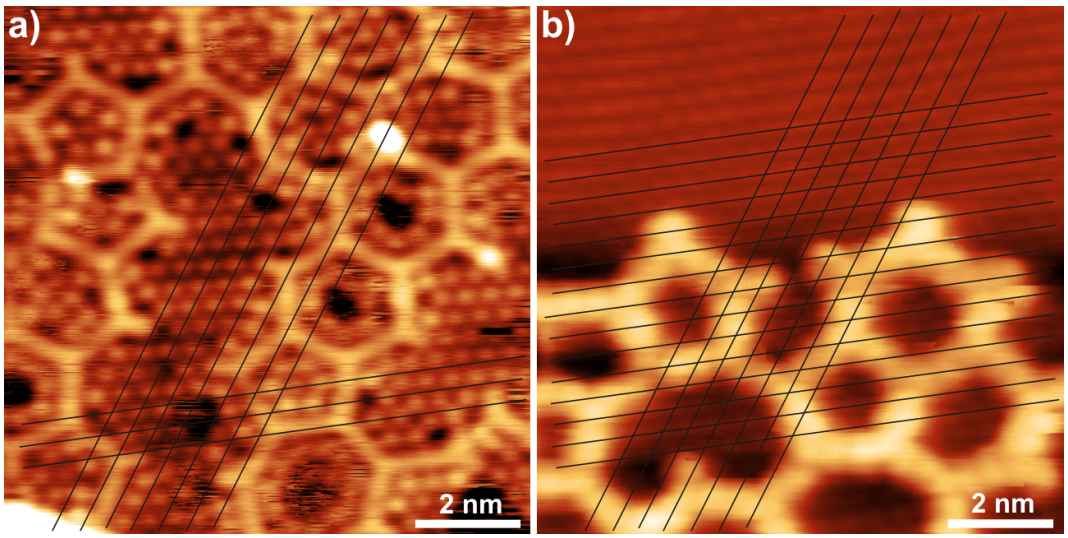

Figure B.5: STM images acquired after a) room temperature iodination (2×10^{-6} mbar, ∼20 min, U_T = +114 mV, I_T = 200 pA). vs. b) "hot iodination" (1×10^{-6} mbar, ∼6 min, U_T = -561 mV, I_T = 20 pA). The black lines serve as guide to the eye. After room temperature exposure the iodine atoms on either side of the covalent networks or within the pores are not adsorbed on the same lattice, but form incoherent domains. This is a strong indication for a non-closed layer. In contrast, after "hot iodination" all iodine atoms including those within the pores occupy sites of a coherent lattice. This provides evidence for a closed iodine layer underneath the covalent networks.

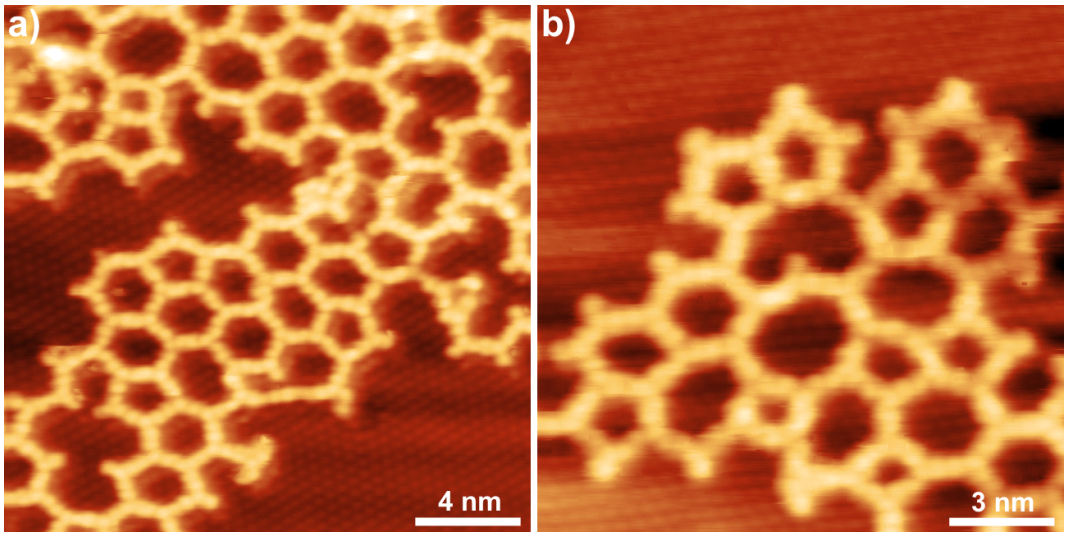

Figure B.6: STM images of BIB-derived covalent polyphenylene networks on Au(111) acquired after iodine exposure (1×10^{-6} mbar, ∼6 min) at elevated sample temperatures, i.e. "hot iodination". a) (U_T = +825 mV, I_T =20 pA). b) (U_T = -561 mV, I_T =20 pA). These images show a fully closed iodine layer (hexagonal structure in the background). Moreover, the covalent networks appear with internal contrast, resembling frontier molecular orbitals of free-standing networks.

Appendix C

Supplementary Information for TMB on Au(111)

C.1 DFT Simulations

All dimer motifs, metal−organic, and covalent zero-generation STs were simulated by DFT using the software Gaussian[181] with the B3LYP functional[182, 183] and LANL2DZ basis sets for all atoms.[184, 185, 186] Additional simulations with the PBE functional[187] resulted in similar geometries. Periodic type A and B chains as well as first generation metal−organic and covalent STs were simulated by DFT using the software CP2K[188, 189] with the PBE functional and DZVP basis sets for all atoms. CP2K calculations used periodic cells with a vertical dimension of 12 Å, while the dimensions in the lateral nonperiodic directions were chosen so as to leave at least 7 Å vacuum between adjacent molecules or chains. Motif 2 dimers adsorbed on Au(111) structures were also simulated using CP2K software and the PBE functional with the empirical dispersion correction (DFT-D2).[190] Owing to the large system size, the Au(111) surface was modeled using a single layer consisting of 10 × 14 unit cells with 140 Au atoms; the SZVP basis set was used for the Au surface atoms, and the DZVP basis set for the Au adatoms and all other atoms. Atomic positions in the single Au(111) layer were fixed, while the adsorbate was fully optimized.

C.2 Monte-Carlo Simulations

MC simulations used both monomers and dimers as basic building blocks. Monomers only consisted of four segments representing the phenyl rings. Dimers were modeled as rigid planar structures composed of nine interconnected segments, i.e., eight phenyl rings and one linking sulfur atom (cf. Figure C.2). The sulfur atoms of the thioether linkages between dimers were not explicitly considered but implemented through the allowed bonding configurations, leaving an empty lattice site at the respective position of the sulfur atoms (cf. Figure C.2). In all simulations, each of the segments was allowed to occupy one vertex (adsorption site) of a triangular lattice. This lattice defines adsorption sites and orientations of the dimers but does not represent the actual Au(111) surface.

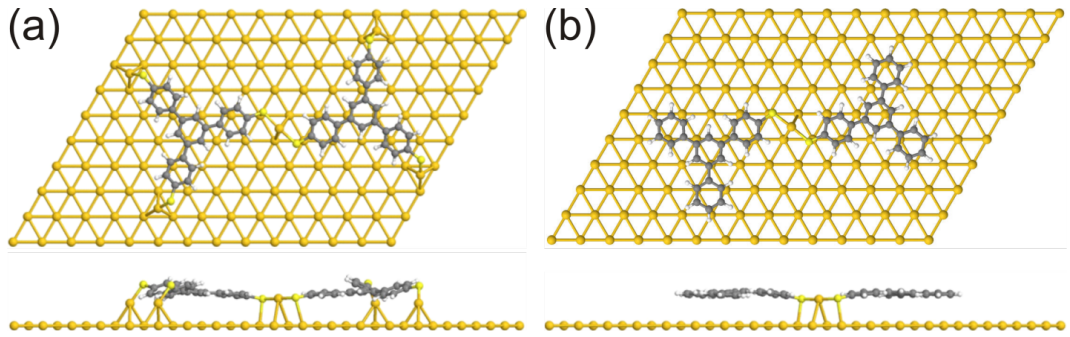

Figure C.1: DFT optimized geometries of S-Au-S linked motif 2 dimers on Au(111). The surface was approximated by a single layer of Au(111) with Au atoms frozen in bulk-like positions. Upper and lower rows depict top- and side-views, respectively. Different termini were considered: (a) peripheral thiolate groups that similarly bind to Au adatoms versus (b) hydrogen terminated, i.e. the peripheral thiolate groups were replaced by hydrogen atoms. Initially, the dimers were placed 0.55 nm above the surface (on average), and adopted the depicted geometries after optimization with the central Au atoms adsorbed in twofold bridge sites. This adsorption geometry also facilitates additional bonds between the sulfur atoms in the S-Au-S linkage and Au surface atoms. Anchoring through the peripheral thiolate groups in (a) imposes additional geometrical constraints, resulting in tilted phenyl rings and a relatively large average carbon adsorption height of 0.351 nm with a similarly large standard deviation of 0.053 nm. In contrast, the hydrogen terminated motif 2 dimer remains almost planar on Au(111) with notably smaller average carbon adsorption height of 0.319 nm and reduced standard deviation of 0.015 nm. The S-Au adatom bond lengths amount to 0.233 nm for (a) and 0.234 nm for (b), respectively.

Molecule–surface interactions were assumed to be equal for all lattice sites; i.e., the potential energy landscape of the surface was entirely flat. This simplification is justified by the relatively high formation temperature of the STs of ∼250 ° C where diffusion barriers are no longer playing a decisive role. The simulations were performed on a 200 × 200 rhombic section of the lattice using the standard Monte Carlo method in canonical ensemble (CMC).[162, 191] Periodic boundary conditions were applied to minimize edge effects. Dimers were not allowed to overlap or occupy neighboring sites of the lattice. Bonding was only possible in configurations that feature a 120 ° bond angle (cf. Figure C.2). Each intermolecular bond resulted in a contribution to the interaction energy of ε=−1; all other nonbonding intermolecular configurations resulted in a zero contribution to the interaction energy (ε=0). According to the CMC formalism, the system size, number of adsorbed dimers N, and temperature T were fixed. The simulations started with a set of dimers at random positions with random orientations. The system was equilibrated by typically 10^6 × N MC steps, where translation and rotation of dimers was attempted in each step. To this end, a dimer was selected at random and its potential energy E_0 evaluated in its current position with contributions from adjacent molecules equal to ε. Accordingly, only neighboring molecules in a bonding configuration contribute to E_0. Next, an attempt was made to move the selected dimer to a new position. The random translation of the dimer was accompanied by a random in-plane rotation by a multiple of 60 ° around its central segment. If all required lattice sites in the new position were unoccupied, the corresponding potential energy E_n was calculated using the same procedure as for E_0. If moving to the new position already resulted in an overlap with other dimers, the considered dimer was left in its original position. To accept the new position, the conventional Metropolis criterion was used with the acceptance probability $p = min[1, exp(-\Delta E/kT)]$, where $\triangle E = E_n - E_0$ and k is the Boltzmann constant. The calculated acceptance probability p was compared with a uniformly distributed random number $r \epsilon$ (0,1). If $r < p$ the new position was accepted; otherwise, the move was discarded. The results reported herein were calculated for $N = 700$ and $T = 0.12$. The energies and temperatures are reduced values expressed in the units of ε and $|\epsilon|/k$, respectively.

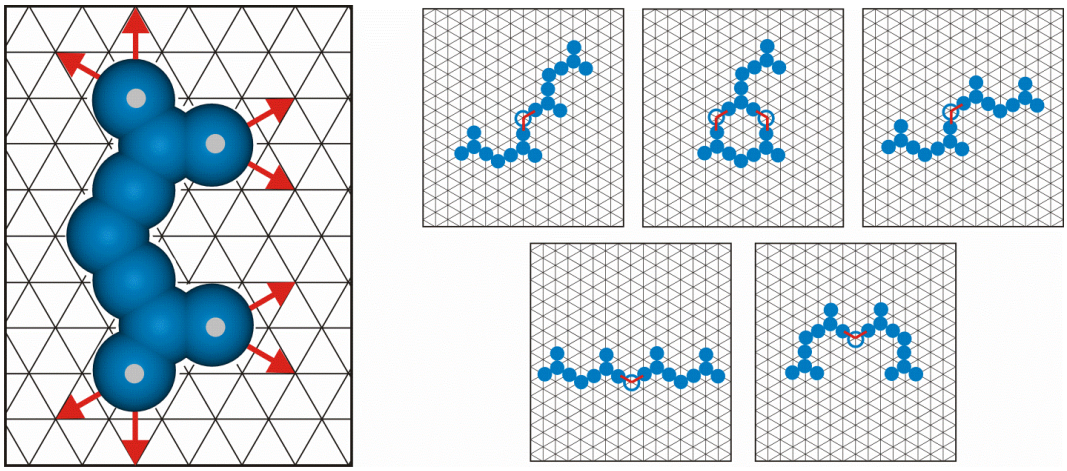

Figure C.2: (left) Schematic representation of the thioether linked dimer used as basic building block in MC simulations. Dimers consist of nine interconnected segments that represent the eight phenyl rings and the sulfur atom of the internal thioether linkage, respectively. Dimers can form intermolecular bonds at their four terminal segments (marked with gray dots) in the directions indicated by the red arrows. The right hand side depicts examples for allowed bond configurations between dimers featuring an overall bond angle of 120° (indicated by the red lines). Note that the sulfur atoms of the inter-dimer thioether linkages are not explicitly taken into account. However, all allowed bond configurations feature an empty lattice site at the position of the linking sulfur atom (marked by blue circles) that can be viewed as virtual sulfur atoms.

C.3 Supplementary STM Images

Owing to their intermediate bond strength, single S-Au-S linkages are still reversible even at room temperature. This gives rise to dynamic behavior and reconfigurations of the metal-organic structures:

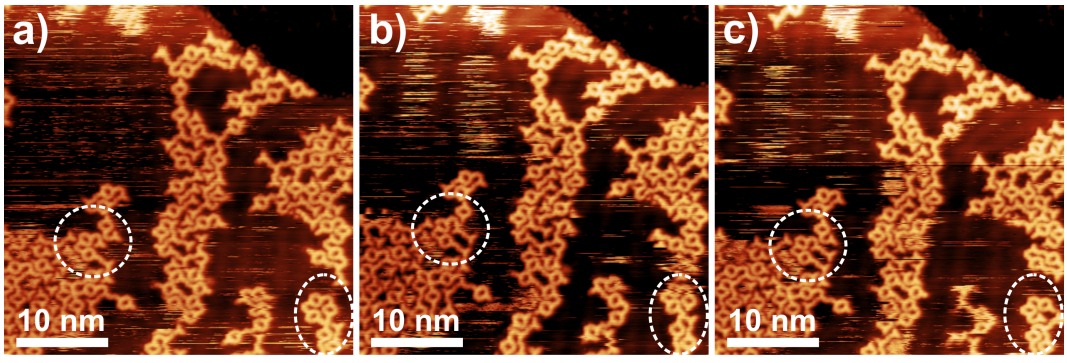

Figure C.3: (a) – (c) Series of subsequent STM images of TMB on Au(111) after room temperature deposition acquired from the same sample area (time per frame: ∼185 s, U_T = +1.39 V, I_T = 47 pA). The dashed ovals highlight areas with dynamic reconfigurations.

Sample annealing at 200 °C improved the order and resulted in extended type A and B chains. Type B chains showed a higher tendency for defect formation,

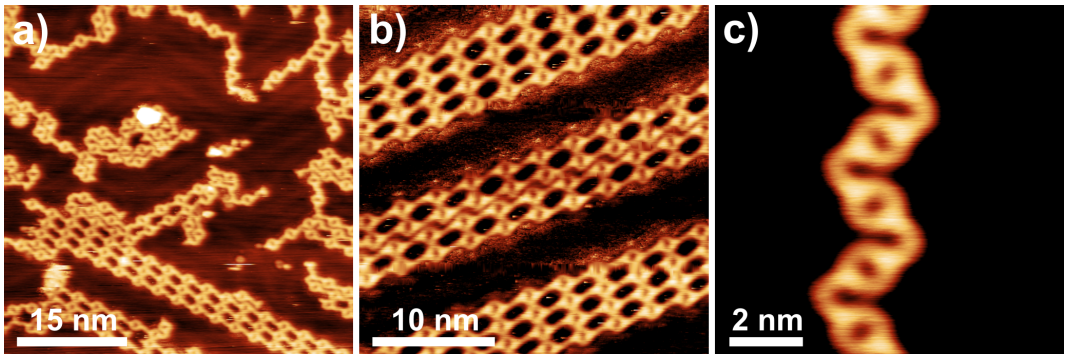

Figure C.4: STM images of TMB on Au(111) acquired after annealing at 200 °C. (a) Overview (U_T = +1.64 V, I_T = 38.0 pA). (b) Close-up of braided type A chains (U_T = +1.64 V, I_T = 37.9 pA). Interestingly, all four individual type A chains are in phase for the upper and lower braids. (c) Close-up of a defect free segment of a type B chain (U_T = +1.84 V, I_T = 37.6 pA).

whereas type A chains were mostly grouped into molecular braids that were aligned along the herringbone reconstruction.

However, annealing at 200 °C not only resulted in extended chains, but also in less regular aggregates and shorter chain segments. Those appeared either as separate entities or as groups of similarly oriented chains mostly at step-edges (as in Figure C.5(b)). Interestingly these aggregates locally modified the herringbone reconstruction, a further indication for involvement of Au adatoms.

Further sample annealing at 250 °C resulted in triangular structures on terraces and type C chains aligned along step-edges:

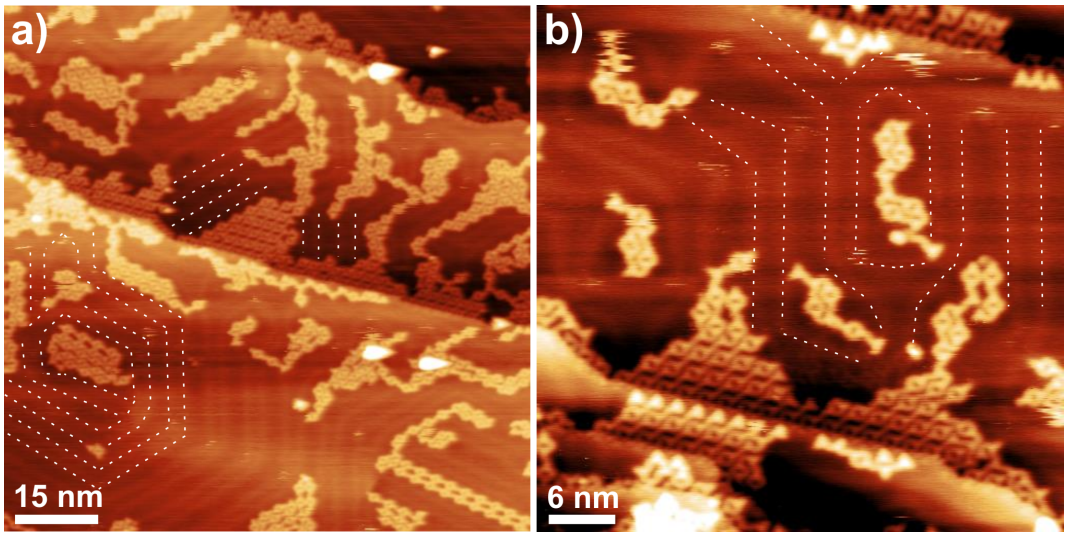

Figure C.5: STM images of TMB on Au(111) acquired after annealing at 200 °C. (a) Overview (U_T = +1.84 V, I_T = 37.3 pA). (b) Close-up (U_T = +1.67 V, I_T = 49.9 pA). The white dashed lines serve as guides to the eye and mark the soliton lines of the Au(111) herringbone reconstruction.

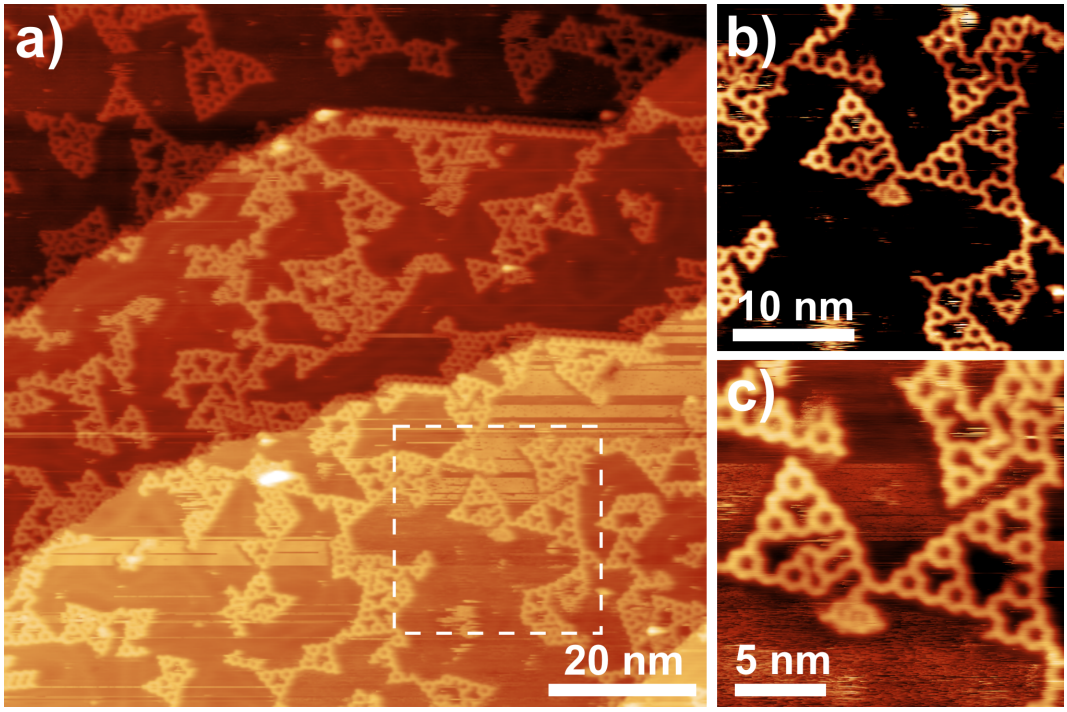

Figure C.6: STM images of TMB on Au(111) acquired after annealing at 250 °C. (a) Overview showing the alignment of type C chains along step-edges and STs on terraces (U_T = +1.47 V, I_T = 38.0 pA). (b) /(c) Close-ups (U_T = +1.67 V, I_T = 37.7 pA) of the area marked in (a) showing less well defined STs with defects.

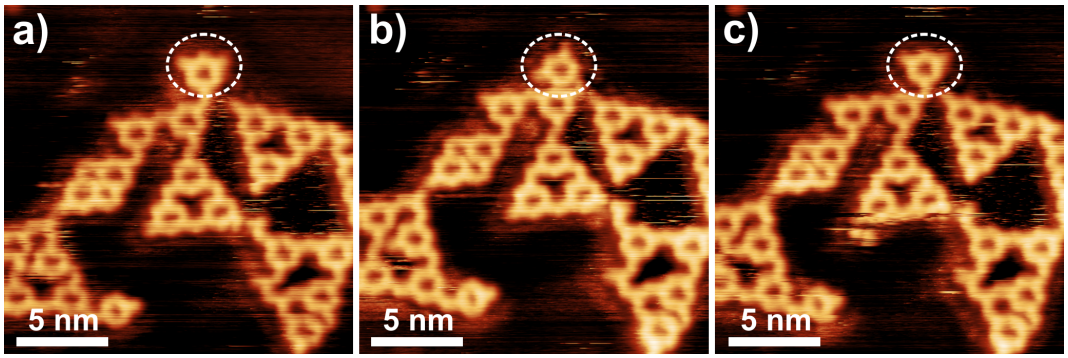

Figure C.7: (a) – (c) Series of sequential STM images of TMB on Au(111) acquired after annealing at 250 °C from the same sample area (time in between frames: ∼204 s, time per frame: ∼102 s; tunneling parameters: (a) U_T = +1.80 V, I_T = 38.7 pA; (b) U_T = +1.71 V, I_T = 39.7 pA; (c) U_T = +1.71 V, I_T = 38.7 pA. This series demonstrates orientational flexibility of a cyclic trimer that is attached to a larger aggregate. The nature of the linkage between trimer and larger aggregate is not entirely clear, but a slightly shorter bond length suggests a covalent C-S-C thioether linkage.

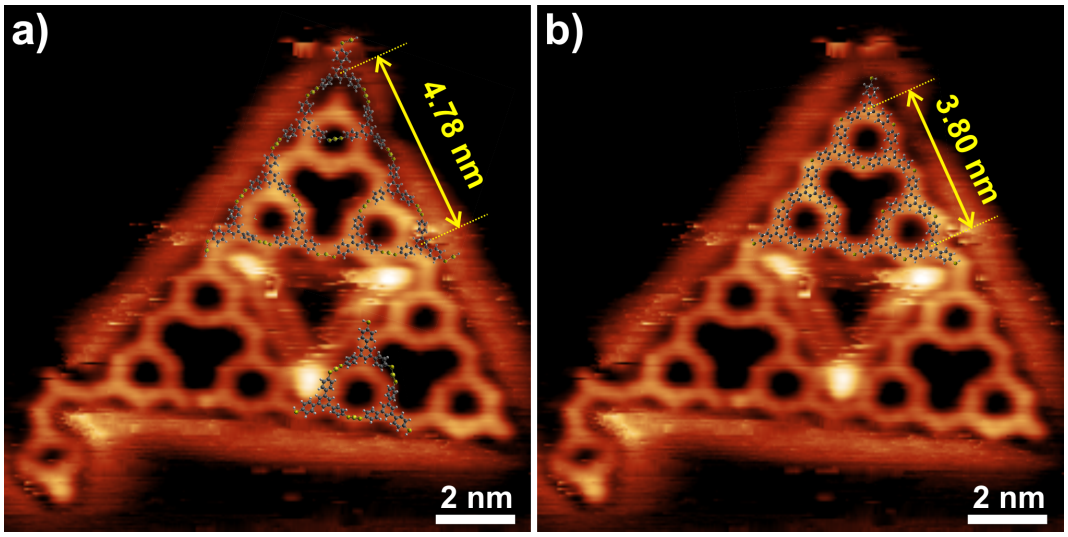

Figure C.8: STM image of a second generation ST acquired after room temperature deposition of TMB onto Au(111) and subsequent annealing to 250 °C (U_T = -1.63 V, I_T = 38.1 pA). The overlays represent DFT optimized geometries. (a) Scaled overlays with models based on coordinative S-Au-S linkages. Both the model of the zero generation ST in the lower half and the model of the first generation ST in the upper half exhibit a center-to-center distance of 1.59 nm between adjacent molecules. As evident from the overlay, these hypothetical metal-organic structures are significantly larger than the experimentally observed structures. (b) Scaled overlay with a model based on covalent C-S-C linkages. The covalent model of the first generation ST features a center-to-center distance of 1.27 nm between adjacent molecules, resulting in a perfect size and geometry match.

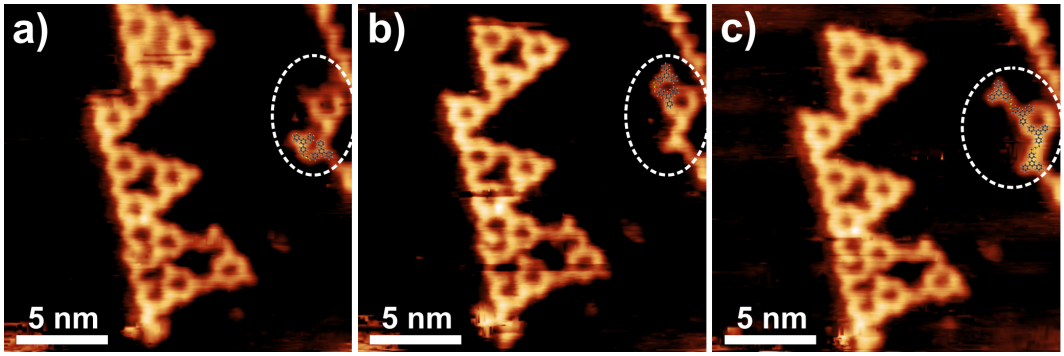

Figure C.9: (a) – (c) Series of sequential STM images of TMB on Au(111) acquired after annealing at 250 °C from the same sample area (time between frames: ∼204 s, time per frame: ∼102 s, U_T = +1.71 V, I_T = 39.8 pA). The covalent triangular structures on the left hand side do not change between the subsequent images and remain static, whereas the metal-organic structures on the right hand side exhibit dynamic reconfiguration. Provided that all intermediate steps were captured, the following processes were observed: a motif 3 dimer at the lower part decomposes; the released molecule first forms another motif 3 dimer at the upper part that subsequently transforms into a motif 2 dimer.

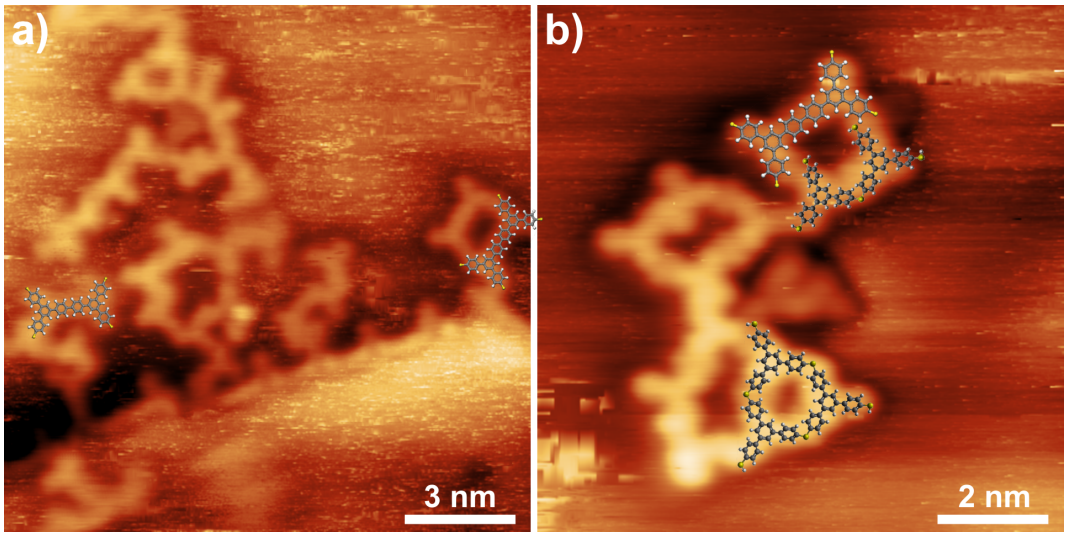

Figure C.10: STM images of TMB on Au(111) acquired after annealing at 300 °C from two independent experimental runs. (a) Scaled overlays with covalently C-C linked dimers yield a perfect size and geometry match (U_T = +1.0 V, I_T = 50 pA). (b) Zoom out of the STM image already shown in the section 6.3 as Figure 6.5(c) (U_T = +1.63 V, I_T = 39.1 pA). The structure directly underneath the covalently C-C linked dimer matches well with a thioether linked motif 4 dimer. The cyclic trimer at the lower right agrees very well with a covalent zero generation ST based on thioether linkages. The other structures cannot be fitted with these clearly identified motifs, and might thus represent chemically and structurally distinct linkages (e.g. disulfur bridges) that cannot unambiguously be identified solely based on STM images.

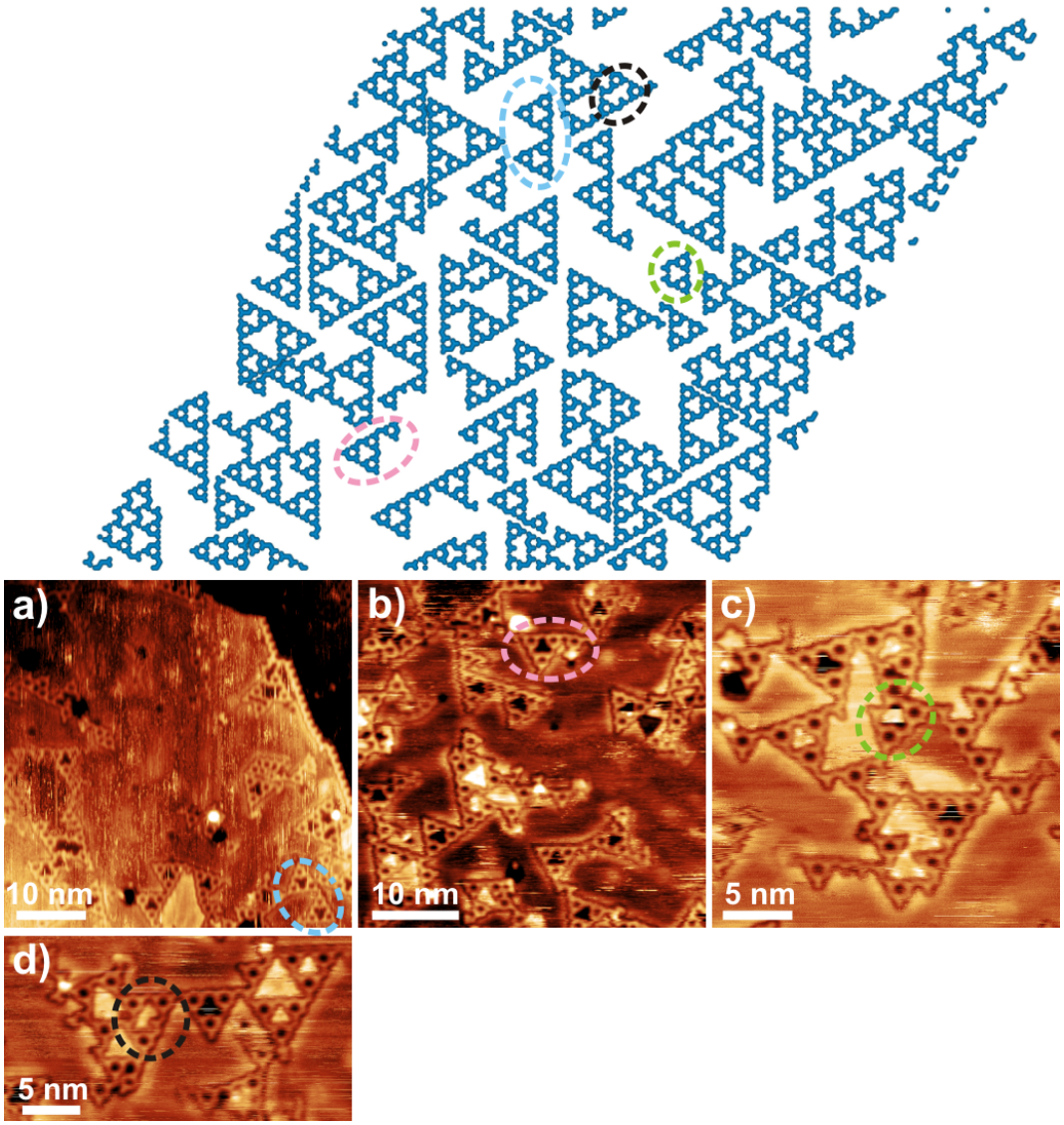

Figure C.11: Upper part: MC simulation based on dimers as basic building blocks. The sulfur atoms in the thioether linkages are not depicted for clarity. Lower part: STM images of TMB on Au(111) acquired after annealing at 230 °C. Tunneling parameters: (a) $U_T = +1.00$ V, $I_T = 40$ pA; (b) – (d) $U_T = +1.00$ V, $I_T = 50$ pA; The dashed ovals mark aggregates that were similarly observed in both experiment and simulation.

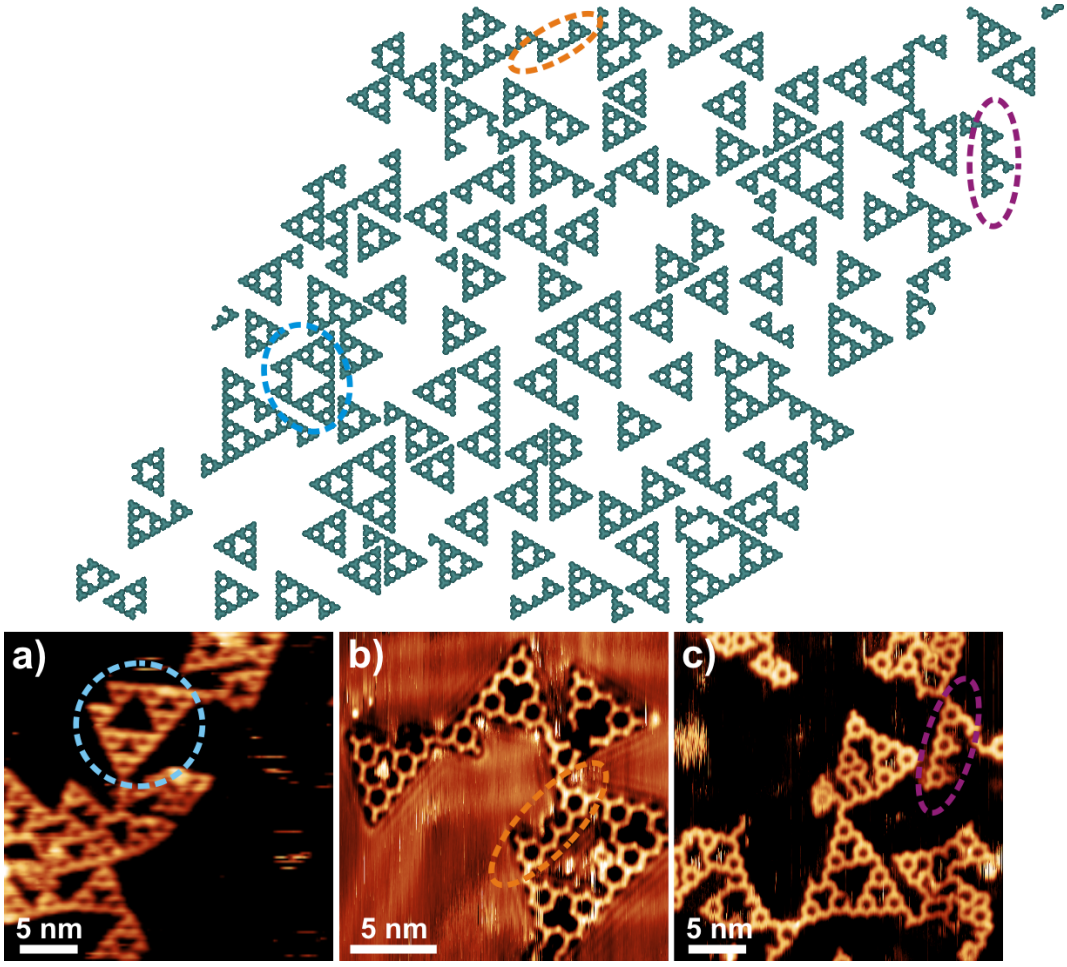

Figure C.12: Upper part: MC simulation based on monomers as basic building blocks. The sulfur atoms in the thioether linkages are not depicted for clarity. Lower part: STM images of TMB on Au(111) acquired after annealing at 250 °C. The MC simulations with monomers and dimers are essentially similar. However, for the monomer simulation the growing aggregates were not allowed to move or rotate anymore already from the dimer stage on. Tunneling parameters: (a) U_T = +1.69 V, I_T = 37.5 pA; (b) U_T = +1.6 V, I_T = 37.9 pA; (c) U_T = +1.67 V, I_T = 37.7 pA; The dashed ovals mark aggregates that were similarly observed in both experiment and simulation.

List of Abbreviations

2D	Two-dimensional
BIB	1,3-bis(*p*-bromophenyl)-5-(*p*-iodophenyl)benzene
CHP	Cyclohexa-*m*-phenylene
CVD	Chemical vapor deposition
DFT	Density functional theory
DIB	1,3-diiodobenzene
FAN	Fantrip
FWHM	Full-width at half-maximum
HOMO	Highest occupied molecular orbital
HREELS	High resolution electron energy loss spectroscopy
IRRAS	Infrared reflection-absorption spectroscopy
LUMO	Lowest unoccupied molecular orbital
MC	Monte Carlo
MO	Molecular orbital
NEXAFS	Near edge X-ray absorption fine structure
PDOS	Partial density of states
PEY	Partial electron yield
RT	Room temperature
SAM	Self-assembled monolayer
ST	Sierpiński triangles
STM	Scanning tunneling microscopy
STS	Scanning tunneling spectroscopy
TDM	Transition dipole moment
TERS	Tip-enhanced Raman spectroscopy

TEY	Total electron yield
TMB	1,3,5-tris(4-mercaptophenyl)benzene
ToF-SIMS	Time-of-flight secondary ion mass spectrometry
UHV	Ultra-high vacuum
w.r.t	with respect to
XPS	X-ray photoelectron spectroscopy
XRD	X-ray diffraction

List of Figures

2.1 Schematic of STM tunneling process 8
2.2 Energy level diagram for the emitted photoelectrons in XPS . . . 10
2.3 XP spectrum of the S 2p doublet 13
2.4 NEXAFS angle dependency of resonance intensities 17

3.1 Three geometrical configurations of benzene dimer 26
3.2 Bonding configurations of benzene dimers as idealized π-system . 27
3.3 Reaction scheme of anthracene dimerization 32

4.1 STM image of DIB on Cu(111) 35
4.2 Bias dependent STM imaging of DIB on Cu(111) 35
4.3 Side by side DFT calculations and STM image simulations of DIB on Cu(111) 36
4.4 DIB trimer orientation wrt iodine (STM image and DFT calculation) 37
4.5 STM images of mobility of DIB derivatives at domain edges . . . 39
4.6 STM images of emergence of cyclo hexamer in DIB on Cu(111) structures 39
4.7 STM images of collective movement of DIB derived trimer rows . 40
4.8 STM image of DIB complex structure on Cu(111) 41

5.1 XP spectra of I 3d and C 1s before and after iodination of BIB on Ag(111) 47
5.2 XP spectra of C 1s: Gaussian vs. Asymmetric fit 48
5.3 STM images of BIB netwroks on Ag(111) after iodination 50
5.4 STM images of two types of iodine superstructures on Ag(111) . . 51
5.5 Time series of STM images of iodine monolayer 51
5.6 Line profiles of STM image of BIB network absorbed on iodine or Ag(111) 52
5.7 DFT-optimized structure of a free-standing polyphenylene network and corresponding electron density contour plots of HOMO and LUMO 52
5.8 NEXAFS spectra of BIB networks on Ag(111) 53
5.9 Angle determination of BIB networks on Ag(111): before and after iodination 54
5.10 DFT geometries and PDOS of carbon atoms for *p*-terphenyl on pristine and iodine-terminated Ag(111) 55
5.11 Sharpening of C 1s NEXAFS spectra: BIB networks on Ag(111) . 56
5.12 STM images of BIB networks on Au(111) after RT iodination . . 60
5.13 XP spectra of I 3d before and after iodination of BIB on Au(111) 61

5.14 STM images of iodine vacancies mobility: BIB networks on Au(111) 62
5.15 Line profiles of STM image of BIB networks vs BIB monomers on iodine terminated Au(111) 63
5.16 XP spectra of C 1s before and after iodination of BIB on Au(111) 64
5.17 NEXAFS spectra of BIB networks on Au(111) 65
5.18 Angle determination of BIB networks on Au(111): before and after iodination 66
5.19 Sharpening of C 1s NEXAFS spectra: BIB networks on Au(111) . 66
5.20 XP spectra of I 3d and C 1s: before and after iodination and after annealing 67
5.21 STM images of BIB networks on Au(111) after hot iodination . . 68
5.22 STM images of BIB networks on Au(111) after hot iodination with overlayed iodine lattice 69
5.23 Line profiles of STM images of BIB networks on Au(111) for RT and hot iodination. 70
5.24 STM images of hot iodinated sample after annealing 71

6.1 STM images of TMB on Au(111) at RT 77
6.2 STM images of TMB on Au(111) after annealing at 200 °C 77
6.3 STM images of TMB on Au(111) after annealing at 250 °C 78
6.4 STM images of molecular zipper derived from TMB on Au(111) after annealing at 250 °C 80
6.5 STM images of TMB on Au(111) after annealing at 300 °C 80
6.6 XP spectra of S2p at RT and after annealing at 200, 250, and 300 °C: TMB on Au(111) 81
6.7 Gas phase DFT-optimized structures of various TMB motifs . . . 83
6.8 STM images of TMB on Au(111) after annealing at 250 °C: Coexistence of coordinative S-Au-S and covalent C-S-C linkages 86
6.9 MC simulation based on dimers: TMB on Au(111) 87

7.1 STM images of FAN on Au(111) 94
7.2 NEXAFS spectra of FAN on Au(111) 95
7.3 Angle determination of FAN on Au(111) 96
7.4 DFT adsorption geometries of FAN on Au(111) 97
7.5 NEXAFS spectra of FAN on iodine-terminated Au(111) 98
7.6 Angle determination of FAN on iodine-terminated Au(111) 99
7.7 STM images of FAN on iodine-terminated Au(111) 100
7.8 Schematic of topochemical photopolymerization of FAN self-assembly 102
7.9 STM images of FAN on iodine-terminated Au(111) after 10 min irradiation 103
7.10 STM image of FAN on iodine-terminated Au(111) after 60 min irradiation 105
7.11 STM images of FAN on iodine-terminated Au(111) after 15 and 30 min irradiation 105
7.12 Similarity of the FAN ordered structure on iodine-terminated Au(111) after 30 min irradiation with uncommon self-assembly of FAN on Au(111) 106
7.13 ToF-SIMS of FAN reference and irradiated samples 107

7.14 STM images of laser irradiated FAN on iodine-terminated Au(111): film vs. bulk single crystal 109

A.1 STM image of the DIB complex structure with corresponding line-profile 119
A.2 DFT optimized adsorption geometries of DIB iodinated trimers . 121
A.3 DFT optimized adsorption geometries of DIB diradicalic trimers . 122
A.4 STM image simulations of DIB iodinated trimers. 123
A.5 STM image simulations of DIB diradicalic trimers 124
A.6 Electron density difference plot of DIB diradicalic trimers 125
A.7 PDOS on the carbon atoms of the DIB diradicalic trimer in vacuum and on the surface 125
A.8 Atom-wise Bader charge analysis of the carbon atoms of the DIB diradicalic trimer and the two adsorbed iodine atoms bonded to the trimer 126
A.9 DFT optimized adsorption geometries of the benzene-1,3-diradical on Cu(111) 126
A.10 DFT optimized adsorption geometries of the benzene-1,3-diradical on Cu(110) 127

B.1 DFT-optimized adsorption geometries of terphenyl on pristine Ag(111) 130
B.2 DFT-optimized adsorption geometries of terphenyl on top of iodine terminated Ag(111) 130
B.3 DFT-optimized adsorption geometries of terphenyl on top of iodine terminated Ag(111) for various initial dihedral angles 131
B.4 Additional STM image of BIB networks on Au(111) after RT iodination 132
B.5 STM images of BIB networks on Au(111) with overlayed iodine lattice for RT vs. hot iodination 133
B.6 Additional STM images of BIB networks on Au(111) after hot iodination 133

C.1 DFT optimized S-Au-S linked motif 2 dimers on Au(111) 136
C.2 Schematic representation of boundary conditions of MC simulations 138
C.3 STM images of dynamic reconfigurations of TMB on Au(111) after RT deposition 138
C.4 STM images of TMB on Au(111) acquired after annealing at 200 °C 139
C.5 STM images of TMB modifying herringbone reconstruction 140
C.6 STM images of TMB on Au(111) acquired after annealing at 250 °C 140
C.7 Series of STM images demonstrating orientational flexibility of a cyclic trimer of TMB on Au(111) 141
C.8 STM images of a second generation ST with DFT overlays of S-Au-S and C-S-C linkages 141
C.9 Series of STM images of dynamic reconfiguration of metal-organic structures of TMB on Au(111) 142
C.10 STM images of TMB on Au(111) acquired after annealing at 300 °C with scaled overlays 142

C.11 MC simulation of TMB on Au(111) based on dimers and similar aggregates observed in STM images 143
C.12 MC simulation of TMB on Au(111) based on monomer and similar aggregates observed in STM image 144

List of Publications

1. Solvent-free on-surface synthesis of boroxine COF monolayers
   S. Spitzer, **A. Rastgoo-Lahrood**, K. Macknapp, V. Ritter, S. Sotier, W. M. Heckl and M. Lackinger, *Chem. Commun.*, DOI: 10.1039/c7cc01131h, 2017.

2. Reversible intercalation of iodine monolayers between on-surface synthesised covalent polyphenylene networks and Au(111)
   A. Rastgoo-Lahrood, M. Lischka, J. Eichhorn, D. Samanta, M. Schmittel, W. M. Heckl and M. Lackinger, *Nanoscale,* 9:4995-5001, 2017.

3. From Au—thiolate chains to thioether Sierpiski triangles: the versatile surface chemistry of 1,3,5-tris(4-mercaptophenyl)benzene on Au(111)
   A. Rastgoo-Lahrood, N. Martsinovich, M. Lischka, J. Eichhorn, P. Szabelski, D. Nieckarz, T. Strunskus, K. Das, M. Schmittel, W. M. Heckl and M. Lackinger, *ACS Nano,* 10:10901-10911, 2016.

4. Post-synthetic decoupling of on-surface-synthesized covalent nanostructures from Ag(111)
   A. Rastgoo-Lahrood, J. Björk, M. Lischka, J. Eichhorn, S. Kloft, M. Fritton, T. Strunskus, D. Samanta, M. Schmittel, W. M. Heckl and M. Lackinger, *Angew. Chem. Int. Ed.,* 55:7650-7654, 2016.

5. 1,3-Diiodobenzene on Cu(111) – an exceptional case of on-surface Ullmann coupling
   A. Rastgoo-Lahrood, J. Björk, W. M. Heckl and M. Lackinger, *Chem. Commun.,* 51:13301-13304, 2015.

6. On-surface Ullmann polymerization via intermediate organometallic networks on Ag(111)
   J. Eichhorn, T. Strunskus, **A. Rastgoo-Lahrood**, D. Samanta, M. Schmittel, and M. Lackinger, *Chem. Commun.,* 50:7680-7682, 2014.

7. From benzenetrithiolate self-assembly to copper-sulfide adlayers on Cu(111): temperature-induced irreversible and reversible phase transitions
   T. Sirtl, M. Lischka, J. Eichhorn, **A. Rastgoo-Lahrood**, T. Strunskus, W. M. Heckl, and M. Lackinger, *J. Phys. Chem. C,* 118(7):3590-3598, 2014.

8. Control of intermolecular bonds by deposition rates at room temperature: hydrogen bonds vs. metal-coordination in trinitrile monolayers
   T. Sirtl, S. Schlögl, **A. Rastgoo-Lahrood**, J. Jelic, S. Neogi, M. Schmittel, W. M. Heckl, K. Reuter, and M. Lackinger, *J. Am. Chem. Soc.,* 135:691-695, 2013.

9. X-ray photoelectron spectroscopy on implanted argon as a tool to follow local structural changes in thin films
   A. Rastgoo-Lahrood, T. de los Arcos , M. Prenzel, A. von Keudell, and J. Winter, *Thin Solid Films*, 520:1625–1630, 2011.

Bibliography

[1] A. Gourdon. On-surface covalent coupling in ultrahigh vacuum. *Angew. Chem. Int. Ed.*, 47:6950–6953, 2008.

[2] M. Lackinger and W. M. Heckl. A STM perspective on covalent intermolecular coupling reactions on surfaces. *J. Phys. D: Appl. Phys.*, 44:464011, 2011.

[3] R. Lindner and A. Kühnle. On-surface reactions. *ChemPhysChem*, 16(8):1582–1592, 2015.

[4] F. Klappenberger, Y. Q. Zhang, J. Björk, S. Klyatskaya, M. Ruben, and J. V. Barth. On-surface synthesis of carbon-based scaffolds and nanomaterials using terminal alkynes. *Acc. Chem. Res.*, 48:2140–2150, 2015.

[5] D. F. Perepichka and F. Rosei. Extending polymer conjugation into the second dimension. *Science*, 323:216–217, 2009.

[6] J. W. Colson and W. R. Dichtel. Rationally synthesized two-dimensional polymers. *Nat. Chem.*, 5:453–465, 2013.

[7] J. M. Cai, P. Ruffieux, R. Jaafar, M. Bieri, T. Braun, S. Blankenburg, M. Muoth, A. P. Seitsonen, M. Saleh, X. L. Feng, K. Müllen, and R. Fasel. Atomically precise bottom-up fabrication of graphene nanoribbons. *Nature*, 466:470–473, 2010.

[8] J. A. Lipton-Duffin, J. A. Miwa, M. Kondratenko, F. Cicoira, B. G. Sumpter, V. Meunier, D. F. Perepichka, and F. Rosei. Step-by-step growth of epitaxially aligned polythiophene by surface-confined reaction. *Proc. Natl. Acad. Sci. USA*, 107:11200–11204, 2010.

[9] R. Gutzler, H. Walch, G. Eder, S. Kloft, W. M. Heckl, and M. Lackinger. Surface mediated synthesis of 2D covalent organic frameworks: 1,3,5-tris(4-bromophenyl)benzene on graphite(001), Cu(111), and Ag(110). *Chem. Commun.*, pages 4456–4458, 2009.

[10] L. Grill, M. Dyer, L. Lafferentz, M. Persson, M. V. Peters, and S. Hecht. Nano-architectures by covalent assembly of molecular building blocks. *Nat. Nanotechnol.*, 2:687–691, 2007.

[11] M. Kittelmann, P. Rahe, M. Nimmrich, C. M. Hauke, A. Gourdon, and A. Kühnle. On-surface covalent linking of organic building blocks on a bulk insulator. *ACS Nano*, 5:8420–8425, 2011.

[12] C. Morchutt, J. Björk, S. Krotzky, R. Gutzler, and K. Kern. Covalent coupling via dehalogenation on Ni(111) supported boron nitride and graphene. *Chem. Commun.*, 51:2440–2443, 2015.

[13] J. C. Love, L. A. Estroff, J. K. Kriebel, R. G. Nuzzo, and G. M. Whitesides. Self-assembled monolayers of thiolates on metals as a form of nanotechnology. *Chem. Rev.*, 105:1103–1169, 2005.

[14] C. Vericat, M. E. Vela, and R. C. Salvarezza. Self-assembled monolayers of alkanethiols on Au(111): surface structures, defects and dynamics. *Phys. Chem. Chem. Phys.*, 7:3258–3268, 2005.

[15] P. Kissel, D. J. Murray, W. J. Wulftange, V. J. Catalano, and B. T. King. A nanoporous two-dimensional polymer by single-crystal-to-single-crystal photopolymerization. *Nat. Chem.*, 6:774–778, 2014.

[16] D. M. Eigler and E. K. Schweizer. Positioning single atoms with a scanning tunneling microscope. *Nature*, 344:524–526, 1990.

[17] J. V. Barth. Molecular architectonic on metal surfaces. *Annu. Rev. Phys. Chem.*, 58:375–407, 2007.

[18] G. Binnig, H. Rohrer, C. Gerber, and E. Weibel. 7x7 reconstruction on Si(111) resolved in real space. *Phys. Rev. Lett.*, 50:120–123, 1983.

[19] C. J. Chen. *Introduction to Scanning Tunneling Microscopy.* Oxford University Press, 1993.

[20] N. Yao and Z. Wang. *Handbook of microscopy for nanotechnology.* Springer, 2005.

[21] I.S. Tilinin, M.K. Rose, J.C. Dunphy, M. Salmeron, and M.A. Van Hove. Identification of adatoms on metal surfaces by STM: experiment and theory. *Surf. Sci.*, 418(3):511–520, 1998.

[22] W. A. Hofer. Challenges and errors: interpreting high resolution images in scanning tunneling microscopy. *Prog. Surf. Sci.*, 71:147–183, 2003.

[23] M.-L. Bocquet, J. Cerdà, and P. Sautet. Transformation of molecular oxygen on a platinum surface: A theoretical calculation of STM images. *Phys. Rev. B*, 59:15437–15445, Jun 1999.

[24] P. H. Lippel, R. J. Wilson, M. D. Miller, Ch. Wöll, and S. Chiang. High-resolution imaging of copper-phthalocyanine by scanning-tunneling microscopy. *Phys. Rev. Lett.*, 62:171–174, Jan 1989.

[25] Thomas Müller. *Scanning Tunneling Microscopy of Physisorbed Monolayers: From Self-Assembly to Molecular Devices*, pages 1–30. Springer Berlin Heidelberg, Berlin, Heidelberg, 2007.

[26] J. Tersoff and D. Hamann. Theory and application for the scanning tunneling microscope. *Phys. Rev. Lett.*, 50:1998–2001, 1983.

[27] J. Bardeen. Tunnelling from a many-particle point of view. *Phys. Rev. Lett.*, 6:57–59, Jan 1961.

[28] M. Büttiker, Y. Imry, R. Landauer, and S. Pinhas. Generalized many-channel conductance formula with application to small rings. *Phys. Rev. B*, 31:6207–6215, May 1985.

[29] Y. Meir and N. S. Wingreen. Landauer formula for the current through an interacting electron region. *Phys. Rev. Lett.*, 68:2512–2515, Apr 1992.

[30] O. M. Ochs. Entwicklung eines ultrahochvakuumtauglichen Raster-Tunnel-Mirkroskops und integration in eine bestehende vakuumanlage. Master thesis, University of applied sciences Munich, 2013.

[31] C. D. Wagner, W. M. Riggs, L. E. Davis, and J. F. Moulder. *Handbook of X-ray photoelectron spectroscopy.* Perkin-Elmer Corporation, 1978.

[32] M. Grasserbauer, H. J. Dudek, and M. F. Ebel. *Angewandte Oberflächenanalyse mit SIMS, AES und XPS.* Springer-Verlag Berlin Heidelberg, 1986.

[33] W. Demtröder. *Atoms, molecules and photons: an introduction to atomic-, molecular- and quantum physics.* Graduate Texts in Physics. Springer, 2010.

[34] E. Merzbacher. *Quantum Mechanics.* John Wiley & Sons, 1998.

[35] P. Van der Heide. *X-ray photoelectron spectroscopy: an introduction to principles and practices.* John Wiley & Sons, 2012.

[36] Helmholtz Center Berlin for Materials and Energy GmbH. *HE-SGM beamline.* http://www.helmholtz-berlin.de (2017/01/17).

[37] VG Scienta. *ELECTRON SPECTROMETER SCIENTA R3000.* http://www.scientaomicron.com/ (2017/01/17).

[38] Georg Hähner. Near edge X-ray absorption fine structure spectroscopy as a tool to probe electronic and structural properties of thin organic films and liquids. *Chem. Soc. Rev.*, 35:1244–1255, 2006.

[39] M. Klues, K. Hermann, and G. Witte. Analysis of the Near-Edge X-ray-Absorption Fine-Structure of anthracene: A combined theoretical and experimental study. *J. Chem. Phys.*, 140:014302–9, 2014.

[40] K. A. Simonov, N. A. Vinogradov, A. S. Vinogradov, A. V. Generalov, E. M. Zagrebina, N. Martensson, A. A. Cafolla, T. Carpy, J. P. Cunniffe, and A. B. Preobrajenski. Effect of substrate chemistry on the bottom-up fabrication of graphene nanoribbons: Combined core-level spectroscopy and STM study. *J. Phys. Chem. C*, 118:12532–12540, 2014.

[41] J. Stöhr. *NEXAFS Spectroscopy.* Springer, Berlin, 1992.

[42] K. Weiss, S. Gebert, M. Wühn, H. Wadepohl, and Ch. Wöll. Near edge X-ray absorption fine structure study of benzene adsorbed on metal surfaces: Comparison to benzene cluster complexes. *J. Vac. Sci. Technol. A*, 16:1017–1022, 1998.

[43] D. Hübner, F. Holch, M.L.M. Rocco, K.C. Prince, S. Stranges, A. Schöll, E. Umbach, and R. Fink. Isotope effects in high-resolution NEXAFS spectra of naphthalene. *Chem. Phys. Lett.*, 415:188–192, 2005.

[44] C. Joachim, J. K. Gimzewski, and A. Aviram. Electronics using hybrid-molecular and mono-molecular devices. *Nature*, 408:541–548, 2000.

[45] J. R. Heath and M. A. Ratner. Molecular electronics. *Phys. Today*, 56:43–49, 2003.

[46] T. Kudernac, S. B. Lei, J. A. A. W. Elemans, and S. De Feyter. Two-dimensional supramolecular self-assembly: nanoporous networks on surfaces. *Chem. Soc. Rev.*, 38:402–421, 2009.

[47] M. Di Giovannantonio and et al. Insight into organometallic intermediate and its evolution to covalent bonding in surface-confined ullmann polymerization. *ACS Nano*, 7:8190–8198, 2013.

[48] M. Bieri, M. T. Nguyen, O. Groning, J. M. Cai, M. Treier, K. Ait-Mansour, P. Ruffieux, C. A. Pignedoli, D. Passerone, M. Kastler, K. Müllen, and R. Fasel. Two-dimensional polymer formation on surfaces: Insight into the roles of precursor mobility and reactivity. *J. Am. Chem. Soc.*, 132:16669–16676, 2010.

[49] A. Nitzan and M.A. Ratner. Electron transport in molecular wire junctions. *Science*, 300:1384–1389, 2003.

[50] L. Lafferentz, F. Ample, H. Yu, S. Hecht, C. Joachim, and L. Grill. Conductance of a single conjugated polymer as a continuous function of its length. *Science*, 323:1193–1197, 2009.

[51] M. Koch, F. Ample, C. Joachim, and L. Grill. Voltage-dependent conductance of a single graphene nanoribbon. *Nature Nanotech.*, 7:713–717, 2012.

[52] L.F. Lindoy and I.M. Atkinson. *Self assembly in supramolecular systems.* The Royal Society of Chemistry, 2000.

[53] D.S. Lawrence, T. Jiang, and M. Levett. Self-assembling supramolecular complexes. *Chem. Rev.*, 95:2229–2260, 1995.

[54] G.R. Desiraju. *The Crystal as a Supramulecular Entity.* Wiley, 1996.

[55] P Espinet, M. A. Esteruelas, L. A. Oro, J. L. Serrano, and E. Sola. Transition-metal liquid-crystals - advanced materials within the reach of the coordination chemist. *Coord. Chem. Rev.*, 117:215–274, 1992.

[56] R. Bissell and N. Boden. Liquid-crystals display new potential. *Chem. Br.*, 31:38–41, 1995.

[57] J. P. Collin, P. Gavina, V. Heitz, and J.-P. Sauvage. Construction of one-dimensional multicomponent molecular arrays: Control of electronic and molecular motions. *Eur. J. Inorg. Chem.,*, pages 1–14, 1998.

[58] C. J. Jones. Transition metals as structural components in the construction of molecular container. *Chem. Soc. Rev.*, 27:289–299, 1998.

[59] C. D. Bain and S. D. Evans. Laying it on thin. *Chem. Br.*, 31:46–48, 1995.

[60] A. Kühnle. Self-assembly of organic molecules at metal surfaces. *Curr. Opin. Colloid Interface Sci.*, 14:157–168, 2009.

[61] L. Bartels. Tailoring molecular layers at metal surfaces. *Nat. Chem.*, 2:87–95, 2010.

[62] R. Otero, J. M. Gallego, A. L. Vázquez de Parga, N. Martin, and R. Miranda. Molecular self-assembly at solid surfaces. *Adv. Mater.*, 23:5148–5176, 2011.

[63] H. Walch, J. Dienstmaier, G. Eder, R. Gutzler, S. Schlögl, T. Sirtl, K. Das, M. Schmittel, and M. Lackinger. Extended two-dimensional metal-organic frameworks based on thiolate-copper coordination bonds. *J. Am. Chem. Soc.*, 133:7909–7915, 2011.

[64] A. Rastgoo-Lahrood, N. Martsinovich, M. Lischka, J. Eichhorn, P. Szabelski, D. Nieckarz, T. Strunskus, K. Das, M. Schmittel, W. M. Heckl, and M. Lackinger. From Au-thiolate chains to thioether Sierpiński triangles: The versatile surface chemistry of 1,3,5-tris(4-mercaptophenyl)benzene on Au(111). *ACS Nano*, 10:10901–10911, 2016.

[65] B. Hammer and J. K. Norskov. Why gold is the noblest of all the metals. *Nature*, 376:238–240, 1995.

[66] B. Hammer and J. K. Norskov. Electronic factors determining the reactivity of metal surfaces. *Surf. Sci.*, 343:211–220, 1995.

[67] B. Hammer and J. K. Norskov. Theoretical surface science and catalysis calculations and concepts. *Advances in Catalysis*, 45:71–129, 2000.

[68] T. Classen, G. Fratesi, G. Costantini, S. Fabris, F. L. Stadler, C. Kim, S. de Gironcoli, S. Baroni, and K. Kern. Templated growth of metal-organic coordination chains at surfaces. *Angew. Chem. Int. Ed.*, 44:6142–6145, 2005.

[69] N. Lin, A. Dmitriev, J. Weckesser, J. V. Barth, and K. Kern. Real-time single-molecule imaging of the formation and dynamics of coordination compounds. *Angew. Chem. Int. Ed.*, 41:4779–4783, 2002.

[70] G.C. Maitland, M. Rigby, E.B. Smith, and W.A. Wakeham. *Intermolecular Forces: Their Origin and Determination.* Oxford University Press, 1981.

[71] A.D. Buckingham, A.C. Legon, and S.M. Robers, editors. *Principles of Molecular Recognition*. Blackie Academic & Professional, 1993.

[72] N.W. Alcock. *Bonding and Structure*. Ellis-Horwood, 1990.

[73] F. L. Leite, C. C. Bueno, A. L. Da Róz, E. C. Ziemath, and O. N. Oliveira. Theoretical models for surface forces and adhesion and their measurement using atomic force microscopy. *Int. J. Mol. Sci.*, 13:12773–12856, 2012.

[74] E. V. Anslyn and D. A. Dougherty. *Modern Physical Organic Chemistry*. University Science Books, 2004.

[75] M. O. Sinnokrot, E. F. Valeev, and C. D. Sherrill. Estimates of the ab initio limit for π-π interactions: The benzene dimer. *J. Am. Chem. Soc.*, 124, 2002.

[76] C. A. Hunter, J. Singh, and J. M. Thornton. π-π interactions: the geometry and energetics of phenylalanine-phenylalanine interactions in proteins. *J. Mol. Biol.*, 218:837–846, 1991.

[77] T. Dahl. The nature of stacking interactions between organic molecules elucidated by analysis of crystal structures. *Acta Chem. Scand.*, 48:95–106, 1994.

[78] C. A. Hunter and J. K. M. Sanders. The nature of π-π interactions. *J. Am. Chem. Soc.*, 112:5525, 1990.

[79] R. K. Raju, J. W. G. Bloom, Y. An, and S. E. Wheeler. Substituent effects on non-covalent interactions with aromatic rings: Insights from computational chemistry. *Chemphyschem*, 12:3116–3130, 2011.

[80] P. Messina, A. Dmitriev, N. Lin, H. Spillmann, M. Abel, J. V. Barth, and K. Kern. Direct observation of chiral metal-organic complexes assembled on a Cu(100) surface. *J. Am. Chem. Soc.*, 124:14000–14001, 2002.

[81] N. Lin, S. Stepanow, F. Vidal, K. Kern, M. S. Alam, S. Strömsdörfer, V. Dremov, P. Müller, A. Landa, and M. Ruben. Surface-assisted coordination chemistry and self-assembly. *Dalton Trans.*, 0:2794–2800, 2006.

[82] T. Sirtl, M. Lischka, J. Eichhorn, A. Rastgoo-Lahrood, T. Strunskus, W. M. Heckl, and M. Lackinger. From benzenetrithiolate self-assembly to copper sulfide adlayers on Cu(111): Temperature-induced irreversible and reversible phase transitions. *J. Phys. Chem. C*, 118(111):3590–3598, 2014.

[83] U. Schlickum, F. Klappenberger, R. Decker, G. Zoppellaro, S. Klyatskaya, M. Ruben, K. Kern, H. Brune, and J. V. Barth. Surface-confined metal-organic nanostructures from co-directed assembly of linear terphenyl-dicarbonitrile linkers on Ag(111). *J. Phys Chem. C*, 114:15602–15606, 2010.

[84] T. Sirtl, S. Schlögl, A. Rastgoo-Lahrood, J. Jelic, S. Neogi, M. Schmittel, W. M. Heckl, K. Reuter, and M. Lackinger. Control of intermolecular bonds by deposition rates at room temperature: hydrogen bonds versus metal coordination in trinitrile monolayers. *J. Am. Chem. Soc.*, 135:691–695, 2013.

[85] N. N. Greenwood and A. Earnshaw. *Chemistry of the elements*. Pergamon Press, Oxford Oxfordshire; New York, 1984.

[86] N. Lin, S. Stepanow, M. Ruben, and J. V. Barth. Surface-confined supramolecular coordination chemistry. *Top Curr Chem*, 287:1–44, 2008.

[87] S. L. Tait, A. Langner, N. Lin, S. Stepanow, C. Rajadurai, M. Ruben, and K. Kern. One-dimensional self-assembled molecular chains on Cu(100): Interplay between surface-assisted coordination chemistry and substrate commensurability. *J. Phys. Chem. C*, 111:10982–10987, 2007.

[88] P. Maksymovych, D. C. Sorescu, and J. T. Yates. Gold-adatom-mediated bonding in self-assembled short-chain alkanethiolate species on the Au(111) surface. *Phys. Rev. Lett.*, 97:146103, 2006.

[89] J. V. Barth, H. Brune, G. Ertl, and R. J. Behm. Scanning tunneling microscopy observations on the reconstructed Au(111) surface: Atomic structure, long-range superstructure, rotational domains, and surface defects. *Phys. Rev. B*, 42:9307–9318, 1990.

[90] J. N. Israelachvili. *Intermolecular and surface forces*. Academic Press, 2011.

[91] K. P. C. Vollhardt and N. E. Schore. *Organic Chemistry: Structure and Function*. Clancy Marshall, 1999.

[92] T. Okuyama and H. Maskill. *Organic chemistry: a mechanistic approach*. OUP Oxford, 2013.

[93] A. P. Côté, A. I. Benin, N. W. Ockwig, M. O'Keeffe, A. J. Matzger, and O. M. Yaghi. Porous, crystalline, covalent organic frameworks. *Science*, 310:1166–1170, 2005.

[94] S. Weigelt, C. Busse, C. Bombis, M. M. Knudsen, K. V. Gothelf, T. Strunskus, C. Woll, M. Dahlbom, B. Hammer, E. Laegsgaard, F. Besenbacher, and T. R. Linderoth. Covalent interlinking of an aldehyde and an amine on a Au(111) surface in ultrahigh vacuum. *Angew. Chem. Int. Ed.*, 46:9227–9230, 2007.

[95] F. Ullmann and J. Bielecki. Über synthesen in der biphenylreihe. *Ber. Dtsch. Chem. Ges.*, 34:2174–2185, 1901.

[96] F. Ullmann, G. Meyer, O. Loewenthal, and E. Gilli. über symmetrische biphenylderivate. *Justus Liebigs Ann. Chem.*, 332:38–81, 1904.

[97] M. Xi and B. E. Bent. Iodobenzene on Cu(111): Formation and coupling of adsorbed phenyl groups. *Surf. Sci.*, 278, 1992.

[98] M. Xi and B. E. Bent. Mechanisms of the Ullmann coupling reaction in adsorbed monolayers. *J. Am. Chem. Soc.*, 115:7426–7433, 1993.

[99] M. M. Blake, S. U. Nanayakkara, S. A. Claridge, L. C. Fernandez-Torres, E. C. H. Sykes, and P. S. Weiss. Identifying reactive intermediates in the Ullmann coupling reaction by scanning tunneling microscopy and spectroscopy. *J. phys. Chem. A*, 113:13167–13172, 2009.

[100] J. Eichhorn, T. Strunskus, A. Rastgoo-Lahrood, D. Samanta, M. Schmittel, and M. Lackinger. On-surface Ullmann polymerization via intermediate organometallic networks on Ag(111). *Chem. Commun.*, 50:7680–7682, 2014.

[101] H. Walch, R. Gutzler, T. Sirtl, G. Eder, and M. Lackinger. Material- and orientation-dependent reactivity for heterogeneously catalyzed carbon-bromine bond homolysis. *J. Phys. Chem. C*, 114:12604–12609, 2010.

[102] M. O. Blunt, J. C. Russell, N. R. Champness, and P. H. Beton. Templating molecular adsorption using a covalent organic framework. *Chem. Commun.*, 46:7157–7159, 2010.

[103] J. Eichhorn, D. Nieckarz, O. Ochs, D. Samanta, M. Schmittel, P. J. Szabelski, and M. Lackinger. On-surface Ullmann coupling: The influence of kinetic reaction parameters on the morphology and quality of covalent networks. *ACS Nano*, 8:7880–7889, 2014.

[104] G. W. Breton and X. Vang. Photodimerisation of anthracene: A $[4\pi_s+4\pi_s]$ photochemical cycloaddition. *J. Chem. Educ.*, 75:81–82, 1998.

[105] R. B. Woodward and Roald Hoffmann. Stereochemistry of electrocyclic reactions. *J. Am. Chem. Soc.*, 87:395–397, 1965.

[106] J. Clayden, N. Greeves, S. Warren, and Wothers P. *Organic chemistry*. Oxford University Press, 2001.

[107] H. Bouas-Laurent, A. Castellan, J-P. Desvergne, and R. Lapouyade. Photodimerization of anthracenes in fluid solution: structural aspects. *Chem. Soc. Rev.*, 29:43–55, 2000.

[108] H. D. Becker. Unimolecular photochemistry of anthracenes. *Chem. Rev.*, 93:145–172, 1993.

[109] V. R. Sastri, R. Schulman, and D. C. Roberts. Poly(7,16-dihydroheptacenes): a new type of obligate ladder polymer conformationally restricted to two dimensions. *Macromolecules*, 15:939–947, 1982.

[110] G. M. J. Schmidt. Photodimerization in the solid state. *Pure Appl. Chem.*, 27:647–678, 1971.

[111] J. Björk, F. Hanke, and S. Stafstrom. Mechanisms of halogen-based covalent self-assembly on metal surfaces. *J. Am. Chem. Soc.*, 135:5768–5775, 2013.

[112] S. Schlögl, W. M. Heckl, and M. Lackinger. On-surface radical addition of triply iodinated monomers on Au(111) - the influence of monomer size and thermal post-processing. *Surf. Sci.*, 606:999–1004, 2012.

[113] J. A. Lipton-Duffin, O. Ivasenko, D. F. Perepichka, and F. Rosei. Synthesis of polyphenylene molecular wires by surface-confined polymerization. *Small*, 5:592–597, 2009.

[114] M. Bieri, S. Blankenburg, M. Kivala, C. A. Pignedoli, P. Ruffieux, K. Müllen, and R. Fasel. Surface-supported 2D heterotriangulene polymers. *Chem. Commun.*, 47:10239–10241, 2011.

[115] Q. Fan, C. Wang, Y. Han, J. Zhu, J. Kuttner, G. Hilt, and J. M. Gottfried. Surface-assisted formation, assembly, and dynamics of planar organometallic macrocycles and zigzag shaped polymer chains with C-Cu-C bonds. *ACS Nano*, 8:709–718, 2014.

[116] P. H. Citrin, P. Eisenberger, and R. C. Hewitt. Adsorption sites and bond lengths of iodine on Cu(111) and Cu(100) from surface extended X-Ray-absorption fine structure. *Phys. Rev. Lett.*, 45:1948–1951, 1980.

[117] E. C. H. Sykes, P. Han, S. A. Kandel, K. F. Kelly, G. S. McCarty, and P. S. Weiss. Substrate-mediated interactions and intermolecular forces between molecules adsorbed on surfaces. *Acc. Chem. Res.*, 36:945–953, 2003.

[118] L. Lafferentz, V. Eberhardt, C. Dri, C. Africh, G. Comelli, F. Esch, S. Hecht, and L. Grill. Controlling on-surface polymerization by hierarchical and substrate-directed growth. *Nat. Chem.*, 4:215–220, 2012.

[119] R. Gutzler, L. Cardenas, J. Lipton-Duffin, M. El Garah, L. E. Dinca, C. E. Szakacs, C. Y. Fu, M. Gallagher, M. Vondracek, M. Rybachuk, D. F. Perepichka, and F. Rosei. Ullmann-type coupling of brominated tetrathienoanthracene on copper and silver. *Nanoscale*, 6:2660–2668, 2014.

[120] G. Eder, E. F. Smith, I. Cebula, W. M. Heckl, P. H. Beton, and M. Lackinger. Solution preparation of two-dimensional covalently linked networks by polymerization of 1,3,5-tri(4-iodophenyl)benzene on Au(111). *ACS Nano*, 7:3014–3021, 2013.

[121] Q. T. Fan, J. M. Gottfried, and J. F. Zhu. Surface-catalyzed C-C covalent coupling strategies toward the synthesis of low-dimensional carbon-based nanostructures. *Acc. Chem. Res.*, 48:2484–2494, 2015.

[122] C. Mattevi, H. Kim, and M. Chhowalla. A review of chemical vapour deposition of graphene on copper. *J. Mater. Chem.*, 21:3324–3334, 2011.

[123] M. B. Wieland, A. G. Slater, B. Mangham, N. R. Champness, and P. H. Beton. Fullerenes as adhesive layers for mechanical peeling of metallic, molecular and polymer thin films. *Beilstein J. Nanotechnol.*, 5:394–401, 2014.

[124] A. Rastgoo Lahrood, J. Björk, W. M. Heckl, and M. Lackinger. 1,3-diiodobenzene on Cu(111): an exceptional case of on-surface Ullmann coupling. *Chem. Commun.*, 51:13301–13304, 2015.

[125] J. Bushell, A. F. Carley, M. Coughlin, P. R. Davies, D. Edwards, D. J. Morgan, and M. Parsons. The reactive chemisorption of alkyl iodides at Cu(110) and Ag(111) surfaces: A combined STM and XPS study. *J. Phys. Chem. B*, 109:9556–9566, 2005.

[126] S. Doniach and M. Sunjic. Many-electron singularity in X-Ray photoemission and X-Ray line spectra from metals. *J. Phys. C: Solid. St. Phys.*, 3:285–291, 1970.

[127] J. Repp, G. Meyer, S. M. Stojkovic, A. Gourdon, and C. Joachim. Molecules on insulating films: Scanning-tunneling microscopy imaging of individual molecular orbitals. *Phys. Rev. Lett.*, 94:026803, 2005.

[128] D. Käfer and G. Witte. Evolution of pentacene films on Ag(111): Growth beyond the first monolayer. *Chem. Phys. Lett.*, 442:376–383, 2007.

[129] Y. Zou, L. Kilian, A. Schöll, T. Schmidt, R. Fink, and E. Umbach. Chemical bonding of PTCDA on Ag surfaces and the formation of interface states. *Surf. Sci.*, 600:1240–1251, 2006.

[130] P. Ruffieux, J. M. Cai, N. C. Plumb, L. Patthey, D. Prezzi, A. Ferretti, E. Molinari, X. L. Feng, K. Müllen, C. A. Pignedoli, and R. Fasel. Electronic structure of atomically precise graphene nanoribbons. *ACS Nano*, 6:6930–6935, 2012.

[131] R. Gutzler, W. M. Heckl, and M. Lackinger. Combination of a knudsen effusion cell with a quartz crystal microbalance: In situ measurement of molecular evaporation rates with a fully functional deposition source. *Rev. Sci. Instrum.*, 81(1):015108, 2010.

[132] P. Ruffieux, S. Y. Wang, B. Yang, C. Sanchez-Sanchez, J. Liu, T. Dienel, L. Talirz, P. Shinde, C. A. Pignedoli, D. Passerone, T. Dumslaff, X. L. Feng, K. Müllen, and R. Fasel. On-surface synthesis of graphene nanoribbons with zigzag edge topology. *Nature*, 531:489–493, 2016.

[133] A. Rastgoo-Lahrood, J. Björk, M. Lischka, J. Eichhorn, S. Kloft, M. Fritton, T. Strunskus, D. Samanta, M. Schmittel, W. M. Heckl, and M. Lackinger. Post-synthetic decoupling of on-surface-synthesized covalent nanostructures from Ag(111). *Angew. Chem. Int. Ed.*, 55:7650–7654, 2016.

[134] L. D. S. Lapitan, B. J. V. Tongol, and S. L. Yau. In situ scanning tunneling microscopy imaging of electropolymerized poly(3,4-ethylenedioxythiophene) on an iodine-modified Au(111) single crystal electrode. *Electrochim. Acta*, 62:433–440, 2012.

[135] X. P. Gao and M. J. Weaver. Probing redox-induced molecular-transformations by atomic-resolution scanning tunneling microscopy - iodide adsorption and electrooxidation on Au(111) in aqueous-solution. *J. Am. Chem. Soc.*, 114:8544–8551, 1992.

[136] W. Haiss, J. K. Sass, X. Gao, and M. J. Weaver. Iodine adlayer structures on Au(111) as discerned by atomic-resolution scanning tunneling microscopy - relation to iodide electrochemical adsorption. *Surf. Sci.*, 274:L593–L598, 1992.

[137] A. Migani and F. Illas. A systematic study of the structure and bonding of halogens on low-index transition metal surfaces. *J. Phys. Chem. B*, 110:11894–11906, 2006.

[138] R. G. Nuzzo and D. L. Allara. Adsorption of bifunctional organic disulfides on gold surfaces. *J. Am. Chem. Soc.*, 105:4481–4483, 1983.

[139] R. L. Whetten, J. T. Khoury, M. M. Alvarez, S. Murthy, I. Vezmar, Z. L. Wang, P. W. Stephens, C. L. Cleveland, W. D. Luedtke, and U. Landman. Nanocrystal gold molecules. *Adv. Mater.*, 8:428–433, 1996.

[140] A. C. Templeton, W. P. Wuelfing, and R. W. Murray. Monolayer-protected cluster molecules. *Acc. Chem. Res.*, 33:27–36, 2000.

[141] M. A. Reed, C. Zhou, C. J. Müller, T. P. Burgin, and J. M. Tour. Conductance of a molecular junction. *Science*, 278:252–254, 1997.

[142] M. Dorogi, J. Gomez, R. Osifchin, R. P. Andres, and R. Reifenberger. Room-temperature coulomb blockade from a self-assembled molecular nanostructure. *Phys. Rev. B*, 52:9071–9077, 1995.

[143] D. I. Gittins, D. Bethell, D. J. Schiffrin, and R. J. Nichols. A nanometre-scale electronic switch consisting of a metal cluster and redox-addressable groups. *Nature*, 408:67–69, 2000.

[144] X. D. Cui, A. Primak, X. Zarate, J. Tomfohr, O. F. Sankey, A. L. Moore, T. A. Moore, D. Gust, G. Harris, and S. M. Lindsay. Reproducible measurement of single-molecule conductivity. *Science*, 294:571–574, 2001.

[145] M. Marschall, J. Reichert, A. Weber-Bargioni, K. Seufert, W. Auwärter, S. Klyatskaya, G. Zoppellaro, M. Ruben, and J. V. Barth. Random two-dimensional string networks based on divergent coordination assembly. *Nat. Chem.*, 2:131–137, 2010.

[146] G. R. Newkome, P. Wang, C. N. Moorefield, T. J. Cho, P. P. Mohapatra, S. Li, S.-H. Hwang, O. Lukoyanova, L. Echegoyen, J. A. Palagallo, V. Lancu, and S.-W. Hla. Nanoassembly of a fractal polymer: A molecular "Sierpiński hexagonal gasket". *Science*, 312:1782–1785, 2006.

[147] J. Shang, Y. Wang, M. Chen, J. Dai, X. Zhou, J. Kuttner, G. Hilt, X. Shao, J. M. Gottfried, and K. Wu. Assembling molecular Sierpiński triangle fractals. *Nat. Chem.*, 7:389–393, 2015.

[148] X. Zhang, N. Li, G. C. Gu, H. Wang, D. Nieckarz, P. Szabelski, Y. He, Y. Wang, C. Xie, Z. Y. Shen, J. T. Lu, H. Tang, L. M. Peng, S. M. Hou, K. Wu, and Y. F. Wang. Controlling molecular growth between fractals and crystals on surfaces. *ACS Nano*, 9:11909–11915, 2015.

[149] X. Zhang, N. Li, L. W. Liu, G. C. Gu, C. Li, H. Tang, L. M. Peng, S. M. Hou, and Y. F. Wang. Robust Sierpiński triangle fractals on symmetry-mismatched Ag(100). *Chem. Commun.*, 52:10578–10581, 2016.

[150] N. Li, X. Zhang, G. C. Gu, H. Wang, D. Nieckarz, P. Szabelski, Y. He, Y. Wang, J. T. Lue, H. Tang, L. M. Peng, S. M. Hou, K. Wu, and Y. F. Wang. Sierpiński-triangle fractal crystals with the C_{3v} point group. *Chin. Chem. Lett.*, 26:1198–1202, 2015.

[151] Q. Sun, L. L. Cai, H. H. Ma, C. X. Yuan, and W. Xu. On-surface construction of a metal-organic Sierpiński triangle. *Chem. Commun.*, 51:14164–14166, 2015.

[152] G. C. Gu, N. Li, L. W. Liu, X. Zhang, Q. M. Wu, D. Nieckarz, P. Szabelski, L. M. Peng, B. K. Teo, S. M. Hou, and Y. F. Wang. Growth of covalently bonded Sierpiński triangles up to the second generation. *RSC Adv.*, 6:66548–66552, 2016.

[153] J. Noh, E. Ito, K. Nakajima, J. Kim, H. Lee, and M. Hara. High-resolution STM and XPS studies of thiophene self-assembled monolayers on Au(111). *J. Phys. Chem. B*, 106:7139–7141, 2002.

[154] H. Wang, S. Chen, L. Li, and S. Jiang. Improved method for the preparation of carboxylic acid and amine terminated self-assembled monolayers of alkanethiolates. *Langmuir*, 21:2633–2633, 2005.

[155] C. M. Whelan, M. R. Smyth, and C. J. Barnes. HREELS, XPS, and electrochemical study of benzenethiol adsorption on Au(111). *Langmuir*, 15:116–126, 1999.

[156] T. Sirtl, J. Jelic, J. Meyer, K. Das, W. M. Heckl, W. Moritz, J. Rundgren, M. Schmittel, K. Reuter, and M. Lackinger. Adsorption structure determination of a large polyaromatic trithiolate on Cu(111): combination of LEED-I(V) and DFT-vdW. *Phys. Chem. Chem. Phys.*, 15:11054–11060, 2013.

[157] P. Maksymovych and J. T. Yates. Au adatoms in self-assembly of benzenethiol on the Au(111) surface. *J. Am. Chem. Soc.*, 130:7518–7519, 2008.

[158] A. L. Vance, T. M. Willey, A. J. Nelson, T. van Buuren, C. Bostedt, L. J. Terminello, G. A. Fox, M. Engelhard, and D. Baer. XAS and XPS characterization of monolayers derived from a dithiol and structurally related disulfide-containing polyamides. *Langmuir*, 18:8123–8128, 2002.

[159] T. Ishida, N. Choi, W. Mizutani, H. Tokumoto, I. Kojima, H. Azehara, H. Hokari, U. Akiba, and M. Fujihira. High-resolution X-ray photoelectron spectra of organosulfur monolayers on Au(111): S(2p) spectral dependence on molecular species. *Langmuir*, 15:6799–6806, 1999.

[160] Y. W. Yang and L. J. Fan. High-resolution XPS study of decanethiol on Au(111): Single sulfur-gold bonding interaction. *Langmuir*, 18:1157–1164, 2002.

[161] P. Angelova, E. Solel, G. Parvari, A. Turchanin, M. Botoshansky, A. Gölzhäuser, and E. Keinan. Chemisorbed monolayers of corannulene penta-thioethers on gold. *Langmuir*, 29:2217–2223, 2013.

[162] D. Nieckarz and P. Szabelski. Simulation of the self-assembly of simple molecular bricks into Sierpiński triangles. *Chem. Commun.*, 50:6843–6845, 2014.

[163] D. Nieckarz and P. Szabelski. Chiral and fractal: from simple design rules to complex supramolecular constructs. *Chem. Commun.*, 52:11642–11645, 2016.

[164] C.-F. Chen and Y.-X. Ma. *Iptycenes chemistry: from synthesis to applications*. Springer, 2013.

[165] A. Bashir-Hashemi, H. Hart, and D. L. Ward. Tritriptycene: a D_{3h} C_{62} hydrocarbon with three u-shaped cavities. *J. Am. Chem. Soc.*, 108:6675–6679, 1986.

[166] R. Bhola, P. Payamyar, D. J. Murray, B. Kumar, A. J. Teator, M. U. Schmidt, S. M. Hammer, A. Saha, J. Sakamoto, A. D. Schlüter, and B. T. King. A two-dimensional polymer from the anthracene dimer and triptycene motifs. *J. Am. Chem. Soc.*, 135:14134–14141, 2013.

[167] D. J. Murray, D. D. Patterson, P. Payamyar, R. Bhola, W. T. Song, M. Lackinger, A. D. Schlüter, and B. T. King. Large area synthesis of a nanoporous two-dimensional polymer at the air/water interface. *J. Am. Chem. Soc.*, 137:3450–3453, 2015.

[168] P. C. M. Grim, S. De Feyter, A. Gesquiere, P. Vanoppen, M. Rücker, S. Valiyaveettil, G. Moessner, K. Müllen, and F. C. De Schryver. Submolecularly resolved polymerization of diacetylene molecules on the graphite surface observed with scanning tunneling microscopy. *Angew. Chem. Int. Ed.*, 36:2601–2603, 1997.

[169] T. Takami, H. Ozaki, M. Kasuga, T. Tsuchiya, Y. Mazaki, D. Fukushi, A. Ogawa, M. Uda, and M. Aono. Periodic structure of a single sheet of a clothlike macromolecule (atomic cloth) studied by scanning tunneling microscopy. *Angew. Chem. Int Ed.*, 36:2755–2757, 1997.

[170] A. Miura, S. De Feyter, M. M. S. Abdel-Mottaleb, A. Gesquiere, P. C. M. Grim, G. Moessner, M. Sieffert, M. Klapper, K. Mullen, and F. C. De Schryver. Light- and STM-tip-induced formation of one-dimensional and two-dimensional organic nanostructures. *Langmuir*, 19:6474–6482, 2003.

[171] B. Valeur and M. N. Berberan-Santos. *Molecular Fluorescence: Principles and Applications*. Wiley-VCH Verlag, 2001.

[172] H. U. Yang, J. D'Archangel, M. L. Sundheimer, E. Tucker, G. D. Boreman, and M. B. Raschke. Optical dielectric function of silver. *Phys. Rev. B*, 91:235137, 2015.

[173] R. L. Olmon, B. Slovick, T. W. Johnson, D. Shelton, S. H. Oh, G. D. Boreman, and M. B. Raschke. Optical dielectric function of gold. *Phys. Rev. B*, 86:235147, 2012.

[174] G. Kresse and J. Furthmüller. Efficient iterative schemes for ab initio total-energy calculations using a plane-wave basis set. *Phys. Rev. B*, 54:11169–11186, 1996.

[175] P. E. Blöchl. Projector augmented-wave method. *Phys. Rev. B*, 50:17953–17979, 1994.

[176] M. Dion, H. Rydberg, E. Schröder, D. C. Langreth, and B. I. Lundqvist. Van der Waals density functional for general geometries. *Phys. Rev. Lett.*, 92:246401, 2004.

[177] T. Thonhauser, V. R. Cooper, S. Li, A. Puzder, P. Hyldgaard, and D. C. Langreth. Van der Waals density functional: Self-consistent potential and the nature of the van der Waals bond. *Phys. Rev. B*, 76:125112, 2007.

[178] I. Hamada. van der Waals density functional made accurate. *Phys. Rev. B*, 89:121103, 2014.

[179] J. Björk and S. Stafström. Adsorption of large hydrocarbons on coinage metals: A van der Waals density functional study. *ChemPhysChem*, 15:2851–2858, 2014.

[180] N. Lorente and M. Persson. Theoretical aspects of tunneling-current-induced bond excitation and breaking at surfaces. *Faraday Discuss.*, 117:277–290, 2000.

[181] M. J. Frisch, G. W. Trucks, H. B. Schlegel, G. E. Scuseria, M. A. Robb, J. R. Cheeseman, G. Scalmani, V. Barone, B. Mennucci, G. A. Petersson, H. Nakatsuji, M. Caricato, X. Li, H. P. Hratchian, A. F. Izmaylov, J. Bloino, G. Zheng, J. L. Sonnenberg, M. Hada, M. Ehara, and et al. Gaussian 09, Revision D.01, Gaussian Inc., Wallingford CT, 2013.

[182] Axel D. Becke. Density-functional thermochemistry. III. the role of exact exchange. *J. Chem. Phys.*, 98:5648–5652, 1993.

[183] C. Lee, W. Yang, and R. G. Parr. Development of the Colle-Salvetti correlation-energy formula into a functional of the electron density. *Phys. Rev. B*, 37:785–789, 1988.

[184] T. H. Dunning Jr. and P. J. Hay. In. *Modern Theoretical Chemistry;*, Ed. H. F. Schaefer III, Vol. 3, Plenum, New York, 1977:pp 1–28.

[185] P. J. Hay and W. R. Wadt. Ab initio effective core potentials for molecular calculations - potentials for the transition-metal atoms Sc to Hg. *J. Chem. Phys.*, 82:270–283, 1985.

[186] P. J. Hay and W. R. Wadt. Ab initio effective core potentials for molecular calculations. potentials for K to Au including the outermost core orbitals. *J. Chem. Phys.*, 82:299–310, 1985.

[187] J. P. Perdew, K. Burke, and M. Ernzerhof. Generalized gradient approximation made simple. *Phys. Rev. Lett.*, 77:3865–3868, 1996.

[188] J. VandeVondele, M. Krack, F. Mohamed, M. Parrinello, T. Chassaing, and J. Hutter. Quickstep: Fast and accurate density functional calculations using a mixed Gaussian and plane waves approach. *Comput. Phys. Commun.*, 167:103–128, 2005.

[189] J. Hutter, M. Iannuzzi, F. Schiffmann, and J. VandeVondele. CP2K: atomistic simulations of condensed matter systems. *WIREs Comput. Mol. Sci.*, 4:15–25, 2014.

[190] S. Grimme. Semiempirical GGA-type density functional constructed with a long-range dispersion correction. *J. Comput. Chem.*, 27:1787–1799, 2006.

[191] D. Frenkel and B. Smit. *Understanding Molecular Simulation: From Algorithms to Applicationsirtl.* Academic Press, 2002.

Curriculum Vitae

Atena Rastgoo Lahrood

11/2011-Pres.	Doktorandin, Physik Technische Universität München (TUM)
04/2009-08/2011	MSc. Physik Ruhr-Universität Bochum (RUB)
10/2007-03/2009	BSc. Physik Ruhr-Universität Bochum (RUB)

Acknowledgments

I would like to thank my supervisor Markus Lackinger, for invaluable guidance throughout my PhD, the intensive scientific discussions and thoughtful feedback on my research. My special thanks go to Wolfgang Heckl, for the opportunity to complete my research in his laboratory.
I am also very thankful to:
- Stephan Kloft for the construction of STM and constant technical support.
- My colleagues in the STM research group, Matthias, Massimo, Lukas, Oliver, and Saskia for their collaboration in the UHV projects and pleasant atmosphere in the laboratory and social activities.
- My former colleagues, Thomas Sirtl and Stefan Schlögl, who patiently answered all my questions at the beginning of my PhD.
- The workshop of the faculty of geoscience at LMU, especially Günter Hesberg for manufacturing the components of the UHV system.
- Prof. Dr. Stefan Sotier for his support in the scientific field and support in ToF-SIMS measurements.
- Our external collaborators:

- Prof. Jonas Björk and Dr. Natalia Martsinovich for DFT calculations.
- Dr. Pawel Szabelski and Damian Nieckarz for Monte-Carlo simulations.
- Dr. Thomas Strunskus for his support during measurements at BESSY II and inputs on data analysis.
- Prof. Benjamin King and Prof. Michael Schmittel for the synthesis of molecules studied in this thesis.
- Dr. Stefan Reichlmaier for supervising ToF-SIMS measurements.

My heartfelt thanks go to my friends, who became a part of my life during the last years for all the emotional support, entertainment, particularly to Farzad for his proof-reading.
At the end, I am eternally grateful for the unconditional love and support of my family, who always had faith in me and encouraged me to pursue my goals.